

<sup>1</sup> Observation of the Higgs boson in the  $WW^*$   
<sup>2</sup> channel and search for Higgs boson pair  
<sup>3</sup> production in the  $b\bar{b}b\bar{b}$  channel with the  
<sup>4</sup> ATLAS detector

<sup>5</sup> A DISSERTATION PRESENTED  
<sup>6</sup> BY  
<sup>7</sup> TOMO LAZOVICH  
<sup>8</sup> TO  
<sup>9</sup> THE DEPARTMENT OF PHYSICS

<sup>10</sup> IN PARTIAL FULFILLMENT OF THE REQUIREMENTS  
<sup>11</sup> FOR THE DEGREE OF  
<sup>12</sup> DOCTOR OF PHILOSOPHY  
<sup>13</sup> IN THE SUBJECT OF  
<sup>14</sup> PHYSICS

<sup>15</sup> HARVARD UNIVERSITY  
<sup>16</sup> CAMBRIDGE, MASSACHUSETTS  
<sup>17</sup> MAY 2016

<sup>18</sup> ©2016 – TOMO LAZOVICH

<sup>19</sup> ALL RIGHTS RESERVED.

<sup>20</sup> **Observation of the Higgs boson in the  $WW^*$  channel and search  
<sup>21</sup> for Higgs boson pair production in the  $b\bar{b}b\bar{b}$  channel with the  
<sup>22</sup> ATLAS detector**

<sup>23</sup> ABSTRACT

<sup>24</sup> This dissertation presents the observation and measurement of the Higgs boson in the  $H \rightarrow WW^* \rightarrow$   
<sup>25</sup>  $\ell\nu\ell\nu$  channel at  $\sqrt{s} = 7$  TeV and  $\sqrt{s} = 8$  TeV and a search for Higgs pair production in the  $HH \rightarrow$   
<sup>26</sup>  $b\bar{b}b\bar{b}$  channel at  $\sqrt{s} = 13$  TeV with the ATLAS detector in  $pp$  collisions at the Large Hadron Collider.

<sup>27</sup> First, the discovery of a particle consistent with the Higgs boson in  $4.8 \text{ fb}^{-1}$  at  $\sqrt{s} = 7$  TeV and  
<sup>28</sup>  $5.8 \text{ fb}^{-1}$  at  $\sqrt{s} = 8$  TeV is discussed. Then, the measurement of the Higgs boson signal strength  
<sup>29</sup> and cross section in both the gluon fusion and vector boson fusion (VBF) production modes using  
<sup>30</sup>  $20.3 \text{ fb}^{-1}$  of  $\sqrt{s} = 8$  TeV data combined with  $4.8 \text{ fb}^{-1}$  of 7 TeV data is shown. The combined signal  
<sup>31</sup> strength is measured to be  $\mu = 1.09^{+0.23}_{-0.21}$ . The total observed significance of the  $H \rightarrow WW^*$  process  
<sup>32</sup> is observed to be  $6.1\sigma$  (with  $5.8\sigma$  expected). Advanced methods for background reduction and estima-  
<sup>33</sup> tion, particularly in same-flavor lepton final states, are shown. The VBF signal strength is measured to  
<sup>34</sup> be  $\mu_{\text{VBF}} = 1.27^{+0.53}_{-0.45}$  with an observed significance of  $3.2\sigma$  (with  $2.7\sigma$  expected). In the VBF chan-  
<sup>35</sup> nel, a selection requirement based method, the precursor to the final multivariate technique used for the  
<sup>36</sup> result, is detailed.

<sup>37</sup> Finally, a search for Higgs pair production in the  $b\bar{b}b\bar{b}$  final state with  $3.2 \text{ fb}^{-1}$  at  $\sqrt{s} = 13$  TeV is  
<sup>38</sup> presented. A particular focus is placed on a tailored signal region for resonant production of Higgs pairs  
<sup>39</sup> at high masses. No significant excesses are observed, and upper limits on cross sections are placed for  
<sup>40</sup> spin-2 Randall Sundrum gravitons (RSG) and narrow spin-0 resonances. The cross section of  $\sigma(pp \rightarrow$   
<sup>41</sup>  $G_{\text{KK}}^* \rightarrow hh \rightarrow b\bar{b}b\bar{b})$  with  $k/\bar{M}_{\text{Pl}} = 1$  is constrained to be less than  $70 \text{ fb}$  for masses in the range  
<sup>42</sup>  $600 < m_{G_{\text{KK}}^*} < 3000 \text{ GeV}$ . The cross section upper limits for  $\sigma(pp \rightarrow H \rightarrow hh \rightarrow b\bar{b}b\bar{b})$  ranges  
<sup>43</sup> from 30 to  $300 \text{ fb}$  in the mass range of  $500 < m_H < 3000 \text{ GeV}$ .

# Contents

44

45	o INTRODUCTION	I
46	I Theoretical and Experimental Background	5
47	I THE PHYSICS OF THE HIGGS BOSON	6
48	1.1 The Standard Model of Particle Physics	6
49	1.2 Electroweak Symmetry Breaking and the Higgs	8
50	1.3 Higgs Boson Production and Decay	10
51	1.4 Higgs Pair Production in the Standard Model	15
52	1.5 Higgs Pair Production in Theories Beyond the Standard Model	17
53	1.6 Conclusion	21
54	2 THE ATLAS DETECTOR AND THE LARGE HADRON COLLIDER	23
55	2.1 The Large Hadron Collider	24
56	2.2 The ATLAS Detector	26
57	2.3 The ATLAS Muon New Small Wheel Upgrade	37
58	2.4 Object Reconstruction in ATLAS	41
59	II Observation and measurement of Higgs boson decays to $WW^*$ in LHC	
60	Run 1 at $\sqrt{s} = 7$ and 8 TeV	50
61	3 $H \rightarrow WW^* \rightarrow \ell\nu\ell\nu$ ANALYSIS STRATEGY	51
62	3.1 Introduction	51
63	3.2 The $H \rightarrow WW^* \rightarrow \ell\nu\ell\nu$ signal in ATLAS	52
64	3.3 Background processes	53
65	3.4 Shared signal region selection requirements	56
66	3.5 Background reduction in same-flavor final states	60
67	3.6 Parameters of interest and statistical treatment	64
68	4 THE DISCOVERY OF THE HIGGS BOSON AND THE ROLE OF THE $H \rightarrow WW^* \rightarrow \ell\nu\ell\nu$ CHANNEL	70
69	4.1 Introduction	70

71	4.2	Data and simulation samples . . . . .	71
72	4.3	$H \rightarrow WW \rightarrow e\nu\mu\nu$ search . . . . .	71
73	4.4	$H \rightarrow \gamma\gamma$ search . . . . .	76
74	4.5	$H \rightarrow ZZ \rightarrow 4\ell$ search . . . . .	77
75	4.6	Combined results . . . . .	78
76	4.7	Conclusion . . . . .	80
77	5	OBSERVATION OF VECTOR BOSON FUSION PRODUCTION OF $H \rightarrow WW^* \rightarrow \ell\nu\ell\nu$	83
78	5.1	Introduction . . . . .	83
79	5.2	Data and simulation samples . . . . .	84
80	5.3	Object selection . . . . .	88
81	5.4	Analysis selection . . . . .	91
82	5.5	Background estimation . . . . .	100
83	5.6	Systematic uncertainties . . . . .	110
84	5.7	Results . . . . .	113
85	6	COMBINED RUN I $H \rightarrow WW^* \rightarrow \ell\nu\ell\nu$ RESULTS	118
86	6.1	Introduction . . . . .	118
87	6.2	Results of gluon fusion $H \rightarrow WW^* \rightarrow \ell\nu\ell\nu$ search . . . . .	119
88	6.3	Signal strength measurements in ggF and VBF production . . . . .	121
89	6.4	Measurement of Higgs couplings to vector bosons and fermions . . . . .	124
90	6.5	Higgs production cross section measurement . . . . .	125
91	6.6	Conclusion . . . . .	126
92	III	Search for Higgs pair production in the $HH \rightarrow b\bar{b}b\bar{b}$ channel in LHC	
93		Run 2 at $\sqrt{s} = 13$ TeV	128
94	7	SEARCH FOR HIGGS PAIR PRODUCTION IN BOOSTED $b\bar{b}b\bar{b}$ FINAL STATES	129
95	7.1	Introduction . . . . .	129
96	7.2	Motivation . . . . .	130
97	7.3	Data and simulation samples . . . . .	132
98	7.4	Event reconstruction and object selection . . . . .	134
99	7.5	Event selection . . . . .	137
100	7.6	Data-driven background estimation . . . . .	142
101	7.7	Systematic uncertainties . . . . .	148
102	7.8	Results . . . . .	151

103	<b>8 COMBINED LIMITS FROM BOOSTED AND RESOLVED SEARCHES</b>	153
104	8.1 Introduction . . . . .	153
105	8.2 Resolved results . . . . .	154
106	8.3 Search technique and results . . . . .	154
107	8.4 Limit setting . . . . .	155
108	<b>IV Looking ahead</b>	159
109	<b>9 CONCLUSION</b>	160
110	<b>APPENDIX A <i>b</i>-TAGGING PERFORMANCE AT HIGH <math>p_T</math></b>	164
111	A.1 Changes in MV2 score at high $p_T$ . . . . .	164
112	A.2 Effect of multiple <i>b</i> -quarks inside one jet . . . . .	166
113	A.3 Changes in track quality at high $p_T$ . . . . .	168
114	<b>REFERENCES</b>	171

# Listing of figures

116	I.1	The particles of the Standard Model and their properties [6]. . . . .	7
117	I.2	The four most common Higgs boson production modes at the LHC: (a) gluon-gluon fusion, (b) vector boson fusion, (c) $W/Z + H$ production, (d) $t\bar{t}H$ production . . . . .	11
118	I.3	Higgs production cross sections as a function of center of mass energy ( $\sqrt{s}$ ) at a $pp$ collider [18]. . . . .	12
119	I.4	Higgs boson branching ratios as a function of $m_H$ [18]. . . . .	14
120	I.5	The two leading diagrams for Standard Model di-Higgs production at the LHC: (a) box diagram, (b) Higgs self coupling . . . . .	16
121	I.6	Diagrams with new vertices for non-resonant Higgs pair production arising in composite Higgs models . . . . .	18
122	I.7	Generic Feynman diagram for resonant Higgs pair production in BSM theories . . . . .	18
123	I.8	Branching ratios for a spin-2 Randall-Sundrum graviton as a function of mass computed in MadGraph with the CP <sub>3</sub> -Origins implementation [25, 31] . . . . .	19
124	I.9	$\sigma \times \text{BR}(HH)$ for RSG as a function of mass computed in MadGraph with the CP <sub>3</sub> -Origins implementation [25, 31] . . . . .	20
125	I.10	RSG width as a function of mass computed in MadGraph with the CP <sub>3</sub> -Origins implementation [25, 31] . . . . .	20
126	I.11	Branching ratios for heavy Higgs $H$ in Type I (left) and Type II (right) 2HDM models with $\tan \beta = 1.5$ and $\cos(\beta - \alpha) = 0.1(0.01)$ for Type I (Type II). [29] . . . . .	21
127			
128	2.1	A schematic view of the LHC ring [37] . . . . .	24
129	2.2	A full diagram of the ATLAS detector [33] . . . . .	27
130	2.3	The ATLAS coordinate system . . . . .	28
131	2.4	Layout of the ATLAS Inner Detector system [41] . . . . .	29
132	2.5	Layout of the ATLAS calorimeter system [33] . . . . .	31
133	2.6	Layout of the ATLAS muon system [33] . . . . .	33
134	2.7	Predicted field integral as a function of $ \eta $ for the ATLAS magnet system [33] . . . . .	35
135	2.8	ATLAS trigger rates for Level-1 triggers as a function of instantaneous luminosity in 2012 and 2015 operation. These are single object triggers for electromagnetic clusters (EM), muons (MU), jets (J), missing energy (XE), and $\tau$ leptons (TAU). The threshold of the trigger is given in the name in GeV. [43] . . . . .	36

146	2.9	Instantaneous luminosity as a function of time for data recorded by ATLAS at different center of mass energies [44, 45] . . . . .	37
148	2.10	MDT tube hit (solid) and segment (dashed) efficiency as a function of hit rate per tube [46]	38
149	2.11	Trigger rate as a function of $p_T$ threshold with and without the NSW upgrade [46] . . . . .	39
150	2.12	Illustrations of the geometry (left) and operating principle (right) of the micromegas detector [46] . . . . .	40
152	2.13	Geometry of the sTGC detector [46] . . . . .	40
153	2.14	Illustration of particle interactions in ATLAS [49] . . . . .	42
154	2.15	Electron performance: (a) reconstruction efficiency as a function of electron $E_T$ [51] (b) energy resolution in simulation as a function of $ \eta $ for different energy electrons [52] . . . . .	43
155	2.16	Muon performance: (a) reconstruction efficiency as a function of muon $p_T$ (b) dimuon mass resolution as a function of average $p_T$ [53] . . . . .	44
158	2.17	Jet energy response after calibration as a function of true $p_T$ in simulation [57] . . . . .	46
159	2.18	Summary of the inputs to the MV2 $b$ -tagging algorithm . . . . .	47
160	2.19	Light jet rejection (1/efficiency) vs. $b$ -jet efficiency for MV1 and its input algorithms (a) [58] and MV2 (b) [59] in simulated $t\bar{t}$ events. The numbers in the algorithm names in (b) refer to the fraction of charm events used in the MV2 training. . . . .	47
163	2.20	Resolution of $E_T^{\text{miss}}$ components as a function of $\sum E_T$ before pileup suppression with different pileup techniques [61] . . . . .	49
165	3.1	Branching ratios for a $WW$ system. $q$ refers to quarks. $\ell$ can be either an electron or muon, and the leptonic branching ratios of the $\tau$ are included. For example, the $\ell\nu qq$ final state includes one $W$ decaying to $e\nu$ , $\mu\nu$ , or $\tau\nu$ . $\tau_h$ refer to hadronic decays of the $\tau$ . . . . .	53
168	3.2	Feynman diagram for Standard Model $WW$ production . . . . .	54
169	3.3	Feynman diagrams for top pair production (left) and $Wt$ production (right) . . . . .	54
170	3.4	An example Feynman diagram of $W$ +jets production . . . . .	55
171	3.5	An example Feynman diagram of $Z$ +jets production . . . . .	56
172	3.6	An illustration of the unique analysis signal regions [62]. The most sensitive regions for both gluon fusion and vector boson fusion production are underlined. . . . .	57
174	3.7	A graphical illustration of the $E_{T,\text{rel}}^{\text{miss}}$ calculation . . . . .	58
175	3.8	Predicted backgrounds (compared with data) as a function of $n_j$ (a and b) and $n_b$ (c) after pre-selection requirements . . . . .	59
177	3.9	An event display of a $Z/\gamma^*$ + jets event illustrating the effect of pileup interactions . . . . .	61
178	3.10	The RMS of different missing transverse momentum definitions as a function of the average number of interactions per bunch crossing . . . . .	61
180	3.11	The difference between the true and reconstructed values of the missing transverse momentum (a) and $m_T$ (b) in a gluon fusion signal sample . . . . .	63

182	3.12	Comparison of $f_{\text{recoil}}$ distributions for $Z/\gamma^* + \text{jets}$ , $H \rightarrow WW^*$ , and other backgrounds with real neutrinos. . . . .	64
183			
184	3.13	Signal significance as a function of required value for $f_{\text{recoil}}$ and $p_{\text{T},\text{rel}}^{\text{miss}(\text{trk})}$ in the ggF $H \rightarrow WW^*$ with $n_j = 0$ . . . . .	65
185			
186	4.1	Jet multiplicity distribution in data and MC after applying lepton, jet, and $E_{\text{T},\text{rel}}^{\text{miss}}$ selections. The $WW$ and top backgrounds have been normalized using control samples, and the hashed band indicates the total uncertainty on the prediction. [1] . . . . .	72
187			
188	4.2	Comparison of $m_{\text{T}}$ between data and simulation in the $n_j = 0$ $WW$ (a) and $n_j = 1$ top (b) control samples [1] . . . . .	74
189			
190	4.3	$m_{\text{T}}$ distribution in the $H \rightarrow WW \rightarrow e\nu\mu\nu$ $n_j \leq 1$ channels for 8 TeV data [1]. . . . .	76
191			
192	4.4	Diphoton mass spectrum in 7 and 8 TeV data. Panel a) shows the unweighted data distribution superimposed on the background fit, while panel c) shows the data where each event category is weighted by its signal to background ratio. Panels b) and d) show the respective distributions with background subtracted [1]. . . . .	77
193			
194	4.5	Four lepton invariant mass spectrum ( $m_{4\ell}$ ) in 7 and 8 TeV data compared to background estimate. A 125 GeV SM Higgs signal is shown in blue [1]. . . . .	78
195			
196	4.6	Local $p_0$ distribution as a function of hypothesized Higgs mass for the $H \rightarrow ZZ^* \rightarrow 4\ell$ (a), $H \rightarrow \gamma\gamma$ (b), and $H \rightarrow WW^* \rightarrow \ell\nu\ell\nu$ (c) channels. Dashed curves show expected results, while solid curves show observed. Red curves are from 7 TeV data, blue curves from 8 TeV, and black curved combined [1]. . . . .	80
197			
198	4.7	Combined 95% CL limits (a), local $p_0$ values (b), and signal strength measurement (c) as a function of Higgs mass [1]. . . . .	81
199			
200	4.8	Comparison of measured signal strength $\mu$ for a 126 GeV Higgs in the 7 and 8 TeV datasets [1]. . . . .	82
201			
202	4.9	Two dimensional likelihood as a function of signal strength $\mu$ and Higgs mass $m_H$ [1]. . . . .	82
203			
204	5.1	A comparison of the subleading lepton $p_{\text{T}}$ spectrum between VBF $H \rightarrow WW^*$ production and $t\bar{t}$ background . . . . .	85
205			
206	5.2	Leading jet $\eta$ in VBF $H \rightarrow WW^*$ (red) and $t\bar{t}$ (black) . . . . .	93
207			
208	5.3	Distributions of (a) $m_{jj}$ , (b) $\Delta y_{jj}$ , (c) $C_{\ell 1}$ , and (d) $\Sigma m_{\ell j}$ , for the VBF analysis. The top panels compare simulation and data, while the bottom panels show normalized distributions for all background processes and signal [62]. . . . .	95
209			
210	5.4	A cartoon of the WW final state. Momenta are represented with thin arrows, spins with thick arrows. [62] . . . . .	96
211			
212	5.5	Event display of a VBF candidate event [62]. . . . .	98
213			
214	5.6	Distributions of $m_{\ell\ell}$ (top left), $\Delta\phi_{\ell\ell}$ (top right), and $m_{\text{T}}$ (bottom), Higgs topology variables used in the selection requirements of the cut-based signal region and as inputs to the BDT result. These are plotted after all of the BDT pre-training selection cuts [62]. . . . .	99
215			
216			
217			

218	5.7	Distributions of $m_{jj}$ (top left), $\Delta y_{jj}$ (top right), $\sum C_\ell$ (bottom), VBF topology variables used in the selection requirements of the cut-based signal region and as inputs to the BDT result. These are plotted after all of the BDT pre-training selection cuts [62]. . . . .	100
219			
220	5.8	Distributions of $m_{jj}$ (a) and $O_{\text{BDT}}$ (b) in the VBF $n_b = 1$ top CR [62]. . . . .	103
221			
222	5.9	Comparison of $m_{jj}$ shape in a same flavor $Z \rightarrow \ell\ell$ control region and the VBF cut-based signal region. . . . .	104
223			
224	5.10	General illustration of the ABCD region definitions for $Z/\gamma^* \rightarrow \ell\ell$ background estimation. . . . .	105
225			
226	5.11	Distribution of $m_{\text{T}2}$ in the $WW$ validation region of the VBF analysis [62]. . . . .	107
227			
228	5.12	Extrapolation factors for the $W + \text{jets}$ estimate derived for muons (a) and electrons (b) as a function of lepton $p_T$ [62]. . . . .	109
229			
230	5.13	Background composition in final VBF signal region [62]. . . . .	110
231			
232	5.14	Variations in the top background extrapolation factor in the cut-based analysis due to PDF uncertainties, binned in $m_{\text{T}}$ . . . . .	112
233			
234	5.15	Variations in the top background extrapolation factor in the cut-based analysis due to QCD scale uncertainties, binned in $m_{\text{T}}$ . . . . .	112
235			
236	5.16	Post-fit distributions in the cut-based VBF analysis. Panel (a) shows the one-dimensional $m_{\text{T}}$ distribution, while (b) shows the data candidates split into the bins of $m_{\text{T}}$ and $m_{jj}$ used in the final fit [62]. . . . .	115
237			
238	5.17	Postfit distributions in the BDT VBF analysis [62]. . . . .	116
239			
240	5.18	Overlap between cut-based and BDT VBF signal region candidates in the $m_{jj}$ - $m_{\text{T}}$ plane. .	117
241			
242	6.1	Post-fit $m_{\text{T}}$ distribution in the $n_j \leq 1$ regions [62]. . . . .	120
243			
244	6.2	Best fit signal strength $\hat{\mu}$ as a function of hypothesized $m_H$ [62]. . . . .	122
245			
246	6.3	Local $p_0$ as a function of $m_H$ [62]. . . . .	122
247			
248	6.4	Likelihood as a function of $\mu_{\text{VBF}}/\mu_{\text{ggF}}$ [62]. . . . .	123
249			
250	6.5	Likelihood scan as a function of $\mu_{\text{VBF}}$ and $\mu_{\text{ggF}}$ [62]. . . . .	124
251			
252	6.6	Likelihood scan as a function of $\kappa_F$ and $\kappa_V$ [62]. . . . .	125
253			
254	6.7	Comparison of signal strength measurements in different Higgs decay channels on ATLAS [91].	127
255			
256	7.1	Parton luminosity ratios as a function of resonance mass $M_X$ for 13/8 TeV and 7/8 TeV [92].	130
257			
258	7.2	Summary of $HH$ branching ratios [93]. . . . .	131
259			
260	7.3	Minimum $\Delta R$ between $B$ decay vertices for different RSG masses in a $G_{\text{KK}}^* \rightarrow HH \rightarrow 4b$ sample with $c = 1$ . . . . .	132
261			
262	7.4	Trigger efficiency for events passing all signal region selections as a function of mass in $G_{\text{KK}}^* \rightarrow HH \rightarrow 4b$ samples with $c = 1$ [102]. In the trigger names, “j” refers to a jet or jets. “ht” refers to $H_T$ , the scalar sum of transverse momenta in the event. “bloose” refers to a loose $b$ -tagging requirement applied to the jet. “aor” refers to anti- $k_T$ jets with $R = 1.0$ . The numbers at the end are the thresholds on the given quantity in GeV. . . . .	134
263			

254	7.5	Comparison of untrimmed and trimmed jet masses for large radius jets in a RSG sample with $m_{G_{\text{KK}}^*} = 1 \text{ TeV}$ . JES (JMS) refers to the standard jet energy (mass) scale calibration for ATLAS [57]. . . . .	135
255			
256	7.6	Efficiency of finding two $b$ -jets from each Higgs in an RSG event using calorimeter jets with $R = 0.3$ or different track jet radii [106] . . . . .	136
257			
258	7.7	Illustration of the boosted selection requirements on Higgs candidates. Each large-radius calorimeter jet (Higgs candidate) must contain two track jets . . . . .	138
259			
260	7.8	Estimated significance as a function of signal mass for RSG $c = 1$ models in the $3b$ (a) and $4b$ (b) regions for different $b$ -tagging efficiency working points . . . . .	139
261			
262	7.9	Acceptance $\times$ efficiency as a function of mass for (a) RSG and (b) narrow heavy scalar signal models [109]. . . . .	140
263			
264	7.10	Efficiency of requiring 3 or 4 $b$ -tagged track jets vs. RSG mass. The efficiency quoted is relative to the previous selection requirements (rather than an absolute efficiency). . . . .	141
265			
266	7.11	MV2c20 $b$ -tagging efficiency for each of the four track jets in the boosted $4b$ selection as a function of RSG mass for $c = 1$ models. . . . .	142
267			
268	7.12	$M_J^{\text{sublead}}$ vs. $M_J^{\text{lead}}$ in a $2 b$ -tag data sample. The signal region is defined by the inner black contour ( $X_{hh} < 1.6$ ) and the sideband region is defined by the outer contour ( $R_{hh} >$ $35.8 \text{ GeV}$ ). The region between the black contours is the control region. The mass region which is enriched in $t\bar{t}$ background is also shown for illustration. [109] . . . . .	143
269			
270	7.13	An illustration of the data-driven background estimation technique for the boosted analysis	145
271			
272	7.14	Leading large-R jet mass in the $3b$ (a) and $4b$ (b) sideband regions. The multijet and $t\bar{t}$ backgrounds are estimated using the data-driven methods described above. Because their normalizations are derived in the sideband region, the total background normalization is constrained by default to match the normalization of the data [109]. . . . .	146
273			
274	7.15	Di-jet invariant mass ( $M_{2J}$ ) in the $3b$ (a) and $4b$ (b) control regions. The multijet and $t\bar{t}$ backgrounds are estimated using the data-driven methods described above [109]. . . . .	147
275			
276	7.16	Di-jet invariant mass ( $M_{2J}$ ) in the $3b$ (a) and $4b$ (b) signal regions. The multijet and $t\bar{t}$ backgrounds are estimated using the data-driven methods described above. In the $3b$ re- gion, a graviton signal with $m_{G_{\text{KK}}^*} = 1.8 \text{ TeV}$ and $c = 1$ is overlaid, with the cross section multiplied by a factor of 50 so that the signal is visible. In the $4b$ region, signals with $m_{G_{\text{KK}}^*} = 1.0 \text{ TeV}$ and $m_{G_{\text{KK}}^*} = 1.5 \text{ TeV}$ are overlaid, both with $c = 1$ and the yields multiplied by factors of 2 and 5 respectively [109]. . . . .	152
277			
278	8.1	Di-jet invariant mass ( $M_{2J}$ ) in the resolved signal region. A graviton signal with $m_{G_{\text{KK}}^*} =$ $800 \text{ GeV}$ and $c = 1$ is overlaid. [109]. . . . .	155
279			
280	8.2	Expected and observed upper limit as a function of mass for $G_{\text{KK}}^*$ in the RSG model with (a) $c = 1$ and (b) $c = 2$ , as well as (c) $H$ with fixed $\Gamma_H = 1 \text{ GeV}$ , at the 95% confidence level in the $\text{CL}_s$ method. [109] . . . . .	158
281			
282			
283			
284			
285			

291	9.1	Combined ATLAS and CMS measurements in Run 1 for (a) Higgs signal strength in gluon		
292		fusion and VBF and (b) Higgs couplings normalized to their SM predictions . . . . .	162	
293	9.2	Discovery significance for RSG models at the HL-LHC in three different budget scenar-		
294		ios [116]. Systematic uncertainties on the background prediction ( $\sigma_B$ ) of 2.5% and 5.0%		
295		are both tested. . . . .	163	
296	A.1	$p_T$ of the leading track jet in the leading calorimeter jet for different signal masses in RSG		
297		$c = 1$ models . . . . .	165	
298	A.2	MV <sub>2c2o</sub> score for the leading track jet (a) and subleading track jet (b) of the leading calorime-		
299		ter jet for different signal masses in RSG $c = 1$ models . . . . .	165	
300	A.3	IP <sub>3D</sub> log-likelihood ratio ( $\log(p_b/p_u)$ ) of the leading track jet in the leading calorimeter		
301		jet for different signal masses in RSG $c = 1$ models . . . . .	166	
302	A.4	Mass (a) and number of tracks (b) for the secondary vertices computed with the SV1 algo-		
303		rithm. When no secondary vertex is found, the quantities are assigned to default negative		
304		values. . . . .	167	
305	A.5	Mass (a) and number of tracks (b) for vertices computed with the JetFitter algorithm.		
306		When no vertices are found, the quantities are assigned to default negative values. . . . .	167	
307	A.6	MV <sub>2c2o</sub> score (a) and SV1 mass (b) for leading track jets with two truth $b$ quarks ( $n_{tb,lead} =$		
308		2) compared to those with only one truth $b$ ( $n_{tb,lead} = 1$ ). . . . .	168	
309	A.7	Track fit $\chi^2/n_{DOF}$ (a) and number of pixel detector hits (b) for the leading track of the		
310		leading track jet in different mass RSG $c = 1$ samples . . . . .	169	
311	A.8	MV <sub>2c2o</sub> score (a) and SV1 mass (b) for leading track jets whose leading track jet has at least		
312		four pixel hits ( $N_{pix} \geq 4$ ) compared to those which do not ( $N_{pix} < 4$ ). . . . .	170	

# Listing of tables

313

314	1.1	Production cross sections for a 125 GeV Higgs boson at $\sqrt{s} = 8$ TeV with scale and PDF uncertainties [18]. . . . .	13
315	1.2	Branching ratios for a 125 GeV Higgs boson [18]. . . . .	15
316	1.3	Possible channels for Higgs searches. Checkmarks denote the most sensitive production modes [5]. . . . .	16
317	1.4	Production cross sections for pair production of a 125 GeV Higgs boson at $\sqrt{s} = 14$ TeV with total uncertainty [20]. The uncertainties include QCD scale and PDF variations as well as uncertainties on $\alpha_S$ . . . . .	17
318			
322	2.1	Evolution of LHC machine conditions [39, 40] . . . . .	26
323	2.2	Performance requirements for the ATLAS detector [33]. . . . .	37
324	2.3	Signal efficiencies for $WH$ production with $H \rightarrow b\bar{b}$ and $H \rightarrow WW^* \rightarrow \mu\nu qq$ under different trigger configurations [46]. . . . .	41
325			
326	3.1	A summary of backgrounds to the $H \rightarrow WW^* \rightarrow \ell\nu\ell\nu$ signal . . . . .	56
327			
328	4.1	Monte carlo generators used to model signal and background for the Higgs search [1]. . . . .	71
329	4.2	Normalization factors (ratio of data and MC yields in a control sample) for the Standard Model $WW$ and top backgrounds in the $H \rightarrow WW^* \rightarrow \ell\nu\ell\nu$ analysis [1]. Only statistical uncertainties are shown. . . . .	74
330			
331	4.3	Data and expected yields for signal and background in the final $H \rightarrow WW^* \rightarrow \ell\nu\ell\nu$ signal region. Uncertainties shown are both statistical and systematic. [1] . . . . .	75
332			
333	4.4	Summary of the expected and observed significance and measured signal strengths in the combined 7 and 8 TeV datasets for the Higgs discovery analysis [1]. . . . .	79
334			
335	5.1	Single lepton triggers used for electrons and muons. A logical “or” of the triggers listed for each lepton type is taken. Units are in GeV, and the $i$ denotes an isolation requirement in the trigger. . . . .	85
336			
337	5.2	Di-lepton triggers used for different flavor combinations. The two thresholds listed refer to leading and sub-leading leptons, respectively. The di-muon trigger only requires a single lepton at level-1. . . . .	85
338			
339			
340			

341	5.3	Trigger efficiency for signal events and relative gain of adding a dilepton trigger on top of the single lepton trigger selection. The first lepton is the leading, while the second is the sub-leading. Efficiencies shown here are for the ggF signal in the $n_j = 0$ category but are comparable for the VBF signal. . . . .	86
342	5.4	Monte Carlo samples used to model the signal and background processes [62]. . . . .	87
343	5.5	$p_T$ dependent isolation requirements for muons. Muons are required to have the amount of calorimeter or track based cone sums be less than this fraction of their $p_T$ . . . . .	89
344	5.6	$p_T$ dependent requirements for electrons. Electrons are required to have the amount of calorimeter or track based cone sums be less than this fraction of their $E_T$ . . . . .	90
345	5.7	Summary of event selection for the $n_j \geq 2$ VBF analysis in the 8 TeV cut-based analysis [62]. . . . .	97
346	5.8	Background composition after each requirement in the $n_j \geq 2$ VBF analysis in the 8 TeV cut-based analysis [62]. . . . .	97
347	5.9	Top normalization factors computed at each stage of the cut-based selection. Uncertainties are statistical only. . . . .	102
348	5.10	Top normalization factors computed for each bin of $O_{\text{BDT}}$ . Uncertainties are statistical only. . . . .	102
349	5.11	$Z/\gamma^* \rightarrow \tau\tau$ correction factors for the VBF cut-based analysis. Uncertainties are statistical only. . . . .	105
350	5.12	$Z/\gamma^* \rightarrow \ell\ell$ normalization factors for cut-based and BDT analyses. Uncertainties are statistical only. . . . .	106
351	5.13	Systematic uncertainties for various processes in the cut-based VBF analysis, given in units of % change in yield. Values are given for the low $m_{jj}$ signal region. . . . .	III
352	5.14	Composition of the post-fit uncertainties (in %) on the total signal ( $N_{\text{sig}}$ ), total background ( $N_{\text{bkg}}$ ), and individual background yields in the VBF analysis [62]. . . . .	114
353	5.15	Event selection for the VBF BDT analysis. The event yields in (a) are shown after the pre-selection and the additional requirements applied before the BDT classification (see text). The event yields in (b) are given in bins in $O_{\text{BDT}}$ after the classification [62]. . . . .	114
361	6.1	All signal regions definitions input into final statistical fit [62]. . . . .	119
362	6.2	Post-fit yields in the different ggF and VBF dedicated signal regions [62]. . . . .	120
371	7.1	Summary of requirements on objects used in the $X \rightarrow HH \rightarrow b\bar{b}b\bar{b}$ search . . . . .	137
372	7.2	Effect of boosted selection on data, RSG signal models, $t\bar{t}$ , and $Z+\text{jets}$ . The numbers from simulation are normalized with the MC generator cross section and do not take into account the data driven estimates described in section 7.6 [110]. . . . .	142
374	7.3	Mass region definitions used for background estimation . . . . .	144

376	7.4	Parameters derived for exponential fit to background $M_{2J}$ shape in the $3b$ and $4b$ signal regions [10] . . . . .	146
377	7.5	The number of events in data and predicted background events in the boosted 3-tag and 4-tag sideband and control regions. The uncertainties shown are statistical only. [109] . . .	147
378	7.6	Summary of systematic uncertainties in the total background and signal event yields (expressed in %) in the boosted 3-tag and 4-tag signal regions. Systematic uncertainties on the signal normalization are shown for models with $m_{G_{KK}^*} = 1.5$ TeV and both $c = 1$ and $c = 2$ as well as a narrow width heavy scalar. . . . .	149
379	7.7	Alternate fit functions used to model the $M_{2J}$ distribution in the QCD multijet background. In the equations, $x = M_{2J}/\sqrt{s}$ . . . . .	150
380	7.8	Observed yields in the 3-tag and 4-tag signal regions for the boosted analysis compared to the predicted number of background events Errors correspond to the total uncertainties in the predicted event yields. The yields for a graviton with $m_{G_{KK}^*} = 1$ TeV and $c = 1$ are also shown. [109] . . . . .	151
381	8.1	Observed yields in the resolve selection 4-tag signal region compared to the predicted number of background events Errors correspond to the total uncertainties in the predicted event yields. The yields for a graviton with $m_{G_{KK}^*} = 800$ GeV and $c = 1$ are also shown. [109] . . . . .	154
382			
383			
384			
385			
386			
387			
388			
389			
390			
391			
392			
393			



# Acknowledgments

396 I have been a member of the Harvard ATLAS group for many years now, first as an undergraduate and  
397 then as a graduate student. As a result, I have had the privilege of interacting with many amazing people  
398 there over the years and have accumulated a large list of folks to thank.

399 First and foremost, I must thank the two people who have effectively been my academic parents since I  
400 started in the Harvard group: João Guimarães da Costa and Melissa Franklin. Melissa Franklin and João  
401 Guimarães da Costa. They have both been so important to both my academic and personal development  
402 that I can't even put one before the other. João has been an excellent PhD advisor, showing me how to  
403 look at the big picture and helping me navigate the sometimes complicated politics of ATLAS. He got me  
404 started on my first projects with ATLAS as a young college sophomore before there was even beam in the  
405 LHC (go cosmic ray muons!). He has also been a constant source of advice and support, even when we  
406 have been on different continents. Melissa gave me my start in HEP as a summer student on CDF and  
407 has been an unbelievable mentor throughout my time at Harvard. I still remember our weekly chalkboard  
408 particle physics lessons after that first summer. She also graciously took me on as a co-advisee after João  
409 moved on to his new position at IHEP. I am incredibly lucky to have had both of them as advisors.

410 Another mentor who was essential to my development as a graduate student is Paolo Giromini. His un-  
411 canny knowledge and intuition about detectors is unmatched and I am very grateful to have had the chance  
412 to work with him on the micromegas for the ATLAS New Small Wheel upgrade project. I owe essentially  
413 all my practical knowledge about detectors (and building things in general) to him. I also appreciated his  
414 unique sense of humor which made sometimes difficult tasks much easier to get through.

415 I am grateful to John Huth and Masahiro Morii for their helpful advice as the other professors in the  
416 Harvard ATLAS group as well. I especially thank John for helping me get started on the micromegas  
417 trigger project and being a great professor to TF particle physics for. Additionally I thank Howard Georgi  
418 for serving as my third committee member and offering me feedback throughout my graduate career.

419 I also owe enormous thanks to Hugh Skottowe, the postdoc that I worked most closely with in my early  
420 years as a graduate student. He was always able to help me through complicated tasks in everything from  
421 writing code to understanding difficult physics concepts. I particularly enjoyed walking down to his office  
422 in Palfrey at random times and talking through whatever problem I was tackling on that day.

423 Alex Tuna, the second postdoc that I worked closely with at Harvard, deserves great thanks as well. He  
424 helped me push through to the end of my graduate career and offered great advice along the way.

425 Being at Harvard, I have seen an incredible array of graduate students graduate before me: Ben Smith,  
426 Verena Martinez Outschoorn, Srivas Prasad, Michael Kagan, Giovanni Zevi Della Porta, Laura Jeanty,  
427 Kevin Mercurio, William Spearman, and Andy Yen. I want to thank them all for showing me what a good  
428 physicist looks like and for patiently answering my questions and offering insightful advice about physics  
429 and life.

430 Getting through graduate school would not have been possible without the support and friendship of  
431 the other students in our group. Thanks to Emma Tolley for geeking out with me about cool comput-  
432 ing stuff, going to taste delicious beers with me, and helping start the Palfrey tradition of Taco Tuesdays.  
433 Thanks to Brian Clark for being a great friend and housing companion both in Kirkland House and in our  
434 tiny summer apartment in Geneva (and thanks to his partner Allison Goff for the same reasons!). Thanks  
435 to Siyuan Sun for giving me my first aikido lesson and always being there for great conversations, big and  
436 small. Tony (Baojia) Tong deserves special recognition for working with me on the  $4b$  analysis and putting  
437 up with my sometimes strange requests (and giving me rides to the Val Thoiry Migros so I wouldn't have  
438 to pay exorbitant Geneva grocery prices!). Stephen Chan is probably the only student in the group who  
439 both understands my references to the Sopranos and makes some of his own. To the younger graduate  
440 students - Karri Di Petrillo, Jennifer Roloff, Julia Gonski, and Ann Wang - I want to say thank you for  
441 making the group a fun and lively place to be and giving all of us energy that the older graduate students  
442 like myself can sometimes lack.

443 I'd like to thank Annie Wei and Gray Putnam, the two undergraduates I have worked with as a graduate  
444 student. Their unbelievable intuition and quickness in picking up difficult particle physics concepts is  
445 inspiring.

446 I would also like to thank all of the postdocs that I have interacted with in my time in the Harvard group:  
447 Kevin Black, Alberto Belloni (who would always ask me “Do you have it?”...I can now say that I do!),  
448 Shulamit Moed, Corrinne Mills, Geraldine Conti, David Lopez Mateos, Chris Rogan, Valerio Ippolito,  
449 and Stefano Zambito.

450 There are many people on ATLAS who have helped me get to this point as well. In the *WW* group, I  
451 have to thank Jonathan Long, Joana Machado Miguens, Ben Cerio, Philip Chang, Bonnie Chow, Richard  
452 Polifka, Heberth Torres, Tae Min Hong, and Jennifer Hsu for being wonderful colleagues and making the  
453 entire analysis run smoothly. In the *4b* group, I have to thank Qi Zeng, Tony Tong, Alex Tuna, Michael  
454 Kagan, Max Bellomo, John Alison, and Patrick Bryant.

455 Kirkland House was my home for the last three years of graduate school and was an wonderful envi-  
456 ronment and support system. I want to thank my fellow tutors, especially Brian Clark and Allison Goff  
457 (again), Zach Abel, Kelly Bodwin, Alex Lupsasca, John and Pam Park, Luke and Erin Walczewski, and  
458 Philip Gant for their friendship and support. I also want to thank Kate Drizos Cavell, Bob Butler, and the  
459 Faculty Deans Tom and Verena Conley.

460 There are still a few friends that haven’t been covered yet and deserve great thanks. Jake Connors and  
461 Meredith MacGregor have been absolutely wonderful friends and I thank them in particular for the many  
462 home-cooked meals and great conversations we’ve had in their apartment. Nihar Shah has been my friend  
463 and confidant since we were both wee freshmen in Harvard Yard. Gareth Kafka, though he sits on the  
464 “neutrino” side of Palfrey House, has made days there more fun and has also been an enthusiastic partici-  
465 pant in the Palfrey Taco Tuesdays.

466 Being at Harvard necessarily means having to navigate through bureaucracy at some point or another.  
467 I thank Lisa Cacciabuado, Carol Davis, and Jacob Barandes for always having open doors and being the  
468 most kind, helpful people in the Physics department.

469 I thank Venky Narayananuriti for putting on a great SPU course that I was proud to be a part of and  
470 TF for. I’d also like to thank Jim Waldo for offering me much advice about working in Computer Science  
471 and giving me a fun data project to be a part of in my free time.

472 I grew up in a very tight knit Serbian community on the south side of Chicago which helped make me

473 the person I am today. I would like to thank all of the people at St. Simeon Mirotochivi Serbian Orthodox  
474 Church who have always been sources of enthusiasm and support in my life.

475 I would not be here without the unconditional love and constant support and encouragement of my  
476 family. To my pokojni Deda Branko and Miloje, my pokojni Baba Milka, and my Baba Desa, I want to  
477 say thank you for instilling in me at an early age the love of curiosity and storytelling that I have carried  
478 throughout my life. To my sister Angelina, I want to say thank you for always loving me and being my  
479 partner in crime throughout our childhoods. To my parents, Miroljub and Nada, Tata and Mama, I really  
480 cannot express how grateful I am to you and how much I owe you. As I look back now I see how I am a  
481 combination of both of your best qualities and every day I am in situations where I understand more and  
482 more the lessons you made sure to teach me and the sacrifices you made to make sure I got the best possible  
483 education. I love you all.

484 Finally, I have to thank my soul mate, the one person in my life who understands me more than anyone  
485 else, my fiancée Kelly Brock. You are my sounding board, my support system, my cheerleader (figuratively  
486 and literally!), my best friend, my role model, and my everything. I would not have gotten through grad-  
487 uate school without you and my life would not be the same without you. I cannot wait to start our new  
488 lives together as the married doctors, tackling whatever comes our way with the same zeal with which we  
489 tackled graduate school. I love you with all my heart and soul.

# 0

490

491

## Introduction

492     The Higgs boson is often described as one of the cornerstones of particle physics. When the Standard  
493     Model was first developed as a theory to describe the fundamental particles and forces of nature, physicists  
494     were faced with a dilemma. The electroweak theory beautifully characterized both electromagnetism and  
495     the weak force with a single underlying framework. However, the mass of the weak  $W$  and  $Z$  bosons  
496     was puzzling given the fact that their electromagnetic counterpart, the photon, is massless. The Higgs  
497     mechanism was developed as the leading theory for the origin of this electroweak symmetry breaking. It  
498     predicted the existence of an additional spin-0 boson in the Standard Model, the Higgs boson. Generations  
499     of collider experiments searched for this elusive particle. This dissertation presents the story of the Higgs  
500     boson from its discovery to its use as a tool in the search for physics beyond the Standard Model with the  
501     ATLAS detector at the Large Hadron Collider (LHC).

502     One of the first priorities for the LHC when it began colliding proton beams in 2010 was the search for  
503     the Higgs boson. This search was initially tackled in three main channels:  $H \rightarrow \gamma\gamma$ ,  $H \rightarrow ZZ^* \rightarrow 4\ell$ ,

504 and  $H \rightarrow WW^* \rightarrow \ell\nu\ell\nu$ . Each channel has its own merits, but the  $WW^*$  mode is particularly suited  
505 to searching over a wide range of masses. The  $H \rightarrow WW^*$  branching ratio is large and it is the primary  
506 decay channel above the  $2m_W$  mass threshold. Despite the fact that the full Higgs invariant mass cannot  
507 be reconstructed in the  $H \rightarrow WW^* \rightarrow \ell\nu\ell\nu$  channel, its signal to background ratio makes it ideal for  
508 measurement of Higgs properties such as the production cross section and couplings.

509 In 2012, the ATLAS and CMS experiments announced the discovery of a new particle consistent with  
510 the Higgs boson [1, 2]. In ATLAS, this discovery was made with  $4.8 \text{ fb}^{-1}$  collected at  $\sqrt{s} = 7 \text{ TeV}$   
511 and  $5.8 \text{ fb}^{-1}$  at  $\sqrt{s} = 8 \text{ TeV}$ . This dissertation first presents the search for gluon fusion production  
512 of the Higgs in the  $H \rightarrow WW^* \rightarrow \ell\nu\ell\nu$  channel, which played an important role in this discovery.  
513 Selection requirements which were optimized to maximize the discovery significance in this channel, as  
514 well as background estimation procedures, are discussed.

515 After its discovery, interest in the Higgs shifted to focus on the measurement of its properties. As a  
516 result, extensions of the initial discovery analysis in larger datasets had two main goals. Improvement of  
517 signal to background ratio was important to allow for precision measurements. Also, searches for rarer  
518 production modes of the Higgs were a priority. The first such extension presented in this dissertation  
519 is a tailored selection for  $\ell\nu\ell\nu$  final states with same flavor leptons. Novel variables for the reduction of  
520 the  $Z+\text{jets}$  background that could remain robust under increasing LHC instantaneous luminosities are  
521 shown. The second post-discovery result shown is the first observation of Vector Boson Fusion (VBF)  
522 production of the Higgs boson in the  $H \rightarrow WW^* \rightarrow \ell\nu\ell\nu$  channel.

523 VBF production of the Higgs boson is particularly interesting in the  $H \rightarrow WW^* \rightarrow \ell\nu\ell\nu$  final state.  
524 In this combination of production and decay modes, the Higgs boson couples exclusively to  $W$  bosons,  
525 allowing for precise measurement of the Higgs- $W$  coupling constant. However, it is challenging to observe  
526 VBF Higgs production because its cross section at the LHC is an order of magnitude lower than gluon  
527 fusion production. The large  $H \rightarrow WW^*$  branching ratio thus presents another advantage over other  
528 final states. Additionally, VBF production of the Higgs boson creates two forward jets in addition to the  
529 Higgs, and these jets can be used to isolate VBF Higgs events from other production modes. The VBF  
530  $H \rightarrow WW^* \rightarrow \ell\nu\ell\nu$  analysis first created a selection requirement based signal region using variables

531 constructed specifically for the VBF Higgs production topology. This “cut-based” analysis is presented in  
532 detail in this dissertation. These VBF topology variables, once validated in the cut-based analysis, were  
533 then input into a multivariate boosted decision tree discriminant to achieve the first observation of VBF  
534 Higgs production in this final state with the full  $20.3 \text{ fb}^{-1}$  of  $\sqrt{s} = 8 \text{ TeV}$  data in ATLAS.

535 After a two year shutdown, the LHC restarted in 2015 with a center of mass energy of  $\sqrt{s} = 13 \text{ TeV}$ .  
536 This increase improved the LHC’s ability to probe for physics beyond the Standard Model, and the Higgs  
537 sector remained one of the largest regions of unprobed phase space where such new physics could be dis-  
538 covered. Production of high mass resonances benefited most from the center of mass energy increase. In  
539 particular, the cross section for a generic gluon-initiated 2 TeV resonance increased tenfold with the in-  
540 crease from 8 to 13 TeV. Therefore, a natural next step in studies of the Higgs was a search for a new  
541 heavy resonance which decays into a pair of Higgs bosons. The final result shown in this dissertation is a  
542 search for resonant di-Higgs production in the  $X \rightarrow HH \rightarrow b\bar{b}b\bar{b}$  final state with  $3.2 \text{ fb}^{-1}$  recorded by  
543 ATLAS at  $\sqrt{s} = 13 \text{ TeV}$ . This search has the unique advantage that it can both probe physics beyond  
544 the Standard Model and gain further understanding of the Standard Model through constraints on SM  
545 pair production of the Higgs.

546 As mentioned above, this dissertation begins by discussing the discovery of the Higgs and the role of  
547 the  $H \rightarrow WW^* \rightarrow \ell\nu\ell\nu$  channel. It then presents the first observation of the VBF production mode  
548 in  $H \rightarrow WW^* \rightarrow \ell\nu\ell\nu$  with the full ATLAS Run 1 dataset, as well as the final combined Run 1 mea-  
549 surements of gluon fusion Higgs production from this channel. Finally, it presents a search for Higgs pair  
550 production in the  $HH \rightarrow b\bar{b}b\bar{b}$  channel. It is organized into four parts.

551 Part 1 presents the theoretical and experimental background required for the subsequent parts. Chap-  
552 ter 1 gives an overview of Higgs physics, particularly single and double Higgs production in the Standard  
553 Model and beyond. Chapter 2 presents details regarding the Large Hadron Collider and the ATLAS experi-  
554 ment. The evolution of machine conditions, descriptions of the ATLAS sub-detectors, and an overview of  
555 object reconstruction in ATLAS are all shown. A brief interlude on the ATLAS Muon New Small Wheel  
556 upgrade is also given, as this upgrade has been a focus of my graduate work and will have an important  
557 impact on ATLAS’ ability to study the Higgs at the High Luminosity LHC.

558 Part 2 discusses the observation and measurement of the Higgs in the  $H \rightarrow WW^* \rightarrow \ell\nu\ell\nu$  channel  
559 in the ATLAS Run 1 dataset at  $\sqrt{s} = 7$  and 8 TeV. Because I worked in this channel from before the  
560 discovery through to the final analysis of the Run 1 dataset, Part 2 is organized in such a way to allow  
561 easy presentation of multiple analyses on different subsets of the full Run 1 dataset. Chapter 3 presents  
562 a general overview of the  $H \rightarrow WW^*$  analysis strategy and defines many of the variables and common  
563 elements used in the rest of Part 2. Chapter 4 presents the discovery of the Higgs boson, focusing on the  
564 role of the  $WW^*$  channel in this discovery. Chapter 5 presents the first observation of the VBF production  
565 mode of the Higgs in the  $WW^*$  channel, a result from the full Run 1 ATLAS dataset. In this chapter, the  
566 focus is mainly on the cut-based VBF analysis. The cut-based analysis was an important first step to the  
567 final VBF result which used a boosted decision tree. Where appropriate, connections between the cut-  
568 based and BDT analyses are shown and their compatibility is discussed. Finally, the VBF analysis was an  
569 important input into the combined Run 1  $H \rightarrow WW^* \rightarrow \ell\nu\ell\nu$  result, which used both the gluon fusion  
570 and VBF channels in a combined fit to infer properties of the Higgs, including its couplings to the gauge  
571 bosons and its production cross section. This is the topic of Chapter 6.

572 Part 3 presents a search for Higgs pair production in the  $HH \rightarrow b\bar{b}b\bar{b}$  channel. Chapter 7 presents  
573 an overview of this search in the boosted regime, where the Higgs pairs are the result of the decay of a  
574 heavy resonance. Chapter 8 shows the combined results between the boosted regime and the resolved  
575 regime, which is sensitive to lower mass resonances and non-resonant Higgs pair production. Finally, Part  
576 4 presents a conclusion and brief outlook of future Higgs physics with ATLAS.

# Part I

577

578

## Theoretical and Experimental Background

*In modern physics, there is no such thing as “nothing.”*

Richard Morris

# 1

579

580

## The Physics of the Higgs Boson

581     This chapter presents an overview of the Standard Model of Particle Physics and in particular the physics  
582     of the Higgs boson. First, a brief overview of the Standard Model and its history are presented. Then, a  
583     description of the Higgs mechanism of electroweak symmetry breaking is given. Next, the physics of single  
584     Higgs boson production and decay is described. The Standard Model also allows for production of two  
585     Higgs bosons and this is detailed as well. Finally, di-Higgs production in two beyond the Standard Model  
586     (BSM) theories - Randall-Sundrum gravitons (RSG) and Two Higgs Doublet Models (2HDM) - is shown.

587     **I.I THE STANDARD MODEL OF PARTICLE PHYSICS**

588     The Standard Model (SM) of Particle Physics is a quantum field theory describing the fundamental  
589     particles of nature and the forces that govern their interactions. Several comprehensive treatments of the  
590     SM already exist in the literature [3–8] and this section will not rehash those. Rather, this section presents  
591     a brief overview of the SM particles and forces in order to define them for subsequent discussions.

592      The Standard Model consists of two primary categories of fundamental particles: fermions (spin 1/2  
 593      particles) and bosons (integer spin particles). The SM also describes three forces: electromagnetism, the  
 594      weak nuclear force, and the strong nuclear force. Gravity is not included in the theory and is largely irrele-  
 595      vant at the scales currently probed by collider experiments. Within the fermions, there are both quarks  
 596      (which interact via all three forces) and the leptons. The charged leptons interact via electromagnetic and  
 597      weak interactions, while neutrinos (neutral leptons) interact only via the weak force. Within the bosons,  
 598      there are the  $W^\pm$  and  $Z$  bosons (the mediators of the weak force), the gluon ( $g$ , the mediator of the strong  
 599      force), and the photon ( $\gamma$ ), the mediator of the electromagnetic force. Finally, there is the Higgs boson,  
 600      a fundamental spin-0 particle resulting from the Higgs mechanism of electroweak symmetry breaking.

601      Figure 1.1 summarizes the fermions and bosons of the SM.

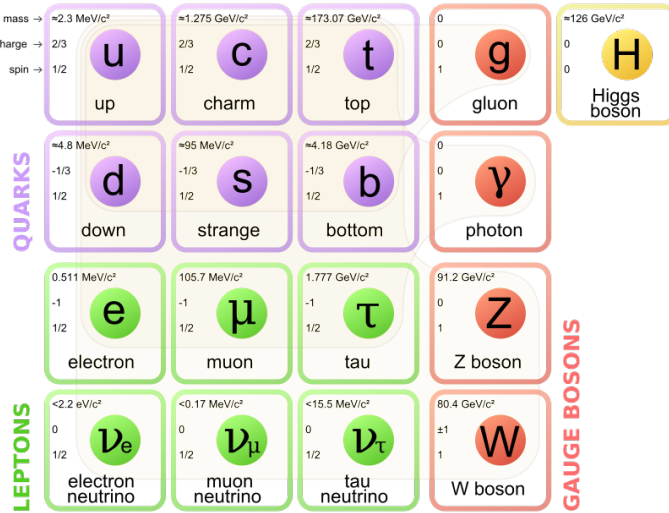


Figure 1.1: The particles of the Standard Model and their properties [6].

602      The Standard Model coalesced into a unified theoretical framework in the 1960s through the work  
 603      of Glashow, Weinberg, Salam, and others on the theory of electroweak interactions [9–12]. This theory  
 604      characterized both the electromagnetic and weak interactions as unified under a single gauge symmetry  
 605      group, namely  $SU(2) \times U(1)$ . At low enough energy scales (on the order of the  $W$  and  $Z$  masses, the  
 606      electroweak symmetry is broken, as evidenced by the fact that the weak bosons have mass while the photon  
 607      does not. The discovery of the Higgs boson in 2012 confirmed the Higgs mechanism as the most likely  
 608      candidate for this electroweak symmetry breaking [1, 2]. The electroweak theory is then combined with

609 the theory of quantum chromodynamics (which models the strong sector as a non-Abelian  $SU(3)$  gauge  
610 group) to form the complete SM [13].

611 1.2 ELECTROWEAK SYMMETRY BREAKING AND THE HIGGS

612 In the Standard Model Lagrangian, it is difficult to include mass terms for the  $W$  and  $Z$  bosons without  
613 breaking the fundamental gauge symmetry of the Lagrangian. A traditional mass term does not preserve  
614 the  $SU(2) \times U(1)$  symmetry. Additionally, scattering of massive  $W$  and  $Z$  bosons violate unitarity and  
615 these diagrams diverge at high energy scales. In the 1960s, Higgs, Brout, Englert, Guralnik, Kibble, and  
616 Hagen developed a mechanism for spontaneous symmetry breaking via the addition of a complex scalar  
617 doublet to the SM. Three of the four real degrees of freedom of this complex field would go to the lon-  
618 gitudinal modes of the  $W^\pm$  and  $Z$ , thus allowing them to have mass [14–17]. The remaining degree of  
619 freedom would manifest as an additional scalar, known now as the Higgs boson.

620 The mechanism works by introducing a Lagrangian for the newly introduced field that still respects the  
621 symmetry of the Standard Model inherently, but with a minimum at a non-zero vacuum expectation value  
622 for the field. In this minimum of the potential, the electroweak symmetry is broken. Specifically, consider  
623 a complex scalar doublet  $\Phi$  with four degrees of freedom, as shown in equation 1.1.

$$\Phi = \begin{pmatrix} \phi^+ \\ \phi^0 \end{pmatrix} = \frac{1}{\sqrt{2}} \begin{pmatrix} \phi_1^+ + i\phi_2^+ \\ \phi_1^0 + i\phi_2^0 \end{pmatrix} \quad (1.1)$$

624 The minimal potential of a self-interacting Higgs that still respects the SM symmetry is given in equa-  
625 tion 1.2.

$$V(\Phi) = \mu^2 \Phi^\dagger \Phi + \lambda (\Phi^\dagger \Phi)^2 \quad (1.2)$$

626 If the  $\mu^2$  term of this potential is positive, then the potential has a minimum at  $\Phi = 0$  and the SM  
627 symmetry is preserved. However, if instead  $\mu^2 < 0$ , then the minimum is at a finite value of  $\Phi$ , namely

$$\Phi_{\min} = \frac{1}{\sqrt{2}} \begin{pmatrix} 0 \\ v \end{pmatrix} \quad (1.3)$$

628 where  $v = \sqrt{\mu^2/\lambda}$ . Because this is the location of the minimum, it corresponds to the vacuum expecta-  
 629 tion value for the field ( $\langle \Phi \rangle = \Phi_{\min}$ ). The excitations of the Higgs can then be parameterized as

$$\Phi = \frac{1}{\sqrt{2}} \begin{pmatrix} 0 \\ v + H \end{pmatrix} \quad (1.4)$$

630 The full scalar Lagrangian, including the kinetic term, is then given as

$$\mathcal{L}_s = (D^\mu \Phi)^\dagger (D_\mu \Phi) - V(\Phi) \quad (1.5)$$

631 where the covariant derivative is defined as

$$D_\mu = \partial_\mu + \frac{ig}{2} \tau^a W_\mu^a + ig' Y B_\mu \quad (1.6)$$

632 and  $W^1, W^2, W^3$  and  $B$  are the  $SU(2)$  and  $U(1)$  gauge fields of the electroweak theory, respectively.  $g$   
 633 and  $g'$  are the corresponding coupling constants. With the scalar Lagrangian in place, the physical gauge  
 634 fields can then be written as

$$W_\mu^\pm = \frac{1}{\sqrt{2}} (W_\mu^1 \mp i W_\mu^2) \quad (1.7)$$

635

$$Z_\mu = \frac{-g' B_\mu + g W_\mu^3}{\sqrt{g^2 + g'^2}} \quad (1.8)$$

636

$$A_\mu = \frac{g B_\mu + g' W_\mu^3}{\sqrt{g^2 + g'^2}} \quad (1.9)$$

637 Equation 1.7 corresponds to the charged  $W^+$  and  $W^-$  bosons, equation 1.8 corresponds to the neutral  $Z$   
 638 boson, and equation 1.9 corresponds to the neutral photon. The masses of the particles also arise from the  
 639 Lagrangian. The photon has zero mass, while the masses of the  $W$  and  $Z$  bosons are given in equation 1.10.

640

$$M_W^2 = \frac{1}{4} g^2 v^2$$

$$M_Z^2 = \frac{1}{4} (g^2 + g'^2) v^2 \quad (1.10)$$

641 The fermion masses also arise through a coupling with the Higgs via the Yukawa interaction (for a detailed  
642 description, see [8]). In this case the coupling between the Higgs and the fermions goes as

$$g_{Hf\bar{f}} = \frac{m_f}{v} \quad (\text{i.ii})$$

643 The full Lagrangian of Higgs interactions can be written as

$$\mathcal{L}_{\text{Higgs}} = -g_{Hf\bar{f}}\bar{f}fH + \frac{g_{HHH}}{6}H^3 + \frac{g_{HHHH}}{24}H^4 + \delta_V V_\mu V^\mu \left( g_{HV}VH + \frac{g_{HHV}}{2}H^2 \right) \quad (\text{i.12})$$

644 with

$$\begin{aligned} g_{HV} &= \frac{2m_V^2}{v} & g_{HHV} &= \frac{2m_V^2}{v^2} \\ g_{HHH} &= \frac{3m_H^2}{v} & g_{HHHH} &= \frac{3m_H^2}{v^2} \end{aligned} \quad (\text{i.13})$$

645 Here,  $V$  refers to the  $W^\pm$  and  $Z$ , and  $\delta_W = 1$  while  $\delta_Z = 1/2$ . Phenomenologically, there are a few  
646 features of this Lagrangian that are useful to note. First, note that the Higgs mass is a free parameter of the  
647 theory that must be determined experimentally. Second, note that the coupling of the Higgs to the vector  
648 bosons and fermions scales with the masses of these particles, a fact that is important when considering  
649 both the production and decays of the particle. Also note that the branching ratio of the Higgs to  $W$   
650 bosons will be twice that of the branching ratio to  $Z$  if the Higgs mass is large enough to produce the  
651 particles on shell because of the extra symmetry factor associated with the  $W$  coupling. Finally, note the  
652 presence of the cubic and quartic Higgs self interaction terms, which can lead to final states with multiple  
653 Higgs bosons produced.

### 654 1.3 HIGGS BOSON PRODUCTION AND DECAY

655 This section discusses the properties of Higgs production and decay mechanisms. The details presented  
656 here will focus on the properties of a 125 GeV Higgs boson, as this is the mass closest to that of the newly  
657 discovered Higgs.

658    1.3.1    HIGGS PRODUCTION

659    The Higgs is produced by four main production modes at the Large Hadron Collider - gluon-gluon  
 660    fusion (ggF), vector boson fusion (VBF), associated production with a  $W$  or  $Z$  boson, or associated pro-  
 661    duction with top quarks ( $t\bar{t}H$ ). Figure 1.2 shows the Feynman diagrams for these four modes.

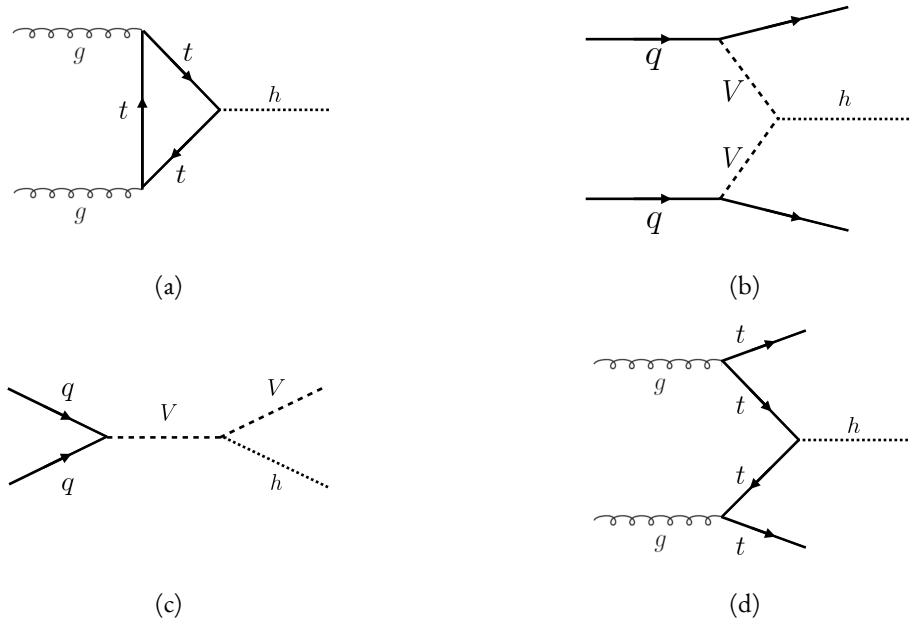


Figure 1.2: The four most common Higgs boson production modes at the LHC: (a) gluon-gluon fusion, (b) vector boson fusion, (c)  $W/Z + H$  production, (d)  $t\bar{t}H$  production

662    In gluon-gluon fusion, gluons from the incoming protons fuse via a top-quark loop to produce a Higgs.  
 663    The top quark is the dominant contribution in the loop due to its heavy mass and the fact that the Higgs-  
 664    fermion coupling constant scales with fermion mass. In vector boson fusion, the incoming quarks each  
 665    radiate a  $W$  or  $Z$  boson which fuse to produce the Higgs. This production mode results in a final state  
 666    with a Higgs boson and two additional jets which tend to be forward because they carry the longitudinal  
 667    momentum of the incoming partons. The Higgs can also be produced in association with a  $W$  or  $Z$  boson.  
 668    The  $W/Z$  is produced normally and then radiates a Higgs (this mode is also sometimes known as “Higgs-  
 669    strahlung”). Finally, the Higgs can be produced in association with two top quarks. Each incoming gluon  
 670    splits into a  $t\bar{t}$  pair, and one of the top pairs combines to create a Higgs. Figure 1.3 shows the production  
 671    cross section for a 125 GeV Higgs boson in each of these modes at a  $pp$  collider as a function of center of

672 mass energy.

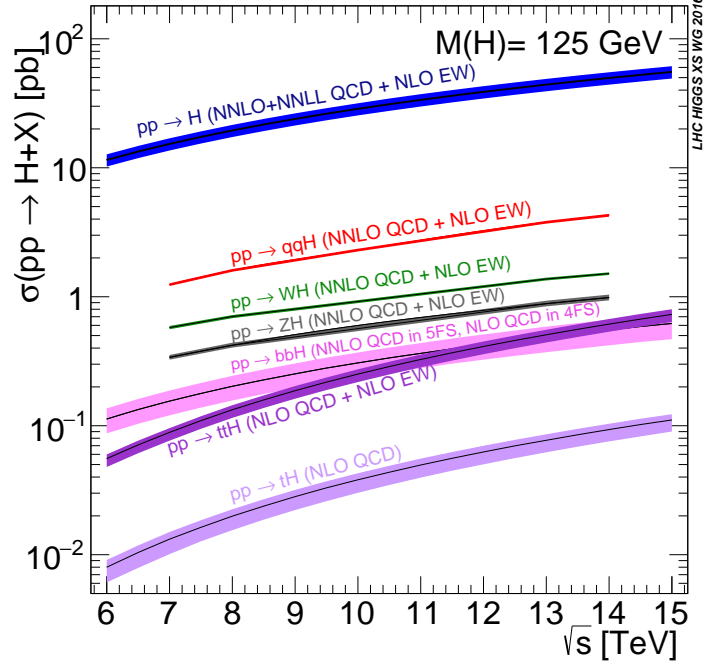


Figure 1.3: Higgs production cross sections as a function of center of mass energy ( $\sqrt{s}$ ) at a  $pp$  collider [18].

673 In figure 1.3, note that gluon fusion has the largest cross section, while VBF is the second largest at ap-  
 674 proximately a factor of 10 smaller. The figure also includes the less commonly studied  $b\bar{b}H$  and  $tH$  modes.  
 675 While the  $b\bar{b}H$  mode has a larger cross section than  $t\bar{t}H$ , it also has larger backgrounds and is thus less sensi-  
 676 tive. The  $tH$  mode is not as sensitive as  $t\bar{t}H$  due to its lower cross section. At  $\sqrt{s} = 8$  TeV, ggF production  
 677 of a 125 GeV Higgs has a cross section of 19.47 pb, while VBF has a cross section of 1.601 pb [18]. The  
 678 cross sections of all of the main Higgs production modes at this center of mass energy, as well as their un-  
 679 certainties from varying the renormalization and factorization scales and PDFs, are summarized in table 1.1  
 680 for a 125 GeV Higgs.

Production mode	$\sigma$ ( pb)	QCD scale uncert. (%)	PDF + $\alpha_s$ uncert. (%)
Gluon fusion	19.47	+7.3 / - 8.0	3.1
Vector boson fusion	1.601	+0.3 / - 0.2	2.2
$WH$	0.7026	+0.6 / - 0.9	2.0
$ZH$	0.4208	+2.9 / - 2.4	1.7
$b\bar{b}H$	0.2021	+20.7 / - 22.3	
$t\bar{t}H$	0.1330	+4.1 / - 9.2	4.3
$tH$ ( $t$ -channel)	0.01869	+7.3 / - 16.5	4.6
$tH$ ( $s$ -channel)	$1.214 \times 10^{-3}$	+2.8 / - 2.4	2.8

Table 1.1: Production cross sections for a 125 GeV Higgs boson at  $\sqrt{s} = 8$  TeV with scale and PDF uncertainties [18].

### 681 1.3.2 HIGGS BRANCHING RATIOS

682 The fact that the Higgs couples more strongly to more massive particles is crucial for understanding its  
 683 branching ratios. The width for Higgs decays to fermions is given in equation 1.14 [5].

$$\Gamma(H \rightarrow f\bar{f}) = \frac{N_c \sqrt{2} G_F m_f^2 m_H}{8\pi} \quad (1.14)$$

684 In this case,  $N_c$  is the number of colors,  $G_F$  is the Fermi constant,  $m_f$  is the mass of the fermion, and  
 685  $m_H$  is the mass of the Higgs. Note that the width scales with the square of the fermion mass. (This also  
 686 assumes that the Higgs mass is large enough to decay with both the fermions on shell.)

687 The decay width to  $WW$ , in the case where both  $W$  bosons are produced on shell ( $m_H \geq 2m_W$ ), is  
 688 given in equation 1.15 [5].

$$\Gamma(H \rightarrow W^+ W^-) = \frac{\sqrt{2} G_F M_W^2 m_H}{16\pi} \frac{\sqrt{1-x_W}}{x_W} (3x_W^2 - 4x_W + 4) \quad (1.15)$$

689 where  $m_W$  is the mass of the  $W$  and  $x_W = 4M_W^2/m_H^2$ . To get the branching ratio to  $ZZ$  (in the regime  
 690 where  $m_H \geq 2m_Z$ ), the equation is divided by 2 to account for identical particles in the final state, and  
 691  $x_W$  is replaced with  $x_Z = 4M_Z^2/m_H^2$ . This is shown in equation 1.16 [5].

$$\Gamma(H \rightarrow ZZ) = \frac{\sqrt{2} G_F M_Z^2 m_H}{32\pi} \frac{\sqrt{1-x_Z}}{x_Z} (3x_Z^2 - 4x_Z + 4) \quad (1.16)$$

692 The more general formula for Higgs branching into  $WW$  or  $ZZ$ , taking into account the case where one  
 693 or both vector bosons is off-shell, is shown in equation 1.17 [19].

$$\Gamma(H \rightarrow V^*V^*) = \frac{1}{\pi^2} \int_0^{M_H^2} \frac{dq_1^2 M_V \Gamma_V}{(q_1^2 - M_V^2)^2 + M_V^2 \Gamma_V^2} \int_0^{(M_H - q_1)^2} \frac{dq_2^2 M_V \Gamma_V}{(q_2^2 - M_V^2)^2 + M_V^2 \Gamma_V^2} \Gamma_0 \quad (1.17)$$

694 Here,  $q_1^2$  and  $q_2^2$  are the invariant masses of the virtual gauge bosons,  $M_V$  is the  $W$  or  $Z$  mass, and  $\Gamma_V$  is  
 695 the  $W$  or  $Z$  width.  $\Gamma_0$  is the squared matrix element, which is given in equation 1.18 [19].

$$\Gamma_0 = \frac{G_F M_H^3}{8\sqrt{2}\pi} \delta_V \sqrt{\lambda(q_1^2, q_2^2, M_H^2)} \left[ \lambda(q_1^2, q_2^2, M_H^2) + \frac{12q_1^2 q_2^2}{M_H^4} \right] \quad (1.18)$$

696 The function  $\lambda$  is defined as  $\lambda(x, y, z) = (1 - x/z - y/z)^2 - 4xy/z^2$ . The integral in the general off-  
 697 shell boson case is much more difficult to interpret than the simpler on-shell branching ratios, but it can be  
 698 evaluated numerically. These formulas can also be visualized as a function of Higgs mass. Figure 1.4 shows  
 the branching ratios as a function of the Higgs mass. There are a few interesting features to note in this

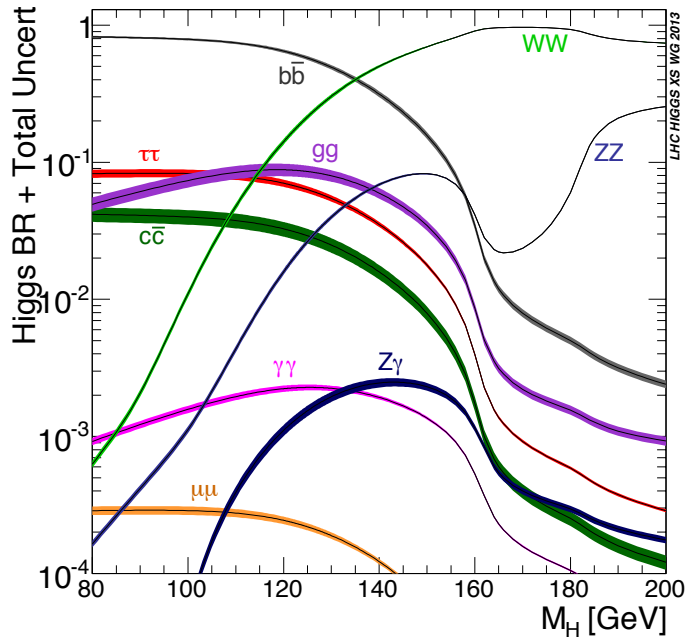


Figure 1.4: Higgs boson branching ratios as a function of  $m_H$  [18].

699  
 700 figure. First, note that at high Higgs masses, once on-shell production of both  $W$  and  $Z$  bosons is possible,

701 these two decays are the dominant ones due to the large masses of the  $W/Z$ . Also note that the branching  
 702 ratio to  $W$ s is twice that of  $Z$ s at these large masses due to the  $\delta_V$  symmetry factor noted previously. At  
 703 125 GeV, the Higgs is accessible through many different decay modes. The largest branching ratio is the  
 704 decay  $H \rightarrow b\bar{b}$  at 58.24% [18]. This branching is larger than the  $WW/ZZ$  decays because one of the two  
 705 bosons must be produced off-shell for  $m_H = 125$  GeV. The second largest branching ratio is to  $WW^*$  at  
 706 21.37 % (before taking into account the branching ratios of the  $W$ ). Table 1.2 summarizes the branching  
 707 ratios for a 125 GeV Higgs. Note that there is in fact a Higgs branching ratio to  $\gamma\gamma$  even though photons  
 708 are massless. This decay happens through a loop (the largest contributions to the loop are top and  $W$ )  
 709 which suppresses the branching ratio.

Decay	Branching ratio (%)
$b\bar{b}$	58.24
$WW^*$	21.37
$gg$	8.187
$\tau\tau$	6.272
$c\bar{c}$	2.891
$ZZ^*$	2.619
$\gamma\gamma$	0.2270
$Z\gamma$	0.1533
$\mu\mu$	0.02176

Table 1.2: Branching ratios for a 125 GeV Higgs boson [18].

710 Note that the branching ratios alone do not tell the full story of which Higgs channels are the most  
 711 sensitive. For example, a  $H \rightarrow b\bar{b}$  search in gluon fusion production is incredibly difficult due to the  
 712 large QCD dijet background at the LHC. However, in associated production of the Higgs, where a  $W$   
 713 or  $Z$  gives additional final state particles that can be used to reduce background, a search for  $H \rightarrow b\bar{b}$   
 714 can be sensitive. The combinations of production and decay modes that are most commonly studied are  
 715 summarized in table 1.3 [5].

#### 716 1.4 HIGGS PAIR PRODUCTION IN THE STANDARD MODEL

717 The Standard Model also allows for processes that produce two Higgs bosons in the final state, known  
 718 as Higgs pair production or di-Higgs production. The two main production mechanisms are shown in

Decay	Inclusive (incl. ggF)	VBF	$WH/ZH$	$t\bar{t}H$
$H \rightarrow \gamma\gamma$	✓	✓	✓	✓
$H \rightarrow bb$			✓	✓
$H \rightarrow \tau^+\tau^-$		✓		
$H \rightarrow WW^* \rightarrow \ell\nu\ell\nu$	✓	✓	✓	
$H \rightarrow ZZ \rightarrow 4\ell$	✓			
$H \rightarrow Z\gamma \rightarrow \ell\ell\gamma$	very low			

Table 1.3: Possible channels for Higgs searches. Checkmarks denote the most sensitive production modes [5].

figure 1.5. The two diagrams in figure 1.5 interfere destructively with one another, resulting in a low overall

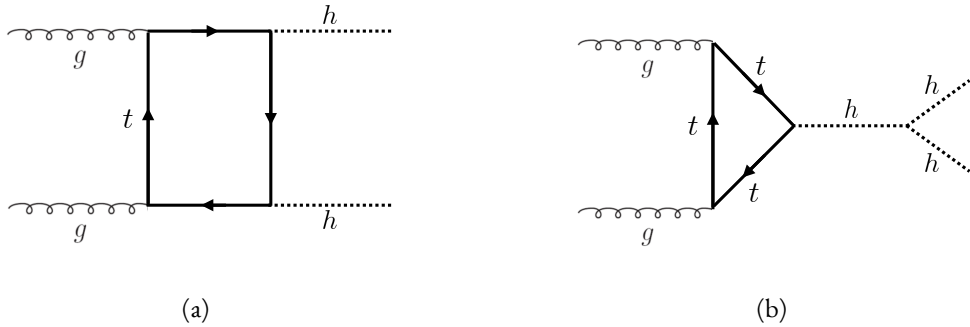


Figure 1.5: The two leading diagrams for Standard Model di-Higgs production at the LHC: (a) box diagram, (b) Higgs self coupling

719

720 cross section for di-Higgs production at the LHC. Nevertheless, Higgs pair production is quite interesting  
 721 to study because it gives direct access to the  $\lambda$  parameter of the Higgs potential, also known as the Higgs  
 722 self coupling. The diagram in figure 1.5(b) is sensitive to this coupling through the triple Higgs vertex.

723 One can substitute the gluon fusion production of diagram 1.5(b) with any of the other production  
 724 modes previously discussed. These other modes do not suffer from interference with the box diagram in  
 725 figure 1.5(a) due to the presence of additional particles in the final state. They still have a lower cross section  
 726 than the gluon fusion mode, however. The cross sections for di-Higgs production in the different modes,  
 727 as well as their uncertainties, are shown in table 1.4 [20]. These are shown for  $\sqrt{s} = 14$  TeV as the higher  
 728 center of mass energy is more sensitive to this process. Note that the scale of cross section quoted is now  
 729 in fb rather than pb.

Production mode	$\sigma$ ( fb)	Total uncert. (%)
Gluon fusion	33.89	+37.2/ - 27.8
Vector boson fusion	2.01	+7.6/ - 5.1
$W H H$	0.57	+3.7/ - 3.3
$Z H H$	0.42	+7.0/ - 5.5
$t \bar{t} H$	1.02	-

Table 1.4: Production cross sections for pair production of a 125 GeV Higgs boson at  $\sqrt{s} = 14$  TeV with total uncertainty [20]. The uncertainties include QCD scale and PDF variations as well as uncertainties on  $\alpha_S$ .

## 730 1.5 HIGGS PAIR PRODUCTION IN THEORIES BEYOND THE STANDARD MODEL

731 The Standard Model Higgs pair production cross section is rather small, and datasets on the scale of  
 732 the full lifetime of the LHC will be required to obtain sensitive measurements of the Higgs self-coupling.  
 733 However, the discovery of the Higgs also gives particle physicists a new tool that can be exploited in the  
 734 search for new physics beyond the Standard Model. In particular, Higgs pair production is a promising  
 735 channel in the search for new physics. The cross section for di-Higgs production can be altered through  
 736 both resonant and non-resonant production of Higgs pairs. In non-resonant production, di-Higgs pro-  
 737 duction vertices can arise from the presence of a new strong sector and additional colored particles [21–23].  
 738 Figure 1.6 shows examples of the types of vertices that can arise. In the resonant case, new heavy particle  
 739 can decay to Higgs pairs. Such new particles can include heavy Higgs bosons arising in two Higgs doublet  
 740 models (2HDM) or Higgs portal models as well as heavy gravitons in Randall-Sundrum theories [21, 24–  
 741 30]. Figure 1.7 shows a generic diagram for a heavy resonance decaying to two Higgs bosons. In the 2HDM,  
 742  $X$  corresponds to the heavy CP-even scalar  $H$ . In the Randall-Sundrum model,  $X$  corresponds to a heavy  
 743 spin-2 graviton  $G$ . The next sections provide more detail on the phenomenology of resonant Higgs pro-  
 744 duction in Randall-Sundrum and 2HDM models, as these models will later be tested in a dedicated search  
 745 for resonant production of boosted Higgs pairs.

### 746 1.5.1 RANDALL-SUNDRUM GRAVITONS

747 The Randall-Sundrum model is a proposed solution to the hierarchy problem that posits a five-dimensional  
 748 warped spacetime that contains two branes: one where the force of gravity is very strong and a second brane

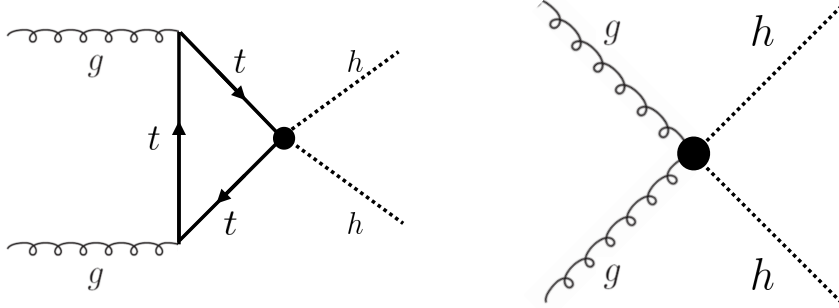


Figure 1.6: Diagrams with new vertices for non-resonant Higgs pair production arising in composite Higgs models

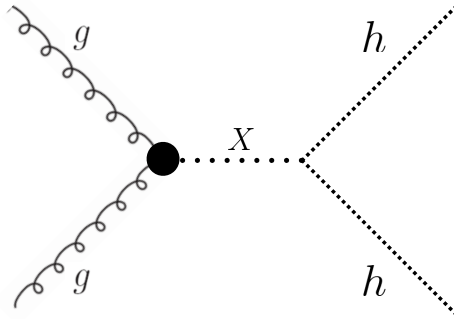


Figure 1.7: Generic Feynman diagram for resonant Higgs pair production in BSM theories

at the TeV scale corresponding to the known Standard Model sector [24]. In the theory, the branes are weakly coupled and the graviton probability function drops exponentially going from the gravity brane to the SM brane, rendering gravity weak on the SM brane. The experimental consequence of this theory is a tower of widely spaced (in mass) Kaluza-Klein graviton resonances. In theories where the fermions are localized to the SM brane, production of gravitons from fermion pairs is suppressed and the primary mode of production is gluon fusion [25]. These gravitons have a substantial branching fraction to Higgs pairs, ranging from 6.43% for gravitons with a mass of 500 GeV to 7.66% at 3 TeV. Figure 1.8 shows the branching ratios of the spin-2 Randall Sundrum graviton (RSG) as a function of its mass. The predominant decays are to  $t\bar{t}$  above the mass threshold for that channel.

These models have two free parameters - the mass of the graviton and a curvature parameter  $k$ . Typically, rather than  $k$ , the theory is parameterized using  $c \equiv k/\bar{M}_{\text{pl}}$ , where  $\bar{M}_{\text{pl}}$  is the reduced Planck mass. The cross section for production of the RSG decreases as a function of mass and is strongly dependent on the

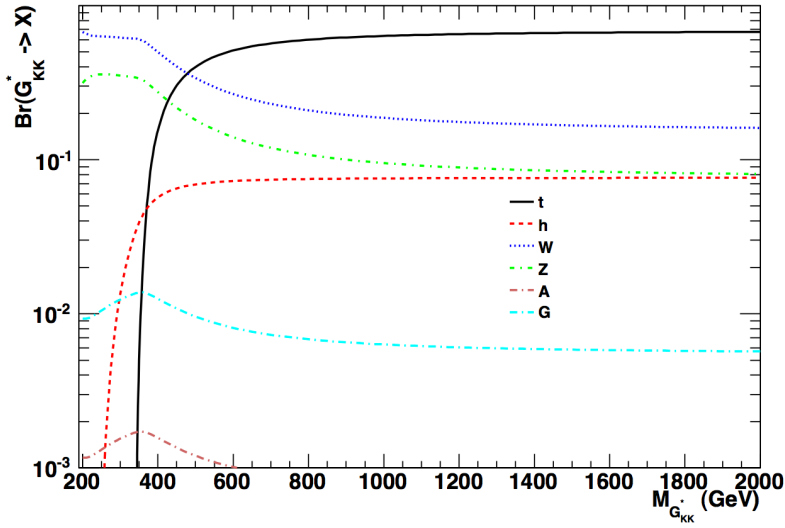


Figure 1.8: Branching ratios for a spin-2 Randall-Sundrum graviton as a function of mass computed in MadGraph with the CP<sub>3</sub>-Origins implementation [25, 31]

761 gluon PDF. The increase in center of mass energy from 8 to 13 TeV in LHC Run 2 greatly increases the  
 762 cross section at higher mass. Figure 1.9 shows the cross section as a function of graviton mass at  $\sqrt{s} =$   
 763 13 TeV for RSG models with  $c = 1.0$  and  $c = 2.0$ .

764 Another interesting feature of the theory is that the width of the graviton increases with both  $c$  and  $m_G$ .  
 765 Figure 1.10 shows the graviton width for both  $c = 1.0$  and  $c = 2.0$  as a function of mass. In  $c = 1.0$ ,  
 766 the width starts at 8.365 GeV for a mass of 300 GeV and increases to 187.2 GeV at a mass of 3 TeV.  
 767 Similarly, with  $c = 2.0$ , the width starts at 33.46 GeV for  $m_G = 300$  GeV and increases to 748.8 GeV  
 768 at a mass of 3 TeV.

### 769 1.5.2 TWO HIGGS DOUBLET MODELS

770 In Two Higgs Doublet Models (2HDM), a second complex scalar doublet is added to SM [27–29]. In  
 771 this case, all four degrees of freedom in the second doublet correspond to new particles, meaning that there  
 772 are five total scalars from the two Higgs doublets -  $h$  (light CP-even Higgs),  $H$  (heavy CP-even Higgs),  $A$   
 773 (heavy CP-odd Higgs), and  $H^\pm$  (charged Higgs). The model is parameterized by two main parameters.  
 774 The first,  $\tan \beta \equiv \frac{v_2}{v_1}$ , is the ratio of the vacuum expectation values of the two Higgs doublets (where  $v_1$   
 775 corresponds to the  $v$  in the SM Higgs model described above). The second parameter is  $\alpha$ , a mixing angle

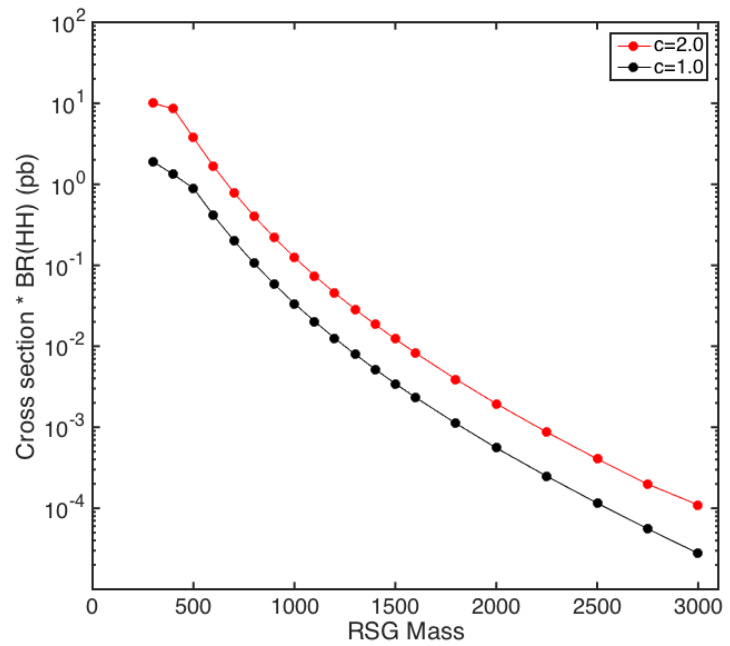


Figure 1.9:  $\sigma \times \text{BR}(HH)$  for RSG as a function of mass computed in MadGraph with the CP3-Origins implementation [25, 31]

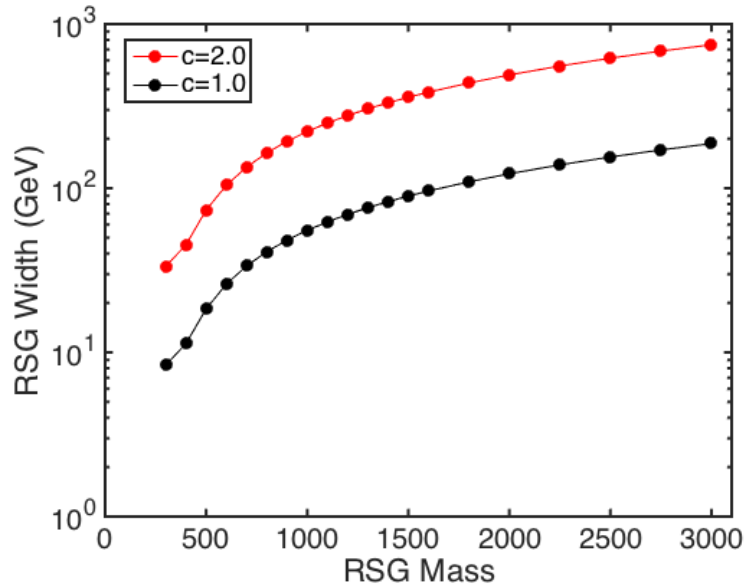


Figure 1.10: RSG width as a function of mass computed in MadGraph with the CP3-Origins implementation [25, 31]

776 between the heavy and light Higgs fields. Models are also often parameterized with  $\cos(\beta - \alpha)$  rather  
 777 than  $\alpha$  directly. The limit where  $\cos(\beta - \alpha) = 0$  is called the alignment limit, and it is in this limit that  
 778 the light Higgs  $h$  has the same couplings as a Standard Model Higgs.

779 2HDM models are usually separated into two main types - Type I and Type II. In Type I models, the  
 780 charged fermions only couple to the second Higgs doublet, leading to a fermiophobic light Higgs. In  
 781 Type II models, up-type quarks couple to the first doublet while down-type quarks couple to the second  
 782 doublet. One specific realization of a Type II 2HDM is the Minimal Supersymmetric Standard Model  
 783 (MSSM).

784 Resonant di-Higgs production in this model can proceed through decays of the heavy CP-even Higgs  
 785  $H \rightarrow hh$ . The branching ratio for  $H \rightarrow hh$  depends on the model type as well as the values of  $\tan \beta$  and  
 786  $\cos \beta - \alpha$ . Figure 1.II shows the branching ratios as a function of the mass of the heavy scalar  $H$  for both  
 787 Type I and Type II models. Depending on the type of model  $hh$  can be a substantial fraction of the decays  
 788 of  $H$ .

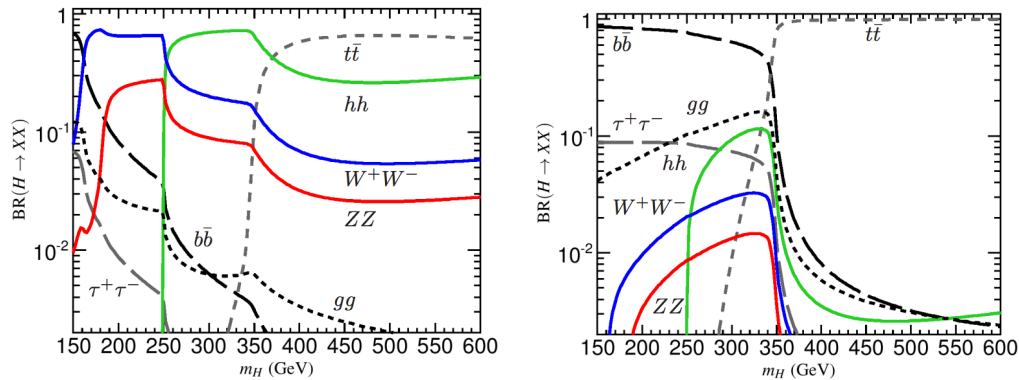


Figure 1.II: Branching ratios for heavy Higgs  $H$  in Type I (left) and Type II (right) 2HDM models with  $\tan \beta = 1.5$  and  $\cos(\beta - \alpha) = 0.1(0.01)$  for Type I (Type II). [29]

## 789 1.6 CONCLUSION

790 Studying the Higgs sector is essential for understanding the details of how mass arises in the Standard  
 791 Model and how the electroweak symmetry is broken. The discovery of the Higgs boson also opens the  
 792 door for its use as a tool to search for new physics, and Higgs pair production is an ideal candidate for

<sup>793</sup> this study. Even if no BSM physics is found in Higgs pair production, searches for Higgs pairs will put  
<sup>794</sup> constraints on the Higgs self coupling and thus further knowledge of the Standard Model and the details  
<sup>795</sup> of the Higgs potential.

*The enthusiasm and motivation to explore particle physics  
at the high-energy frontier knows no borders between the  
nations and regions of the planet.*

Peter Jenni

# 2

796

797

798

## The ATLAS detector and the Large Hadron Collider

799 This chapter presents an overview of the experimental systems used to conduct the measurements pre-  
800 sented in this thesis. First, a brief overview of the accelerator, the Large Hadron Collider, will be given.  
801 In this section, the accelerator conditions relevant to data-taking are presented as well. Next, an overview  
802 of the ATLAS experiment is given. The basics of each sub-detector's role are summarized, as well as the  
803 details of the datasets accumulated. Then, a brief interlude on the ATLAS Muon New Small Wheel up-  
804 grade is presented. While this new detector does not have a direct impact on any of the datasets taken so  
805 far, it will have an impact on future analyses and the work done on it is briefly summarized here. Finally,  
806 an overview of object reconstruction in ATLAS is given. While the details of all of the algorithms will not  
807 be presented in detail, aspects of the reconstruction performance such as object resolutions are shown as  
808 these are relevant to the two studies presented later in this thesis.

809    2.1 THE LARGE HADRON COLLIDER

810    The Large Hadron Collider (LHC) is a proton-proton collider at the CERN laboratory in Geneva,  
811    Switzerland [32]. It is designed for a maximum collision center of mass energy of  $\sqrt{s} = 14$  TeV and has a  
812    circumference of 26.7 kilometers. Four main experiments are located at the interaction points (IP) of the  
813    accelerator: ATLAS (A Toroidal LHC ApparatuS), CMS (the Compact Muon Solenoid), ALICE (A Large  
814    Ion Collider Experiment), and LHCb [33–36]. The studies performed in this thesis were all completed with  
815    the ATLAS detector. Figure 2.1 shows a schematic of the LHC ring and the various experiments.

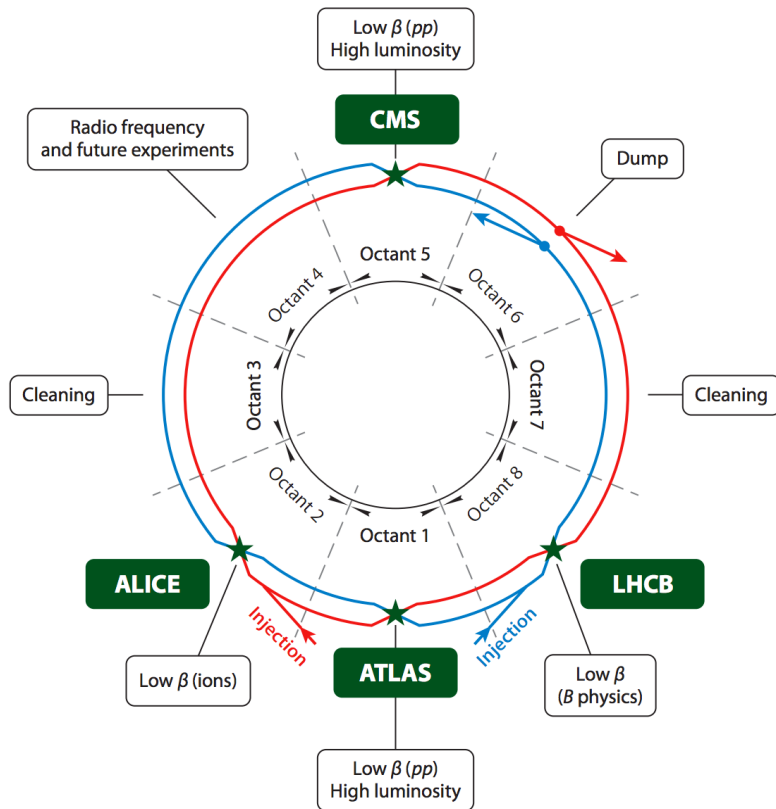


Figure 2.1: A schematic view of the LHC ring [37]

816    One of the most interesting features of the LHC is in its magnet design. Because the tunnel does not  
817    have room for separate superconducting magnets for each of the beam pipes, the LHC employs a twin-bore  
818    magnet design. Each magnet must hold an 8.3 Tesla magnetic field in order to bend the proton beams at  
819     $\sqrt{s} = 14$  TeV. The superconducting magnets are cooled to a temperature of 1.9 Kelvin with superfluid

820 helium.

821 2.1.1 INSTANTANEOUS LUMINOSITY

822 The rate of physics events expected from the accelerator is dependent on the instantaneous luminosity  
823 of the machine and the cross section of the physics process,  $R_{\text{events}} = L\sigma$ . Here,  $R_{\text{events}}$  is the number  
824 of events per second,  $L$  is the instantaneous luminosity of the machine, and  $\sigma$  is the cross section for the  
825 physics process being measured. The instantaneous luminosity of the LHC is determined by numerous  
826 factors related to machine conditions. Equation 2.1 gives the equation for instantaneous luminosity of  
827 Gaussian beam profile [37].

$$L = \frac{N_b^2 n_b f_{\text{rev}} \gamma_r}{4\pi \epsilon_n \beta^*} F \quad (2.1)$$

828 The LHC collides protons in bunches, and in the above equation  $N_b$  is the number of protons per bunch  
829 while  $n_b$  is the number of bunches per beam. Nominally, the LHC can hold up to 2808 proton bunches.  
830  $f_{\text{rev}}$  is the revolution frequency.  $\epsilon_n$  is the normalized transverse beam emittance, a measurement of the  
831 average spread of the particles position-momentum space which has the dimension of length.  $\beta^*$  is the  
832 value of the *beta* function for the beam at the interaction point. It relates the emittance to the Gaussian  
833 width of the beam with  $\sigma_{\text{beam}} = \sqrt{\epsilon \cdot \beta}$ .  $F$  is a reduction factor that corrects for the fact that the beams  
834 are colliding at an angle at the IP.

835 Another way of writing the instantaneous luminosity is shown in equation 2.2. In this case, the instanta-  
836 neous luminosity is written as the ratio of the rate of inelastic collisions with the inelastic cross section [38].

837

$$L = \frac{R_{\text{inel}}}{\sigma_{\text{inel}}} = \frac{\mu n_b f_{\text{rev}}}{\sigma_{\text{inel}}} \quad (2.2)$$

838 In this case,  $\mu$  is the average number of interactions per bunch crossing in the accelerator.  $\mu$  is a use-  
839 ful parameter for characterizing the amount of activity recorded in an experiment. As the instantane-  
840 ous luminosity and thus  $\mu$  increase, there are more interactions per bunch crossing and more activity in the  
841 detector. This is often characterized with  $\langle \mu \rangle$ , the measured per bunch crossing  $\mu$  value averaged over all  
842 bunch crossings. The interactions inside each bunch crossing that are not the main physics process of in-

843 terest are often referred to as “pileup” interactions, and  $\langle \mu \rangle$  is a measurement of the level of pileup in the  
844 detector.

845 **2.1.2 EVOLUTION OF MACHINE CONDITIONS**

846 This thesis uses datasets taken at three different center of mass energies:  $\sqrt{s} = 7\text{ TeV}$  data taken in the  
847 year 2011,  $\sqrt{s} = 8\text{ TeV}$  data taken in the year 2012, and  $\sqrt{s} = 13\text{ TeV}$  data taken in the year 2015. In  
848 addition to increasing center of mass energy, the instantaneous luminosity and parameters that determine  
849 it were evolving. Table 2.1 summarizes that machine conditions in each of these datasets.

	2011	2012	2015	Design
$\sqrt{s} [\text{TeV}]$	7	8	13	14
Number of bunches	1380	1380	1825	2808
Max. protons per bunch	$1.45 \times 10^{11}$	$1.7 \times 10^{11}$	$1.2 \times 10^{11}$	$1.15 \times 10^{11}$
Bunch spacing [ns]	50	50	25	25
Max. instantaneous luminosity [ $\text{cm}^{-2}\text{s}^{-1}$ ]	$3.7 \times 10^{33}$	$7.7 \times 10^{33}$	$5 \times 10^{33}$	$10^{34}$
$\beta^* [\text{m}]$	1.0	0.6	0.8	0.55
$\langle \mu \rangle$	11.6	20.7	13.7	-

Table 2.1: Evolution of LHC machine conditions [39, 40]

850 **2.2 THE ATLAS DETECTOR**

851 The ATLAS detector is a multi-purpose particle detector experiment at the LHC’s Point 1 [33]. It has  
852 nearly  $4\pi$  coverage in solid angle around the interaction point. It consists of an inner detector for mea-  
853 suring charged particles, electromagnetic and hadronic calorimeters, and a muon spectrometer. Figure 2.2  
854 gives an overview of the detector.

855 **2.2.1 COORDINATE SYSTEM**

856 Before defining the properties of the individual detectors, it is important to establish the coordinate  
857 system used. Figure 2.3 shows a schematic of the coordinate system. The azimuthal plane (perpendicular  
858 to the beam line) is defined as the  $x$ - $y$  plane. The angle in this plane is referred to as  $\phi$ . The angle relative



Figure 2.2: A full diagram of the ATLAS detector [33]

859 to the beam axis is referred to as  $\theta$ . Rather than using  $\theta$  directly as a coordinate, the experiment often uses  
 860 the pseudorapidity  $\eta$ .  $\eta$  is defined in equation 2.3.

$$\eta = \ln \left( \tan \left( \frac{\theta}{2} \right) \right) \quad (2.3)$$

861 Pseudorapidity is the massless approximation of rapidity, the angle used to parameterize boosts in spe-  
 862 cial relativity. This is important for two reasons. First, it means that differences in  $\eta$  are Lorentz invariant.  
 863 Second, particle production is roughly constant in pseudorapidity. Particles with  $\eta$  close to zero are re-  
 864 ferred to as “central”, while those at high  $|\eta|$  are called “forward”. In general, two main detector topologies  
 865 can be seen in figure 2.2. There are “barrel” elements, which surround the beam line cylindrically and are  
 866 in the central region of the detector. In the forward region, there are “endcap” regions which are arranged  
 867 as disks perpendicular to the beam line.

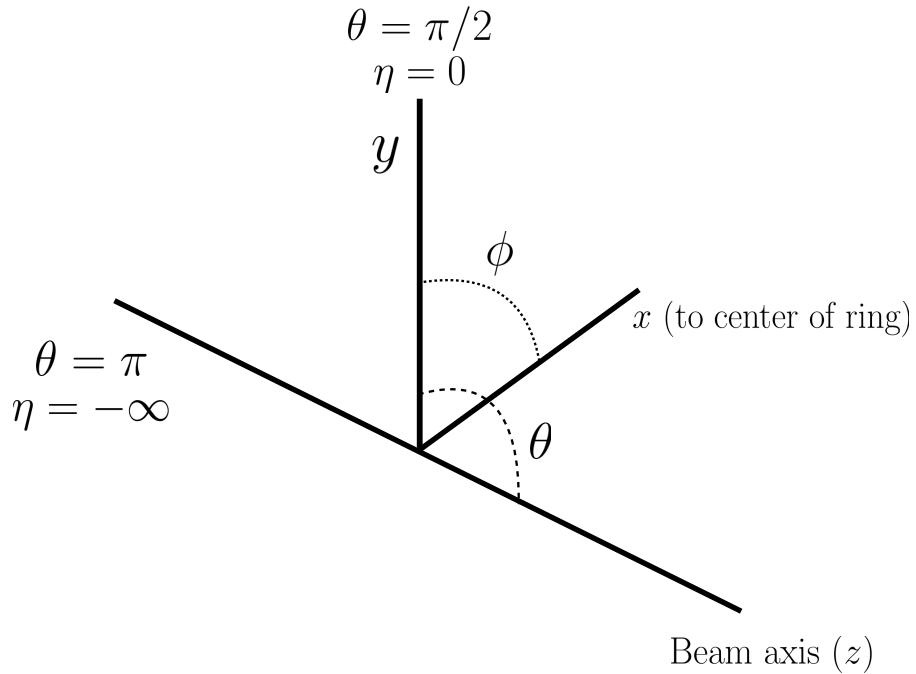


Figure 2.3: The ATLAS coordinate system

### 868 2.2.2 INNER DETECTOR

869 The ATLAS Inner Detector (ID) system is built for precision tracking of charged particles. It covers  
 870 the range  $|\eta| < 2.5$ . In this range, approximately 1000 particles are generated every bunch crossing in the  
 871 detector. This requires having fine granularity to achieve the resolutions required for good momentum  
 872 measurement and vertex reconstruction.

873 The ID consists of three sub-components: the pixel detector, semiconductor tracker (SCT), and trans-  
 874 sition radiation tracker (TRT). It is surrounded by a solenoid providing a 2 T axial magnetic field which  
 875 bends particles in the transverse plane to allow for momentum measurement. Figure 2.4 shows the layout  
 876 of each of these components.

### 877 PIXEL DETECTOR

878 The pixel detector is the first detector particles traverse after being generated in proton collisions and  
 879 is the most granular detector. Its operation is crucial for precision tracking and vertex reconstruction as



Figure 2.4: Layout of the ATLAS Inner Detector system [41]

well as higher level object reconstruction like tagging of jets from  $b$ -quarks. The basic sensing element in this subdetector is a silicon pixel detector. The operating principle for the silicon pixels is that of a  $p$ - $n$  junction. When a charged particle passes through, it creates electron-hole pairs that are then separated by the electric field. The sensors are  $250\ \mu\text{m}$  thick and use oxygenated  $n$ -type wafers with readout pixels on the  $n^+$  side of the detector [33]. Overall, the pixel detector has 1744 sensors and 80.4 million readout channels.

In the barrel region, the pixel detector has three concentric layers of sensors surrounding the beamline. In the endcap region, it consists of disks perpendicular to the beam axis. The detector is segmented in the  $R$ - $\phi$  plane and in  $z$ . Usually, three pixel layers are crossed by a charged particle track. The intrinsic accuracies of the sensors are  $10\ \mu\text{m}$  in  $R$ - $\phi$  and  $115\ \mu\text{m}$  in  $z$  (or  $R$  for the endcap).

#### 890 INSERTABLE B-LAYER

In Run 2, a new innermost pixel layer, known as the insertable B-layer (IBL), was added to the Inner Detector [42]. This layer was added to cope with the higher luminosities planned in LHC Run 2 and at the

893 high luminosity HL-LHC. Additionally it improves tracking position resolution which in turn improves  
894 the vertexing and  $b$ -tagging capabilities in ATLAS. The detector sits directly on a new beam pipe, only  
895 33.25 mm away from the collision points in the azimuthal plane.

896 **SEMICONDUCTOR TRACKER (SCT)**

897 The semiconductor tracker (SCT) consists of silicon microstrips and comprises the next four layers  
898 of the ID. This sub-detector has 6.4cm long sensors that are daisy-chained into strips with a strip pitch  
899 of  $80\ \mu\text{m}$  [33]. Some of the strips have a small stereo angle to allow for measurement of both angular  
900 coordinates. In total there are 6.3 million readout channels. The intrinsic accuracies are  $17\ \mu\text{m}$  in  $R\text{-}\phi$   
901 and  $580\ \mu\text{m}$  in  $z$  (or  $R$  in the endcap).

902 **TRANSITION RADIATION TRACKER (TRT)**

903 The transition radiation tracker (TRT) serves two purposes. First, it consists of 4mm diameter straw  
904 tubes filled with a 70/27/3% gas mixture of xenon, carbon dioxide, and oxygen to provide tracking of  
905 charged particles. Particles typically have 36 TRT straw tube hits per track. The material in between  
906 the straws is designed to induce transition radiation which can be useful for particle identification. As  
907 particles pass between media with different dielectric constants, they emit transition radiation that can  
908 cause additional showers in the TRT. In particular it is useful for discrimination between electrons and  
909 pions or other charged hadrons, as the amount of transition radiation is proportional to the Lorentz factor  
910 of the particle.

911 **2.2.3 CALORIMETERS**

912 The calorimeter system consists of two main sub-components: a fine granularity electromagnetic calorime-  
913 ter tailored for the measurement of photons and electrons and multiple coarser hadronic calorimeters ded-  
914 icated to the measurement of hadronic showers [33]. The calorimeter system has broader coverage than  
915 the inner detector, covering the region out to  $|\eta| < 4.9$ . It is also designed to deliver good containment of  
916 showers so as to limit leakage into the muon system. Figure 2.5 shows the layout of the calorimeter system.

917 Both the electromagnetic and hadronic calorimeters are sampling calorimeters. They alternate active  
918 material for energy measurement with passive material for energy absorption. The materials used for each  
919 purpose vary based on the type of calorimeter and its location in the detector.

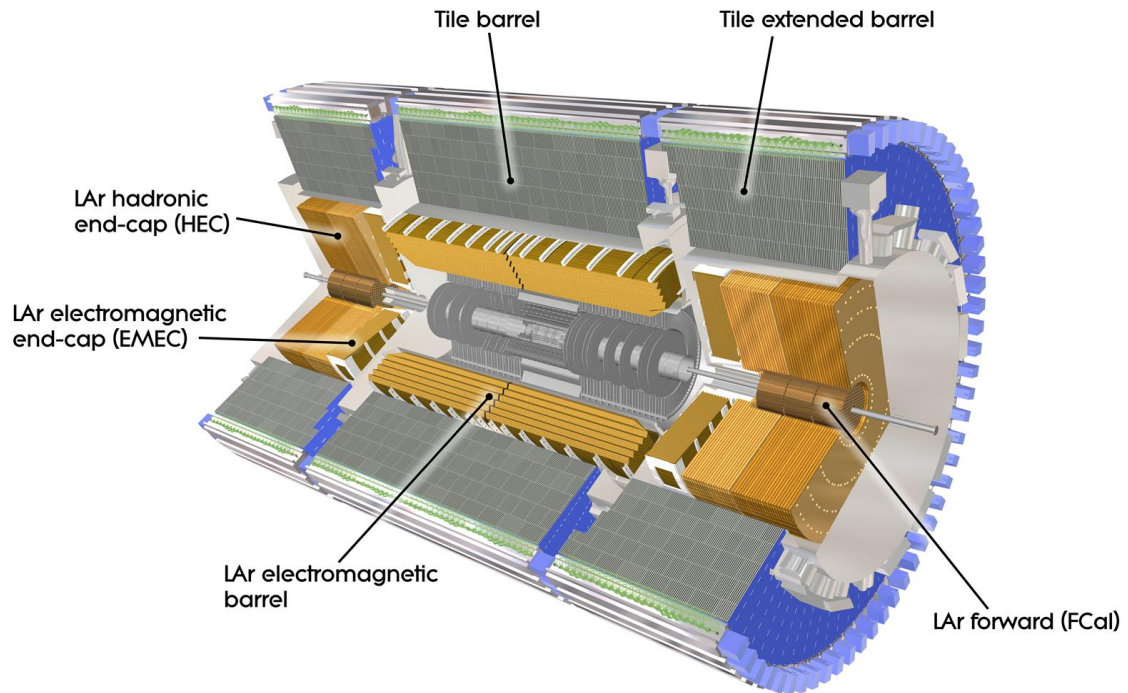


Figure 2.5: Layout of the ATLAS calorimeter system [33]

## 920 ELECTROMAGNETIC CALORIMETER

921 The electromagnetic calorimeter (EM calorimeter) use liquid Argon (LAr) as its active material and  
922 lead as its passive material. It is arrange in an accordion geometry to increase the absorption area while still  
923 allowing it to have no azimuthal cracks (complete symmetry in  $\phi$ ). The EM calorimeter is divided into a  
924 barrel portion that extends to  $|\eta| < 1.475$  and an endcap portion going from  $1.375 < |\eta| < 3.2$ . The  
925 region where these two units overlap is called the “transition region”.

926 In order to provide good containment the calorimeter depth must be optimized. Typically, for elec-  
927 tromagnetic calorimeters the depth is measured in radiation lengths. In general, the intensity of a par-  
928 ticle beam attenuates exponentially in distance with a constant equal to the radiation length. That is,

929  $I(x) = I_0 e^{-x/X_0}$ , where  $I$  is the intensity,  $x$  is the distance traveled, and  $X_0$  is the radiation length.  
930 The ATLAS EM calorimeter is designed to have  $> 22$  radiation lengths in the barrel and  $> 24$  in the  
931 endcap [33].

932 **HADRONIC CALORIMETERS**

933 There are three types of hadronic calorimeters present in ATLAS: the tile calorimeter (TileCal), hadronic  
934 endcap (HEC), and forward calorimeter (FCal). Each one is optimized for stopping of hadronic showers  
935 and the materials chosen are specific to their placement in the detector.

936 The TileCal is a scintillating tile calorimeter placed directly outside the EM calorimeter. It uses steel as  
937 the absorber and plastic scintillator tiles as the active material. It has coverage in the barrel at  $|\eta| < 1.0$   
938 and in the “extended barrel” region of  $0.8 < |\eta| < 1.7$ .

939 The HEC had two wheels perpendicular to the beam line per endcap and is located directly behind the  
940 EM calorimeter endcap modules. The HEC covers the region from  $1.5 < |\eta| < 3.2$ , overlapping slightly  
941 with both the tile calorimeter and the forward calorimeter. Like the EM calorimeter, it uses liquid Argon  
942 as the active material, but it uses copper as the absorber.

943 The FCal covers the most forward regions of the calorimeter system, extending to the region of  $3.1 <$   
944  $|\eta| < 4.9$ . It again uses liquid argon as its active material. For absorber, it consists of an innermost module  
945 made of copper followed by a module made of tungsten.

946 The hadronic equivalent of radiation length is called the interaction length and is denoted as  $\lambda$ . In the  
947 barrel, the hadronic calorimeter depth is approximately  $9.7\lambda$ , while in the endcap is  $10\lambda$ . The outer  
948 supports contribute an additional  $1.3\lambda$ . This is been shown to be sufficient to limit punch-through of  
949 showers to the muon system [33].

950 **2.2.4 MUON SPECTROMETER**

951 The muon spectrometer is dedicated to measuring the momentum and position of muons. It consists  
952 of tracking and trigger chambers which are unique in the barrel and endcap regions. The magnetic field  
953 for bending of muons is provided by a system of three large air-core toroid magnets (from which ATLAS

954 derives its name.) These magnets provide 1.5 to 5.5 Tm of bending power at  $0 < |\eta| < 1.4$  and approx-  
 955 imately 1 to 7.5 Tm in the endcap region of  $1.6 < |\eta| < 2.7$ . The entire muon system covers the range  
 956  $0 < |\eta| < 2.7$ . Monitored drift tubes (MDTs) are used for tracking in the barrel and the two outer layers  
 957 of the endcap, while cathode strip chambers (CSCs) are used to provide tracking in the innermost endcap  
 958 wheel. In the barrel, resistive plate chambers (RPCs) are used as trigger chambers while thin gap chambers  
 959 (TGCs) are used in the endcap. Figure 2.6 shows the layout of the ATLAS muon system. The entire muon  
 960 system is designed with the specification of providing a 10% momentum resolution for a 1 TeV muon.

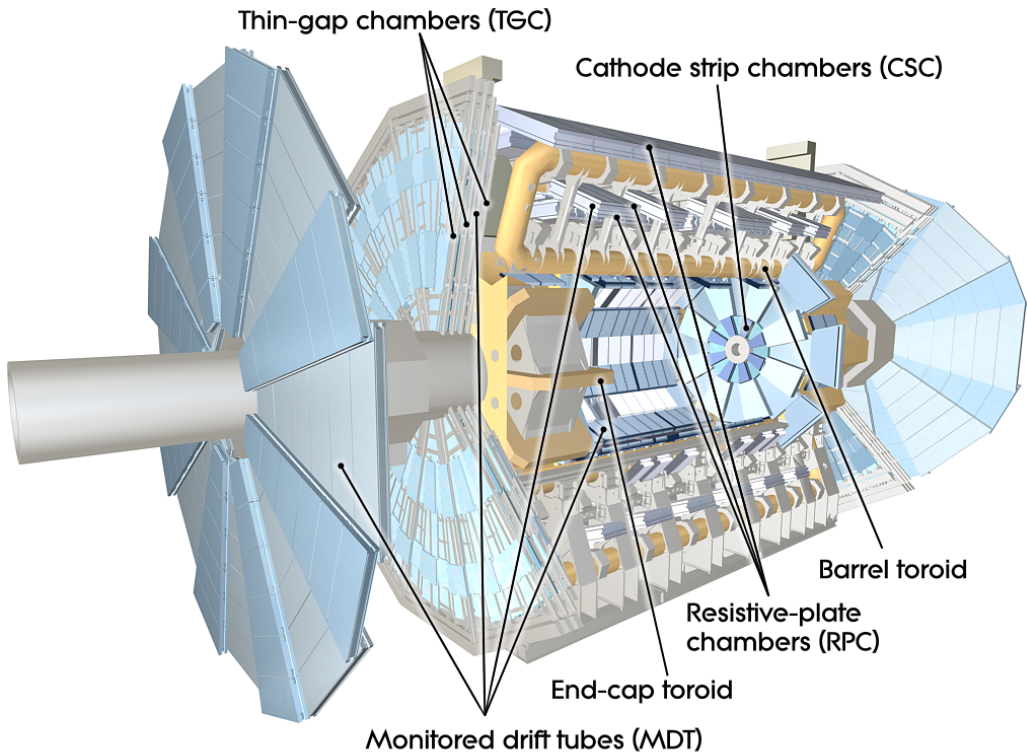


Figure 2.6: Layout of the ATLAS muon system [33]

## 961 MONITORED DRIFT TUBES (MDTs)

962 The monitored drift tubes (MDTs) are aluminum 3cm diameter tubes filled with a 93/7 % mixture of  
 963 Argon and CO<sub>2</sub>, with trace amounts of water. As a charged particle traverses the tube, it ionizes the gas  
 964 and the ions drift to a wire at the center of the tube. The radial distance of traversal of the particle in the

965 tube is determined by the drift time of the electrons, allowing for fine position resolution. The tubes have  
966 an average resolution of  $80 \mu\text{m}$  per tube and a maximum drift time of approximately 700ns. The tubes  
967 are oriented so that they give precision measurement in  $\eta$  and run along  $\phi$ . They cover  $|\eta| < 2.7$ , except  
968 in the innermost layer of the endcap where they only go to  $|\eta| < 2.0$  [33].

969 **CATHODE STRIP CHAMBERS (CSCs)**

970 The cathode strip chambers cover a narrow window of the innermost endcap region at  $2.0 < |\eta| <$   
971 2.7. In this region the background rates in the cavern are particularly high and the CSCs are designed to  
972 handle these higher rates. The CSCs are multiwire proportional chambers with wires pointing in the radial  
973 direction (away from the beam pipe). The wire serves as an anode and there are two types of segmented  
974 cathode strip, one perpendicular to the wires which gives the precision measurement and one parallel which  
975 provides the transverse coordinate. It has an 80/20 gas mixture of Argon and CO<sub>2</sub> [33].

976 **RESISTIVE PLATE CHAMBERS (RPCs)**

977 The resistive plate chambers (RPCs) are gaseous electrode-plate detectors covering the region  $|\eta| <$   
978 1.05. They consist of two resistive plates separated by a distance of 2 mm. The gas mixture used is a  
979 94.7/5/0.3% mixture of C<sub>2</sub>H<sub>2</sub>F<sub>4</sub>, Iso-C<sub>4</sub>H<sub>10</sub>, and SF<sub>6</sub>. It has readout strips with a pitch of 23-35 mm  
980 for both  $\eta$  and  $\phi$  measurement and thus provides measurement of the azimuthal coordinate in the barrel  
981 that the MDTs do not. The thin gas gap allows for a quick response time which makes it ideal for use in the  
982 trigger. There are three layers of RPCs which are referred to as the three trigger stations. They allow for  
983 both a low  $p_T$  and high  $p_T$  trigger. The coincidence of hits in the innermost chambers allows for triggering  
984 of muons between 6 and 9 GeV, while the outermost layer allows the trigger to select high momentum  
985 tracks in the range of 9 to 35 GeV [33].

986 **THIN GAP CHAMBERS (TGCs)**

987 The thin gap chambers (TGCs) are multiwire proportional chambers where the wire to cathode dis-  
988 tance (1.4mm) is smaller than the wire-to-wire distance (1.8 mm). They contain a gas mixture of CO<sub>2</sub>  
989 and *n*-pentane and use a high electric field to gain good time resolution. They serve two functions in the

990 end-cap system. First, they serve as the trigger chambers. Second, they also provide azimuthal coordinate  
 991 measurement which the MDTs do not. They sit on the inner and middle layers of the endcap. The outer-  
 992 most layer's azimuthal coordinate is determined by extrapolation [33].

993 **2.2.5 MAGNET SYSTEM**

994 As mentioned previously, there are two independent magnet systems in ATLAS. The first is a 2 T  
 995 solenoid field in the inner detector which provides bending in the azimuthal plane. The second is an ap-  
 996 proximately 0.5 T toroidal field in the muon system which provides bending in  $\eta$ . Figure 2.7 shows the  
 997 predicted field integral as a function of  $|\eta|$  [33].

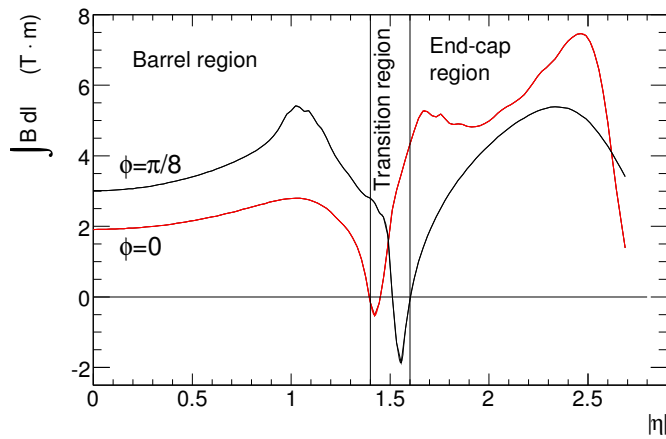


Figure 2.7: Predicted field integral as a function of  $|\eta|$  for the ATLAS magnet system [33]

998 **2.2.6 TRIGGER SYSTEM**

999 The ATLAS trigger system searches for signatures of muons, electrons, photons, hadronically decaying  
 1000  $\tau$  leptons, and jets in order to save these events for further analysis. The trigger system in ATLAS is de-  
 1001 signed to reduce the maximum LHC event rate of 40 MHz to a more reasonable rate that can be recorded.  
 1002 The trigger first consists of a fast, hardware based system called the Level-1 (L1) trigger. The L1 trigger  
 1003 consists of independent dedicated detector sub-components that can seed regions of interest (RoIs) for  
 1004 further analysis downstream. For muons, the RPCs and TGCs are used, while in the calorimeter coarsely  
 1005 grained sections of calorimeter cells called towers are used. Once regions of interest are seeded, a software

1006 based system called the High Level Trigger (HLT) is used to reconstruct objects and integrate information  
 1007 from different parts of the detector. In Run 1 of ATLAS, the HLT consisted of two separate stages: the  
 1008 level 2 (L2) trigger and the event filter (EF).

1009 The maximum trigger rate that the L1 trigger can handle is 75 kHz. In the HLT, the rate of events  
 1010 written to disk is approximately 200 Hz. Figure 2.8 shows the trigger rates for different L1 triggers in 2012  
 1011 and 2015 for ATLAS [43].

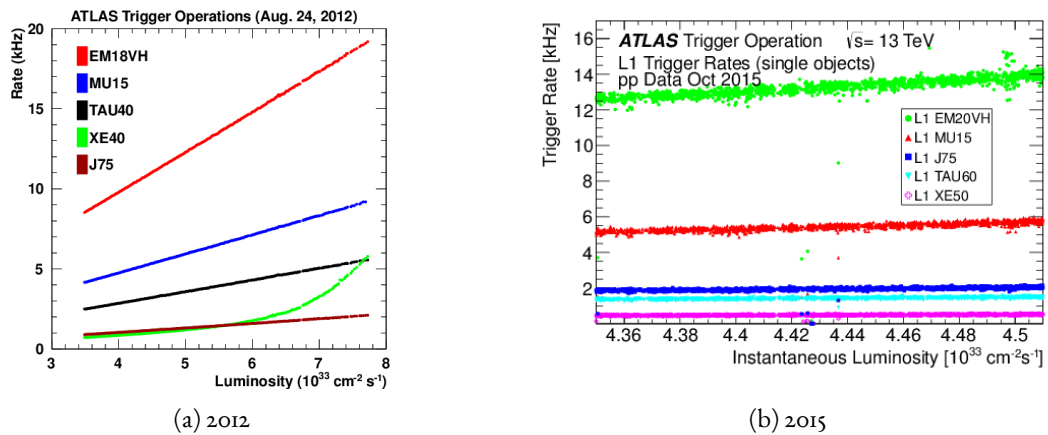


Figure 2.8: ATLAS trigger rates for Level-1 triggers as a function of instantaneous luminosity in 2012 and 2015 operation. These are single object triggers for electromagnetic clusters (EM), muons (MU), jets (J), missing energy (XE), and  $\tau$  leptons (TAU). The threshold of the trigger is given in the name in GeV. [43]

## 1012 2.2.7 ATLAS DATASETS

1013 ATLAS has collected data at center of mass energies of 7, 8, and 13 TeV. Figure 2.9 shows the integrated  
 1014 luminosity as a function of time for each of the three collected datasets. At  $\sqrt{s} = 7$  TeV, ATLAS recorded  
 1015  $5.08 \text{ fb}^{-1}$ . Increased instantaneous luminosity in 2012 led to a larger dataset of  $21.3 \text{ fb}^{-1}$  recorded at  
 1016  $\sqrt{s} = 8$  TeV. After Long Shutdown 1 (LS1) of the LHC and a restart in 2015, ATLAS recorded  $3.9 \text{ fb}^{-1}$   
 1017 of data at  $\sqrt{s} = 13$  TeV. [44, 45]

## 1018 2.2.8 DETECTOR PERFORMANCE

1019 Table 2.2 summarizes the design requirements for each of the different sub-detectors. This table shows  
 1020 the energy and momentum resolution of each tracking, calorimetry, and muon measurements.

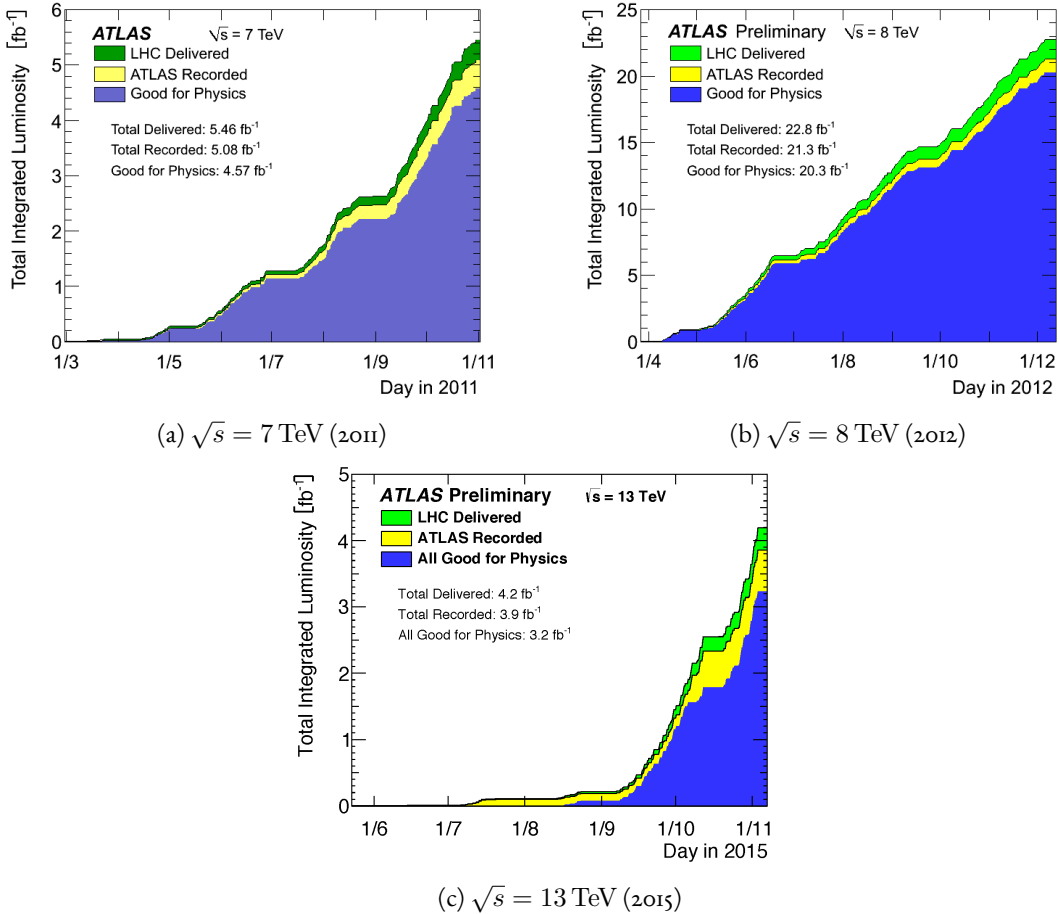


Figure 2.9: Instantaneous luminosity as a function of time for data recorded by ATLAS at different center of mass energies [44, 45]

	Required resolution
Tracking	$\sigma_{p_T}/p_T = 0.05\% p_T \oplus 1\%$
EM calorimetry	$\sigma_E/E = 10\%/\sqrt{E} \oplus 0.7\%$
Hadronic calorimetry	
Barrel and end-cap	$\sigma_E/E = 50\%/\sqrt{E} \oplus 3\%$
Forward	$\sigma_E/E = 100\%/\sqrt{E} \oplus 10\%$
Muon spectrometer	$\sigma_{p_T}/p_T$ at $p_T = 1 \text{ TeV}$

Table 2.2: Performance requirements for the ATLAS detector [33].

## 2.3 THE ATLAS MUON NEW SMALL WHEEL UPGRADE

As the LHC continues operation, it is scheduled to be upgraded in several phases to allow it to reach higher instantaneous luminosities and thus collect larger datasets. These conditions will open new doors

1024 for study of rare physics processes but will also present interesting challenges that must be faced. ATLAS  
 1025 will require new detector technologies to cope with the increased background rates in the cavern in these  
 1026 high luminosity conditions. One such upgrade, scheduled to be installed during Long Shutdown 2 (LS2)  
 1027 of the LHC in 2018, is the ATLAS Muon New Small Wheel (NSW) upgrade [46]. The NSW will replace  
 1028 the innermost end-cap wheel of the muon system with new technologies, as this is the part of the muon  
 1029 detector closest to the beam and thus suffers from the highest rates.

### 1030 2.3.1 MOTIVATION

1031 The motivation of the NSW is two-fold. First, the objective is to alleviate the decreased tracking ef-  
 1032 ficiency that comes in a high rate environment. As figure 2.10, at the LHC design luminosity both the  
 1033 efficiency of recording hits and reconstructing track segments in the MDTs decreases at the LHC design  
 1034 luminosity.

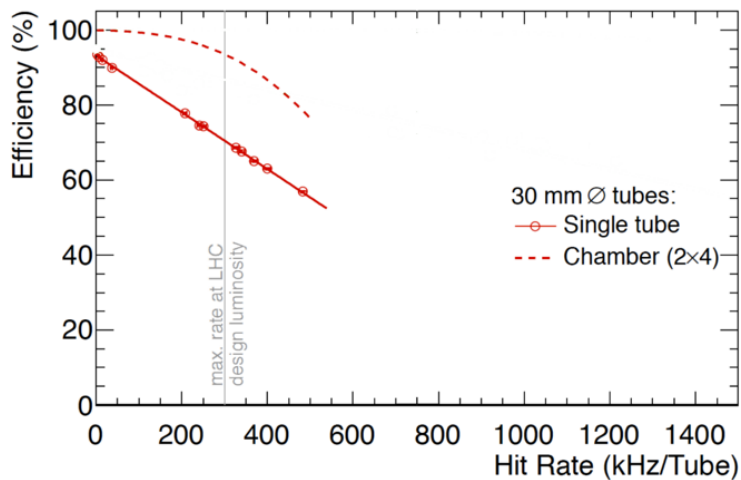


Figure 2.10: MDT tube hit (solid) and segment (dashed) efficiency as a function of hit rate per tube [46]

1035 Second, the NSW will work to alleviate the rate of fake triggers arising in the endcap. Figure 2.11 shows  
 1036 the extrapolated trigger rates as a function of the  $p_T$  threshold with and without the NSW upgrade. As  
 1037 the figure shows, the NSW upgrade will reduce the trigger rate by an order of magnitude compared to the  
 1038 current endcap trigger system.

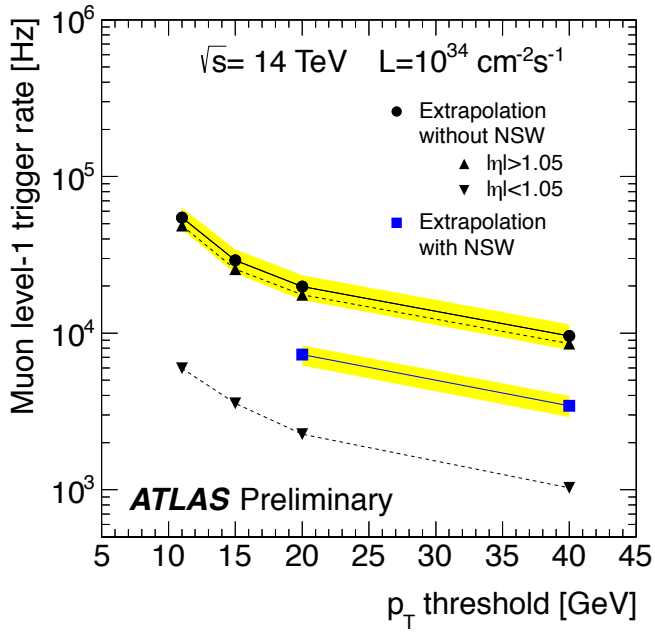


Figure 2.11: Trigger rate as a function of  $p_T$  threshold with and without the NSW upgrade [46]

### 1039 2.3.2 NSW DETECTOR TECHNOLOGIES

1040 The NSW will use two new detector technologies - micromesh gaseous structure detectors (micromegas)  
 1041 and small-strip thin gap chambers (sTGCs) [46, 47]. Unlike the previous detectors, both of these detector  
 1042 technologies can be used for tracking or trigger. However, the micromegas is more suited to tracking be-  
 1043 cause of its good spatial resolution, while the sTGCs have better time resolution and are more suited for  
 1044 the trigger. To maintain a fully redundant system, both technologies are used for both purposes.

#### 1045 MICROMEGAS

1046 Micromegas detectors operate using a thin metallic mesh that sits approximately  $100 \mu\text{m}$  away from the  
 1047 readout electrodes to create the amplification region. Above this mesh, there is a drift region on the order  
 1048 of a few mm in length capped by a drift electrode. As a charged particle traverses the detector, it ionizes gas  
 1049 and the electrons drift down towards readout strips. The timing of the drift can be used to reconstruct the  
 1050 angle of traversal of the particle. This is illustrated in figure 2.12. The micromegas used in ATLAS will be  
 1051 resistive micromegas, where the readout electrodes are topped with resistive strips [48]. This alleviates the

1052 risk of sparking in the large area detectors that ATLAS will use.

1053 In ATLAS, the micromegas drift gap will be 5 mm and the amplification gap will be  $128 \mu\text{m}$ . They are  
1054 filled with the same gas mixture as the MDTs. They will be stacked in an octuplet in an XXUV-UVXX  
1055 geometry, where X refers to straight strips and U and V refer to stereo strips at an angle of  $\pm 1.5^\circ$ . This  
1056 arrangement allows for measurement of the azimuthal coordinate and gives a large lever arm between the  
1057 straight strips for triggering purposes. Figure 2.12 shows the geometry of a single micromegas detector as  
1058 well as its operating principle [46].

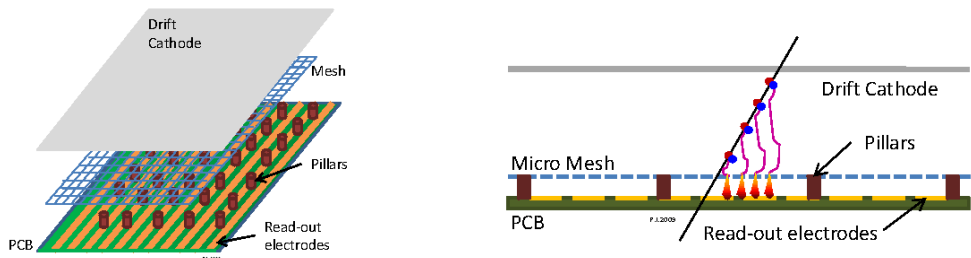


Figure 2.12: Illustrations of the geometry (left) and operating principle (right) of the micromegas detector [46]

1059 sTGCs

1060 The sTGCs are similar to the TGCs already described. They consist of gold-plated tungsten wires with a  
1061 1.8 mm pitch between two cathode planes 1.4 mm away from the wire plane. One cathode plane consists  
1062 of strips with a 3.2 mm pitch (much smaller pitch than the TGCs), while the other consists of coarser  
1063 pads that are used for defining regions of interest in the sTGC trigger algorithm. Figure 2.13 shows the  
1064 basic detector geometry.

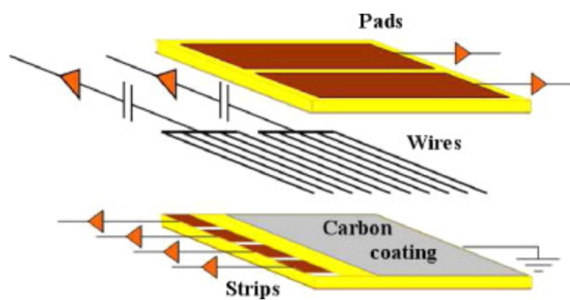


Figure 2.13: Geometry of the sTGC detector [46]

1065 2.3.3 PHYSICS IMPACT

1066 Maintaining low  $p_T$  thresholds for muons while still staying within the trigger rate budget at Level 1  
1067 (20 kHz) for the muon system is crucial for physics analyses to be successful in high luminosity condi-  
1068 tions. One realm where the lepton trigger threshold is especially important is in Higgs physics. In the  
1069  $H \rightarrow WW^*$  analysis, one of the  $W$  bosons is off shell and tends to decay to soft leptons. In associated  
1070 production of a Higgs with a  $W$ , the lepton is also important because the lepton provides the main han-  
1071 dle which allows the event to be triggered. Table 2.3 shows the impact of increasing the trigger thresholds  
1072 on these analyses. It shows that either raising the threshold or using only the barrel both have significant  
1073 impacts on the signal efficiency. With the NSW, the signal efficiency is largely maintained and the triggers  
1074 can be unprescaled.

Threshold	$H \rightarrow b\bar{b}$ (%)	$H \rightarrow WW^*$ (%)
$p_T > 20 \text{ GeV}$	93	94
$p_T > 40 \text{ GeV}$	61	75
$p_T > 20 \text{ GeV} (\text{barrel only})$	43	72
$p_T > 20 \text{ GeV} (\text{with NSW})$	90	92

Table 2.3: Signal efficiencies for  $WH$  production with  $H \rightarrow b\bar{b}$  and  $H \rightarrow WW^* \rightarrow \mu\nu qq$  under different trigger configurations [46].

1075 2.4 OBJECT RECONSTRUCTION IN ATLAS

1076 ATLAS analyses first start by requiring the presence of certain reconstructed physics objects in the event.  
1077 This section will present a brief overview of the algorithms used to reconstruct electrons, muons, jets (in-  
1078 cluding  $b$ -jets), and missing energy<sup>1</sup>. The performance of object reconstruction and measurement will also  
1079 be discussed as these are relevant to the analyses presented later. Figure 2.14 gives an overview of the differ-  
1080 ent sub-detectors that each type of particle will interact with in ATLAS.

---

<sup>1</sup>Reconstruction algorithms for other objects, such as photons and  $\tau$  leptons, are not detailed here as these objects are not used in the presented studies.

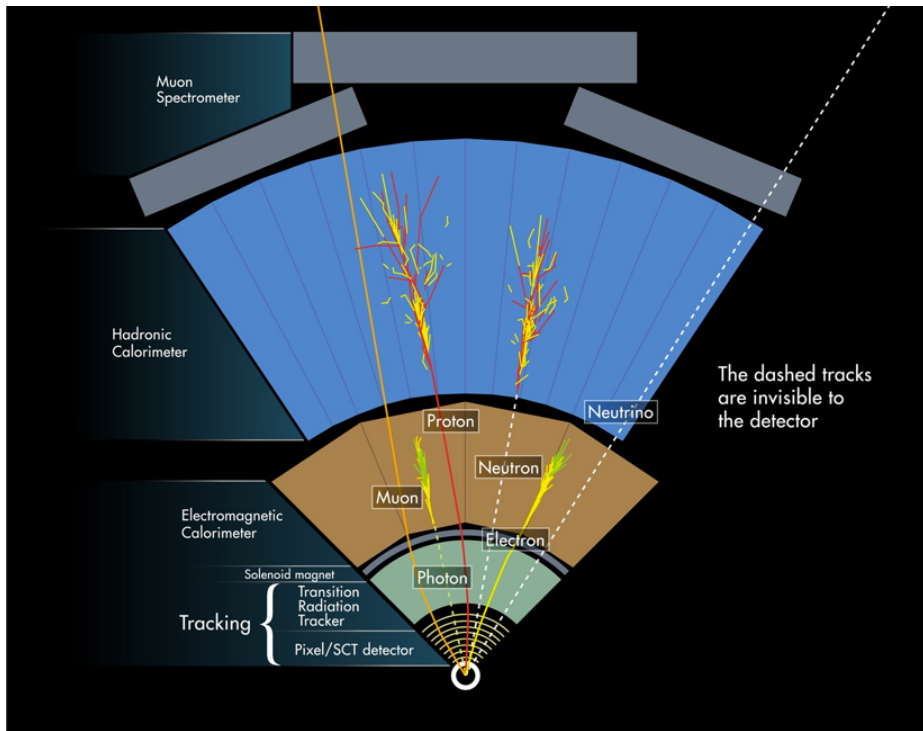


Figure 2.14: Illustration of particle interactions in ATLAS [49]

#### 1081 2.4.I ELECTRONS

1082 Electrons in ATLAS will leave tracks in the inner detector and energy deposits in the electromagnetic  
 1083 calorimeter. The algorithm for recognizing the signature of electrons proceeds in two steps: reconstruction  
 1084 and identification.

1085 In reconstruction, an electron candidate is formed by matching EM calorimeter deposits with ID tracks.  
 1086 The algorithm first chooses seed clusters in the EM calorimeter by using a sliding window algorithm that  
 1087 searches for towers with transverse energy larger than 2.5 GeV. In addition to seed clusters, track candi-  
 1088 dates must be identified in the ID. The algorithm selects seed tracks with  $p_T > 1$  GeV that do not fit well  
 1089 with a pion hypothesis. Once candidate tracks are selected, they are re-fit with a Gaussian Sum Filter (GSF)  
 1090 algorithm to estimate electron parameters [50]. Finally, an electron candidate is formed if at least one track  
 1091 matches to a seed cluster in the calorimeter. The full details of the reconstruction algorithm can be found  
 1092 in reference [51].

1093 Once an electron candidate is present, identification criteria must be applied in order to reject fake elec-

1094 trons from background. Many different variables are used for this identification, most of them related to  
 1095 the shower shape in the EM calorimeter and the amount of leakage into the hadronic calorimeter, as well  
 1096 as information from the ID and in particular the TRT. There are both cut-based and likelihood-based  
 1097 criteria that range from “loose” to “very tight”. For details, see reference [51].

1098 Figure 2.15 shows the algorithm’s reconstruction efficiency of true electrons for different identification  
 1099 criteria as well as the electron energy resolution in simulation [51, 52]. The reconstruction efficiency is  
 1100 measured using both  $Z$  and  $J/\psi$  tag and probe techniques.

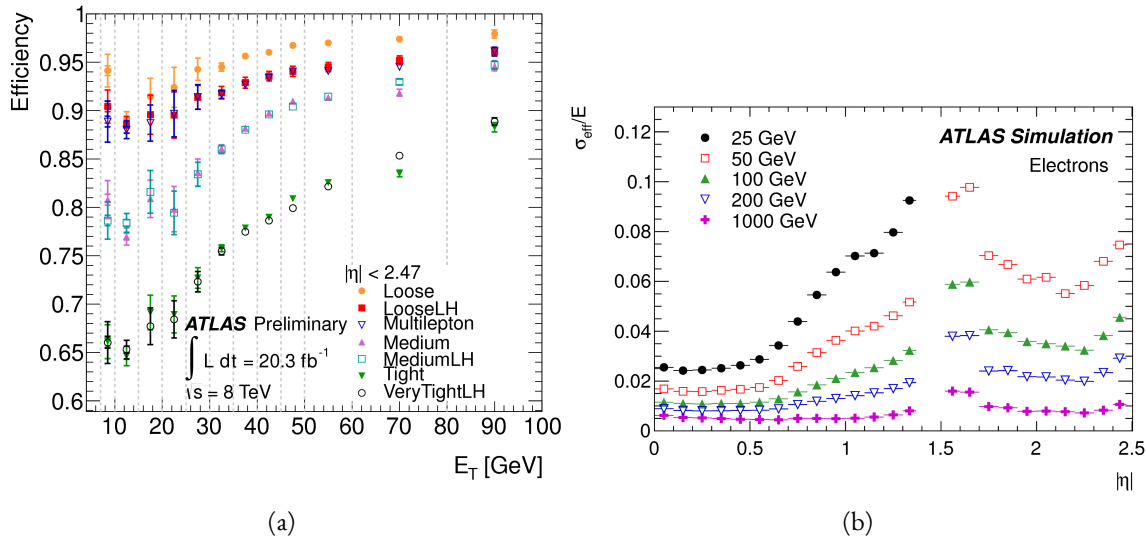


Figure 2.15: Electron performance: (a) reconstruction efficiency as a function of electron  $E_T$  [51] (b) energy resolution in simulation as a function of  $|\eta|$  for different energy electrons [52]

#### 1101 2.4.2 MUONS

1102 The ATLAS detector is designed to stop most particles before they reach the muon spectrometer. Muons,  
 1103 however, are minimum ionizing particles, meaning that they will not lose a significant amount of energy  
 1104 through interactions with the detector and will thus pass through. Therefore, the muon reconstruction  
 1105 works to match tracks in the muon spectrometer with tracks in the inner detector.

1106 The first step of reconstruction is to reconstruct local straight line tracks, called segments, in each muon  
 1107 chamber. Segments are then fit to larger tracks that traverse the entire muon spectrometer. Such muon  
 1108 tracks are referred to as “standalone” tracks (SA) as they only use information from the muon spectrometer.

1109 The standalone tracks are then matched to tracks in the inner detector to form “combined” (CB) muons,  
 1110 where the combined ID and MS fit are used to determine the momentum and direction of the muon. To  
 1111 improve acceptance, segment-tagged and calorimeter-tagged muons are also reconstructed. In these cases,  
 1112 ID tracks are matched to segments in the MS and calorimeter deposits consistent with a minimum ionizing  
 1113 particle, respectively. The details of the reconstruction can be found in reference [53].

1114 As with electrons, once muon candidates are reconstructed they have identification criteria applied to  
 1115 reduce background. These criteria include the  $\chi^2$  match between the ID and MS tracks, the number of  
 1116 hits in the ID, overall ID and MS track fit quality, and additional variables [53]. The criteria range from  
 1117 “loose” to “tight” as with electrons.

1118 Figure 2.16 shows the muon reconstruction efficiency (measured with  $Z$  and  $J/\psi$  tag and probe) and  
 1119 invariant mass resolution [53].

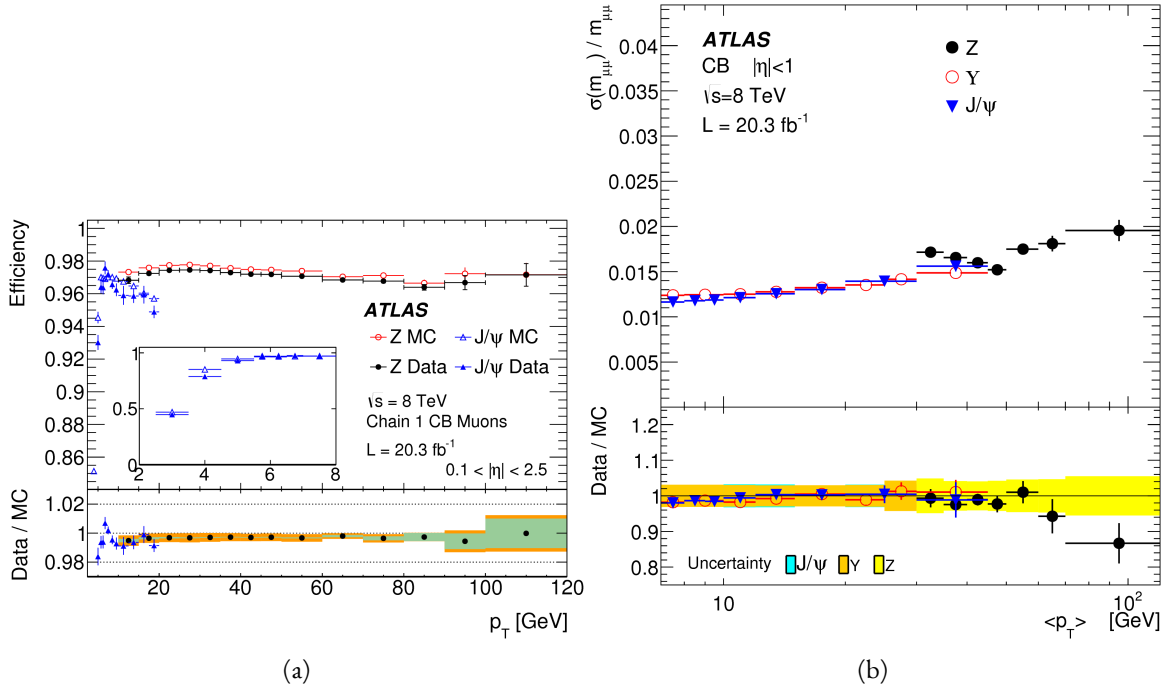


Figure 2.16: Muon performance: (a) reconstruction efficiency as a function of muon  $p_T$  (b) dimuon mass resolution as a function of average  $p_T$  [53]

1120 2.4.3 JETS

1121 When a quark or gluon is produced in collisions, it is not measured directly in ATLAS. Rather, due to  
1122 QCD effects, it produces a collimated spray of hadrons in the direction of the original parton, which is  
1123 known as a jet. Jets are reconstructed in ATLAS using energy deposits in the hadronic calorimeter. The  
1124 first step is build “topological clusters” out of energy deposits in calorimeter cells [54, 55]. This is done  
1125 using strategy where seed cells are chosen by picking cells whose energy measurements are four times the  
1126 amount of noise expected for that cell. Adjacent cells with at least  $2\sigma$  energy measurements are added to  
1127 the cluster, then a final layer of clusters with energy above  $0\sigma$  are added. Once calorimeter clusters are  
1128 formed, they are clustered further into jet candidates using the anti- $k_T$  jet clustering algorithm [56]. This  
1129 algorithm uses a parameter  $R$  that appears in the denominator of the clustering distance metric and defines  
1130 the radial size of the jet in  $\eta$ - $\phi$  space.

1131 The energy response of the calorimeter must be properly characterized in order to reconstruct jet energy.  
1132 Calorimeter clusters can be calibrated either with the EM calibration, where each cluster is assumed to have  
1133 come from the energy deposit of an electron or photon, or the LCW calibration, where local cluster weights  
1134 are computed to allow for local calibration of clusters as hadronic or electromagnetic. The details of the  
1135 jet energy calibration are not detailed here and are discussed in reference [57].

1136 Figure 2.17 shows the jet energy response after calibration in Monte Carlo as a function of the true  $p_T$   
1137 of the jet [57].

1138 2.4.4  $b$ -TAGGING

1139 One important aspect of jet physics is the task of identifying the flavor of parton that produced the  
1140 measured jet. While in general this is very difficult, jets from  $b$ -quarks offer an interesting case where such  
1141 identification is possible.  $B$  mesons have a lifetime on the order of  $10^{-12}$  seconds, which makes a  $c\tau$  on  
1142 the order of millimeters [6]. This type of displaced decay vertex can be identified in detectors like ATLAS  
1143 and allows  $b$ -jets to be distinguished from other flavors of jets<sup>2</sup>.

---

<sup>2</sup>Jets from charm quarks can also be detected in this way but they do not live quite as long so the displacement of the vertex is harder to distinguish

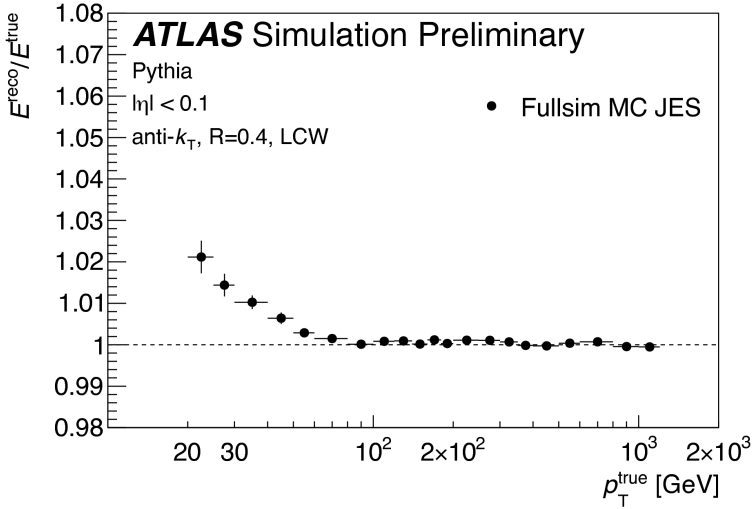


Figure 2.17: Jet energy response after calibration as a function of true  $p_T$  in simulation [57]

1144     ATLAS uses a multivariate machine learning algorithm to identify jets from  $b$ -quarks. The inputs to this  
 1145    algorithm are determined from lower level reconstruction algorithms. There are three distinct algorithms  
 1146    that reconstruct variables which are used as input to the multivariate technique.

1147     The first family is referred to as IPxD (where the x can either be 2 or 3). These algorithms use the trans-  
 1148    verse and longitudinal impact parameters  $d_0$  and  $z_0$  of the tracks inside a jet to determine their consistency  
 1149    with the primary vertex. They two or three dimensional (hence the x) templates for light flavor, charm,  
 1150    and bottom jets and then evaluate the likelihood of the jet coming from each of these types. The likelihood  
 1151    ratios are used as inputs to the multivariate algorithm.

1152     The next two algorithms used as input are referred to as the secondary vertex (SV) and JetFitter (JF)  
 1153    algorithms. The SV algorithm uses tracks inside the jet to fit for vertices that are displaced from the pri-  
 1154    mary vertex. The JF algorithm attempts to reconstruct the full flight path of the  $b$  by looking for multiple  
 1155    displaced vertices along the same line (as  $B$  decays often result in subsequent  $c$  decays).

1156     In Run 1, the multivariate  $b$ -tagging algorithm used a neural network and was referred to as MV1.  
 1157    The details of this algorithm and its inputs are given in reference [58]. In Run 2, the number of inputs  
 1158    was simplified and a boosted decision tree with 24 input variables was used, referred to as MV2 [59]. The  
 1159    MV2 algorithm is a boosted decision tree incorporating twenty-four input variables constructed from three

1160 lower level input algorithms described above. Figure 2.18 summarizes the inputs to MV2. Figure 2.19 shows  
1161 the performance of each of these algorithms.

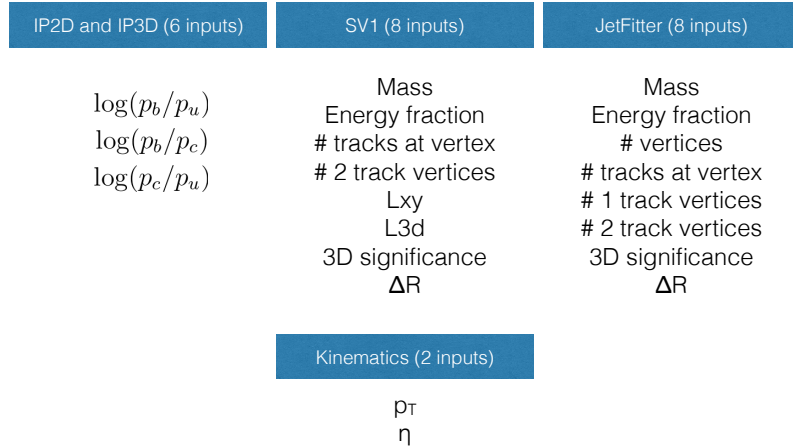


Figure 2.18: Summary of the inputs to the MV2  $b$ -tagging algorithm

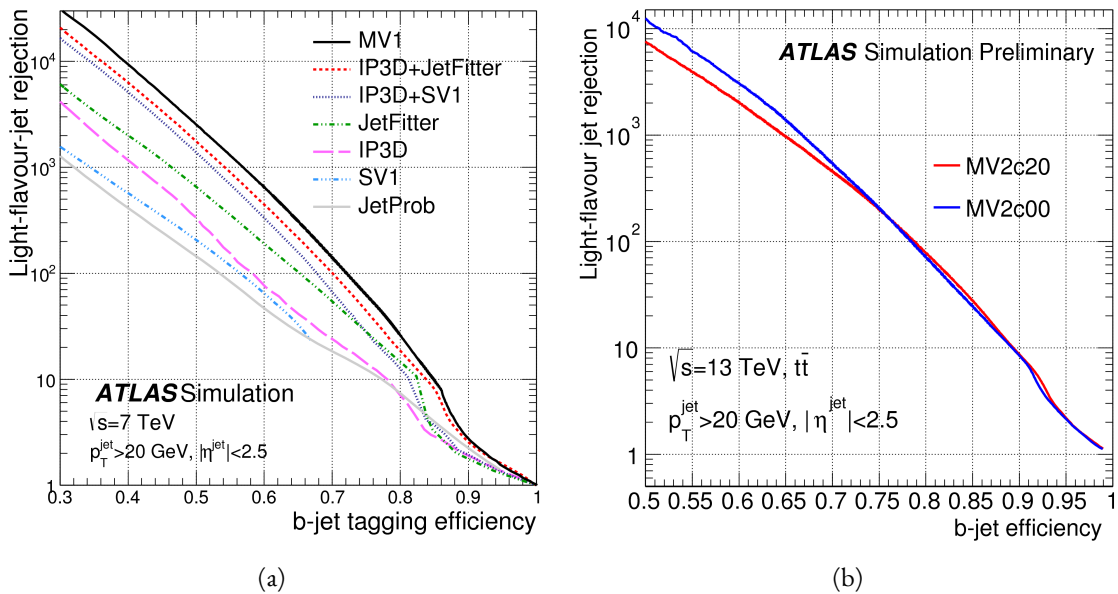


Figure 2.19: Light jet rejection (1/efficiency) vs.  $b$ -jet efficiency for MV1 and its input algorithms (a) [58] and MV2 (b) [59] in simulated  $t\bar{t}$  events. The numbers in the algorithm names in (b) refer to the fraction of charm events used in the MV2 training.

1162    2.4.5 MISSING TRANSVERSE ENERGY

1163    As noted in figure 2.14, neutrinos produced in ATLAS will pass through the detector without interact-  
1164    ing. The only way of detecting the presence of particles like neutrinos (or BSM particles that are long-lived)  
1165    is to use missing transverse momentum. The basic principle of missing transverse energy is to use the mo-  
1166    mentum balance of the incoming protons to infer the presence of missing particles. The net longitudinal  
1167    momentum of the incoming partons that collide is not known (since each carries an unknown fraction of  
1168    the proton's momentum). However, the protons (and thus incoming partons) have no net momentum  
1169    in the plane transverse to the beam line (the  $x$ - $y$ ) plane. Therefore, if there are no un-measured particles  
1170    in the final state, the transverse momenta of all of the final state particles should balance. The magnitude  
1171    of this imbalance is known as missing transverse momentum ( $E_T^{\text{miss}}$ ).

1172    The basic calculation of missing transverse momentum from calorimeter cells is given in equation 2.4 [60].

1173

$$\begin{aligned} E_x^{\text{miss}} &= -\sum_{i=1}^{N_{\text{cell}}} E_i \sin \theta_i \cos \phi_i \\ E_y^{\text{miss}} &= -\sum_{i=1}^{N_{\text{cell}}} E_i \sin \theta_i \sin \phi_i \end{aligned} \quad (2.4)$$

1174    The  $E_T^{\text{miss}}$  calculation is separated into different terms based on the objects that the calorimeter clusters  
1175    are associated with. This way, each cell's contribution is calibrated appropriately according to the object.  
1176    This separation of terms is shown in equation 2.5 [60].

$$\begin{aligned} E_{x(y)}^{\text{miss,calo}} &= E_{x(y)}^{\text{miss},e} + E_{x(y)}^{\text{miss},\gamma} + E_{x(y)}^{\text{miss},\tau} + E_{x(y)}^{\text{miss,jets}} \\ &\quad + E_{x(y)}^{\text{miss,softjets}} + E_{x(y)}^{\text{miss},\mu} + E_{x(y)}^{\text{miss,CellOut}} \end{aligned} \quad (2.5)$$

1177    The CellOut term of the above equation corresponds to calorimeter cells with energy deposits that are  
1178    not associated with other objects. The soft jets term comes from cells associated to jets with  $p_T$  between  
1179    7 and 20 GeV, while the jets term comes from jets with  $p_T > 20$  GeV. Because muons do not deposit  
1180    significant energy in the calorimeter, the muon momentum is used for the muon term [60]. The final  
1181     $E_T^{\text{miss}}$  is calculated using equation 2.6.

$$E_T^{\text{miss}} = \sqrt{(E_x^{\text{miss}})^2 + (E_y^{\text{miss}})^2} \quad (2.6)$$

1182 Figure 2.20 shows the resolution of the components of the  $E_T^{\text{miss}}$  under different pileup suppression techniques [61].

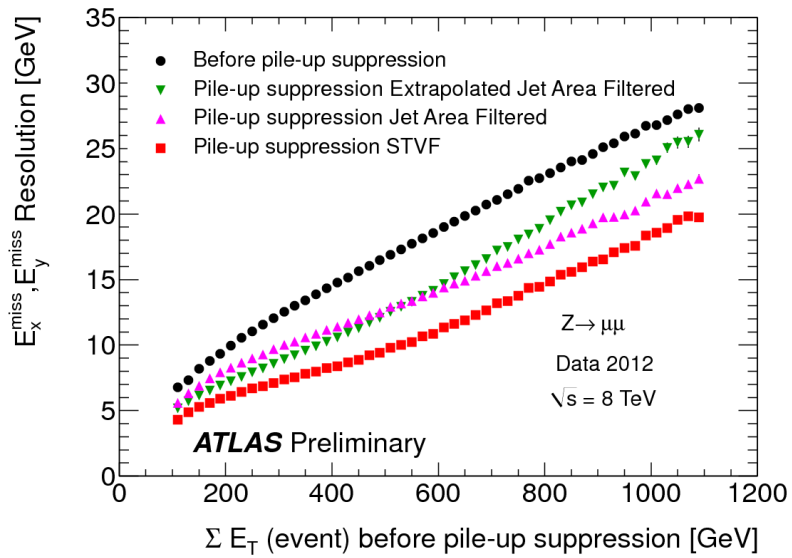


Figure 2.20: Resolution of  $E_T^{\text{miss}}$  components as a function of  $\sum E_T$  before pileup suppression with different pileup techniques [61]

1183

1184

## Part II

1185

Observation and measurement of Higgs

1186

boson decays to  $WW^*$  in LHC Run I at

1187

$\sqrt{s} = 7$  and 8 TeV

*Basic research is what I am doing when I don't know what  
I am doing.*

Wernher von Braun

# 3

1188

1189

## $H \rightarrow WW^* \rightarrow \ell\nu\ell\nu$ Analysis Strategy

### 1190 3.1 INTRODUCTION

1191 This chapter presents an overview of the strategy for searching for a Higgs boson in the  $H \rightarrow WW^* \rightarrow$   
1192  $\ell\nu\ell\nu$  decay topology. Its purpose is to define in broad terms how the search and measurement are under-  
1193 taken, before going into details on the specific sub-categories within the larger analysis. First, the properties  
1194 of the Higgs signal are discussed and the associated backgrounds are presented. Next, the observables used  
1195 to enhance the signal to background ratio are defined. Finally, the parameters of interest in the search  
1196 and measurement will be shown, along with a brief overview of the statistical treatment of the final Higgs  
1197 candidates.

1198 Following this chapter, the results of three different studies within the  $H \rightarrow WW^* \rightarrow \ell\nu\ell\nu$  channel  
1199 are shown. Chapter 4 presents a search for Higgs boson production in gluon fusion mode and the role of  
1200 the  $H \rightarrow WW^*$  channel in its discovery. Chapter 5 shows the search and first observation in ATLAS of  
1201 the Vector Boson Fusion (VBF) production mode of the Higgs in the  $H \rightarrow WW^*$  decay channel. Finally,

1202 chapter 6 shows the combined Run 1  $H \rightarrow WW^*$  results for the measurement of the Higgs cross section  
1203 and relative coupling strengths to other SM particles.

1204 3.2 THE  $H \rightarrow WW^* \rightarrow \ell\nu\ell\nu$  SIGNAL IN ATLAS

1205 The signal studied in this and subsequent chapters is the Higgs boson in the  $WW^*$  final state, where  
1206 each  $W$  boson subsequently decays into a charged lepton and a neutrino. In the simplest decay path, the  
1207 final state consists of two neutrinos and two charged leptons, each of which can be either an electron or a  
1208 muon. If a  $W$  decays to a  $\tau$  lepton, only leptonic decays of the  $\tau$  are considered. The  $\tau$  lepton produce  
1209 additional neutrinos in the final state but still yield two charged leptons (where each lepton is an electron or  
1210 muon). Neutrinos are not detected in ATLAS, so the final state ultimately consists of two reconstructed  
1211 leptons and missing transverse momentum (denoted as  $E_T^{\text{miss}}$ ). Final states where both of the charged  
1212 leptons are electrons or muons are referred to as the “same flavor” ( $ee/\mu\mu$ ) final states, while those with  
1213 one electron and one muon are referred to as “different flavor” ( $e\mu$  or  $\mu e$ ).

1214 There can be additional jets produced in association with the Higgs boson. As described in detail in  
1215 Chapter 1, if the Higgs is produced via vector boson fusion production, there will be two additional forward  
1216 jets in the event. In gluon fusion, one or more jets can be produced through initial state radiation from  
1217 the incoming gluons. Because of the varying background composition as a function of jet multiplicity,  
1218 each bin in this variable has its own dedicated requirements applied in the search and measurement. The  
1219  $n_j = 0$  and  $n_j = 1$  bins are dedicated to gluon fusion production, while the  $n_j \geq 2$  bin has separate  
1220 dedicated searches for ggF and VBF production.

1221 Figure 3.1 shows the relative branching fractions for the  $H \rightarrow WW^*$  process, calculated from the Par-  
1222 ticle Data Group values for the  $W$  and  $\tau$  branching ratios [6]. The largest branching ratio corresponds  
1223 to both  $W$  bosons decaying to quark pairs at 45.44%. The second largest ratio is for one  $W$  decaying lep-  
1224 tonically and the other decaying to quarks, a branching ratio of 34.18%. In all cases,  $\ell$  denotes either an  
1225 electron or muon, and the leptonic branching ratios of the  $\tau$  are included. For example, the  $\ell\nu qq$  final  
1226 state includes one  $W$  decaying to  $e\nu$ ,  $\mu\nu$ , or  $\tau\nu$ . In the case of the  $W \rightarrow \tau\nu$  decay, the  $\tau$  lepton then  
1227 decays to an electron or muon via  $\tau \rightarrow \nu_\tau \ell \nu_\ell$ . Final states with a  $\tau_h$  refer to hadronic decays of the  $\tau$ . The

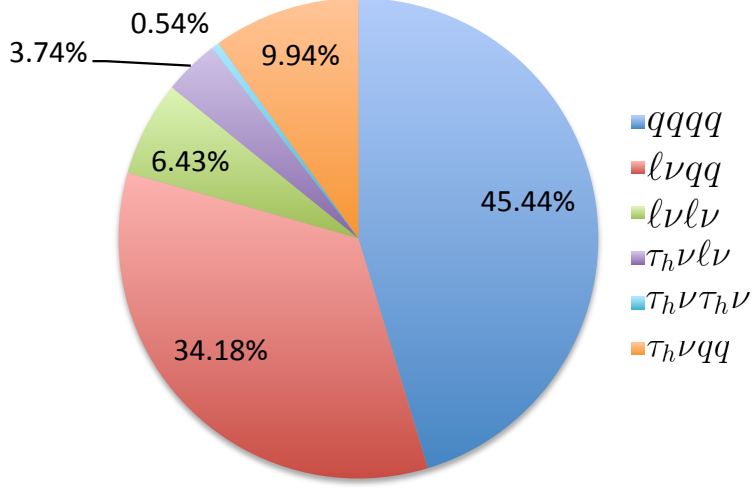


Figure 3.1: Branching ratios for a  $WW$  system.  $q$  refers to quarks.  $\ell$  can be either an electron or muon, and the leptonic branching ratios of the  $\tau$  are included. For example, the  $\ell\nu qq$  final state includes one  $W$  decaying to  $e\nu$ ,  $\mu\nu$ , or  $\tau\nu$ .  $\tau_h$  refer to hadronic decays of the  $\tau$ .

branching ratio of the  $\ell\nu\ell\nu$  final state is 6.43%.

While the  $\ell\nu\ell\nu$  final state is not a large fraction of the branching ratio, there are significant advantages to using this channel in an analysis. First, both the  $qqqq$  and  $\ell\nu qq$  channels suffer from a large QCD multijet background, which is often difficult to model. Second, events in the the  $\ell\nu\ell\nu$  channel in data can be triggered more efficiently due to the presence of two leptons.

### 3.3 BACKGROUND PROCESSES

Many processes from the Standard Model can also produce a final state with two leptons and missing transverse momentum. This section describes the dominant backgrounds to Higgs production and further explains how they can be reduced. Table 3.1 summarizes the different background processes.

#### 3.3.1 STANDARD MODEL WW PRODUCTION

Non-resonant Standard Model diboson production, as shown in figure 3.2, is an irreducible background to Higgs boson production in the  $WW$  final state. It produces the same exact final state objects, namely

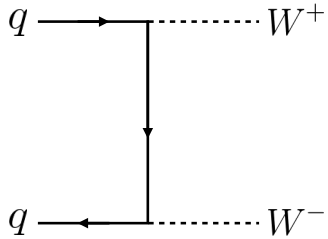


Figure 3.2: Feynman diagram for Standard Model  $WW$  production

leptonically decaying W bosons. There are no additional objects in the final state that allow for background reduction. Therefore the analysis solely relies on the correlations between the leptons to reduce this background.

### 3.3.2 TOP QUARK PRODUCTION

Top quark production can mimic the Higgs in the  $WW^*$  final state as well. Top quarks can be produced either in pairs ( $t\bar{t}$  production) or singly ( $s$ -channel,  $t$ -channel, or associated production  $Wt$ ). The dominant top background are  $t\bar{t}$  and  $Wt$  production.

Because top quarks decay via  $t \rightarrow Wb$ , top pair production can produce a final state with two W bosons that then decay leptonically. In  $Wt$  production, there are two real W bosons produced, as with  $t\bar{t}$ . In both cases, there is at least one  $b$ -jet in the final state. By vetoing on the presence of  $b$ -jets, these top quark backgrounds can be reduced. Figure 3.3 shows the Feynman diagrams for  $t\bar{t}$  and  $Wt$  production.

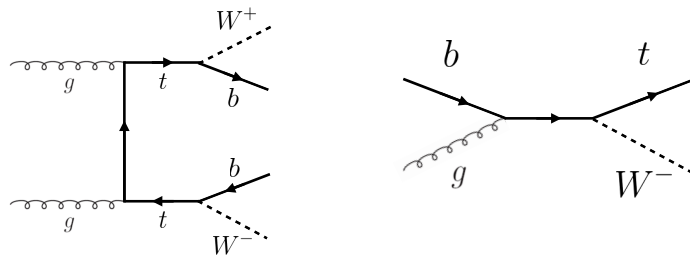


Figure 3.3: Feynman diagrams for top pair production (left) and  $Wt$  production (right)

1251 3.3.3  $W$ +JETS BACKGROUND

1252 Single  $W$  boson production in association with jets is a unique background to Higgs production. The  
1253 other backgrounds considered thus far have all included two prompt leptons, each decaying from a  $W$   
1254 boson, in the final state. In  $W$ +jets production, however, only one reconstructed lepton originates from  
1255 a  $W$ . The second reconstructed lepton is either an algorithmic “fake” or the result of non-prompt decays.  
1256 In the first case, the lepton is a jet misidentified as a lepton by either the electron or muon reconstruction  
1257 algorithms. In the second case, the lepton may be a real lepton but coming from semi-leptonic decays of  
1258 particles inside the shower of the jet. This background can be reduced by requiring that the reconstructed  
1259 lepton have little activity in the surrounding region of the calorimeter (also known as an “isolation”). Fig-  
1260 ure 3.4 shows the Feynman diagram for  $W$ +jets production.

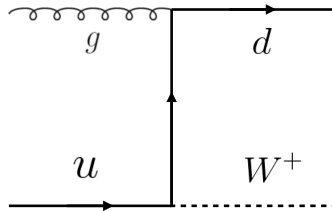


Figure 3.4: An example Feynman diagram of  $W$ +jets production

1261 3.3.4  $Z/\gamma^*$ +JETS BACKGROUND

1262 Production of a  $Z$  boson or virtual photon (also known as Drell-Yan and denoted with  $Z/\gamma^*$ ) in as-  
1263 sociation with jets is also a background to Higgs production. The  $Z$  boson decays to two leptons of the  
1264 same flavor. When the  $Z/\gamma^*$  decays directly to electrons or muons, the background enters the same flavor  
1265 final state. When the  $Z$  decays to two  $\tau$  leptons the background can enter the different flavor final state as  
1266 well. Figure 3.5 shows the production of a  $Z$  in association with one jet. Because there are no neutrinos in  
1267 this final state, variables like  $E_T^{\text{miss}}$  can be used to reduce the background<sup>1</sup>.

<sup>1</sup>The  $E_T^{\text{miss}}$  cut is much more effective for the reduction of  $Z/\gamma^*$  production in the same flavor final state. If the background enters the different flavor final state through  $\tau$  decays, there will be neutrinos present. Other requirements on the lepton invariant mass are made to reduce the  $Z/\gamma^* \rightarrow \tau\tau$  background.



Figure 3.5: An example Feynman diagram of  $Z$ +jets production

1268 **3.3.5 SUBDOMINANT BACKGROUNDS**

1269 There are additional processes which contribute to the background composition. These backgrounds  
1270 are subdominant and contribute less to the total background estimate than those discussed previously.  
1271 The first process is referred to as  $VV$  or “Other diboson” processes and includes multiple Standard Model  
1272 diboson processes, including  $WZ$ ,  $ZZ$ ,  $W\gamma$ ,  $W\gamma^*$ , and  $Z\gamma$  production. Additionally, there is a back-  
1273 ground contribution from QCD multijet production. While the cross section for this process is large, its  
1274 contribution to the  $WW^*$  final state is small because two jets must be misidentified as leptons.

Category	Process	Description
SM $WW$	$WW \rightarrow \ell\nu\ell\nu$	Real leptons and neutrinos
Top quark production	$t\bar{t} \rightarrow WbWb \rightarrow \ell\nu b\bar{b}\nu\bar{b}$	Real leptons, untagged $b$ s
	$tW \rightarrow WbW \rightarrow \ell\nu\ell\nu b$	Real leptons, untagged $b$
	$t\bar{b}, t\bar{q}\bar{b}$	Untagged $b$ , jet misidentified as lepton
Drell-Yan	$Z/\gamma^* \rightarrow ee, \mu\mu$	“Fake” $E_T^{\text{miss}}$
	$Z/\gamma^* \rightarrow \tau\tau \rightarrow \ell\nu\ell\nu\nu\nu$	Real leptons and neutrinos
Other dibosons	$ZZ \rightarrow \ell\ell\nu\nu$	Real leptons and neutrinos
	$W\gamma^*, WZ \rightarrow \ell\nu\ell\ell, ZZ \rightarrow \ell\ell\ell\ell$	Unreconstructed leptons
	$W\gamma, Z\gamma$	$\gamma$ reconstructed as $e$ , unreconstructed lepton
$W$ +jets	$Wj \rightarrow \ell\nu j$	Jet reconstructed as lepton
QCD multijet	$jj$	Jets reconstructed as leptons

Table 3.1: A summary of backgrounds to the  $H \rightarrow WW^* \rightarrow \ell\nu\ell\nu$  signal

1275 **3.4 SHARED SIGNAL REGION SELECTION REQUIREMENTS**

1276 As presented in section 3.2, there are many different combinations of physics objects that can define a  
1277  $H \rightarrow WW^* \rightarrow \ell\nu\ell\nu$  final state. The multiplicity of jets and the flavor combinations of the leptons

1278 both lead to many potential signal regions. Additionally, signal regions can be optimized separately to be  
 1279 sensitive to the distinct production modes of the Higgs. Gluon fusion, vector boson fusion, and associated  
 1280 production of a Higgs all lead to unique final state topologies. Figure 3.6 delineates the different signal  
 1281 regions used in the gluon fusion and vector boson fusion  $H \rightarrow WW^*$  analyses. While there are different  
 1282 optimizations possible in each signal region, there are also some commonly shared selections that will be  
 1283 described here.

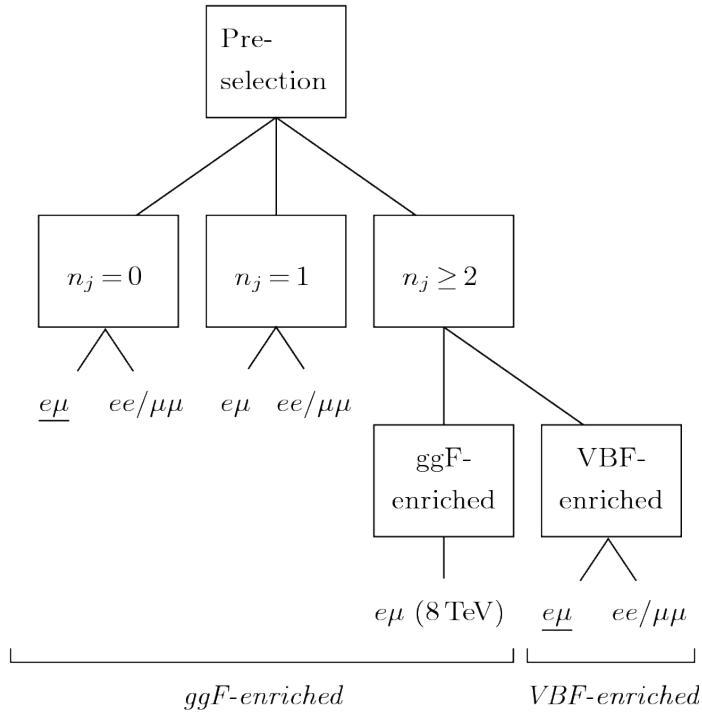


Figure 3.6: An illustration of the unique analysis signal regions [62]. The most sensitive regions for both gluon fusion and vector boson fusion production are underlined.

#### 1284 3.4.1 EVENT PRE-SELECTION

1285 Before being sorted into the distinct signal regions, basic requirements are applied to the reconstructed  
 1286 objects in the event to select Higgs-like event candidates. First, two oppositely charged leptons are required.  
 1287 Once the leptons are selected, the last requirement for event pre-selection is the presence of neutrinos. As  
 1288 neutrinos cannot be detected directly in ATLAS,  $E_T^{\text{miss}}$  can be used as a proxy for the combined neutrino  
 1289 momentum in the transverse plane.

1290 In general, it is expected that the signal should have a harder  $E_T^{\text{miss}}$  spectrum than backgrounds, espe-  
 1291 cially if these backgrounds do not contain neutrinos in the final state. When using  $E_T^{\text{miss}}$ , it is possible  
 1292 mis-measurements of objects in the detector can lead to imbalances in the transverse plane. When such a  
 1293 mis-measurement occurs, the  $E_T^{\text{miss}}$  vector in the transverse plane will often point in the same direction as  
 1294 the mis-measured object. Therefore, a new variable,  $E_{T,\text{rel}}^{\text{miss}}$ , is used in the pre-selection.  $E_{T,\text{rel}}^{\text{miss}}$  is defined  
 1295 in equation 3.1.

$$E_{T,\text{rel}}^{\text{miss}} = \begin{cases} E_T^{\text{miss}} \sin \Delta\phi_{\text{near}} & \text{if } \Delta\phi_{\text{near}} < \pi/2 \\ E_T^{\text{miss}} & \text{otherwise,} \end{cases} \quad (3.1)$$

1296 If the closest object to the  $E_T^{\text{miss}}$  vector is within  $\pi/2$  radians in the transverse plane, the  $E_T^{\text{miss}}$  is projected  
 1297 away from this object. Otherwise, the normal  $E_T^{\text{miss}}$  vector is used. Figure 3.7 shows a graphical illustration  
 of this concept.

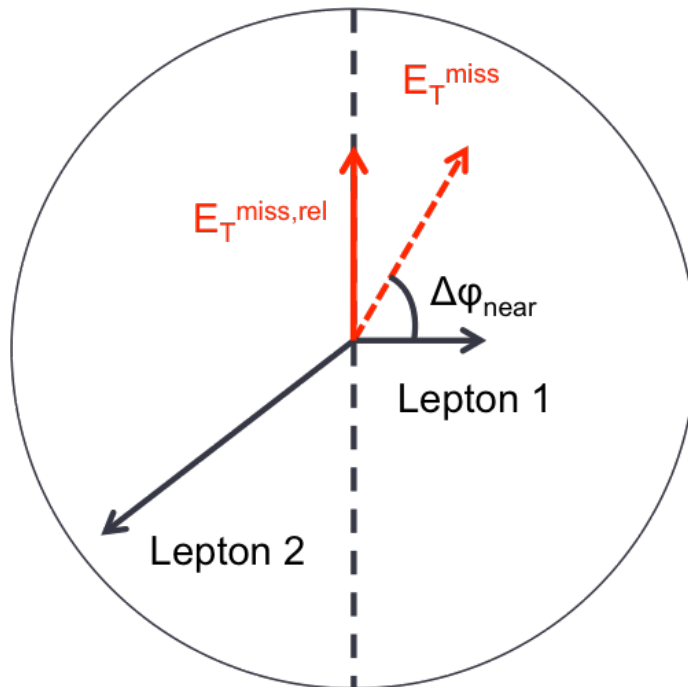


Figure 3.7: A graphical illustration of the  $E_{T,\text{rel}}^{\text{miss}}$  calculation

1298  
 1299 Once the lepton and  $E_T^{\text{miss}}$  pre-selections are made, the analysis is divided into different regions accord-  
 1300 ing to jet multiplicity.

1301    3.4.2 JET MULTIPLICITY

1302    Jet multiplicity, denoted as  $n_j$ , is used to sub-divide the analysis into distinct signal regions. By creating  
 1303    separate signal regions, each bin in jet multiplicity becomes sensitive to different modes of Higgs produc-  
 1304    tion and different backgrounds.

1305    For example, the  $n_j \geq 2$  region is more sensitive to VBF production because of the two high momen-  
 1306    tum jets produced at matrix element level. For gluon fusion production to enter this bin, two initial state  
 1307    radiation jets must be emitted.

1308    Figure 3.8 shows the jet multiplicity in both the different flavor and same flavor regions after the pre-  
 1309    selection. It also shows the background composition in the bins of  $n_b$ . A few trends from this distribution  
 1310    are worth noting. The first is that the Drell-Yan background dominates in the same flavor channels for  
 1311     $n_j \leq 1$ . Second, the top background becomes a clear contributor to the total background for  $n_j \geq$   
 1312    1. Lastly, the SM WW production dominates in the  $n_j = 0$  bin, as it is an irreducible background to  
 1313     $H \rightarrow WW^*$  production. Because of these distinct features, each jet multiplicity bin is treated separately.

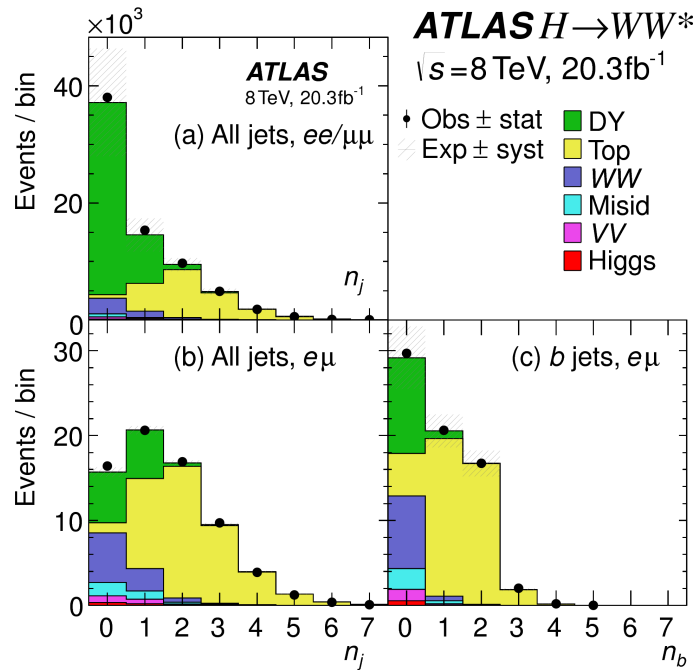


Figure 3.8: Predicted backgrounds (compared with data) as a function of  $n_j$  (a and b) and  $n_b$  (c) after pre-selection requirements

1314    **3.5 BACKGROUND REDUCTION IN SAME-FLAVOR FINAL STATES**

1315    As described in section 3.4.2, the background composition of the same flavor final states is different  
1316    from that of the different flavor states. In particular, Drell Yan processes play a much larger role because  
1317    the  $Z/\gamma^*$  decays to same flavor leptons. Because real neutrinos are absent in the  $Z/\gamma^*$  decays to  $ee$  and  $\mu\mu$ ,  
1318    a requirement on  $E_T^{\text{miss}}$  should largely reduce the background. However, as this section will demonstrate,  
1319    with increasing pileup conditions the resolution of the calorimeter-based  $E_T^{\text{miss}}$  degrades greatly. There-  
1320    fore, two new variables for  $Z/\gamma^*$  background reduction are constructed and described in this section.

1321    **3.5.1 PILEUP AND  $E_T^{\text{miss}}$  RESOLUTION**

1322    Secondary interactions of protons in the colliding bunches of the LHC (known as pileup interactions,  
1323    described in detail in Chapter 2) deposit energy into the ATLAS calorimeter in addition to the energy that  
1324    comes from the hard scatter process of interest. The calculation of  $E_T^{\text{miss}}$  is fundamentally Poissonian.  
1325    Summing up all of the energy deposits in individual calorimeter cells or clusters is similar to a counting  
1326    experiment. The error on a mean of  $N$  in a Poisson distribution is  $\sqrt{N}$ , so the energy resolution scales  
1327    as  $\sqrt{E}$ . As more energy is deposited in the calorimeter, the  $E_T^{\text{miss}}$  resolution degrades, meaning that the  
1328     $E_T^{\text{miss}}$  resolution is particularly sensitive to LHC instantaneous luminosity conditions.

1329    Figure 3.9 shows an event display of a  $Z/\gamma^* + \text{jets}$  event candidate with the twenty-five reconstructed  
1330    primary vertices. This display illustrates that while the interaction of interest only has tracks coming from  
1331    the hardest primary vertex, all of the secondary interactions deposit energy in the calorimeter as well.

1332    Figure 3.10 shows the RMS of the  $E_T^{\text{miss}}$  distribution in  $Z \rightarrow \mu\mu$  events (where there are no real neu-  
1333    trinos) as a function of the number of the average number of interactions. Under 2011 LHC conditions,  
1334    this RMS was approximately 9 GeV, while under 2012 running conditions the resolution worsened to 12  
1335    GeV. The increase in pileup dilutes the  $E_T^{\text{miss}}$  variable's ability to reduce the  $Z/\gamma^*$  background.

1336    **3.5.2 TRACK-BASED DEFINITIONS OF MISSING TRANSVERSE MOMENTUM**

1337    Because the increasing number of secondary proton-proton interactions degrades calorimeter-based  
1338     $E_T^{\text{miss}}$  resolution, a new variable using only contributions from the primary interaction vertex is necessary

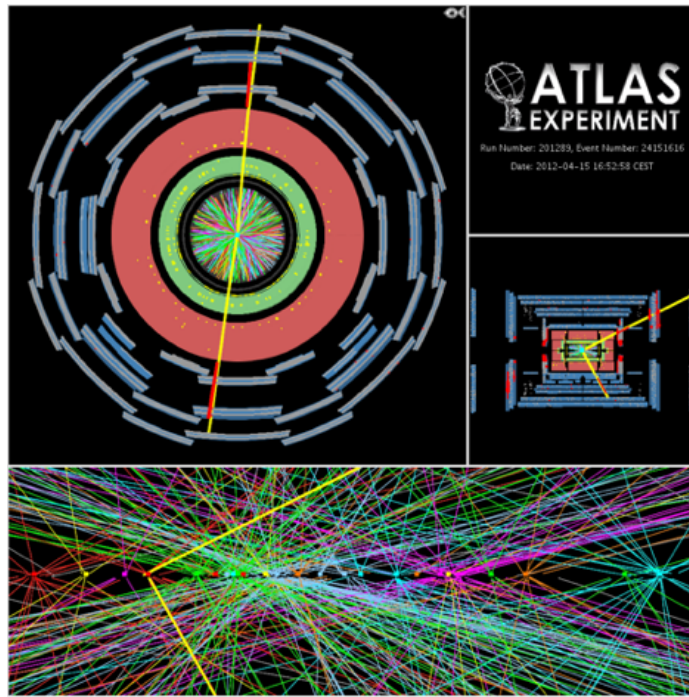


Figure 3.9: An event display of a  $Z/\gamma^*$  + jets event illustrating the effect of pileup interactions

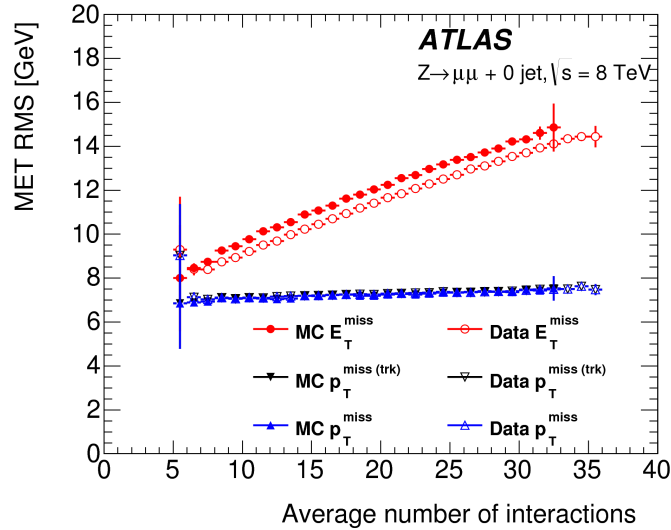


Figure 3.10: The RMS of different missing transverse momentum definitions as a function of the average number of interactions per bunch crossing

<sup>1339</sup> to further reduce the  $Z/\gamma^*$  background. While it is not possible to associate calorimeter energy deposits  
<sup>1340</sup> with a particular vertex, individual charged particle tracks in the Inner Detector are associated to unique  
<sup>1341</sup> vertices. Thus, two track-based definitions of missing transverse momentum , using only tracks coming

1342 from the primary vertex in the event, are used in the analysis. The simplest variable,  $p_T^{\text{miss}(\text{trk})}$ , is the vec-  
 1343 torial sum of the  $p_T$  of all of the tracks from the primary vertex and the selected leptons (excluding the  
 1344 tracks associated with the selected leptons to avoid double counting). Equation 3.2 defines  $p_T^{\text{miss}(\text{trk})}$ .

$$p_T^{\text{miss}(\text{trk})} = - \left( \sum_{\text{selected leptons}} p_T + \sum_{\text{other tracks}} p_T \right), \quad (3.2)$$

1345 To further improve the resolution on the missing transverse momentum, the variable  $p_T^{\text{miss}}$  is used as de-  
 1346 fined in equation 3.3. For selected leptons and jets, the nominal  $p_T$  measurements are used. Tracks are used  
 1347 to estimate the soft component of the missing transverse momentum instead of calorimeter measurements.

1348

$$p_T^{\text{miss}} = - \left( \sum_{\text{selected leptons}} p_T + \sum_{\text{selected jets}} p_T + \sum_{\text{other tracks}} p_T \right), \quad (3.3)$$

1349 Figure 3.10 illustrates that these two new variables accomplish their intended purpose. The resolution as a  
 1350 function of mean number of interactions for both  $p_T^{\text{miss}(\text{trk})}$  and  $p_T^{\text{miss}}$  is much flatter than the dependence  
 1351 for  $E_T^{\text{miss}}$ . Figure 3.11a shows the difference between the true and reconstructed values of missing transverse  
 1352 momentum using both the track-based  $p_T^{\text{miss}}$  and calorimeter based  $E_T^{\text{miss}}$ . The RMS of the distribution  
 1353 improves by 3.5 GeV when using  $p_T^{\text{miss}}$ .

### 1354 3.5.3 DISTINGUISHING $Z/\gamma^*$ +JETS AND $H \rightarrow WW^*$ TOPOLOGIES

1355 In addition to measuring missing transverse momentum, another variable can be constructed to exploit  
 1356 kinematic and topological differences between the  $Z/\gamma^*$  background and  $H \rightarrow WW^*$  signal. Because  
 1357 there are no real neutrinos in the final state (in the case of  $Z/\gamma^* \rightarrow ee, \mu\mu$  decays), the dilepton system will  
 1358 be balanced with the jets produced in the hard scatter. A new variable,  $f_{\text{recoil}}$ , is constructed to estimate  
 1359 the balance between the dilepton system and recoiling jets and is defined in equation 3.4. The transverse  
 1360 plane is divided into four sections, or quadrants, with one quadrant centered on the dilepton vector. The  
 1361 numerator of  $f_{\text{recoil}}$  is the magnitude of the vectorial sum of the  $p_T$  of jets in the quadrant opposite the  
 1362 dilepton system, weighted by each jet's Jet Vertex Fraction (JVF, described in chapter 2). The denominator

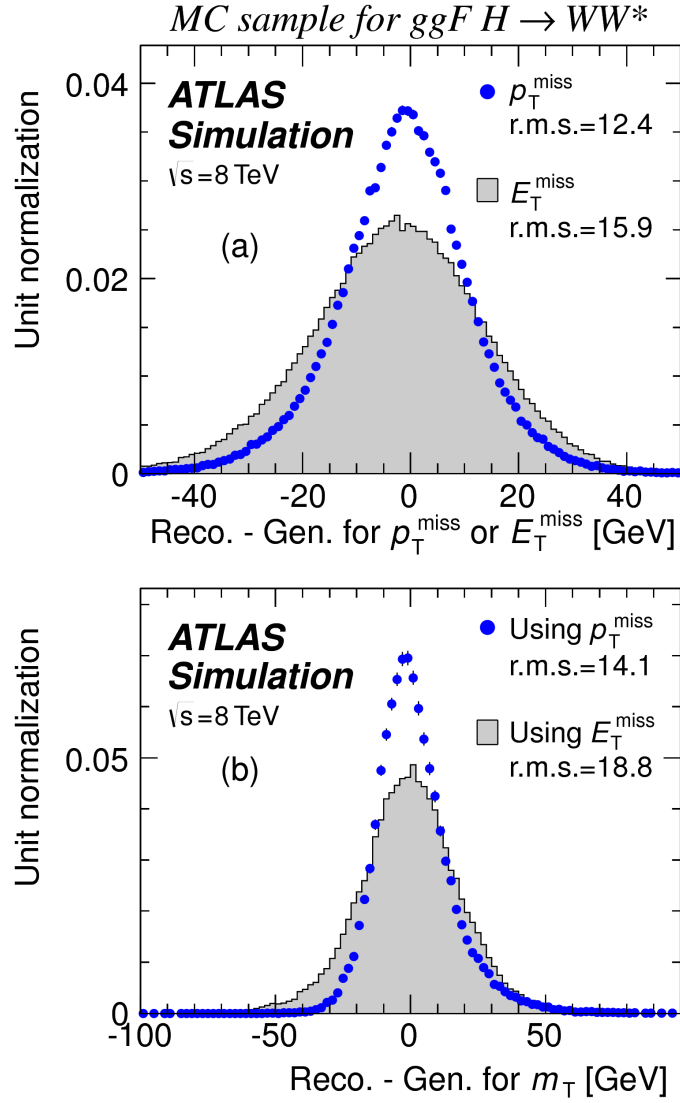


Figure 3.II: The difference between the true and reconstructed values of the missing transverse momentum (a) and  $m_T$  (b) in a gluon fusion signal sample

<sup>1363</sup> is the magnitude of the dilepton  $p_T$ .

$$f_{\text{recoil}} = \left| \sum_{\text{jets } j \text{ in } \wedge} \text{JVF}_j \cdot p_T^j \right| / p_T^{\ell\ell}. \quad (3.4)$$

<sup>1364</sup> Figure 3.12 shows a shape comparison of the  $f_{\text{recoil}}$  distribution in a simulated  $Z/\gamma^* + \text{jets}$  sample, a  
<sup>1365</sup>  $H \rightarrow WW^*$  signal sample, and other backgrounds that contain real neutrinos. The  $Z/\gamma^* + \text{jets}$  events

1366 tend to be more balanced between the dilepton system and recoiling jets, while the processes containing  
 1367 real neutrinos are less balanced in the transverse plane. Thus, a requirement on  $f_{\text{recoil}}$  will reduce the  $Z/\gamma^*$   
 1368 + jets background while maintaining a good signal efficiency.

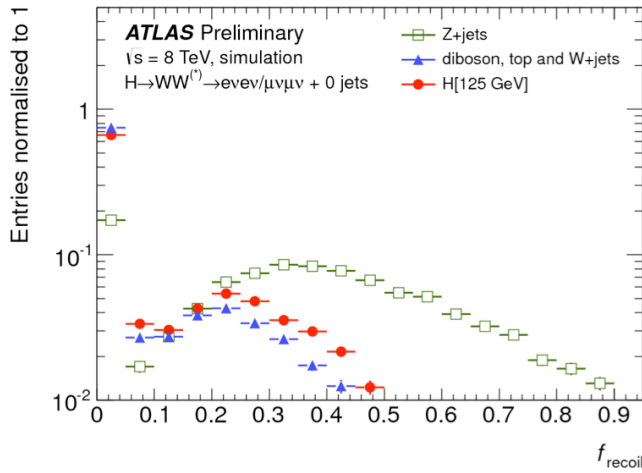


Figure 3.12: Comparison of  $f_{\text{recoil}}$  distributions for  $Z/\gamma^* + \text{jets}$ ,  $H \rightarrow WW^*$ , and other backgrounds with real neutrinos.

### 1369 3.5.4 OPTIMIZING BACKGROUND REDUCTION SELECTION REQUIREMENTS

1370 The requirements on  $p_T^{\text{miss}(\text{trk})}$  and  $f_{\text{recoil}}$  used to reduce the  $Z + \text{jets}$  background must be optimized  
 1371 to maximize expected signal significance in the same flavor channels. Figure 3.13 shows an optimization of  
 1372 the combination of the two requirements in the gluon fusion zero jet bin. Each bin shows the expected  
 1373 signal significance if the  $p_{T,\text{rel}}^{\text{miss}(\text{trk})}$  is required to be greater than the left edge of the bin and the  $f_{\text{recoil}}$  is  
 1374 required to be less than the top edge of the bin. The figure shows that the best signal significance comes  
 1375 from requiring low values of  $f_{\text{recoil}}$  ( $< 0.05$ ) and  $p_{T,\text{rel}}^{\text{miss}(\text{trk})}$  values greater than 45 GeV.

## 1376 3.6 PARAMETERS OF INTEREST AND STATISTICAL TREATMENT

1377 As with any search or measurement, there are particular parameters of the Higgs that the  $H \rightarrow WW^*$   
 1378 analysis is interested in measuring. In this case, the parameters of interest are the mass of the Higgs boson  
 1379 and its production cross section. Because the  $H \rightarrow WW^* \rightarrow \ell\nu\ell\nu$  process does not have a closed final

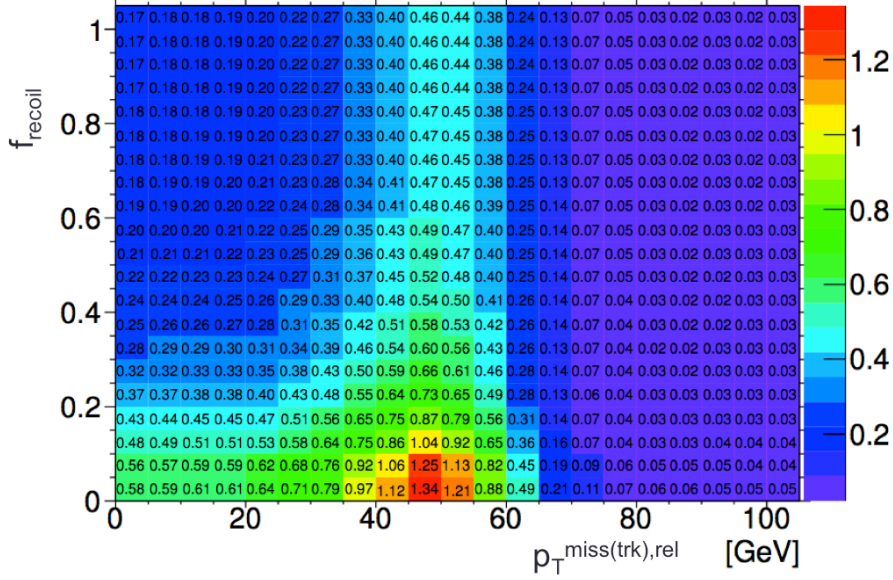


Figure 3.13: Signal significance as a function of required value for  $f_{\text{recoil}}$  and  $p_{T,\text{rel}}^{\text{miss}(\text{trk})}$  in the ggF  $H \rightarrow WW^*$  with  $n_j = 0$

state, it is not possible to measure the full invariant mass of the particle that may have produced the final state. However, a proxy for the invariant mass is defined using transverse plane information and detailed in section 3.6.1. The second parameter of interest is the ratio of the measured cross section to that expected from the Standard Model Higgs, which is denoted a  $\mu$ . This is defined in equation 3.5.

$$\mu = \frac{\sigma}{\sigma_{\text{SM}}} \quad (3.5)$$

All of the likelihoods used in the statistical analysis of the final signal region events are parameterized as a function of  $\mu$ .  $\mu$  is a natural variable for hypothesis testing, as  $\mu = 0$  corresponds to a background only hypothesis and  $\mu = 1$  corresponds exactly to a Standard Model Higgs.

### 3.6.1 TRANSVERSE MASS

The  $H \rightarrow WW^* \rightarrow \ell\nu\ell\nu$  analysis cannot reconstruct the full invariant mass of the Higgs because of the neutrinos in the final state. The transverse mass serves as a proxy for the full invariant mass by

1390 exploiting information from the transverse plane. The transverse mass is defined in equation 3.6.

$$m_T = \sqrt{(E_T^{\ell\ell} + p_T^{\text{miss}})^2 - |\vec{p}_T^{\ell\ell} + \vec{p}_T^{\text{miss}}|^2}, \quad (3.6)$$

1391 Here the  $E_T^{\ell\ell}$  and  $p_T^{\ell\ell}$  are the transverse energy and momentum of the dilepton system, while  $p_T^{\text{miss}}$  is a  
1392 proxy for the transverse momentum of the di-neutrino system. The track-based  $p_T^{\text{miss}}$  is used in the  $m_T$   
1393 rather than the calorimeter based  $E_T^{\text{miss}}$  because it has a better resolution on the true transverse mass.  
1394 Figure 3.11b shows the improvement in the RMS of the difference between the true and reconstructed  
1395 transverse mass in a ggF signal sample. The RMS improves by 4.7 GeV using  $p_T^{\text{miss}}$  in the  $m_T$  calculation.

1396 **3.6.2 STATISTICAL TREATMENT<sup>2</sup>**

1397 **LIKELIHOOD FUNCTION**

1398 The statistical analysis of final event candidates is framed as a hypothesis test, where the null hypoth-  
1399 esis is background-only (no Standard Model Higgs). The first step in the analysis is to form a likelihood  
1400 function for the data. In its simplest form, this likelihood is the probability of observing the number of  
1401 events seen in the final signal region given knowledge of the signal strength. Because observation of events  
1402 is fundamentally a Poisson counting experiment, this simple likelihood can be expressed as a Poisson prob-  
1403 ability of observing  $N$  events given a total number of predicted signal and background events. This basic  
1404 likelihood is shown in equation 3.7.

$$\mathcal{L}(\mu) = P(N|\mu S + B) \quad (3.7)$$

1405 Here,  $P$  is the Poisson probability density function,  $N$  is the total number of observed events,  $\mu$  is the  
1406 signal strength,  $S$  is the predicted number of signal events, and  $B$  is the predicted number of background  
1407 events.

1408 In particle physics, certain background estimates are commonly normalized in so-called “control” re-  
1409 gions and those predictions are scaled by the same normalization factor in the signal region. This leads to a

---

<sup>2</sup>Many thanks to Aaron Armbruster, whose thesis [63] inspired parts of this section.

<sub>1410</sub> slightly more complicated likelihood, which is a function of both the signal strength and the background  
<sub>1411</sub> normalization. This is shown in equation 3.8.

$$\mathcal{L}(\mu, \theta) = P(N|\mu S + \theta B) P(N_{\text{CR}}|\theta B_{\text{CR}}) \quad (3.8)$$

<sub>1412</sub> Here,  $\theta$  serves as a “nuisance parameter”, or a parameter that is not of primary interest but still enters the  
<sub>1413</sub> likelihood. The second Poisson term enforces that the background normalization be consistent with the  
<sub>1414</sub> number of observed events in data in the control region,  $N_{\text{CR}}$ .

<sub>1415</sub> So far, these two formulations of likelihoods have assumed a single signal region and do not take into  
<sub>1416</sub> account any shape information of potential discriminating variables. The  $H \rightarrow WW^*$  analysis is divided  
<sub>1417</sub> into many different categories, the counting experiment described above can be performed in each individ-  
<sub>1418</sub> ual category. As mentioned in section 3.6.1, the transverse mass is used as the primary discriminating vari-  
<sub>1419</sub> able in many of the  $H \rightarrow WW^*$  sub-analyses. The same counting experiment can be performed in each  
<sub>1420</sub> bin of the  $m_T$  distribution to incorporate some shape information. Thus, the total likelihood becomes a  
<sub>1421</sub> product over signal regions and bins of the  $m_T$  distribution. Finally, there are usually many backgrounds  
<sub>1422</sub> that are normalized in control regions. The new formulation of the likelihood takes this into account by  
<sub>1423</sub> including a product over control regions in the second Poisson term. All of these modifications are shown  
<sub>1424</sub> in equation 3.9.

$$\mathcal{L}(\mu, \theta) = \prod_{\substack{\text{SRs } i \\ \text{bins } b}} P\left(N_{ib} \middle| \mu S_{ib} + \sum_{\text{bkg } k} \theta_k B_{kib}\right) \prod_{\text{CRs } l} P\left(N_l \middle| \sum_{\text{bkg } k} \theta_k B_{kl}\right) \quad (3.9)$$

<sub>1425</sub> The final step to obtain the full likelihood used in the analysis is to add nuisance parameters for the  
<sub>1426</sub> systematic uncertainties. In cases where the uncertainty does not affect the shape of  $m_T$  bin-by-bin, each  
<sub>1427</sub> systematic uncertainty  $\epsilon$  is allowed to affect the expected event yields through a linear response function  
<sub>1428</sub> of the nuisance parameter, namely  $\nu(\theta) = (1 + \epsilon)\theta$ . If instead the uncertainty does affect the shape, the  
<sub>1429</sub> effect is instead parameterized by  $\nu_b(\theta) = 1 + \epsilon_b\theta$ . The value of the nuisance parameters for the systematic  
<sub>1430</sub> uncertainty are constrained with a Gaussian term that is added to the likelihood as well. This is of the form  
<sub>1431</sub>  $g(\delta|\theta) = e^{-(\delta-\theta)^2/2}/\sqrt{2\pi}$ , where  $\delta$  is the central value and  $\theta$  is a nuisance parameter. Finally, a last term is

<sup>1432</sup> added to account for the statistical uncertainty in the Monte Carlo samples used, which adds an additional  
<sup>1433</sup> poisson term. The full likelihood used in the final statistical analysis is defined in equation 3.10.

$$\begin{aligned} \mathcal{L}(\mu, \boldsymbol{\theta}) = & \prod_{\substack{\text{SRs i} \\ \text{bins b}}} P \left( N_{ib} \middle| \mu S_{ib} \cdot \prod_{\substack{\text{sig.} \\ r}} \nu_{br}(\theta_r) + \sum_{\text{bkg k}} \theta_k B_{kib} \cdot \prod_{\substack{\text{bkg.} \\ s \\ \text{syst.}}} \nu_{bs}(\theta_s) \right) \\ & \cdot \prod_{\text{CRs l}} P \left( N_l \middle| \sum_{\text{bkg k}} \theta_k B_{kl} \right) \\ & \cdot \prod_{\substack{\text{syst} \\ t}} g(\delta_t | \theta_t) \cdot \prod_{\text{bkg k}} P(\xi_k | \zeta_k \theta_k) \end{aligned} \quad (3.10)$$

<sup>1434</sup> The fourth term of the equation quantifies the uncertainty due to finite Monte Carlo sample size. Here,  
<sup>1435</sup>  $\xi$  represents the central value of the background prediction,  $\theta$  is the associated nuisance parameter,  $\zeta =$   
<sup>1436</sup>  $(B/\delta B)^2$ , where  $\delta B$  is the statistical uncertainty of  $B$ .

<sup>1437</sup> The best fit value of the signal strength  $\mu$  is determined by finding the values of  $\mu$  and  $\boldsymbol{\theta}$  that maximize  
<sup>1438</sup> the likelihood, while setting  $\delta = 0$  and  $\xi = \zeta$ . Once the likelihood is defined, a test statistic must be built  
<sup>1439</sup> for use in hypothesis testing.

#### <sup>1440</sup> TEST STATISTIC

<sup>1441</sup> To distinguish whether the data match a background only or background and signal hypothesis, a test  
<sup>1442</sup> statistic must be used. The  $H \rightarrow WW^*$  analysis uses the profile likelihood technique [64]. The first step  
<sup>1443</sup> in formulating this test statistic is to define the profile likelihood ratio, shown in equation 3.11.

$$\lambda(\mu) = \frac{\mathcal{L}(\mu, \hat{\theta}_\mu)}{\mathcal{L}(\hat{\mu}, \hat{\theta})} \quad (3.11)$$

<sup>1444</sup> Here  $\hat{\theta}_\mu$  is the value of  $\theta$  that maximizes the likelihood for the choice of  $\mu$  being tested. Additionally,  $\hat{\theta}$   
<sup>1445</sup> and  $\hat{\mu}$  represent the values of  $\theta$  and  $\mu$  that gives the overall maximum value of the likelihood.

<sub>1446</sub> Once this is defined, a test statistic  $q_\mu$  is constructed. This is shown in equation 3.12.

$$q_\mu = -2 \ln \lambda(\mu) \quad (3.12)$$

<sub>1447</sub> A higher value of  $q_\mu$  indicates that the data are more incompatible with the hypothesized value of  $\mu$ , and  
<sub>1448</sub>  $q_0$  then corresponds to the value of the test statistic for the background only hypothesis. A  $p_0$  value is  
<sub>1449</sub> then defined to quantify the compatibility between the data and the null hypothesis. The  $p_0$  value is the  
<sub>1450</sub> probability of obtaining a value of  $q_0$  larger than the observed value, and this is shown in equation 3.13.

$$p_0 = \int_{q_0^{\text{obs}}}^{\infty} f(q_\mu | \mu = 0) dq_\mu \quad (3.13)$$

<sub>1451</sub> Here  $f(q_\mu)$  is the probability distribution function of the test statistic. Finally, the  $p_0$  value can be con-  
<sub>1452</sub> verted into a signal significance, using the formula in equation 3.14, or the one-sided tail of the Gaussian  
<sub>1453</sub> distribution.

$$Z_0 = \sqrt{2} \operatorname{erf}^{-1}(1 - 2p_0) \quad (3.14)$$

<sub>1454</sub> The threshold for discovery used in particle physics is  $Z_0 \geq 5$ , more commonly known as a value of  $5\sigma$ .

*The real voyage of discovery consists not in seeking new landscapes, but in having new eyes.*

Marcel Proust

# 4

1455

## 1456 The discovery of the Higgs boson and the role

1457

## of the $H \rightarrow WW^* \rightarrow \ell\nu\ell\nu$ channel

1458

### 4.1 INTRODUCTION

1459

This chapter presents the results of the search for the Higgs boson in  $4.8 \text{ fb}^{-1}$  collected at  $\sqrt{s} = 7 \text{ TeV}$  and  $5.8 \text{ fb}^{-1}$  at  $\sqrt{s} = 8 \text{ TeV}$ . The results of three searches at  $\sqrt{s} = 8 \text{ TeV}$  in the  $H \rightarrow WW^* \rightarrow \ell\nu\ell\nu$ ,  $H \rightarrow \gamma\gamma$ , and  $H \rightarrow ZZ \rightarrow 4\ell$  channels are combined with results of searches at  $\sqrt{s} = 7 \text{ TeV}$  in the same search channels (as well as the  $H \rightarrow \tau\tau$  production and associated production searches for  $H \rightarrow b\bar{b}$ ). The results of this combination are a  $5.9\sigma$  detection of a new particle consistent with a Higgs boson. Rather than going into detail for all of the different Higgs decay searches, this chapter will discuss the three most sensitive channels and in particular focus on  $H \rightarrow WW^* \rightarrow \ell\nu\ell\nu$ . While the focus is on  $WW^*$ , some of the  $ZZ^*$  and  $\gamma\gamma$  results are shown for completeness. The results not discussed here can

1467 be found in the ATLAS Higgs discovery publication [1].

1468 **4.2 DATA AND SIMULATION SAMPLES**

1469 The data sample used for the following results was taken in 2011 and 2012 at center of mass energies  
1470 of 7 and 8 TeV, respectively, with  $4.8 \text{ fb}^{-1}$  collected at 7 TeV and  $5.8 \text{ fb}^{-1}$  collected at 8 TeV. Higgs  
1471 production in the gluon fusion and vector boson fusion modes is modeled with **POWHEG** for the hard  
1472 scattering event and **PYTHIA** for the showering and hadronization. Associated production of a Higgs with a  
1473 vector boson or top quarks is modeled via **PYTHIA**. Table 4.1 shows the Monte Carlo generators used for  
1474 modeling the signal and background processes relevant for the three analyses to be discussed.

Process	Generator
ggF, VBF $H$	<b>POWHEG + PYTHIA</b>
$WH, ZH, t\bar{t}H$	<b>PYTHIA</b>
$W + \text{jets}, Z/\gamma^* + \text{jets}$	<b>ALPGEN + HERWIG</b>
$t\bar{t}, tW, tb$	<b>MC@NLO + HERWIG</b>
$tqb$	<b>ACERMC + PYTHIA</b>
$q\bar{q} \rightarrow WW$	<b>MC@NLO + HERWIG</b>
$gg \rightarrow WW$	<b>GG2WW+ HERWIG</b>
$q\bar{q} \rightarrow ZZ$	<b>POWHEG + PYTHIA</b>
$gg \rightarrow ZZ$	<b>GG2ZZ+ HERWIG</b>
$WZ$	<b>MADGRAPH+ PYTHIA , HERWIG</b>
$W\gamma + \text{jets}$	<b>ALPGEN + HERWIG</b>
$W\gamma^*$	<b>MADGRAPH+ PYTHIA</b>
$q\bar{q}/gg \rightarrow \gamma\gamma$	<b>SHERPA</b>

Table 4.1: Monte carlo generators used to model signal and background for the Higgs search [1].

1475 **4.3  $H \rightarrow WW \rightarrow e\nu\mu\nu$  SEARCH**

1476 The  $H \rightarrow WW \rightarrow e\nu\mu\nu$  search is unique compared to the  $ZZ$  and  $\gamma\gamma$  channels. The Higgs mass  
1477 cannot be fully reconstructed due to the presence of neutrinos in the final state, so the transverse mass  $m_T$   
1478 is used as the final discriminating variable. Compared to the other channels, there are more backgrounds  
1479 here as well, as discussed in chapter 3. The same flavor final states are excluded from this search due to high  
1480 pileup in the 8 TeV dataset.

1481 4.3.I EVENT SELECTION

1482 The analysis requires two opposite charge isolated leptons, with the leading (sub-leading) lepton required  
 1483 to have  $p_T > 25(15)$  GeV. The events are separated into different signal regions depending on which  
 1484 flavor of lepton is leading ( $e\mu$  for leading electron,  $\mu e$  for leading muon). Strict lepton quality cuts are  
 1485 applied to the sample to reduce backgrounds from fake leptons.

1486 Jets are reconstructed with the anti- $k_T$  algorithm with a radius parameter  $R = 0.4$ . The jets are re-  
 1487 quired to have  $p_T > 25$  GeV and  $|eta| < 4.5$ , with jets in the tracking volume required to have a jet  
 1488 vertex fraction of 0.5 and jets in the forward region required to have  $p_T > 30$  GeV. The analysis is sepa-  
 1489 rated into three different signal regions based on jet multiplicity:  $n_j = 0, 1, \geq 2$ .

1490 To indicate the presence of neutrinos in the event, a requirement of  $E_{T,\text{rel}}^{\text{miss}} > 25$  GeV is made<sup>1</sup>. This  
 1491 requirement significantly reduces the QCD multijet and  $Z/\gamma^*$  + jets backgrounds. Figure 4.1 shows the  
 1492 distribution of  $n_j$  in data and simulation after applying these “pre-selection” requirements.

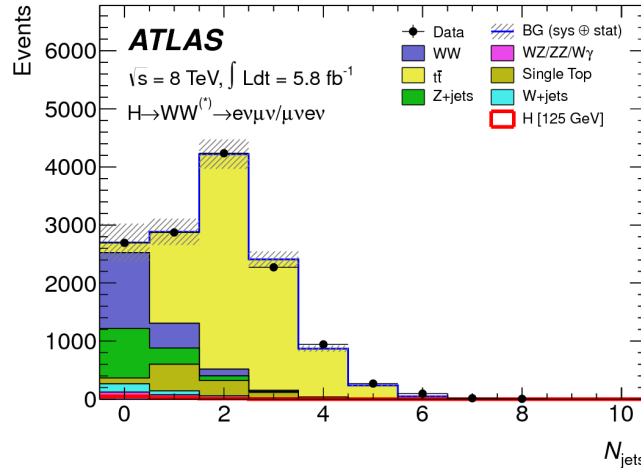


Figure 4.1: Jet multiplicity distribution in data and MC after applying lepton, jet, and  $E_{T,\text{rel}}^{\text{miss}}$  selections. The  $WW$  and top backgrounds have been normalized using control samples, and the hashed band indicates the total uncertainty on the prediction. [1]

1493 Additional selections are applied to require the dilepton topology to correspond to that of a SM Higgs.  
 1494 The requirements are presented here - more detailed discussion on the motivation for each requirement is  
 1495 saved for Chapter 5. In all of the jet multiplicity channels, the dilepton system is required to have a small

---

<sup>1</sup>For the definition of  $E_{T,\text{rel}}^{\text{miss}}$ , see chapter 3

1496 gap in azimuthal angle,  $\Delta\phi_{\ell\ell} < 1.8$ . Similarly, the  $m_{\ell\ell}$  is required to be less than 50 GeV in the lower jet  
1497 multiplicity channels and less than 80 GeV in the  $n_j \geq 2$  channel. In the  $n_j = 0$  channel, the magnitude  
1498 of the dilepton  $p_T$ ,  $p_T^{\ell\ell}$ , is required to be greater than 30 GeV.

1499 In the higher jet multiplicity channels ( $n_j \geq 1$ ), the top background is a more important component  
1500 and must be reduced. The total transverse momentum  $p_T^{\text{sum}}$  is thus required to be less than 30 GeV. Ad-  
1501ditionally, the di- $\tau$  invariant mass  $m_{\tau\tau}$  (dilepton mass computed under the assumption that the neutrinos  
1502from the  $\tau$  decay are emitted collinear to the charged leptons) is used to reject  $Z \rightarrow \tau\tau$  events by requiring  
1503  $|m_{\tau\tau} - m_Z| > 25$  GeV. These variables are also discussed in more detail in Chapter 5.

1504 In the  $n_j \geq 2$  channel, requirements are made to isolate the VBF contribution to Higgs production.  
1505 The kinematics of the two leading jets are used to make these requirements. In particular, the event must  
1506 have  $\Delta y_{jj} > 3.8$  and  $m_{jj} > 500$  GeV, along with a veto on having any additional jets with rapidity  
1507 between the two leading jets.

#### 1508 4.3.2 BACKGROUND ESTIMATION

1509 The details of the background estimation techniques used in the  $H \rightarrow WW^* \rightarrow \ell\nu\ell\nu$  analysis are  
1510 discussed in section 5.5. As that section refers to a later iteration of the analysis, a general discussion is given  
1511 here for completeness. The dominant backgrounds are SM  $WW$  production and top (both pair and  
1512 single) production, and these backgrounds have their normalizations estimated from dedicated control  
1513 regions while their shapes are taken from simulation.

1514 The control sample for the Standard Model  $WW$  background is defined by making the same require-  
1515ments as the signal region with the  $m_{\ell\ell}$  requirement inverted (now requiring  $m_{\ell\ell} > 80$  GeV) and remov-  
1516ing the  $\Delta\phi_{\ell\ell}$  requirement. This creates a control sample that is 70% (40%) pure in the 0(1)-jet region. The  
1517 correction to the pure MC-based background estimate is quantified by defining a normalization factor  $\beta$   
1518 which is the ratio of the data yield to the MC yield ( $N_{\text{data}}/N_{\text{MC}}$ ) in this control sample. Table 4.2 shows  
1519 the  $WW$  normalization factors in the  $n_j = 0$  and  $n_j = 1$  bins (the  $n_j \geq 2$  estimate is taken directly  
1520 from MC).

1521 The top background estimate is also computed separately in each jet multiplicity bin. In the  $n_j = 0$

$n_j$	$\beta_{WW}$	$\beta_t$
= 0	$1.06 \pm 0.06$	$1.11 \pm 0.06$
= 1	$0.99 \pm 0.15$	$1.11 \pm 0.05$
$\geq 2$	-	$1.01 \pm 0.26$

Table 4.2: Normalization factors (ratio of data and MC yields in a control sample) for the Standard Model  $WW$  and top backgrounds in the  $H \rightarrow WW^* \rightarrow \ell\nu\ell\nu$  analysis [1]. Only statistical uncertainties are shown.

channel, the background is first normalized using data after pre-selection requirements with no selection on  $n_j$ . Then, a dedicated  $b$ -tagged control sample is used to evaluate the ratio of one-jet to two-jet events in data. The details of this technique are shown in reference [65]. In the  $n_j = 1$  and the  $n_j \geq 2$  regions, the top background is normalized in a control sample where the signal region selections are applied, but the  $b$ -jet veto is reversed and the Higgs topology requirements on  $m_{\ell\ell}$  and  $\Delta\phi_{\ell\ell}$  are removed. The resulting normalization factors for these techniques are shown in table 4.2.

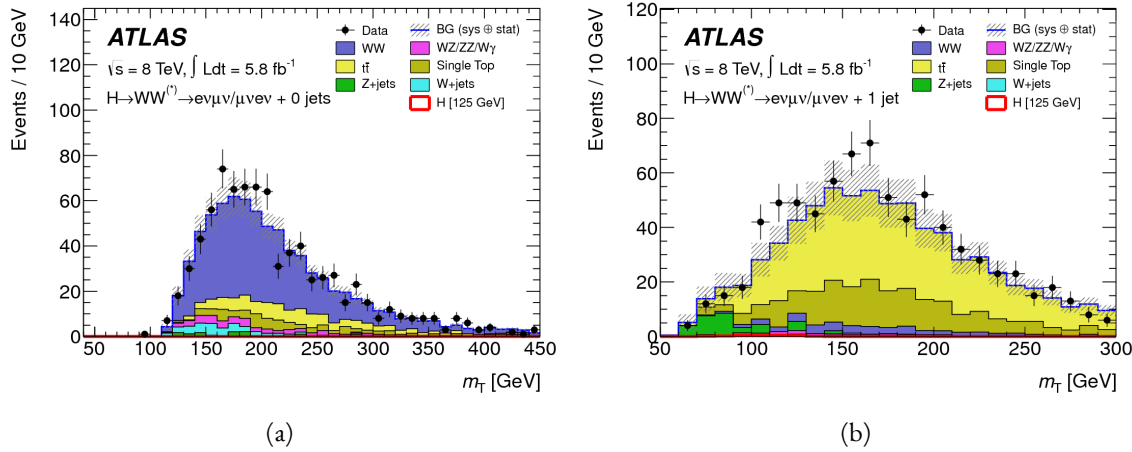


Figure 4.2: Comparison of  $m_T$  between data and simulation in the  $n_j = 0$   $WW$  (a) and  $n_j = 1$  top (b) control samples [1]

The control samples which are used for background normalization can also be used to validate the modeling of the  $m_T$  distribution for each background. Figure 4.2 shows the comparison between data and MC for the  $m_T$  distribution after correcting the normalization of the backgrounds in the  $WW$  and top control regions. Good agreement between data and simulation is seen in both cases.

The  $W + \text{jets}$  background estimate is taken entirely from data using a control sample with one well reconstructed lepton and one anti-identified lepton. All other backgrounds are taken purely from simulation.

1534    4.3.3 SYSTEMATIC UNCERTAINTIES

1535    The systematic uncertainties that have the largest impact on the analysis are the theoretical uncertainties  
 1536    associated with the signal cross section, and these are shared with the  $ZZ^*$  and  $\gamma\gamma$  channels. The uncer-  
 1537    tainties resulting from variations of the QCD scale are  $+7\%/-8\%$  on the final singal yield. Those coming  
 1538    from variations of the parton distribution function (PDF) used in the simulation add a  $\pm 8\%$  uncertainty  
 1539    on the yield. The uncertainties on the branching ratios of the Higgs are  $\pm 5\%$ .

1540    The main experimental uncertainties come from variations of the jet energy scale (JES), jet energy reso-  
 1541    lution, pile-up,  $E_T^{\text{miss}}$ ,  $b$ -tagging efficiency,  $W$ +jets background estimate, and integrated luminosity. For  
 1542    more details, see reference [1].

1543    4.3.4 RESULTS

1544    Table 4.3 shows the signal and background yields in the final signal region after normalizing the back-  
 1545    grounds according to the methods described above.

	$n_j = 0$	$n_j = 1$	$n_j \geq 2$
Signal	$20 \pm 4$	$5 \pm 2$	$0.34 \pm 0.07$
$WW$	$101 \pm 13$	$12 \pm 5$	$0.10 \pm 0.14$
Other dibosons	$12 \pm 3$	$1.9 \pm 1.1$	$0.10 \pm 0.10$
$t\bar{t}$	$8 \pm 2$	$6 \pm 2$	$0.15 \pm 0.10$
Single top	$3.4 \pm 1.5$	$3.7 \pm 1.6$	-
$Z/\gamma^* + \text{jets}$	$1.9 \pm 1.3$	$0.10 \pm 0.10$	-
$W + \text{jets}$	$15 \pm 7$	$2 \pm 1$	-
Total background	$142 \pm 16$	$26 \pm 6$	$0.35 \pm 0.18$
Observed in data	185	38	0

Table 4.3: Data and expected yields for signal and background in the final  $H \rightarrow WW^* \rightarrow \ell\nu\ell\nu$  signal region.  
 Uncertainties shown are both statistical and systematic. [1]

1546    Figure 4.3 shows the  $m_T$  distribution in the  $n_j \leq 1$  channels for 8 TeV data. (No events are observed  
 1547    in data in the  $n_j \geq 2$  channels in this dataset). The excess shown here relatively flat as a function of  
 1548    hypothesized Higgs mass. The combined 7 and 8 TeV data gives an excess with local significance of  $2.8\sigma$   
 1549    with an expected significance of  $2.3\sigma$ , corresponding to a  $\mu$  measurement of  $1.3 \pm 0.5$ .

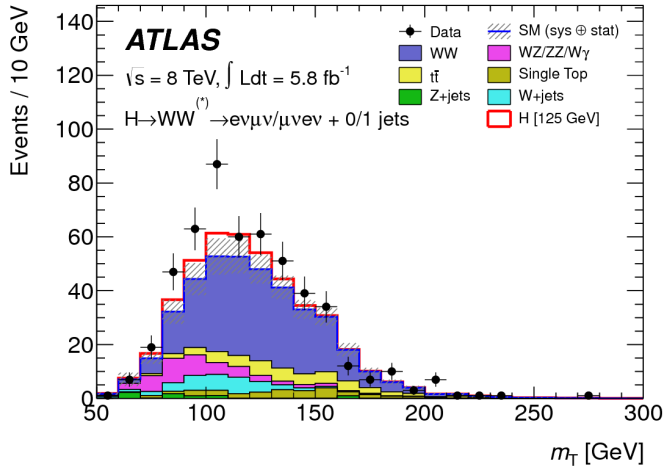


Figure 4.3:  $m_T$  distribution in the  $H \rightarrow WW \rightarrow e\nu\mu\nu n_j \leq 1$  channels for 8 TeV data [1].

#### 1550 4.4 $H \rightarrow \gamma\gamma$ SEARCH

1551 The  $H \rightarrow \gamma\gamma$  search is in essence a search for a peaked excess above the falling SM diphoton mass  
 1552 spectrum, with  $m_{\gamma\gamma}$  as the ultimate discriminating variable. Events are selected by requiring two isolated  
 1553 photons, with the leading (sub-leading) photon required to have  $E_T > 40(30)$  GeV. In the 8 TeV data,  
 1554 the photons are required to pass cut-based identification criteria consistent with a photon in the electro-  
 1555 magnetic calorimeter and little leakage in the hadronic calorimeter.

1556 The main challenges for this analysis are accurate mass reconstruction and background estimation. In  
 1557 order to accurately reconstruct the invariant mass of the di-photon system, both the energy and direction  
 1558 of the photons must be measured well. Therefore, the identification of the primary vertex of the hard  
 1559 interaction is particularly important, and is done using a multivariate likelihood which combines informa-  
 1560 tion about the photon direction and vertex position. The background is modeled with a falling spectrum  
 1561 in  $m_{\gamma\gamma}$  that is parameterized by different functions depending on the category of the event.

##### 1562 4.4.1 RESULTS

1563 The resulting diphoton mass spectrum is shown in figure 4.4. The best fit mass value in the  $\gamma\gamma$  channel  
 1564 alone in the combined 7 and 8 TeV data is 126.5 GeV. The local significance at this point is  $4.5\sigma$ , with  
 1565 an expected significance of  $2.5\sigma$ . Therefore, the measured signal strength  $\mu$  is  $1.8 \pm 0.5$  in this channel.

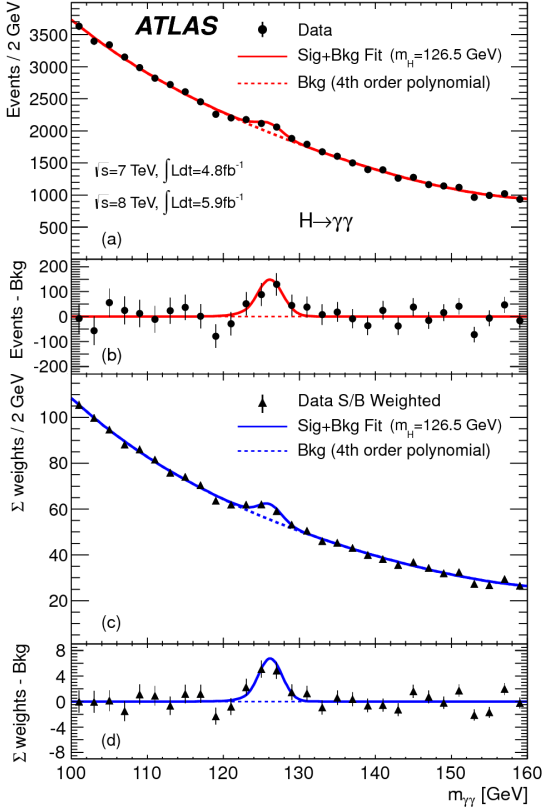


Figure 4.4: Diphoton mass spectrum in 7 and 8 TeV data. Panel a) shows the unweighted data distribution superimposed on the background fit, while panel c) shows the data where each event category is weighted by its signal to background ratio. Panels b) and d) show the respective distributions with background subtracted [1].

#### 1566 4.5 $H \rightarrow ZZ \rightarrow 4\ell$ SEARCH

1567 The  $H \rightarrow ZZ \rightarrow 4\ell$  analysis searches for a Standard Model Higgs boson decaying to two  $Z$  bosons,  
 1568 each of which decays to a pair of same flavor, opposite charge isolated leptons. The ultimate discriminating  
 1569 variable is  $m_{4\ell}$ , or the invariant mass of the four selected leptons. The  $\ell$  denotes an  $e$  or  $\mu$  as with the  
 1570  $H \rightarrow WW^* \rightarrow \ell\nu\ell\nu$  analysis.

1571 Four distinct signal regions are constructed depending on the flavors of the final state, additionally sep-  
 1572 arated by the flavor of the leading lepton pair. These are referred to as  $4e$ ,  $2e2\mu$ ,  $2\mu2e$ ,  $4\mu$ .

1573 The main backgrounds in the  $H \rightarrow ZZ \rightarrow 4\ell$  search are continuum  $ZZ^*$  production,  $Z +$  jets pro-  
 1574 duction, and  $t\bar{t}$ . The  $m_{4\ell}$  distribution for background is estimated from simulation. The normalization  
 1575 of the SM  $ZZ^*$  background is also taken from MC simulation, while the  $Z +$  jets and  $t\bar{t}$  normalizations are

1576 taken from data-driven methods.

1577 **4.5.1 RESULTS**

1578 Figure 4.5 shows the  $m_{4\ell}$  spectrum measured in the 7 and 8 TeV datasets. The total number of events  
1579 observed in the window between 120 and 130 GeV is 13, with 6 events in the  $4\mu$  channel, 2 events in  
1580 the  $4e$  channel, and 5 events in the  $2e2\mu/2\mu2e$ . The best fit  $\mu$  value in the combined 7 and 8 TeV data  
1581 occurs at 125 GeV and is measured to be  $1.2 \pm 0.6$ . The observed significance at this mass is  $3.6\sigma$ , with  
1582 an expected significance of  $2.7\sigma$ .

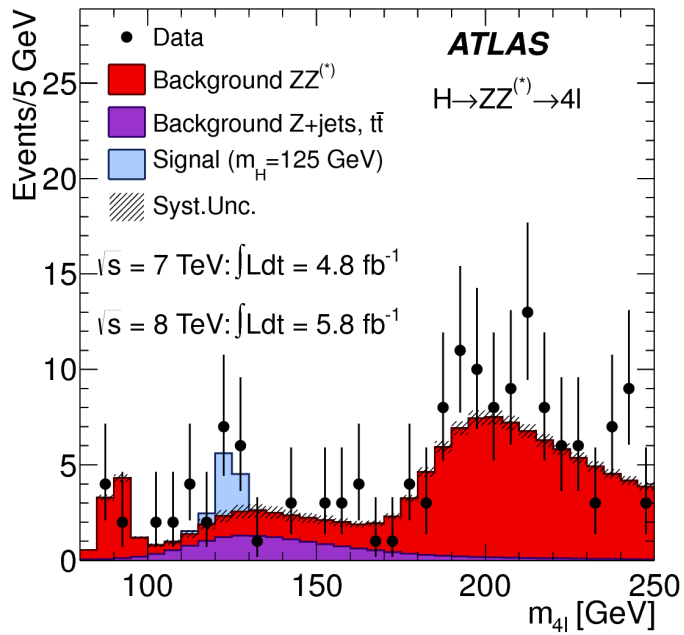


Figure 4.5: Four lepton invariant mass spectrum ( $m_{4\ell}$ ) in 7 and 8 TeV data compared to background estimate. A 125 GeV SM Higgs signal is shown in blue [1].

1583 **4.6 COMBINED RESULTS**

1584 The statistical interpretation of the combined results is undertaken as described in section 3.6.2, with a  
1585 hypothesis test based on a likelihood ratio parameterized by the Higgs signal strength  $\mu$ . The null hypoth-  
1586 esis corresponds to  $\mu = 0$ , while the SM Higgs corresponds to  $\mu = 1$ .

1587      Table 4.4 summarizes the properties of the individual channels as well as the significances of the excesses  
 1588      seen. The most significant observed local excess comes from the  $\gamma\gamma$  channel. Figure 4.6 shows a compari-  
 1589      son of the observed local  $p_0$  values as a function of hypothesized mass for the three different search chan-  
 1590      nels. Both the  $ZZ^*$  and  $\gamma\gamma$  channels have very peaked excesses, while the  $WW^*$  excess can be seen as very  
 1591      broad because the  $m_T$  distribution does not provide detailed information about the true Higgs mass.

Channel	Fit var.	Observed $Z_l$	Expected $Z_l$	$\hat{\mu}$
$H \rightarrow ZZ^* \rightarrow 4\ell$	$m_{4\ell}$	3.6	2.7	$1.2 \pm 0.6$
$H \rightarrow \gamma\gamma$	$m_{\gamma\gamma}$	4.5	2.5	$1.8 \pm 0.5$
$H \rightarrow WW^* \rightarrow e\nu\mu\nu$	$m_T$	2.8	2.3	$1.3 \pm 0.5$
Combined	-	6.0	4.9	$1.4 \pm 0.3$

Table 4.4: Summary of the expected and observed significance and measured signal strengths in the combined 7 and 8 TeV datasets for the Higgs discovery analysis [1].

1592      Figure 4.7 shows the combined exclusion limit,  $p_0$ , and signal strength. The highest local excess comes  
 1593      at a value of 126.5 GeV and corresponds to a  $6.0\sigma$  observed excess.

1594      Figure 4.8 shows a comparison of the measured signal strengths between the different Higgs search  
 1595      channels. All measured  $\mu$  are consistent with unity within their uncertainty, and the combined  $\mu$  mea-  
 1596      surement is  $1.4 \pm 0.3$ .

1597      The likelihood can also be computed in a two-dimensional plane of  $m_H$  and  $\mu$ , and this is shown in  
 1598      figure 4.9. The figure shows that while the  $\gamma\gamma$  and  $ZZ^*$  channels have very good mass resolution, the  
 1599      excess in  $WW^*$  covers a broad mass range. The banana shape of the  $WW^*$  result is due to the fact that  
 1600      the excess in this channel can either be explained by increasing the signal strength or by changing the mass  
 1601      (and thus the cross section). The two parameters are correlated due to the lack of mass sensitivity in this  
 1602      channel.

1603      Because multiple Higgs mass points are searched for, the local significance must be corrected for a look-  
 1604      elsewhere effect to compute a true global significance. The global significance for finding a Higgs anywhere  
 1605      in the mass range of 110 GeV to 600 GeV is  $5.1\sigma$ . This increases slightly to  $5.3\sigma$  if only mass range from  
 1606      110 to 150 GeV.

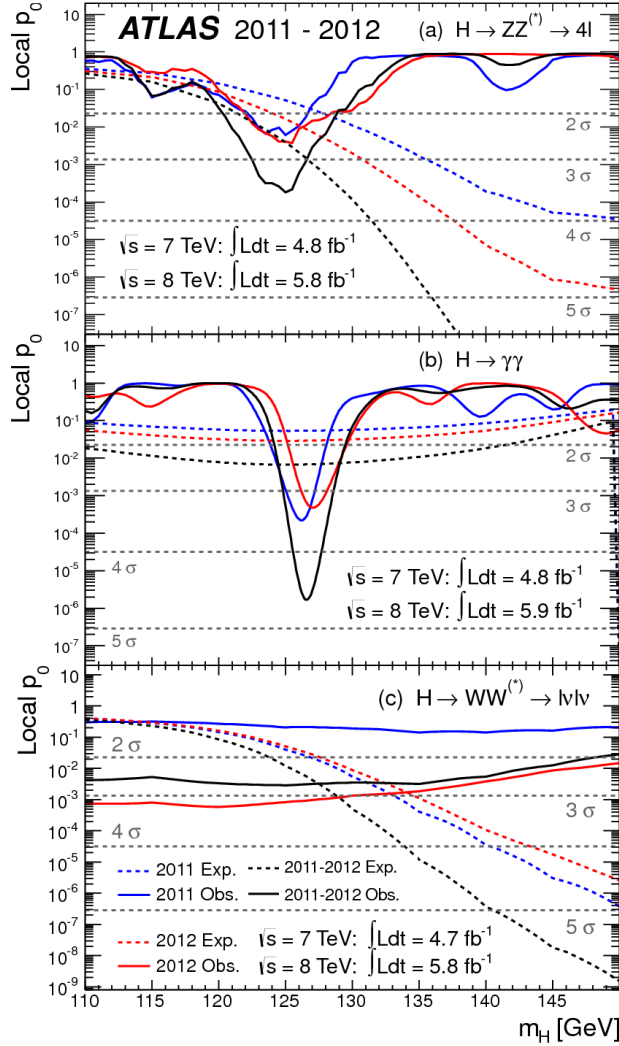


Figure 4.6: Local  $p_0$  distribution as a function of hypothesized Higgs mass for the  $H \rightarrow ZZ^* \rightarrow 4\ell$  (a),  $H \rightarrow \gamma\gamma$  (b), and  $H \rightarrow WW^* \rightarrow \ell\nu\ell\nu$  (c) channels. Dashed curves show expected results, while solid curves show observed. Red curves are from 7 TeV data, blue curves from 8 TeV, and black curved combined [1].

#### 1607 4.7 CONCLUSION

1608 A search for the production of a Standard Model Higgs boson was conducted in  $4.8 \text{ fb}^{-1}$  collected at  
 1609  $\sqrt{s} = 7 \text{ TeV}$  and  $5.8 \text{ fb}^{-1}$  at  $\sqrt{s} = 8 \text{ TeV}$ . A new particle consistent with the Higgs boson was observed,  
 1610 with a mass of  $126.5 \text{ GeV}$  and a global (local) significance of  $5.1(6.0)\sigma$ . This is the first discovery level  
 1611 observation of a particle consistent with the Higgs.

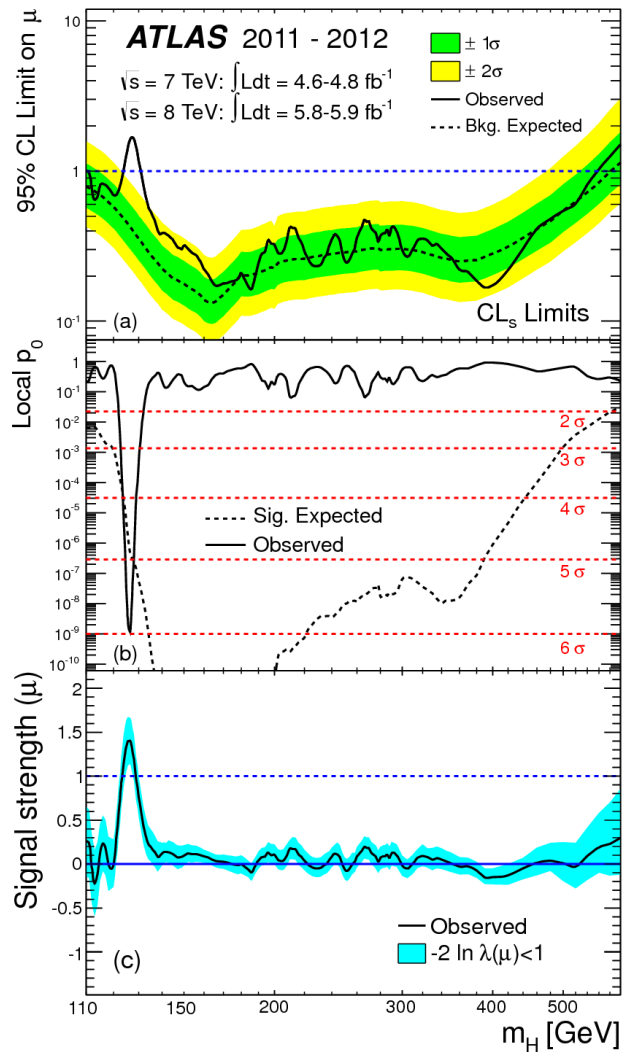


Figure 4.7: Combined 95% CL limits (a), local  $p_0$  values (b), and signal strength measurement (c) as a function of Higgs mass [1].

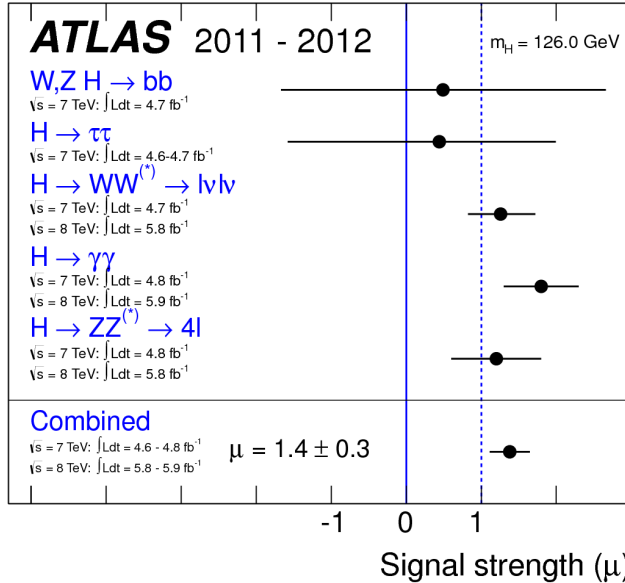


Figure 4.8: Comparison of measured signal strength  $\mu$  for a 126 GeV Higgs in the 7 and 8 TeV datasets [1].

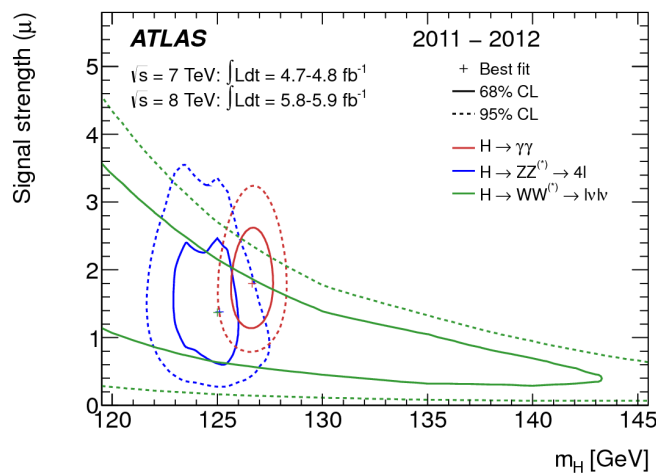


Figure 4.9: Two dimensional likelihood as a function of signal strength  $\mu$  and Higgs mass  $m_H$  [1].

*The imagination of nature is far, far greater than the  
imagination of man.*

Richard Feynman

1612

# 5

1613

## Observation of Vector Boson Fusion

1614

production of  $H \rightarrow WW^* \rightarrow \ell\nu\ell\nu$

1615

### 5.1 INTRODUCTION

1616

After the discovery of a particle consistent with the Higgs boson, the  $H \rightarrow WW^*$  analysis had two main goals. The first goal was to increase the sensitivity of the analysis to fully confirm that the  $H \rightarrow WW^*$  process did indeed exist. The second goal was to characterize the particle as much as possible, including searching for the lower cross-section production modes, in order to confirm that it was indeed a Higgs boson. This chapter presents a dedicated search for Vector Boson Fusion (VBF) production of a Higgs boson decaying via the  $H \rightarrow WW^* \rightarrow \ell\nu\ell\nu$  mode. First, basics of the topology of VBF production are presented. Then, the details of the analysis are shown, including signal region definition, background estimation techniques, and systematic uncertainties. Finally, the results of the analysis are presented. As

1624 will be shown, this analysis is the first and most sensitive observation of the VBF production mode of the  
1625 Higgs on ATLAS.

1626 In the VBF channel, there are both a selection requirement based signal region analysis (known as the  
1627 “cut-based”) and a multivariate analysis which uses a boosted decision tree (known as the BDT analysis).  
1628 The focus of this chapter will be on the cut-based signal region, as this is an important component of the  
1629 VBF analysis and in particular acts as strong validation for the final BDT result. Connections between the  
1630 cut-based and BDT analyses will be discussed where appropriate.

## 1631 5.2 DATA AND SIMULATION SAMPLES

1632 The results presented here are with  $20.3 \text{ fb}^{-1}$  taken at  $\sqrt{s} = 8 \text{ TeV}$  and  $4.5 \text{ fb}^{-1}$  taken at  $\sqrt{s} = 7 \text{ TeV}$ .  
1633 The details of the LHC and detector conditions during this period are given in Chapter 2. The trigger  
1634 selection defining the dataset is discussed in section 5.2.1. The simulation samples used for signal and back-  
1635 ground modeling are given in section 5.2.2.

### 1636 5.2.1 TRIGGERS

1637 The analysis uses a combination of single lepton and dilepton triggers to allow lowering of the  $p_T$   
1638 thresholds and increased signal acceptance. The  $p_T$  threshold on the leptons is a particularly important  
1639 consideration for this signal. Because the second  $W$  produced in the decay can be off-shell, it tends to pro-  
1640 duce lower momentum leptons. Thus, being able to lower the  $p_T$  threshold while still maintaining a low  
1641 background rate is critical. Figure 5.1 shows an example of the subleading lepton  $p_T$  for a VBF  $H \rightarrow WW^*$   
1642 signal compared to the corresponding  $t\bar{t}$  background. Note that the lepton  $p_T$  spectrum is considerably  
1643 softer in the signal sample.

1644 As discussed in Chapter 2, there are multiple levels in the ATLAS trigger system, and there are different  
1645  $p_T$  thresholds imposed for the leptons at each level. Additionally, some triggers have a loose selection  
1646 on the isolation of the lepton (looser than that applied offline in the analysis object selection). Table 5.1  
1647 shows the thresholds used for single lepton triggers, while table 5.2 shows the thresholds coming from  
1648 di-lepton triggers. The single lepton trigger efficiency for muons that pass the analysis object selection is



Figure 5.1: A comparison of the subleading lepton  $p_T$  spectrum between VBF  $H \rightarrow WW^*$  production and  $t\bar{t}$  background

1649 70% for muons in the barrel region ( $|\eta| < 1.05$ ) and 90% in the endcap region. The electron trigger  
 1650 efficiency increases with electron  $p_T$  but the average is approximately 90%. These efficiencies are measured  
 1651 by combined performance and trigger signature groups [66, 67].

	Level-1 threshold	High-level threshold
Electron	18	$24i$
	30	60
Muon	15	$24i$
		36

Table 5.1: Single lepton triggers used for electrons and muons. A logical “or” of the triggers listed for each lepton type is taken. Units are in GeV, and the  $i$  denotes an isolation requirement in the trigger.

	Level-1 threshold	High-level threshold
$ee$	10 and 10	12 and 12
$\mu\mu$	15	18 and 8
$e\mu$	10 and 6	12 and 8

Table 5.2: Di-lepton triggers used for different flavor combinations. The two thresholds listed refer to leading and sub-leading leptons, respectively. The di-muon trigger only requires a single lepton at level-1.

1652 The combination of all triggers shown gives good efficiency for signal events. This efficiency is sum-  
 1653 marized in table 5.3. The relative improvement in efficiency by adding the dilepton triggers is also shown

1654 in the same table. The largest gain comes in the  $\mu\mu$  channel. Overall the trigger selection shows a good  
1655 efficiency for  $H \rightarrow WW^*$  signal events.

Channel	Trigger efficiency	Gain from $2\ell$ trigger
$ee$	97%	9.1%
$\mu\mu$	89%	18.5%
$e\mu$	95%	8.3%
$\mu e$	81%	8.2%

Table 5.3: Trigger efficiency for signal events and relative gain of adding a dilepton trigger on top of the single lepton trigger selection. The first lepton is the leading, while the second is the sub-leading. Efficiencies shown here are for the ggF signal in the  $n_j = 0$  category but are comparable for the VBF signal.

1656 5.2.2 MONTE CARLO SAMPLES

1657 Modeling of signal and background processes in the signal region, in particular for the  $m_T$  distribution,  
1658 is an important consideration for the final interpretation of the analysis. Therefore, careful consideration  
1659 must be paid to which Monte Carlo (MC) generators are used for specific processes. With the exception of  
1660 the  $W + \text{jet}$  and multijet backgrounds, the  $m_T$  shape used as the final discriminant is taken from simulation.  
1661 (Many backgrounds are normalized from data, as described in section 5.5).

1662 Table 5.4 shows the MC generators used for the signal and background processes, as well as their cross  
1663 sections. In order to include corrections up to next-to-leading order (NLO) in the QCD coupling constant  
1664  $\alpha_s$ , the POWHEG [68] generator is often used. In some cases, only leading order generators like ACERMC  
1665 [69] and GG2VV [70] are available for the process in question. If the process requires good modeling for  
1666 very high parton multiplicities, the SHERPA [71] and ALPGEN [72] generators are used to provide merged  
1667 calculations for five or fewer additional partons. These matrix element level calculations must then be  
1668 additionally matched to models of the underlying event, hadronization, and parton shower. There are  
1669 four possible generators for this: SHERPA, PYTHIA 6 [73], PYTHIA 8 [74], or HERWIG [75] + JIMMY [76].  
1670 The simulation additionally requires an input parton distribution function (PDF). The CTEQ [77] PDFs  
1671 are used for SHERPA and POWHEG simulated samples, while CTEQ6Li [78] is used for ALPGEN + HERWIG  
1672 and ACERMC simulations. The Drell-Yan samples are reweighted to the MRST [79] PDFs, as these are  
1673 found to give the best agreement between data and simulation.

Process	MC generator	$\sigma \cdot \mathcal{B}$ (pb)
Signal		
ggF $H \rightarrow WW^*$	POWHEG +PYTHIA 8	0.435
VBF $H \rightarrow WW^*$	POWHEG +PYTHIA 8	0.0356
VH $H \rightarrow WW^*$	PYTHIA 8	0.0253
$WW$		
$q\bar{q} \rightarrow WW$ and $qg \rightarrow WW$	POWHEG +PYTHIA 6	5.68
$gg \rightarrow WW$	GG2VV +HERWIG	0.196
$(q\bar{q} \rightarrow W) + (q\bar{q} \rightarrow W)$	PYTHIA 8	0.480
$q\bar{q} \rightarrow WW$	SHERPA	5.68
VBS $WW + 2$ jets	SHERPA	0.0397
Top quarks		
$t\bar{t}$	POWHEG +PYTHIA 6	26.6
$Wt$	POWHEG +PYTHIA 6	2.35
$t\bar{q}\bar{b}$	ACERMC +PYTHIA 6	28.4
$t\bar{b}$	POWHEG +PYTHIA 6	1.82
Other dibosons ( $VV$ )		
$W\gamma$ ( $p_T^\gamma > 8$ GeV)	ALPGEN +HERWIG	369
$W\gamma^*$ ( $m_{\ell\ell} \leq 7$ GeV)	SHERPA	12.2
$WZ$ ( $m_{\ell\ell} > 7$ GeV)	POWHEG +PYTHIA 8	12.7
VBS $WZ + 2$ jets	SHERPA	0.0126
( $m_{\ell\ell} > 7$ GeV)		
$Z\gamma$ ( $p_T^\gamma > 8$ GeV)	SHERPA	163
$Z\gamma^*$ (min. $m_{\ell\ell} \leq 4$ GeV)	SHERPA	7.31
$ZZ$ ( $m_{\ell\ell} > 4$ GeV)	POWHEG +PYTHIA 8	0.733
$ZZ \rightarrow \ell\ell\nu\nu$ ( $m_{\ell\ell} > 4$ GeV)	POWHEG +PYTHIA 8	0.504
Drell-Yan		
$Z$ ( $m_{\ell\ell} > 10$ GeV)	ALPGEN +HERWIG	16500
VBF $Z + 2$ jets	SHERPA	5.36
( $m_{\ell\ell} > 7$ GeV)		

Table 5.4: Monte Carlo samples used to model the signal and background processes [62].

Once the basic hard scattering process is simulated, it must be passed through a detector simulation and additional pile-up events must be overlaid. The pile-up events are modeled with PYTHIA 8, and the ATLAS detector is simulated with GEANT4 [80]. Because of the unique phase space of the  $H \rightarrow WW^*$

1677 analysis, events are sometimes filtered at generator level to allow for more efficient generation of relevant  
1678 events. The efficiency of the trigger in MC simulation does not always match the measured efficiency in  
1679 data, so trigger scale factors are applied to correct the MC efficiency to the data. These are derived by the  
1680 combined performance groups [66, 67].

### 1681 5.3 OBJECT SELECTION

1682 In order to define the signal region, the analysis must first select the objects to be considered. The details  
1683 of the object reconstruction algorithms are discussed in Chapter 2, while this section gives specific selection  
1684 cuts used in the  $H \rightarrow WW^*$  analysis.

1685 The first step in this process is to select a primary vertex candidates. The event’s primary vertex is the  
1686 vertex with the largest sum of  $p_T^2$  for associated tracks and is required to have at least three tracks with  
1687  $p_T > 450$  MeV. Many of the object selection cuts are then made relative to this chosen primary vertex.

#### 1688 5.3.1 MUONS

1689 The analysis uses combined muon candidates, where a track in the Inner Detector has been matched to  
1690 a standalone track in the Muon Spectrometer. The track parameters are combined statistically in the muon  
1691 reconstruction algorithm [53]. The muons are required to be within  $|\eta| < 2.5$  and have a  $p_T > 10$  GeV.  
1692 To reduce backgrounds coming from mis-reconstructed leptons, there are requirements on the impact  
1693 parameter of the muon relative to the primary vertex. The transverse impact parameter  $d_0$  is required to  
1694 be small relative to its estimated uncertainty, the exact cut value being  $d_0/\sigma_{d_0} < 3$ . The longitudinal  
1695 impact parameter  $z_0$  must satisfy  $|z_0 \sin \theta| < 1$  mm.

1696 As discussed previously, the muons must also be isolated. There are two types of lepton isolations that  
1697 are calculated: track-based and calorimeter-based. For muons, the track-based isolation is defined using the  
1698 scalar sum  $\sum p_T$  for tracks with  $p_T > 1$  GeV (excluding the muon’s track) within a cone of  $\Delta R = 0.3$   
1699 (0.4) for muon with  $p_T > 15$  GeV ( $10 < p_T < 15$  GeV). The final isolation requirement is made my  
1700 requiring that this scalar sum be no more than a certain fraction of the muon’s  $p_T$ . This requirement varies  
1701 with muon  $p_T$  and the exact cuts are defined in table 5.5.

1702      The calorimeter-based muon isolation is defined using as a  $\sum E_T$  calculated from calorimeter cells us-  
 1703      ing the same cone size as the track-based isolation but excluding cells with  $\Delta R < 0.05$  around the muon.  
 1704      This requirement is also defined as a cut on the ratio of the sum to the muon  $p_T$  and varies with muon  $p_T$ .  
 1705      The cut values are also given in table 5.5.  
  
 1706      The isolation requirements loosen as a function of  $p_T$  to allow for larger signal acceptance. At low  $p_T$ ,  
 1707      the isolation is tightened to reduce the  $W + \text{jets}$  background which arises from a misidentified lepton.

$p_T$ range (GeV)	Calorimeter isolation	Track isolation
10 – 15	0.06	0.06
15 – 20	0.12	0.08
20 – 25	0.18	0.12
> 25	0.30	0.12

Table 5.5:  $p_T$  dependent isolation requirements for muons. Muons are required to have the amount of calorimeter or track based cone sums be less than this fraction of their  $p_T$ .

### 1708 5.3.2 ELECTRONS

1709      Electrons are identified by matching reconstructed clusters in the electromagnetic calorimeter with tracks  
 1710      in the inner detector. The electrons are identified using a likelihood based method [50, 51] which takes into  
 1711      account the shower shapes in the calorimeter, the matching of tracks to clusters, and the amount of transi-  
 1712      tion radiation in the TRT. The electrons are required to have  $|\eta| < 2.47$ , and candidates in the transition  
 1713      region between the barrel and endcap ( $1.37 < |\eta| < 1.52$ ) are excluded. As the muons, the electrons  
 1714      are required to have transverse impact parameter significance  $< 3$ , while in the longitudinal direction  
 1715      they must have  $|z_0 \sin \theta| < 0.4$  mm. Some electron requirements also vary with electron  $E_T$ , and these  
 1716      requirements are summarized in table 5.6.

1717      The isolation for electrons are defined similarly to the muons but with unique cuts on the objects in-  
 1718      cluded. The track-based isolation is defined using tracks with  $p_T > 400$  MeV with cone sizes as defined  
 1719      previously. The calorimeter-based isolation also uses the same cone size as the muon, but here the cells  
 1720      within a  $0.125 \times 0.175$  area in  $\eta \times \phi$  around the electron cluster's barycenter are excluded. The other  
 1721      difference with respect to muons is that the denominator of the isolation ratio is the electron's  $E_T$  rather  
 1722      than  $p_T$ . The isolation cuts very with electron  $E_T$  and are defined in table 5.6.

1723 The electron is also required to not be consistent with a vertex coming from a photon conversion.

$p_T$ range (GeV)	Quality cut	Calorimeter isolation	Track isolation
10 – 15	Very tight LH	0.20	0.06
15 – 20	Very tight LH	0.24	0.08
20 – 25	Very tight LH	0.28	0.10
> 25	Medium	0.28	0.10

Table 5.6:  $p_T$  dependent requirements for electrons. Electrons are required to have the amount of calorimeter or track based cone sums be less than this fraction of their  $E_T$ .

### 1724 5.3.3 JETS

1725 Jets are clustered with the anti- $k_T$  reconstruction algorithm using a radius parameter of  $R = 0.4$ . They  
1726 are required to have a jet vertex fraction (JVF) of at least 50%, meaning that half of the tracks associated with  
1727 the jet originated from the primary vertex. Jets with no tracks associated (i.e. those outside the acceptance  
1728 of the ID) do not have this requirement applied. Jets are required to have  $p_T > 25$  GeV if they are within  
1729 the tracking acceptance ( $|\eta| < 2.4$ ). Jets with  $2.4 < |\eta| < 4.5$  are required to have  $p_T > 30$  GeV.  
1730 This tighter requirement reduces jets from pileup in the region where JVF requirements cannot be applied.  
1731 The two highest  $p_T$  jets in the event are referred to as the “VBF” jets and used to compute various analysis  
1732 selections later.

1733 Identification of  $b$ -jets is done using the MV1 algorithm and is limited to the acceptance of the ID ( $|\eta| <$   
1734 2.5). The operating point of MV1 that is used is the one that is 85% efficient for identifying true  $b$ -jets. This  
1735 operating point has a 10.3% of mis-tagging a light quark jet as a  $b$ -jet. In order to improve the rejection of  $b$ -  
1736 jets, a lower threshold than the nominal  $p_T$  threshold described above is used. For the purposes of counting  
1737 the number of  $b$ -jets, jets with  $p_T$  down to 20 GeV are used.

### 1738 5.3.4 OVERLAP REMOVAL

1739 There are some cases where certain reconstructed objects will overlap and one will have to be chosen  
1740 (for example, an electron and a jet in the calorimeter). First, the case of lepton overlap is dealt with. If  
1741 an electron candidate extends into the muon spectrometer, it is removed. If a muon or electron have a  
1742  $\Delta R < 0.1$ , the electron is removed and the muon is kept. If two electron candidates overlap within the

1743 same radius, then the higher  $E_T$  electron is kept. Next, the overlap between leptons and jets is considered.  
1744 If an electron and jet are within  $\Delta R < 0.3$  of one another, the electron is kept and the jet is removed.  
1745 However, if a muon and jet overlap within  $\Delta R < 0.3$ , the jet is kept (as it is likely that the muon is the  
1746 result of a semileptonic decay inside the jet).

1747 Once the overlap removal is complete, the final set of objects used in the analysis is defined.

#### 1748 5.4 ANALYSIS SELECTION

1749 The VBF analysis uses two distinct selections. The first is a more standard selection, referred to as “cut-  
1750 based”, that applies requirements on the VBF variables and uses  $m_T$  as the final discriminating variable.  
1751 The second is a looser selection that uses a Boosted Decision Tree (BDT) score as the final discriminator in  
1752 order to take advantage of the detailed correlations between the VBF variables. While the BDT analysis is  
1753 ultimately more sensitive, the cut-based serves as an important component of the analysis. First, the cut-  
1754 based allows for confirming the modeling and validity of many variables used as input to the BDT. Second,  
1755 because this is the first use of such an MVA technique in the  $H \rightarrow WW^*$  analysis, the cut-based selection  
1756 allows confirmation of the final BDT result with a more traditional analysis. The cut-based techniques are  
1757 the focus of this chapter, but connections to the BDT result will be illustrated when appropriate.

1758 One important note is that because this analysis is dedicated to the measurement of the VBF pro-  
1759 duction mode of the Higgs, events coming from gluon fusion production with the Higgs decaying via  
1760  $H \rightarrow WW^* \rightarrow \ell\nu\ell\nu$  are treated as background events. This will be seen throughout the various predic-  
1761 tions shown.

##### 1762 5.4.1 COMMON PRE-SELECTION

1763 Both the cut-based and BDT analyses have a common pre-selection that is applied before the main signal  
1764 region requirements. The requirements on leptons are common to all  $n_j$  bins. The analysis requires two  
1765 oppositely charged leptons, with the leading lepton required to have  $p_T > 22$  GeV while the subleading  
1766 lepton must have  $p_T > 10$  GeV. Next, to remove low mass  $Z/\gamma^*$  events, a cut on the dilepton mass  
1767  $m_{\ell\ell} > 10$  (12) GeV is applied in the different (same) flavor channel. In the same flavor channels, there is

1768 an additional veto placed on the region around the Z peak, requiring that  $|m_{\ell\ell} - m_Z| > 15$  GeV.

1769 There are also requirements on the amount of missing transverse momentum in the event. These are  
1770 only applied in the same flavor channels, as in the different flavor channels  $t\bar{t}$  is the dominant background  
1771 in  $n_j \geq 2$ . The BDT analysis requires  $p_T^{\text{miss}} > 40$  GeV and  $E_T^{\text{miss}} > 45$  GeV. The cut-based analysis  
1772 must select more tightly on these variables to have maximal sensitivity and thus requires  $p_T^{\text{miss}} > 50$  GeV  
1773 and  $E_T^{\text{miss}} > 55$  GeV.

1774 Finally, because this analysis is focused on VBF, a requirement on the jet multiplicity is placed, with  
1775  $n_j \geq 2$ . Additionally, the analysis requires that there are no jets identified as b-quarks in the event, or  
1776  $n_b = 0$ .

#### 1777 5.4.2 CUT-BASED SELECTION

1778 The cut-based selection places sequential requirements on variables reconstructed from the VBF jets in  
1779 order to increase the signal to background ratio.

#### 1780 GENERAL BACKGROUND REDUCTION

1781 Top pair production is the primary background in the  $n_j \geq 2$  bin. Even though  $n_b = 0$  is required, an  
1782 additional variable is constructed to further suppress the top background. There is often additional QCD  
1783 radiation that accompanies the  $t\bar{t}$  system when it is produced. Therefore, a variable which tests for the  
1784 presence of this additional radiation,  $p_T^{\text{sum}}$ , is constructed. It is defined in equation 5.1.

$$p_T^{\text{sum}} = p_T^{\ell\ell} + p_T^{\text{miss}} + \sum p_T^j \quad (5.1)$$

1785 The first cut after pre-selection in the cut-based analysis requires  $p_T^{\text{sum}} < 15$  GeV to further suppress  $t\bar{t}$   
1786 production.

1787 In the different flavor channels, a cut is made to reduce the contamination from  $Z \rightarrow \tau\tau$  decays.  
1788 The di- $\tau$  invariant mass,  $m_{\tau\tau}$ , is constructed by assuming that the neutrinos from the  $\tau$  decays were  
1789 collinear with the leptons [81]. The analysis requires that this mass not be consistent with a  $Z$  by requiring  
1790  $m_{\tau\tau} < m_Z - 25$  GeV.

1791 VBF TOPOLOGICAL CUTS

1792 The characteristic feature of VBF production of the Higgs is the presence of two additional forward  
1793 jets coming from the incoming partons which radiate the vector bosons that make the Higgs. These jets  
1794 are forward because the outgoing partons still carry the longitudinal momentum of the incoming partons.  
1795 Figure 5.2 shows the distribution of the  $\eta$  for the leading jet in a VBF event compared to a background top  
1796 pair production event. As can be seen, the VBF jets tend to be more forward in  $\eta$ , while the  $t\bar{t}$  jets are more  
1797 central.

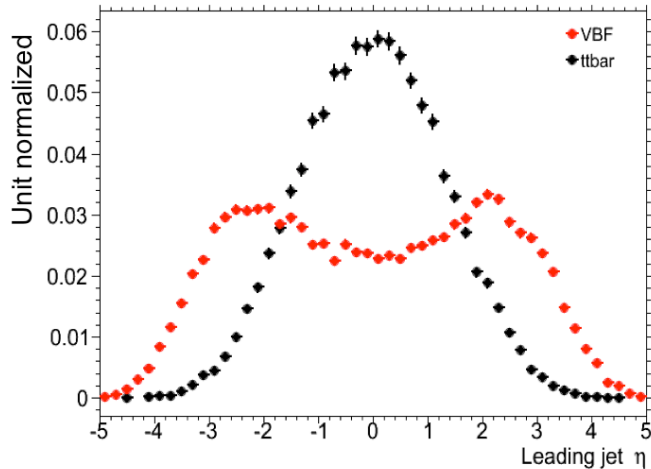


Figure 5.2: Leading jet  $\eta$  in VBF  $H \rightarrow WW^*$  (red) and  $t\bar{t}$  (black)

1798 Because the cross section for VBF production is an order of magnitude smaller than gluon fusion pro-  
1799 duction, these forward jets must be used in order to better reduce background and achieve a good signal to  
1800 background ratio. The dedicated VBF search selection requirements are constructed to maximally exploit  
1801 the features of the unique VBF topology.

1802 Requirements on the VBF jets are collectively referred to as the “VBF topological cuts”. First, a require-  
1803 ment on the dijet invariant mass of the VBF jets,  $m_{jj}$ , is placed, requiring  $m_{jj} > 600$  GeV. Next, the  
1804 event is required to have a large gap in rapidity between the two VBF jets, or  $\Delta y_{jj} > 3.6$ . Both of these  
1805 cuts put tight requirements on the presence of two forward, high  $p_T$  jets moving in opposite directions in

1806 the longitudinal plane.

1807 Beyond requiring the presence of the two forward VBF jets, the analysis also vetoes on the presence  
1808 of any additional jets that fall between the two VBF jets. This cut is referred to as the central jet veto, or  
1809 CJV. Any events with a third jet with  $p_T > 20$  GeV whose rapidity is between the region defined by the  
1810 two VBF jets are vetoed. This can be expressed in terms of a variable called the jet centrality, defined in  
1811 equation 5.2.

$$C_{j3} = \left| \eta_{j3} - \frac{\eta_{j1} + \eta_{j2}}{2} \right| / \frac{|\eta_{j1} - \eta_{j2}|}{2}, \quad (5.2)$$

1812 Here,  $\eta_{j1}$  and  $\eta_{j2}$  are the pseudorapidities of the leading and subleading jets, respectively, while  $\eta_{j3}$  is  
1813 the pseudorapidity of the extra jet in the event (if one exists). Intuitively,  $C_{j3}$  is zero when  $\eta_{j3}$  is directly  
1814 centered between the two jets and unity when  $\eta_{j3}$  is aligned with either of the VBF jets. Thus, the CJV  
1815 can be expressed as a requirement that  $C_{j3} > 1$ .

1816 The decay products of the Higgs tend to be central as well. Thus, the analysis also requires that both  
1817 leptons in the analysis fall within the rapidity gap defined by the jets. This cut is referred to as the outside  
1818 lepton veto, or OLV. A quantitative way to define the cut is to require that the centrality of each lepton  
1819 (defined analogously to that of the third jet in equation 5.2) correspond to the lepton being within the jet  
1820 rapidity gap, or  $C_\ell < 1$  for both leptons.

1821 Figure 5.3a-c shows the  $m_{jj}$ ,  $\Delta y_{jj}$ , and  $C_{\ell 1}$  variables at the stage where all previous cuts in the sequence  
1822 have been made. The agreement between data and Monte Carlo is good, and the bottom panels show their  
1823 power in discriminating the VBF signal from the background processes.

1824 The final signal region is also split into two bins of  $m_{jj}$ , with the first bin corresponding to  $600 \text{ GeV} <$   
1825  $m_{jj} < 1 \text{ TeV}$  and the second bin corresponding to  $m_{jj} > 1 \text{ TeV}$ . The first bin has more statistics but  
1826 also a larger contribution from background, while the second bin has lower statistics but a 1:1 signal to  
1827 background ratio.

## 1828 HIGGS TOPOLOGICAL CUTS

1829 The final state leptons will exhibit unique correlations due to the fact that they are arising from the  
1830 decay of a spin zero resonance. In particular, the spins of the final state leptons and neutrinos must all

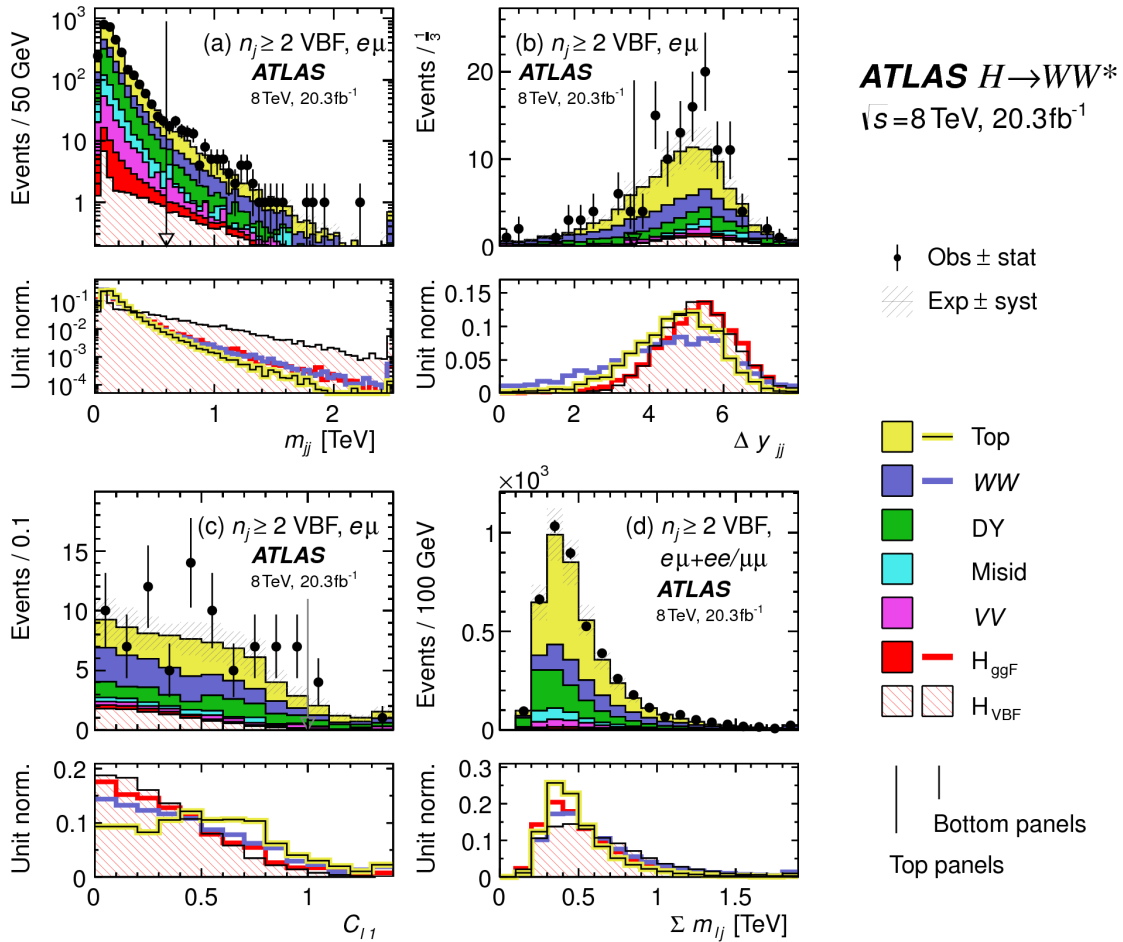


Figure 5.3: Distributions of (a)  $m_{jj}$ , (b)  $\Delta y_{jj}$ , (c)  $C_{\ell 1}$ , and (d)  $\Sigma m_{\ell j}$ , for the VBF analysis. The top panels compare simulation and data, while the bottom panels show normalized distributions for all background processes and signal [62].

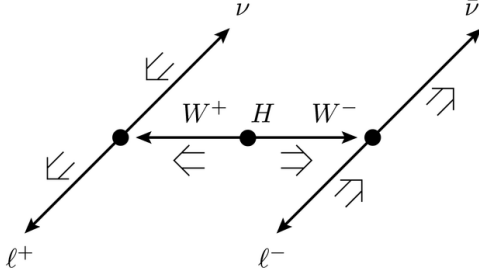


Figure 5.4: A cartoon of the WW final state. Momenta are represented with thin arrows, spins with thick arrows.  
[62]

cancel, as shown in figure 5.4. Because the neutrino has a left handed chirality and the anti-neutrino has a right handed chirality (in the massless neutrino approximation), the spin and momentum of the particles will be anti-aligned and aligned, respectively. In the transverse plane, the momenta of all four final state objects must cancel as well. With the constraint of having both the momenta and the spin alignments cancel, the final state kinematics strongly prefer having a small angle between the leptons in the transverse plane (low  $\Delta\phi_{\ell\ell}$ ). This angular correlation will also lead to low values of the di-lepton invariant mass  $m_{\ell\ell}$ . These unique signal final state kinematic correlations will be exploited to define the ultimate signal region.

The analysis places additional requirements on the final state leptons. Two requirements on dilepton kinematics are made that are common with lower multiplicity jet bins as well. The angle between leptons in the transverse plane,  $\Delta\phi_{\ell\ell}$ , is required to be less than 1.8 radians. Additionally, the dilepton mass  $m_{\ell\ell}$  is required to be less than 50 GeV.

The cut-based analysis uses  $m_T$  as the final discriminating variable as in the ggF focused analysis. The optimal number of bins in  $m_T$  was found to be three bins, with the bin boundaries at 80 and 130 GeV.

Table 5.7 shows a summary of the data and estimated signal and background yields from simulation as each requirement described above is made. The table shows how the overall signal to background ratio grows through the various selection requirements. Table 5.8 shows the background composition after each selection requirement, illustrating which backgrounds are reduced most by certain requirements. Figure 5.5 shows an ATLAS event display of a candidate event in the final signal region.

Selection	Summary					
	$N_{\text{obs}}/N_{\text{bkg}}$	$N_{\text{obs}}$	$N_{\text{bkg}}$	$N_{\text{signal}}$		
				$N_{\text{ggF}}$	$N_{\text{VBF}}$	$N_{\text{VH}}$
$e\mu$ sample	$1.00 \pm 0.00$	61434	61180	85	32	26
$n_b = 0$	$1.02 \pm 0.01$	7818	7700	63	26	16
$p_T^{\text{sum}} < 15$	$1.03 \pm 0.01$	5787	5630	46	23	13
$m_{\tau\tau} < m_Z - 25$	$1.05 \pm 0.02$	3129	2970	40	20	9.9
$m_{jj} > 600$	$1.31 \pm 0.12$	131	100	2.3	8.2	—
$\Delta y_{jj} > 3.6$	$1.33 \pm 0.13$	107	80	2.1	7.9	—
$C_{j3} > 1$	$1.36 \pm 0.18$	58	43	1.3	6.6	—
$C_{\ell 1} < 1, C_{\ell 2} < 1$	$1.42 \pm 0.20$	51	36	1.2	6.4	—
$m_{\ell\ell}, \Delta\phi_{\ell\ell}, m_T$	$2.53 \pm 0.71$	14	5.5	0.8	4.7	—
$ee/\mu\mu$ sample	$0.99 \pm 0.01$	26949	27190	31	14	10.1
$n_b, p_T^{\text{sum}}, m_{\tau\tau}$	$1.03 \pm 0.03$	1344	1310	13	8.0	4.0
$m_{jj}, \Delta y_{jj}, C_{j3}, C_\ell$	$1.39 \pm 0.28$	26	19	0.4	2.9	0.0
$m_{\ell\ell}, \Delta\phi_{\ell\ell}, m_T$	$1.63 \pm 0.69$	6	3.7	0.3	2.2	0.0

Table 5.7: Summary of event selection for the  $n_j \geq 2$  VBF analysis in the 8 TeV cut-based analysis [62].

	Composition of $N_{\text{bkg}}$								
	$N_{WW}$		$N_{\text{top}}$		$N_{\text{misid}}$		$N_{VV}$	$N_{\text{Drell-Yan}}$	
	$N_{WW}^{\text{QCD}}$	$N_{WW}^{\text{EW}}$	$N_{t\bar{t}}$	$N_t$	$N_{Wj}$	$N_{jj}$	$N_{VV}$	$N_{ee/\mu\mu}^{\text{QCD}}$	$N_{\tau\tau}^{\text{EW}}$
$e\mu$ sample	1350	68	51810	2970	847	308	380	51	3260
$n_b = 0$	993	43	3000	367	313	193	273	35	2400
$p_T^{\text{sum}} < 15$	781	38	1910	270	216	107	201	27	2010
$m_{\tau\tau} < m_Z - 25$	484	22	1270	177	141	66	132	7.6	627
$m_{jj} > 600$	18	8.9	40	5.3	1.8	2.4	5.1	0.1	15
$\Delta y_{jj} > 3.6$	11.7	6.9	35	5.0	1.6	2.3	3.3	—	11.6
$C_{j3} > 1$	6.9	5.6	14	3.0	1.3	1.3	2.0	—	6.8
$C_{\ell 1} < 1, C_{\ell 2} < 1$	5.9	5.2	10.8	2.5	1.3	1.3	1.6	—	5.7
$m_{\ell\ell}, \Delta\phi_{\ell\ell}, m_T$	1.0	0.5	1.1	0.3	0.3	0.3	0.6	—	0.5
$ee/\mu\mu$ sample	594	37	23440	1320	230	8.6	137	690	679
$n_b, p_T^{\text{sum}}, m_{\tau\tau}$	229	12.0	633	86	26	0.9	45	187	76
$m_{jj}, \Delta y_{jj}, C_{j3}, C_\ell$	3.1	3.1	5.5	1.0	0.2	0.0	0.7	3.8	0.7
$m_{\ell\ell}, \Delta\phi_{\ell\ell}, m_T$	0.4	0.2	0.6	0.2	0.2	0.0	0.1	1.5	0.3

Table 5.8: Background composition after each requirement in the  $n_j \geq 2$  VBF analysis in the 8 TeV cut-based analysis [62].

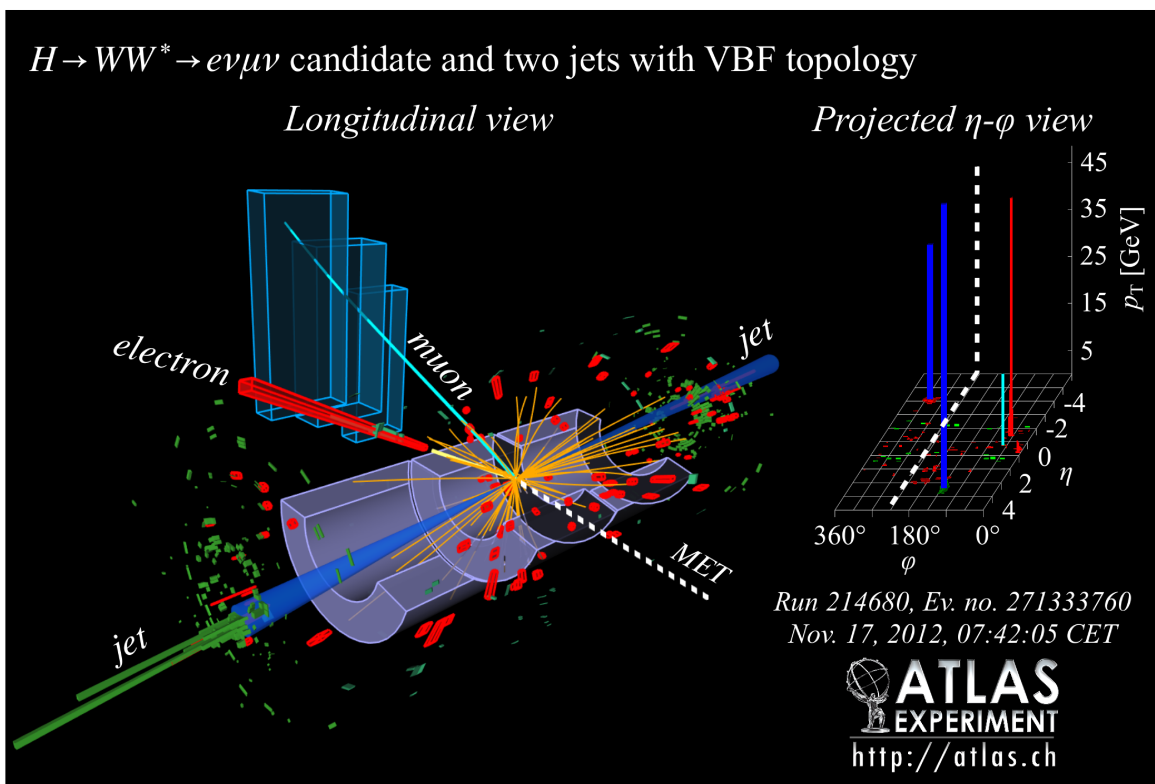


Figure 5.5: Event display of a VBF candidate event [62].

#### 1849 5.4.3 BDT-BASED SELECTION

1850 The boosted decision tree based analysis takes a different philosophy compared to the cut-based. Rather  
 1851 than cutting sequentially on many variables, the BDT analysis uses many of these variables as inputs to  
 1852 the BDT and the output BDT score ( $O_{\text{BDT}}$ ) as the final discriminant. The BDT is trained with the  
 1853 VBF  $H \rightarrow WW^*$  simulation as the signal samples and all other processes as background, including ggF  
 1854  $H \rightarrow WW^*$  production. While the BDT based analysis is treated as a separate result, it has significant  
 1855 overlap with the cut-based selection.

#### 1856 PRE-TRAINING SELECTION AND BDT INPUTS

1857 Before training, the common pre-selection cuts described in section 5.4.1 are applied. Additionally, the  
 1858 central jet veto and outside lepton veto described in section 5.4.2 are applied. The BDT has eight input  
 1859 variables, six of which are also variables that are used in the cut-based analysis. The six shared variables

1860 are  $p_T^{\text{sum}}$ ,  $m_{jj}$ ,  $\Delta y_{jj}$ ,  $m_{\ell\ell}$ ,  $\Delta\phi_{\ell\ell}$ , and  $m_T$ . The seventh variable input in the BDT is a combination of  
 1861 the variables used to do the OLV in the cut-based analysis. The BDT uses as input the sum of lepton  
 1862 centralities, or  $\sum C_\ell = C_{\ell 1} + C_{\ell 2}$ . The final BDT input variable,  $\Sigma m_{\ell j}$ , is constructed to account for  
 1863 the correlations between the jets and leptons in the event. It is the sum of the invariant masses of all four  
 1864 possible lepton-jet combinations.

1865 Figure 5.3d shows the agreement between data and simulation for the  $\Sigma m_{\ell j}$  variable, as well as showing  
 1866 its discriminating power. Figure 5.6 shows the distributions of the Higgs topological variables that are  
 1867 shared between the cut-based and BDT analyses. Figure 5.7 shows the distributions of the VBF topological  
 1868 variables shared between the cut-based and BDT analyses. In both cases, the VBF yield has been scaled by  
 1869 a factor of 50 to better show the shape difference compared to the backgrounds.

1870 Table ?? summarizes the cuts applied for the cut-based and analyses, as well as which variables are used  
 1871 as input to the BDT.

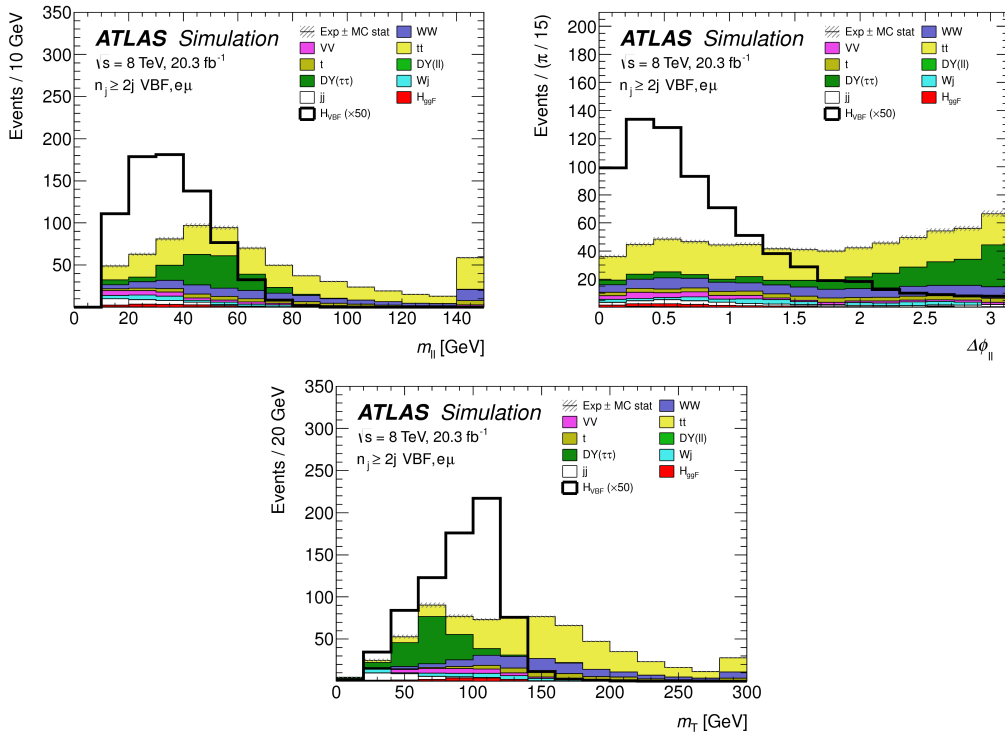


Figure 5.6: Distributions of  $m_{\ell\ell}$  (top left),  $\Delta\phi_{\ell\ell}$  (top right), and  $m_T$  (bottom), Higgs topology variables used in the selection requirements of the cut-based signal region and as inputs to the BDT result. These are plotted after all of the BDT pre-training selection cuts [62].

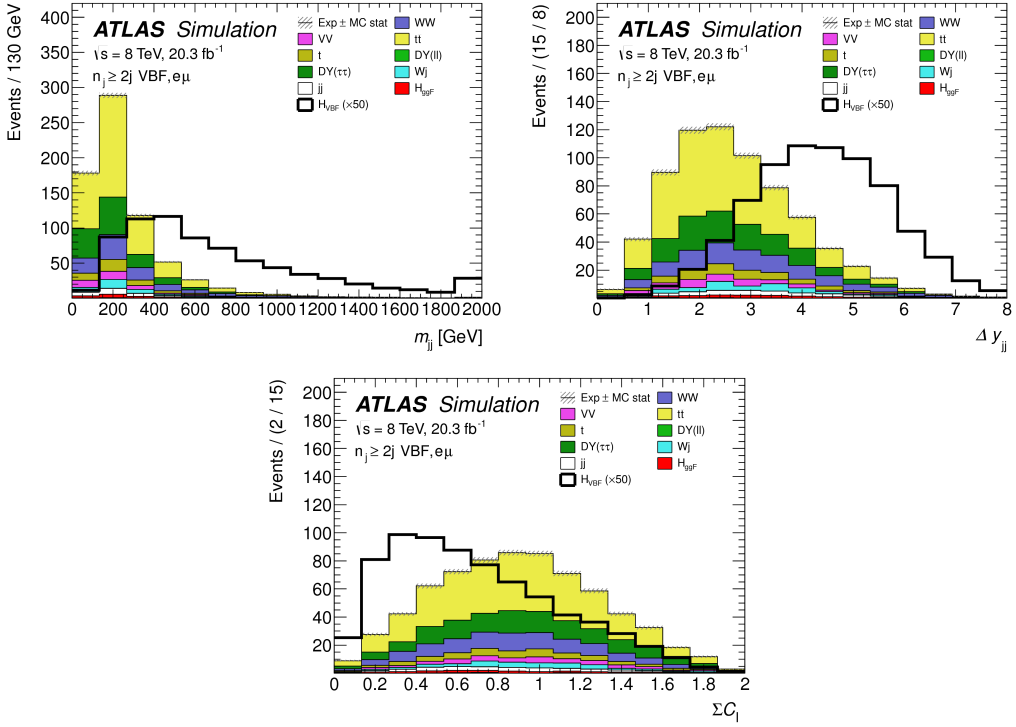


Figure 5.7: Distributions of  $m_{jj}$  (top left),  $\Delta y_{jj}$  (top right),  $\sum C_\ell$  (bottom), VBF topology variables used in the selection requirements of the cut-based signal region and as inputs to the BDT result. These are plotted after all of the BDT pre-training selection cuts [62].

## 1872 5.5 BACKGROUND ESTIMATION

1873 This section describes the procedures used to estimate backgrounds for the VBF analysis in both the  
 1874 cut-based and BDT analyses.

### 1875 5.5.1 GENERAL STRATEGY

1876 Most of the backgrounds in the VBF analysis have shapes estimated from Monte Carlo simulation but  
 1877 normalizations derived from control regions in data. In essence, a normalization factor (denoted with  $\beta$   
 1878 or abbreviated as NF) is derived by scaling the MC yield in the control region to the corresponding yield  
 1879 in data. Once this factor is derived, it can be used to scale the MC estimate of the background in the signal

1880 region. This is illustrated in equation 5.3.

$$B_{\text{SR}}^{\text{est}} = B_{\text{SR}} \times \frac{N_{\text{CR}}}{B_{\text{CR}}} \equiv B_{\text{SR}} \times \beta \quad (5.3)$$

1881 Here,  $B$  denotes the MC yield prediction in the denoted region, while  $N$  denotes the observed number of  
1882 events in data in the denoted region.

1883 Another way of writing the same equation, in terms of an extrapolation factor  $\alpha$  rather than a normal-  
1884 ization factor  $\beta$ . The overall calculation is exactly the same. However, when phrased in this way, it shows  
1885 how the uncertainty on the background estimation can be reduced. This is shown in equation 5.4.

$$B_{\text{SR}}^{\text{est}} = N_{\text{CR}} \times \frac{B_{\text{SR}}}{B_{\text{CR}}} \equiv N_{\text{CR}} \times \alpha \quad (5.4)$$

1886 Phrased this way, the equation shows that with enough statistics in the control region, a large theoretical  
1887 uncertainty on the overall background yield in the signal region can be replaced by a small statistical un-  
1888 certainty coming from the number of data events in the CR and a smaller theoretical uncertainty on the  
1889 extrapolation from the control region to the signal region.

### 1890 5.5.2 TOP BACKGROUND

1891 The normalization factor  $\beta_t$  for the top background in the VBF analysis is derived in a region required  
1892 to have one b-tagged jet, or  $n_b = 1$ . In the cut-based analysis, normalization factors are computed at every  
1893 stage of the cutflow by applying the appropriate cuts in the CR. These NF are then applied to the  $t\bar{t}$  and  
1894 single top event yields in the SR. In the BDT analysis, a single normalization factor is computed for each  
1895 bin of  $O_{\text{BDT}}$  after applying the BDT pre-training cuts described previously. The computed normaliza-  
1896 tion factors are derived with all flavor combinations combined in order to decrease statistical uncertainty.  
1897 Additionally, in the BDT analysis, BDT bins 2 and 3 are merged for the same reason.

1898 Table 5.9 shows the evolution of the  $\beta_t$  through the cut-based selection. Table 5.10 shows the value of  
1899 the  $\beta_t$  in each bin of  $O_{\text{BDT}}$ . In all cases, the computed factors are relatively consistent with unity, with  
1900 the largest discrepancy coming in bin 1 of  $O_{\text{BDT}}$ . The normalization factors in the bins of  $O_{\text{BDT}}$  are also

1901 consistent with those derived in teh cut-based sisgnal region, increasing confidence in the BDT estimation.

Cut	$\beta_t$
$p_T^{\text{sum}} < 15 \text{ GeV}$	$1.03 \pm 0.01$
$m_{\tau\tau} < m_Z - 25$	$1.05 \pm 0.01$
$m_{jj} > 600 \text{ GeV}$	$0.96 \pm 0.06$
$\Delta y_{jj} > 3.6$	$1.02 \pm 0.08$
CJV	$1.13 \pm 0.16$
OLV	$1.01 \pm 0.19$
$m_{jj} < 1 \text{ TeV}$	$0.94 \pm 0.19$
$m_{jj} > 1 \text{ TeV}$	$1.48 \pm 0.66$

Table 5.9: Top normalization factors computed at each stage of the cut-based selection. Uncertainties are statistical only.

$O_{\text{BDT}}$	$\beta_t$
Bin0	$1.09 \pm 0.02$
Bin1	$1.58 \pm 0.15$
Bin2	$0.95 \pm 0.31$
Bin3	$0.95 \pm 0.31$

Table 5.10: Top normalization factors computed for each bin of  $O_{\text{BDT}}$ . Uncertainties are statistical only.

1902 Figure 5.8 shows the  $m_{jj}$  and  $O_{\text{BDT}}$  distributions in the top control region. Overall the modeling looks  
1903 consistent with the data.

1904 While these normalization factors can be computed and applied to the expected background yields listed  
1905 in tables like table ??, in the end the normalization of the top background is profiled (meaning there is a  
1906 dedicated Poisson constraint) and allowed to float in the final statistical fit.

### 1907 5.5.3 $Z/\gamma^* \rightarrow \tau\tau$ BACKGROUND

1908 In the different flavor channels, the  $Z/\gamma^* \rightarrow \tau\tau$  background is an important one. Di-tau production  
1909 can produce an  $e\mu$  final state if each  $\tau$  lepton decays to a different flavor lepton.

1910 In the BDT analysis, a single normalization factor for the background is derived. A control region  
1911 is defined using the pre-training selection cuts, except requiring that  $|m_{\tau\tau} - m_Z| < 25 \text{ GeV}$  so that  
1912 the region is enriched in  $Z/\gamma^* \rightarrow \tau\tau$  background. Additional requirements of  $m_{\ell\ell} < 80(75) \text{ GeV}$

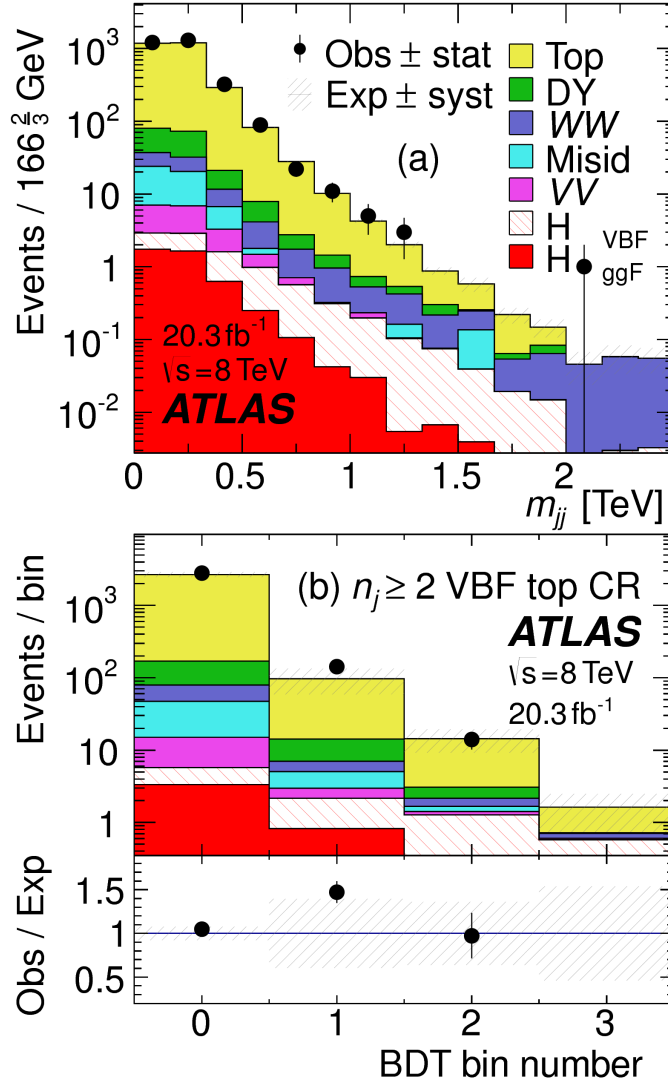


Figure 5.8: Distributions of  $m_{jj}$  (a) and  $O_{\text{BDT}}$  (b) in the VBF  $n_b = 1$  top CR [62].

in the different (same) flavor channel, as well as  $O_{\text{BDT}} > -0.48$  are applied to increase the purity of the region. The final  $\beta_{Z/\gamma^* \rightarrow \tau\tau}$  is calculated to be  $0.9 \pm 0.3$  (statistical uncertainty only). Because of the small contribution of this background in the BDT analysis and the large statistical uncertainty, no additional systematics are calculated. The final SR estimate is scaled by this  $\beta$  and not allowed to float in the fit.

The cut-based corrections are a bit more involved because they need to be applied selection by selection, as well as in the final signal region for the fit. The region is defined including all SR cuts up to the  $Z/\gamma^* \rightarrow \tau\tau$  veto, which is instead made into a Z mass peak requirement as for the BDT region. The  $m_{\ell\ell}$  cut from

1920 the BDT region is included as well. The cut-based approach aims to correct the normalization of the  
 1921  $Z/\gamma^* \rightarrow \tau\tau$  background in two ways. First, an overall normalization factor is computed from the control  
 1922 region. However, the VBF topological cuts are not included in this region, and applying them as is done in  
 1923 the top CR is not feasible due to limited statistics. So, instead, correction factors (CF) to the cut efficiencies  
 1924 of the VBF cuts are derived in a same flavor  $Z \rightarrow \ell\ell$  control region, which has significantly more statistics.  
 1925 The CF is simply the ratio of the cut efficiencies in data and MC derived in this region. In the end, the  
 1926 overall background estimate is given by equation 5.5.

$$N_{Z/\gamma^* \rightarrow \tau\tau}^{\text{est}} = B_{Z/\gamma^* \rightarrow \tau\tau}^{\text{SR}} \times \beta_{\tau\tau} \times \frac{\epsilon_{\text{VBF cuts}}^{\text{data}}}{\epsilon_{\text{VBF cuts}}^{\text{MC}}} \quad (5.5)$$

1927 The hypothesis is that while the normalization correction must be derived in a dedicated region, the ef-  
 1928 ficiency of the VBF cuts should not be sensitive to the type of  $Z/\gamma^*$  process and thus the larger control  
 1929 region can be exploited to derive the CF. Figure 5.9 shows a shape comparison for the  $m_{jj}$  variable in  
 1930  $Z \rightarrow \tau\tau$  events in the signal region and  $Z \rightarrow \ell\ell$  events in the control region. The figure shows that the  
 1931 shapes are indeed comparable and thus any CF derived in the same flavor control region can reliably be  
 1932 applied in the signal region.

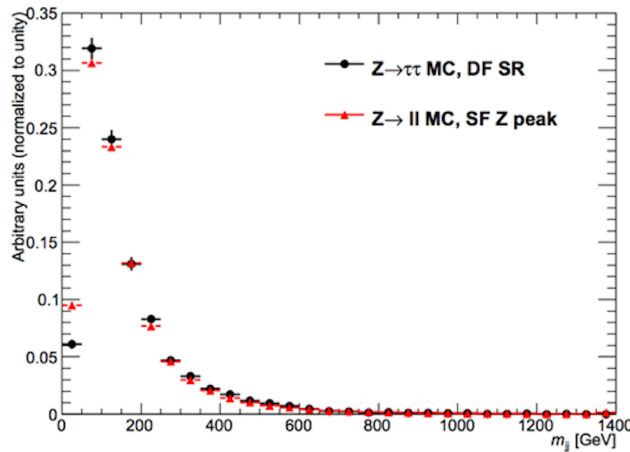


Figure 5.9: Comparison of  $m_{jj}$  shape in a same flavor  $Z \rightarrow \ell\ell$  control region and the VBF cut-based signal region.

1933 Table 5.11 shows the overall normalization factor  $\beta_{\tau\tau}$  and the efficiency correction factors for the various  
 1934 VBF topological cuts. In general, the statistical uncertainties on the cut efficiency corrections are quite

<sup>1935</sup> good, and the MC tends to underestimate the efficiency of the VBF cuts for the  $Z/\gamma^* \rightarrow \tau\tau$  background.  
<sup>1936</sup> The overall normalization factor is also consistent with that calculated for the BDT analysis.

$\beta_{\tau\tau}$	$0.97 \pm 0.04$
Cut	Correction factors
$m_{jj} > 600 \text{ GeV}$	$1.09 \pm 0.01$
$\Delta y_{jj} > 3.6$	$1.14 \pm 0.02$
CJV	$1.20 \pm 0.02$
OLV	$1.17 \pm 0.03$
$m_{jj} < 1 \text{ TeV}$	$1.17 \pm 0.06$
$m_{jj} > 1 \text{ TeV}$	$1.18 \pm 0.13$

Table 5.II:  $Z/\gamma^* \rightarrow \tau\tau$  correction factors for the VBF cut-based analysis. Uncertainties are statistical only.

<sup>1937</sup> **5.5.4  $Z/\gamma^* \rightarrow \ell\ell$  BACKGROUND**

<sup>1938</sup> In the same flavor channels, the  $Z/\gamma^* \rightarrow \ell\ell$  background is dominant and thus must be estimated cor-  
<sup>1939</sup> rectly. In both the BDT and cut-based analyses, the background is estimated using the so-called “ABCD”  
<sup>1940</sup> method. The ABCD method creates four different regions by defining cuts on two variables. One of the  
<sup>1941</sup> regions (A) is the signal region, while the other regions are defined by inverting one of both of the cuts.  
<sup>1942</sup> in this case, the two variables used are  $m_{\ell\ell}$  and  $E_T^{\text{miss}}$ , because inverting either of the SR cuts on these  
<sup>1943</sup> variables will give regions rich in the  $Z/\gamma^* \rightarrow \ell\ell$  background. Figure 5.10 illustrates the general strategy  
<sup>1944</sup> for each region.

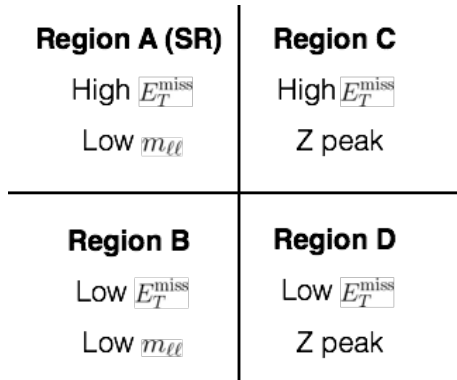


Figure 5.10: General illustration of the ABCD region definitions for  $Z/\gamma^* \rightarrow \ell\ell$  background estimation.

<sup>1945</sup> In both of the cut-based and BDT analyses, the Z peak region is defined with  $|m_{\ell\ell} - m_Z| < 15 \text{ GeV}$ .

1946 In the cut-based analysis, low  $m_{\ell\ell}$  corresponds to  $m_{\ell\ell} < 50$  GeV (this defines the cut-based SR) while  
 1947 in the BDT it is  $m_{\ell\ell} < 75$  GeV. In the cut-based, high and low  $E_T^{\text{miss}}$  are defined as opposite ends of  
 1948 the 55 GeV cut applied for the signal region definition. The BDT low  $E_T^{\text{miss}}$  region is between 25 and  
 1949 45 GeV, while the high  $E_T^{\text{miss}}$  region is  $E_T^{\text{miss}} > 45$  GeV.

1950 Once the regions are defined, the final signal region background estimate is done by taking the estimate  
 1951 in region B and extrapolating it to the signal region (A) by multiplying it by the ratio of regions C and  
 1952 D. Effectively, the  $Z$  peak region is used to estimate the efficiency of the  $E_T^{\text{miss}}$  cut in data, and then this  
 1953 efficiency is applied in the low  $m_{\ell\ell}$  region. An additional correction is also applied for the non-closure of  
 1954 the method in MC. This is summarized in equations 5.6 and 5.7.

$$N_{Z/\gamma^* \rightarrow \ell\ell}^{\text{SR}} = N_{Z/\gamma^* \rightarrow \ell\ell}^B \times \frac{N_{Z/\gamma^* \rightarrow \ell\ell}^C}{N_{Z/\gamma^* \rightarrow \ell\ell}^D} \times f_{\text{corr}} \quad (5.6)$$

$$f_{\text{corr}} = \frac{B_{\text{MC}}^A / B_{\text{MC}}^B}{B_{\text{MC}}^C / B_{\text{MC}}^D} \quad (5.7)$$

1955 Here, the  $N$  refer to data yields in each region with the non  $Z/\gamma^*$  backgrounds subtracted, while  $B$   
 1956 refer to the  $Z/\gamma^*$  yields in MC in each region.

1957 A normalization factor  $\beta_{\ell\ell}$  is computed for each analysis as the ratio of the predicted data yield to the  
 1958 MC yield in the SR. The shape of the BDT distribution is taken from data region B, while the shape of  
 1959 the  $m_T$  distribution in the cut-based analysis is taken from  $Z/\gamma^*$  MC in the SR. The values of the  $\beta_{\ell\ell}$  in  
 1960 the cut-based and BDT analyses from this method are summarized in table 5.12. They are quite consistent  
 1961 with one another within the statistical uncertainties. In the cut-based analysis, the same cut efficiency  
 1962 correction factors shown in table 5.11 are also applied (in product with the  $\beta_{\ell\ell}$ ) in the same flavor channels  
 1963 to this background, as they were derived in the  $Z$  peak region.

	$\beta_{\ell\ell}$
BDT Bin 1	$1.01 \pm 0.15$
BDT Bin 2	$0.89 \pm 0.28$
Cut-based	$0.81 \pm 0.21$

Table 5.12:  $Z/\gamma^* \rightarrow \ell\ell$  normalization factors for cut-based and BDT analyses. Uncertainties are statistical only.

1964    5.5.5     $WW$  AND OTHER DIBOSON BACKGROUNDS

1965    The  $WW$  and other diboson backgrounds have both their shape and normalization taken from MC  
1966    simulation. They are validated in dedicated control regions and found to agree with data well.

1967    As  $WW$  is the largest of these backgrounds and is irreducible, validating the estimate is of particular  
1968    importance. The validation region is constructed by requiring the pre-selection cuts on leptons and  $m_{\ell\ell}$ ,  
1969     $n_b = 0$ , and  $m_T > 100$  GeV. The  $m_{T2}$  variable [82] is an additional discriminant that will isolate  
1970    the  $WW$  background, and a requirement of  $m_{T2} > 160$  GeV is placed to define the  $WW$  validation  
1971    region. This cut gives a 60% purity for the validation region. The derived normalization factor in the  
1972    region is  $1.15 \pm 0.19$  and is thus consistent with unity. Figure 5.11 shows the  $m_{T2}$  distribution and how it  
1973    distinguishes the  $WW$  background.

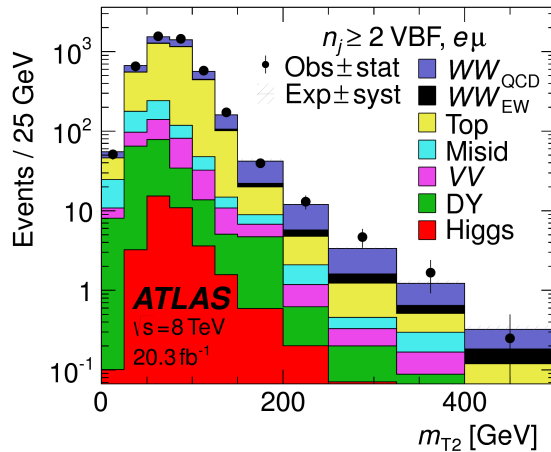


Figure 5.11: Distribution of  $m_{T2}$  in the  $WW$  validation region of the VBF analysis [62].

1974    5.5.6    HIGGS PRODUCTION VIA GLUON-GLUON FUSION

1975    Because this analysis is dedicated to measuring the VBF contribution to Higgs production, the compo-  
1976    nent of Higgs production from gluon-gluon fusion is treated as a background. The shape is taken directly  
1977    from simulation, using the generators described in table 5.4. In the final combined fit of all different signal  
1978    regions, the normalization is controlled by either a combined signal strength parameter  $\mu$ , which controls  
1979    the normalization of both ggF and VBF production, or a separate parameter  $\mu_{ggF}$  depending on the in-

1980 interpretation being presented in the final results.

### 1981 5.5.7 BACKGROUNDS WITH MISIDENTIFIED LEPTONS

1982 As discussed previously, the  $W + \text{jets}$  and QCD multijet backgrounds are derived with fully data-driven  
1983 methods. These backgrounds do not make a large contribution to the final VBF signal region but their  
1984 estimation methods are discussed briefly here.

#### 1985 $W + \text{JETS}$ BACKGROUND

1986 The  $W + \text{jets}$  background enters the signal region by having one of the jets mis-reconstructed as a lep-  
1987 ton. The background is estimated by constructing a control sample with two leptons, where one lepton  
1988 passes the usual lepton quality cuts but the second lepton fails one of those cuts (also known as the “anti-  
1989 identified” lepton). This control region is rich in the  $W + \text{jets}$  contribution because if a second lepton is  
1990 reconstructed in a  $W + \text{jets}$  event it is likely to be poor quality. The purity of this  $W + \text{jets}$  control sample is  
1991 85% to 90% depending on the exact configuration of leptons in the final state.

1992 The signal region estimate of  $W + \text{jets}$  is estimated by extrapolation from the control sample to the sig-  
1993 nal region using extrapolation factors derived in a  $Z + \text{jets}$  control sample in data. The extrapolation factor  
1994 is the ratio of the number of lepton candidates satisfying all quality criteria to the number of lepton can-  
1995 didates anti-identified. This ratio is measured in bins of  $p_T$  and  $\eta$ . Thus, the final signal region estimate  
1996 (binned as the extrapolation factor is binned) is simply the number of events in the anti-identified lepton  
1997 control sample multiplied by the extrapolation factor derived from the  $Z + \text{jets}$  control sample. Figure 5.12  
1998 shows the extrapolation factors derived for electrons and muons.

#### 1999 QCD MULTIJET BACKGROUND

2000 The method for estimating the multijet background is very similar to the  $W + \text{jets}$  estimation method.  
2001 The control sample in this case has two anti-identified leptons but otherwise satisfies all signal region re-  
2002 quirements. The extrapolation factor is estimated from a multijet sample and applied twice to the control  
2003 sample.

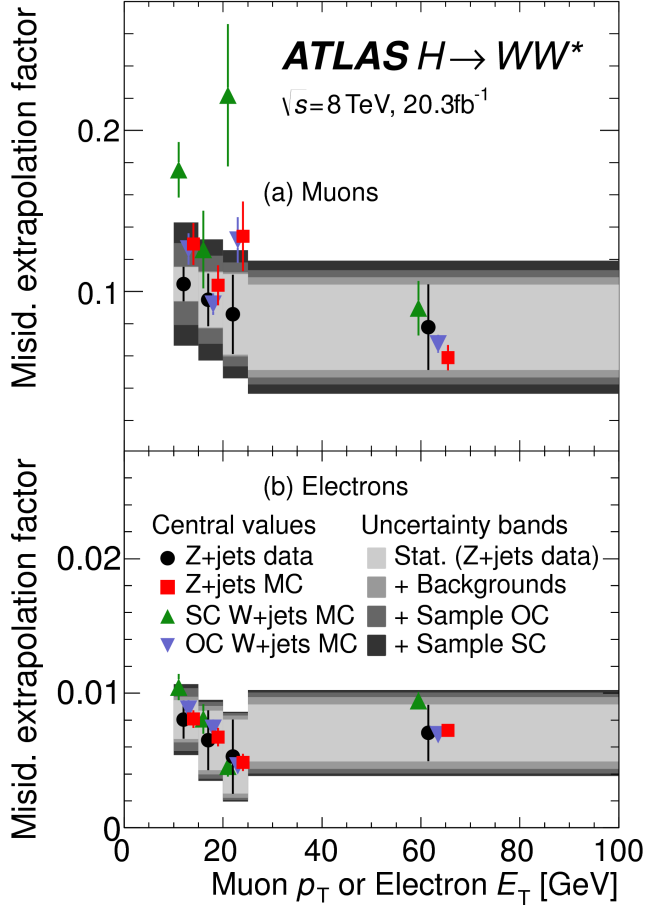


Figure 5.12: Extrapolation factors for the  $W$ +jets estimate derived for muons (a) and electrons (b) as a function of lepton  $p_T$  [62].

### 2004 5.5.8 BACKGROUND COMPOSITION IN FINAL SIGNAL REGION

2005 After all of these estimation procedures, the final signal region composition can be calculated. The esti-  
 2006 mated yields are all shown in table ???. Figure 5.13 shows the relative percentages of the different background  
 2007 for the different flavor and same flavor final states. In  $e\mu$ , the leading backgrounds are top backgrounds,  
 2008 ggF Higgs, and SM  $WW$  production. In  $ee/\mu\mu$ , the leading background is Drell-Yan, followed by top  
 2009 and ggF Higgs.

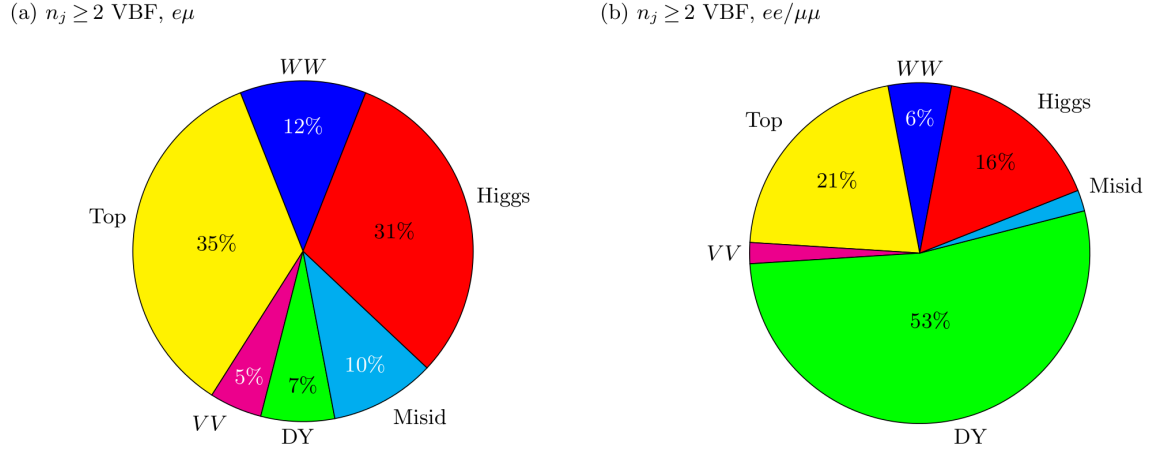


Figure 5.13: Background composition in final VBF signal region [62].

## 2010 5.6 SYSTEMATIC UNCERTAINTIES

2011 There are two main types of systematic uncertainties that are assessed for the analysis. First, theoretical  
 2012 uncertainties associated with the various signal and background yield estimates are discussed. Then, exper-  
 2013 imental uncertainties due to detector effects are shown. Normalization uncertainties refer to uncertainties  
 2014 that affect the cross section of the process in question in the signal region being probed. Shape uncertain-  
 2015 ties refer to systematic uncertainties that affect the shape of the final discriminating variable (either  $m_T$  or  
 2016  $O_{\text{BDT}}$ ).

### 2017 5.6.1 THEORETICAL UNCERTAINTIES

2018 There are four main components to theoretical uncertainties assigned to signal and background pro-  
 2019 cesses taken from Monte Carlo. Each one is a different source of variation in the overall acceptance for  
 2020 that process. The first involves variation of the QCD renormalization and factorization scales used in the  
 2021 calculation. In this case, the two scales are varied independently and simultaneously by factors of two high  
 2022 or low and quantifying the resulting variation in normalization and shape for the process. This approx-  
 2023 imates the correction to the cross section that would come from including the next order of the QCD  
 2024 calculation (referred to as scale uncertainty). Next, there is an uncertainty associated with the PDF set  
 2025 used in generating the events. The uncertainty eigenvectors for the given PDF set are studied, and the en-

2026 envelope of maximal variation is taken as an uncertainty. Finally, there are two uncertainties associated with  
 2027 the choice of MC software (referred to as PDF uncertainty). An uncertainty associated with the generator  
 2028 chosen for the hard scattering process is evaluated by keeping the parton showering software constant but  
 2029 varying the matrix element generator and taking the maximal variation as an uncertainty (referred to as  
 2030 the generator uncertainty). The converse variation can also be done, where the matrix element generator  
 2031 remains constant and the generator used for the underlying event/parton shower modeling is varied (re-  
 2032 ferred to as the UE/PS uncertainty). In cases where the background is normalized in a control region, the  
 2033 systematic uncertainty arises from variations of the extrapolation factor  $\alpha$  between the CR and the SR,  
 2034 which can affect the normalization of the background in the SR.

2035 There are two additional uncertainties that are applied to the Higgs processes as well. First, there are  
 2036 uncertainties assigned to the Higgs total production cross section. Then, there are uncertainties assigned  
 2037 based on the fact that the analysis is done in exclusive jet bins and it is possible for signal events to migrate  
 2038 from one bin to the next depending on the presence or absence of jets. These are assigned using the Jet  
 2039 Veto Efficiency (JVE) procedure [18, 83] for ggF events and the Stewart-Tackmann (ST) method [84] for  
 2040 VBF production.

2041 Table 5.13 shows the total theory uncertainties on the backgrounds in the cut-based analysis. These are  
 2042 the sum in quadrature of the uncertainties from each of the variations described above.

Process	Theory syst. (%)
ggF $H$	48
Top	26
QCD $WW$	37
$Z/\gamma^* \rightarrow \tau\tau$	6.1

Table 5.13: Systematic uncertainties for various processes in the cut-based VBF analysis, given in units of % change  
in yield. Values are given for the low  $m_{jj}$  signal region.

2043 Figures 5.14 and 5.15 show the variations in the extrapolation factor from the PDF and QCD uncertain-  
 2044 ties on the top background estimate, binned in  $m_T$ , for the cut-based analysis. In both cases, there was  
 2045 no significant shape uncertainty but normalization uncertainties were assigned according to the maximal  
 2046 variation. These uncertainties enter into the 26% total uncertainty on top quoted in table 5.13

2047 While the estimate for the same-flavor  $Z/\gamma^* \rightarrow \ell\ell$  background is data-driven, there is still a systematic  
 2048 uncertainty taken for the non-closure of the method in Monte Carlo. This is taken as the maximum of the  
 2049 deviation of the non-closure factor  $f_{\text{corr}}$  from unity and its uncertainty, or  $\max(|1 - f_{\text{corr}}|, \delta f_{\text{corr}})$ . For  
 2050 the cut-based analysis this non-closure uncertainty 23%, while for the BDT analysis it is 17%.

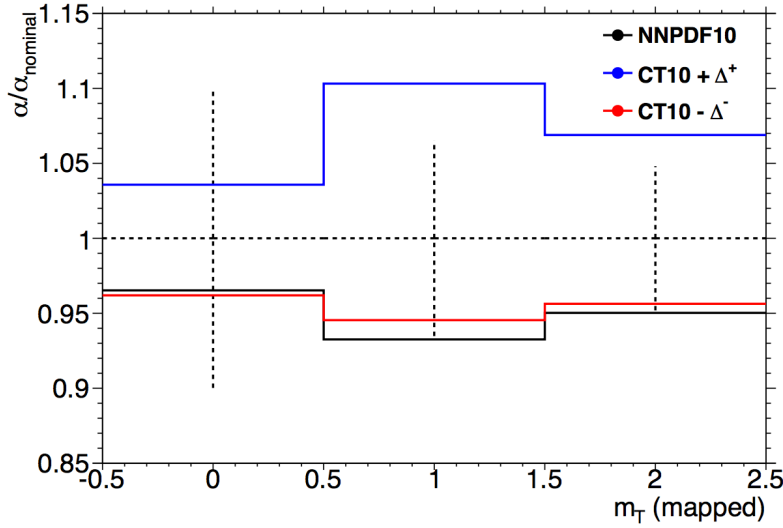


Figure 5.14: Variations in the top background extrapolation factor in the cut-based analysis due to PDF uncertainties, binned in  $m_T$ .

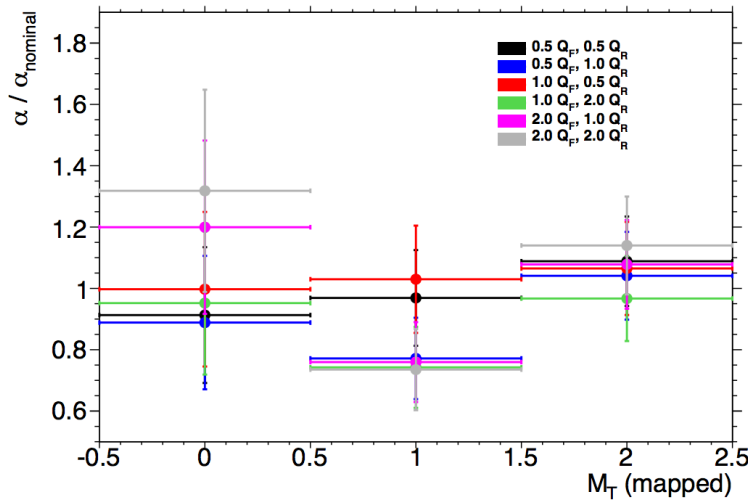


Figure 5.15: Variations in the top background extrapolation factor in the cut-based analysis due to QCD scale uncertainties, binned in  $m_T$ .

2051    5.6.2 EXPERIMENTAL UNCERTAINTIES

2052    In this analysis, the theoretical uncertainties end up being the most dominant, but there are some ex-  
2053    perimental uncertainties that make a contribution as well. The first is the uncertainty on the measured  
2054    integrated luminosity, which affects backgrounds whose normalization is taken from MC and is measured  
2055    to be 2.8% in the 8 TeV dataset [85]. The dominant sources of uncertainty overall are uncertainties on the  
2056    jet energy scale and resolution and the  $b$ -tagging efficiency. Additional sources include lepton uncertain-  
2057    ties on identification, resolution, and trigger efficiency, as well as uncertainties on the missing transverse  
2058    momentum .

2059    The jet energy scale uncertainty is split into several independent components, including jet-flavor de-  
2060    pending calorimeter response uncertainties, uncertainties on modeling of pile-up interactions, uncertain-  
2061    ties on extrapolation from the central to forward detector regions, and MC non-closure [86]. The uncer-  
2062    tainty on energy scale for jets used in this analysis ranges from 1% to 7% depending on the jet  $p_T$  and  $\eta$ .  
2063    The jet energy resolution varies from 5% to 20%, with uncertainties ranging from 2% to 40% (the largest  
2064    uncertainties occurring at the selection threshold).

2065    The  $b$ -tagging efficiency is independently measured in data samples enriched in dileptonic decays of  $t\bar{t}$   
2066    events or in events where a muon is reconstructed in the vicinity of a jet [87, 88]. The efficiencies and  
2067    their uncertainties are binned in  $p_T$  and decomposed into uncorrelated components using an eigenvector  
2068    method [89]. Uncertainties on the efficiency range from 1% to 7.8%. The uncertainty on the rate of  
2069    misidentification of  $c$ -jets as  $b$ -jets ranges from 6-14%, while the uncertainty on the rate of light jet mis-  
2070    tagging ranges from 9-19% depending on  $p_T$  and  $\eta$ .

2071    The total experimental uncertainties on different signal and background components are summarized  
2072    in table 5.14. They are compared to the level of other statistical and systematic uncertainties as well. Overall,  
2073    the experimental uncertainties are sub-dominant compared to the statistical and theoretical uncertainties.

2074    5.7 RESULTS

2075    While the combined results of all the  $H \rightarrow WW^*$  sub-analyses will be discussed in the next chapter,  
2076    this section presents the results of the VBF specific analysis and interpretations. As table ?? shows, the final

Sample	Total error	Stat. error	Expt. syst. err.	Theo. syst. err.
$n_j \geq 2$ VBF-enriched				
$N_{\text{sig}}$	13	—	6.8	12
$N_{\text{bkg}}$	9.2	4.7	6.4	4.5
$N_{WW}$	32	—	14	28
$N_{\text{top}}$	15	9.6	7.6	8.5
$N_{\text{misid}}$	22	—	12	19
$N_{VV}$	20	—	12	15
$N_{\tau\tau}$ (DY)	40	25	31	2.9
$N_{ee/\mu\mu}$ (DY)	19	11	15	—

Table 5.14: Composition of the post-fit uncertainties (in %) on the total signal ( $N_{\text{sig}}$ ), total background ( $N_{\text{bkg}}$ ), and individual background yields in the VBF analysis [62].

2077 cut-based signal region contains 20 events in data with  $m_T < 150$  GeV, 14 coming from the  $e\mu$  channel  
 2078 and 6 coming from the  $ee + \mu\mu$  channel. The BDT analysis has many more candidates due to its looser  
 2079 selection, and the yields in each bin of  $O_{\text{BDT}}$  are shown in table 5.15.

(a) Before the BDT classification

Selection	Summary						Composition of $N_{\text{bkg}}$									
	$N_{\text{obs}}/N_{\text{bkg}}$	$N_{\text{obs}}$	$N_{\text{bkg}}$	$N_{\text{signal}}$			$N_{WW}^{\text{QCD}}$	$N_{WW}^{\text{EW}}$	$N_{tt}$	$N_t$	$N_{Wj}$	$N_{jj}$	$N_{VV}$	Drell-Yan		
				$N_{\text{ggF}}$	$N_{\text{VBF}}$	$N_{\text{VH}}$								$N_{ee/\mu\mu}^{\text{QCD}}$	$N_{\tau\tau}^{\text{QCD}}$	$N_{\tau\tau}^{\text{EW}}$
$e\mu$ sample	$1.04 \pm 0.04$	718	689	13	15	2.0	90	11	327	42	29	23	31	2.2	130	2
$ee/\mu\mu$ sample	$1.18 \pm 0.08$	469	397	6.0	7.7	0.9	37	3	132	17	5.2	1.2	10.1	168	23	1

(b) Bins in  $O_{\text{BDT}}$

$e\mu$ sample																
Bin 0 (not used)	$1.02 \pm 0.04$	661	650	8.8	3.0	1.9	83	9	313	40	26	21	28	2.2	126	1
Bin 1	$0.99 \pm 0.16$	37	37	3.0	4.2	0.1	5.0	1.0	17	3.1	3.3	1.8	2.6	—	4.0	0.2
Bin 2	$2.26 \pm 0.63$	14	6.2	1.2	4.2	—	1.5	0.5	1.8	0.3	0.4	0.3	0.8	—	0.3	0.3
Bin 3	$5.41 \pm 2.32$	6	1.1	0.4	3.1	—	0.3	0.2	0.3	0.1	—	—	0.1	—	0.1	0.1
$ee/\mu\mu$ sample																
Bin 0 (not used)	$1.91 \pm 0.08$	396	345	3.8	1.3	0.8	33	2	123	16	4.1	1.1	8.8	137	20.5	0.5
Bin 1	$0.82 \pm 0.14$	53	45	1.5	2.2	0.1	3.0	0.5	10.4	1.8	0.8	0.2	0.9	26	1.7	0.1
Bin 2	$1.77 \pm 0.49$	14	7.9	0.6	2.5	—	0.8	0.3	1.1	0.2	0.2	—	0.3	4.4	0.3	0.1
Bin 3	$6.52 \pm 2.87$	6	0.9	0.2	1.7	—	0.1	0.2	0.2	—	—	—	—	0.7	—	—

Table 5.15: Event selection for the VBF BDT analysis. The event yields in (a) are shown after the pre-selection and the additional requirements applied before the BDT classification (see text). The event yields in (b) are given in bins in  $O_{\text{BDT}}$  after the classification [62].

2080 Figure 5.16(a) shows the final distribution of data candidates compared to the expected  $m_T$  distribution  
 2081 for signal and background. The data are very consistent with a VBF Higgs hypothesis. Figure 5.16(b) shows

2082 where the data candidates fall in the two-dimensional binning of  $m_T$  and  $m_{jj}$  used in the fit for the cut-  
 2083 based analysis.

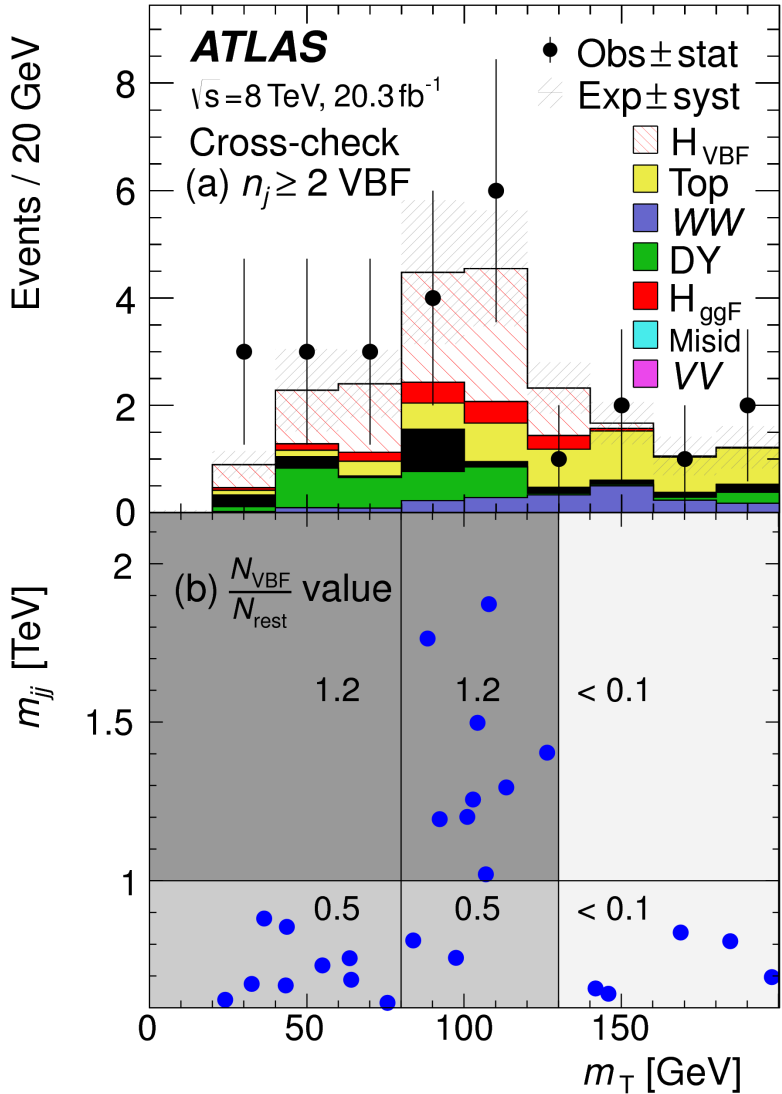


Figure 5.16: Post-fit distributions in the cut-based VBF analysis. Panel (a) shows the one-dimensional  $m_T$  distribution, while (b) shows the data candidates split into the bins of  $m_T$  and  $m_{jj}$  used in the final fit [62].

2084 Figure 5.17 shows the distributions of  $O_{\text{BDT}}$  and  $m_T$  in the VBF BDT analysis. Again the data are quite  
 2085 consistent with a VBF Higgs hypothesis.

2086 Because the cut-based result is used as a validation for the BDT analysis and the two signal regions are  
 2087 not fully orthogonal, it is interesting to explore which events overlap between the two analyses. Of the

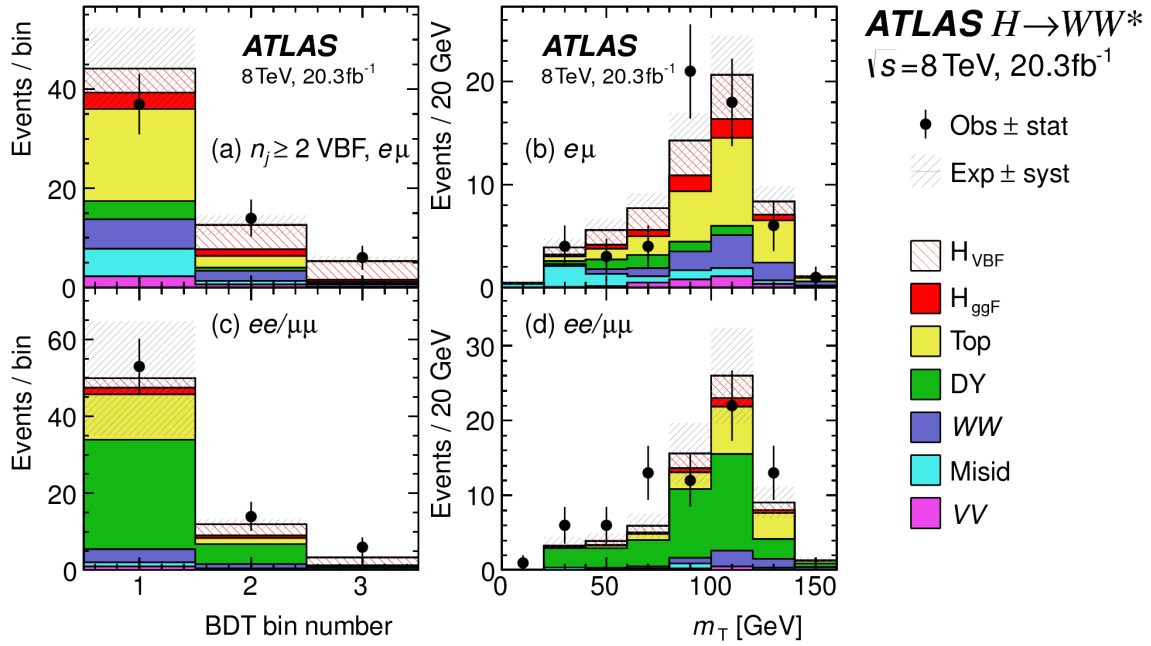


Figure 5.17: Postfit distributions in the BDT VBF analysis [62].

2088 twenty events in the cut-based signal region, only seven were not selected by the BDT analysis, while the  
 2089 other thirteen also enter the BDT signal region. Figure 5.18 shows where the different analysis candidates  
 2090 lie in the  $m_{jj}$ - $m_T$  plane. This shows clearly that the advantage of the BDT analysis is that it can extract  
 2091 signal candidates lower  $m_{jj}$  region due to its ability to recognize correlations with other variables.

2092 While the context of these results in the broader  $H \rightarrow WW^*$  statistical analysis will be presented in  
 2093 the next chapter, the significance of the VBF observation can be shown here. In the BDT analysis, the  
 2094 expected signal significance was  $2.7\sigma$ , while the observed significance was  $3.1\sigma$ . In the cut-based analysis,  
 2095 the expected significance was  $2.1\sigma$  and the observed significance was  $3.0\sigma$ . The compatibility between  
 2096 these two results can be evaluated by computing the probability of observing a larger difference in  $Z_0$  values  
 2097 than the one measured. Using toy Monte Carlo with the ggF signal strength fixed to unity and considering  
 2098 only statistical uncertainties, this probability is computed to be 79%, indicating good agreement between  
 2099 the analyses. This result represents the first observation of the vector boson fusion production of a Higgs  
 2100 boson.

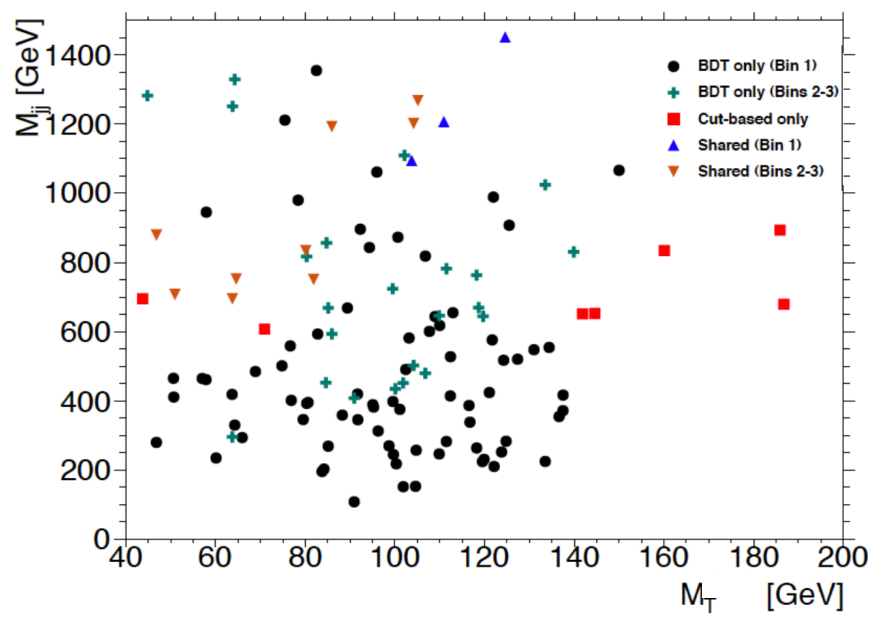


Figure 5.18: Overlap between cut-based and BDT VBF signal region candidates in the  $m_{jj}$ - $m_T$  plane.

*The feeling is less like an ending than just another starting  
point.*

Chuck Palahniuk

# 6

2101

2102

## Combined Run I $H \rightarrow WW^* \rightarrow \ell\nu\ell\nu$

2103

## results

2104

### 6.1 INTRODUCTION

2105

In the final statistical analysis of  $H \rightarrow WW^* \rightarrow \ell\nu\ell\nu$ , the dedicated gluon-gluon fusion and vector boson fusion sensitive signal regions are all combined into a single fit to determine the main parameters of interest, the Higgs signal strength  $\mu$  and mass  $m_H$ . Therefore, while the specific requirements applied for the VBF sensitive analysis are discussed in chapter 5, the final measurement of these parameters can only be discussed in combination with the results of the ggF dedicated analysis. For example, because ggF Higgs production is considered a background in the VBF analysis, the ggF dedicated signal regions can actually constrain the normalization of this background in the VBF dedicated region.

2112

This chapter presents the combined interpretation of results in the  $H \rightarrow WW^* \rightarrow \ell\nu\ell\nu$  analysis

SR category $i$				Fit var.	
$n_j$ , flavor	$\otimes m_{\ell\ell}$	$\otimes p_T^{\ell 2}$	$\otimes \ell_2$		
$n_j = 0$	$e\mu$	$\otimes [10, 30, 55]$	$\otimes [10, 15, 20, \infty]$	$\otimes [e, \mu]$	$m_T$
	$ee/\mu\mu$	$\otimes [12, 55]$	$\otimes [10, \infty]$		$m_T$
$n_j = 1$	$e\mu$	$\otimes [10, 30, 55]$	$\otimes [10, 15, 20, \infty]$	$\otimes [e, \mu]$	$m_T$
	$ee/\mu\mu$	$\otimes [12, 55]$	$\otimes [10, \infty]$		$m_T$
$n_j \geq 2$ ggF	$e\mu$	$\otimes [10, 55]$	$\otimes [10, \infty]$		$m_T$
$n_j \geq 2$ VBF	$e\mu$	$\otimes [10, 50]$	$\otimes [10, \infty]$		$O_{\text{BDT}}$
	$ee/\mu\mu$	$\otimes [12, 50]$	$\otimes [10, \infty]$		$O_{\text{BDT}}$

Table 6.1: All signal regions definitions input into final statistical fit [62].

for gluon fusion and vector boson fusion Higgs production. First, the results of the dedicated gluon fusion search are presented. Then, a comparison of the individual production mode signal strengths ( $\mu_{\text{ggF}}$  and  $\mu_{\text{VBF}}$ ) and a measurement of the combined signal strength ( $\mu$ ) are shown. Subsequently, the measured values of the Higgs couplings to fermions and vector bosons is presented. Finally, the cross section measurement for ggF and VBF production are shown.

## 6.2 RESULTS OF DEDICATION GLUON FUSION $H \rightarrow WW^* \rightarrow \ell\nu\ell\nu$ SEARCH

The details of the dedicated gluon fusion  $H \rightarrow WW^* \rightarrow \ell\nu\ell\nu$  search are not discussed in this thesis and instead left to more comprehensive sources [62]. However, a brief summary of the results are essential for describing the results of the full analysis and interpreting the results of the dedicated VBF search in this broader context.

Table 6.1 shows the individual signal regions that were input into the final statistical fit. The ggF dedicated bins use  $m_T$  as their discriminating variable and are separated into bins of  $p_T$  of the subleading lepton as well. The VBF dedicated bin uses the  $O_{\text{BDT}}$  distribution as its final discriminant.

Table 6.2 shows the yields in the various signal regions in both data and expected signal and back-

2127 grounds. The yields for signal and background are all scaled according to the final normalizations cal-  
2128 culated in the fit.

	$N_{\text{obs}}$	$N_{\text{bkg}}$	$N_{\text{ggF}}$	$N_{\text{VBF}}$
$n_j = 0$	3750	$3430 \pm 90$	$300 \pm 50$	$8 \pm 4$
$n_j = 1$	1596	$1470 \pm 40$	$102 \pm 26$	$17 \pm 5$
$n_j \geq 2, \text{ggF } e\mu$	1017	$960 \pm 40$	$37 \pm 11$	$13 \pm 1.4$
$n_j \geq 2, \text{VBF}$	130	$99 \pm 9$	$7.7 \pm 2.6$	$21 \pm 3$

Table 6.2: Post-fit yields in the different ggF and VBF dedicated signal regions [62].

2129 Figure 6.1 shows the final post-fit  $m_T$  distribution in the  $n_j \leq 1$  regions. The data are very consistent with the hypothesis of ggF Higgs production. These yields are used as input, along with the VBF results

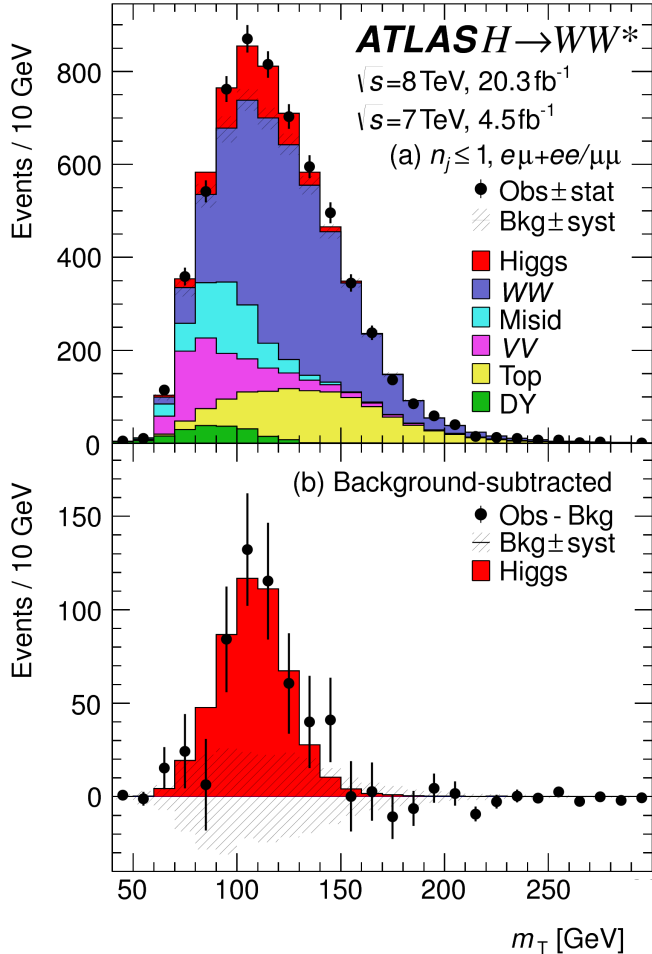


Figure 6.1: Post-fit  $m_T$  distribution in the  $n_j \leq 1$  regions [62].

2130

2131 in chapter 5, for the physical interpretation of results presented in subsequent sections.

2132 **6.3 SIGNAL STRENGTH MEASUREMENTS IN ggF AND VBF PRODUCTION**

2133 When all of the signal regions are combined in the fit, there can be a combined measurement of the  
 2134 signal strength as well as the individual ggF and VBF signal strengths. The combined signal strength is the  
 2135 ratio of the sum of the gluon fusion and VBF cross sections to the theory prediction, or a signal strength  
 2136 for the total Higgs production cross section that this analysis is sensitive to. The final measured combined  
 2137 signal strength  $\mu$  is measured shown in equation 6.1.

$$\begin{aligned} \mu &= 1.09 \quad {}^{+0.16}_{-0.15} \text{ (stat.)} \quad {}^{+0.08}_{-0.07} \left( \begin{array}{l} \text{expt} \\ \text{syst} \end{array} \right) \quad {}^{+0.15}_{-0.12} \left( \begin{array}{l} \text{theo} \\ \text{syst} \end{array} \right) \quad \pm 0.03 \left( \begin{array}{l} \text{lumi} \\ \text{syst} \end{array} \right) \\ &= 1.09 \quad {}^{+0.16}_{-0.15} \text{ (stat)} \quad {}^{+0.17}_{-0.14} \text{ (syst)} \\ &= 1.09 \quad {}^{+0.23}_{-0.21}. \end{aligned} \tag{6.1}$$

2138 Figure 6.2 gives the best fit signal strength  $\hat{\mu}$  as a function of the hypothesized Higgs mass. The value  
 2139 at 125.36 GeV corresponds to the  $\mu$  quoted in equation 6.1. This value of the Higgs mass is used because it  
 2140 is the most precise mass measurement from ATLAS, a result of the combined  $\gamma\gamma$  and  $ZZ$  mass measure-  
 2141 ments [90].

2142 As explained in chapter 3, a probability  $p_0$  can be computed using the test statistic  $q_0$  to quantify the  
 2143 probability that the background could fluctuate to produce an excess at least as large as the one observed  
 2144 in the data. The local  $p_0$  value is shown in figure 6.3 as a function of  $m_H$ . The minimum  $p_0$  value is at  
 2145  $m_H = 130$  GeV and corresponds to a significance of  $6.1\sigma$ . The curve is relatively flat and the significance  
 2146 is the same at 125.36 GeV within the quoted precision. The expected significance for a signal with strength  
 2147  $\mu = 1.0$  is  $5.8\sigma$ . This represents the first discovery level significance measurement in the  $H \rightarrow WW^* \rightarrow$   
 2148  $\ell\nu\ell\nu$  analysis.

2149 All the results presented so far in this section have been for the combined gluon fusion and VBF pro-  
 2150 duction modes. However, each signal strength can be calculated separately in the likelihood as well. There  
 2151 are two ways to do this. First, the likelihood can be parameterized in terms of a single parameter, the ratio

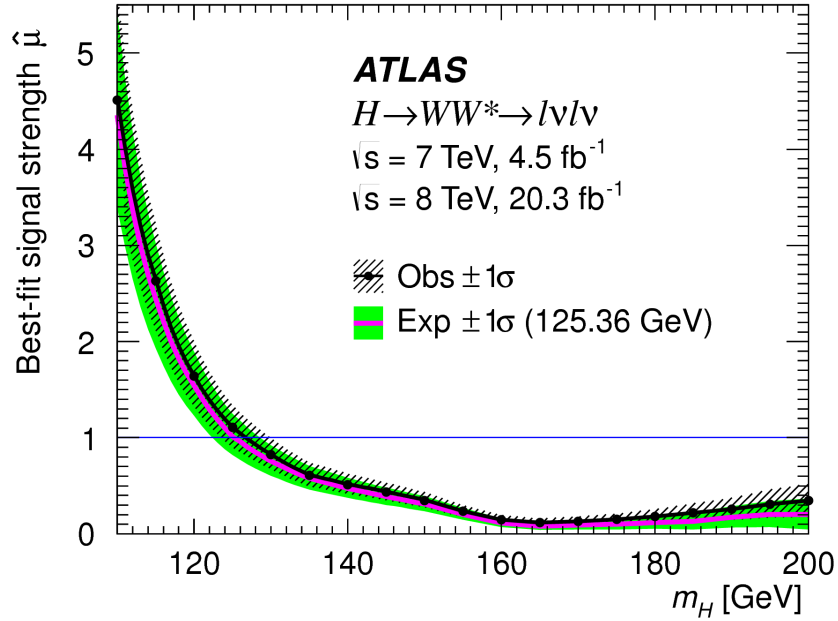


Figure 6.2: Best fit signal strength  $\hat{\mu}$  as a function of hypothesized  $m_H$  [62].

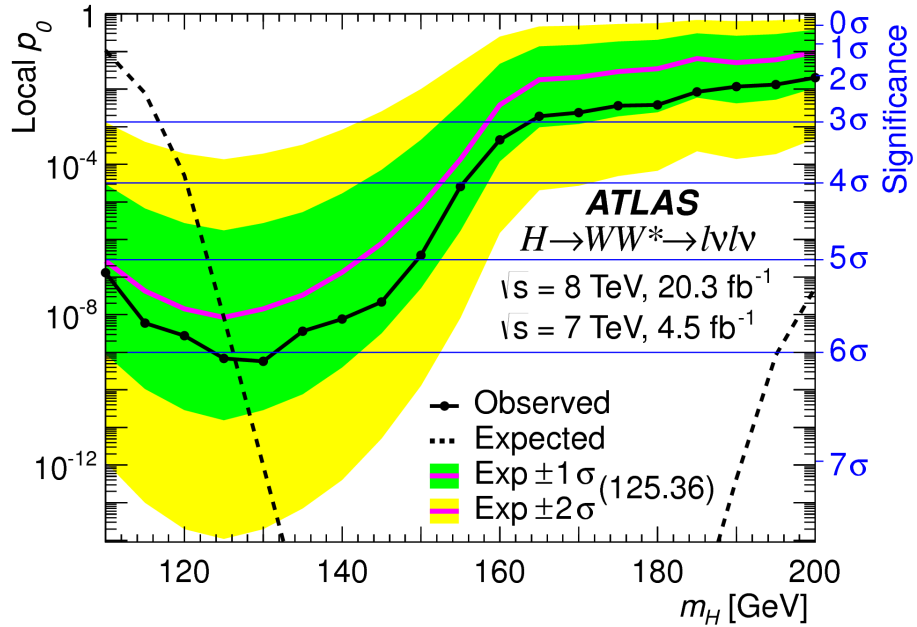


Figure 6.3: Local  $p_0$  as a function of  $m_H$  [62].

of the VBF and gluon fusion signal strengths. With this method, the significance of the VBF observation  
 can be evaluated. Figure 6.4 shows the likelihood as a function of the ratio  $\mu_{\text{VBF}}/\mu_{\text{ggF}}$ .

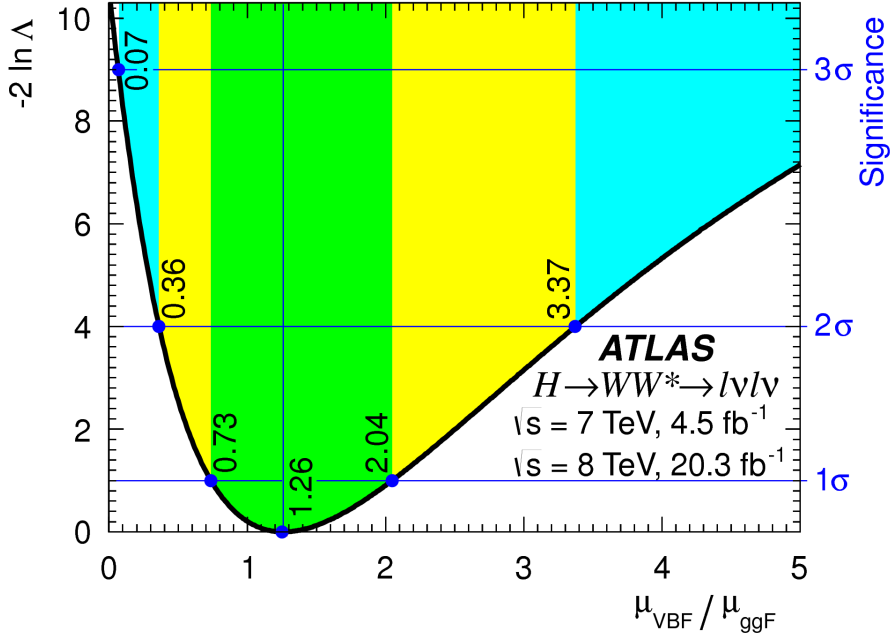


Figure 6.4: Likelihood as a function of  $\mu_{\text{VBF}} / \mu_{\text{ggF}}$  [62].

2154     The best fit value of the ratio of signal strengths is shown in equation 6.2. Within the quoted uncer-  
 2155     tainties, it is consistent with a ratio of unity.

$$\frac{\mu_{\text{VBF}}}{\mu_{\text{ggF}}} = 1.26^{+0.61}_{-0.45} (\text{stat.})^{+0.50}_{-0.26} (\text{syst.}) = 1.26^{+0.79}_{-0.53} \quad (6.2)$$

2156     The null hypothesis for VBF production corresponds to a ratio of  $\mu_{\text{VBF}} / \mu_{\text{ggF}} = 0$ . The likelihood in  
 2157     figure 6.4 gives a significance of  $3.2\sigma$  at  $\mu_{\text{VBF}} / \mu_{\text{ggF}} = 0$ , as quoted in chapter 5.

2158     In addition to the ratio of signal strengths, each signal strength can be varied independently in the like-  
 2159     lihood as well. Figure 6.5 shows the two dimensional likelihood scan in the  $\mu_{\text{ggF}}-\mu_{\text{VBF}}$  plane. The best fit  
 2160     values of the two signal strengths are shown in equation 6.3. Both are consistent with unity within their  
 2161     uncertainties.

$$\begin{aligned} \mu_{\text{ggF}} &= 1.02 \pm 0.19^{+0.22}_{-0.18} = 1.02^{+0.29}_{-0.26} \\ \mu_{\text{VBF}} &= 1.27 \pm 0.40^{+0.44}_{-0.21} = 1.27^{+0.53}_{-0.45}. \end{aligned} \quad (6.3)$$

(stat.) (syst.)

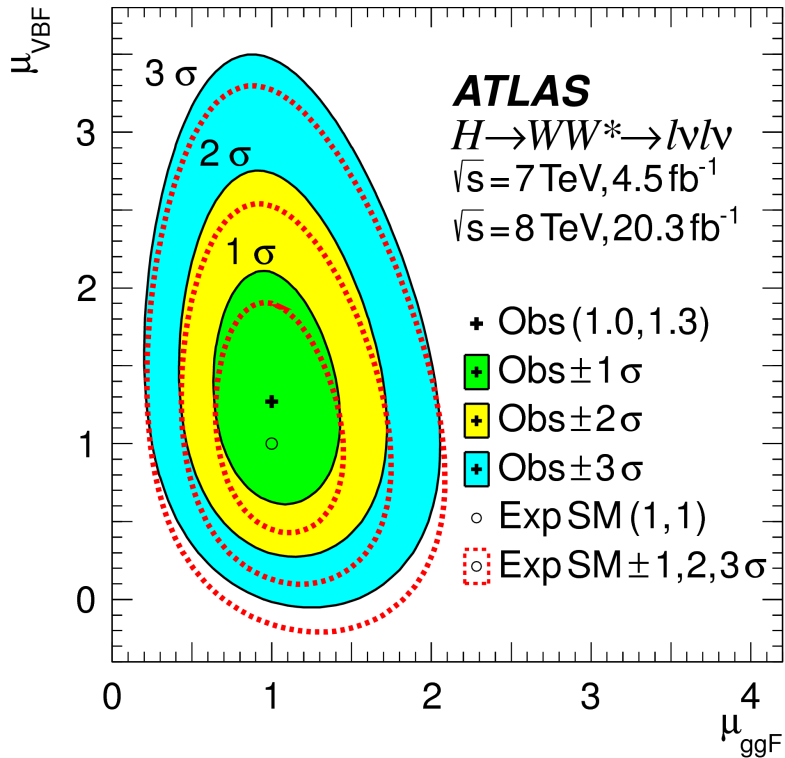


Figure 6.5: Likelihood scan as a function of  $\mu_{\text{VBF}}$  and  $\mu_{\text{ggF}}$  [62].

## 2162 6.4 MEASUREMENT OF HIGGS COUPLINGS TO VECTOR BOSONS AND FERMIONS

2163 Similar to the parameterization of signal strength, the couplings of the Higgs to fermions and bosons  
 2164 can also be parameterized. The parameter of interest in this case is  $\kappa$ , or the ratio of the measured coupling  
 2165 to the standard model expectation. Both the fermion and boson couplings have these so-called scale factors,  
 2166  $\kappa_F$  for fermions and  $\kappa_V$  for bosons. Gluon fusion production is sensitive to the fermion couplings through  
 2167 the top quark loops in its production, while VBF production is sensitive to the vector boson couplings in  
 2168 its production. Both modes are sensitive to the vector boson couplings in their decays. The signal strengths  
 2169 will have dependence on the coupling scale factors as described in equation 6.4 [18].

$$\begin{aligned}\mu_{\text{ggF}} &\propto \frac{\kappa_F^2 \cdot \kappa_V^2}{(\mathcal{B}_{H \rightarrow f\bar{f}} + \mathcal{B}_{H \rightarrow gg}) \kappa_F^2 + (\mathcal{B}_{H \rightarrow VV}) \kappa_V^2} \\ \mu_{\text{VBF}} &\propto \frac{\kappa_V^4}{(\mathcal{B}_{H \rightarrow f\bar{f}} + \mathcal{B}_{H \rightarrow gg}) \kappa_F^2 + (\mathcal{B}_{H \rightarrow VV}) \kappa_V^2}.\end{aligned}\quad (6.4)$$

2170 Figure 6.6 shows the two-dimensional likelihood scan of  $\kappa_F$  and  $\kappa_V$ . The best-fit values are given in equa-  
 2171 tion 6.5. The best-fit values are consistent with unity within their uncertainties.

$$\begin{aligned} \kappa_F &= 0.93 & +0.24 & +0.21 & = 0.93 & +0.32 \\ \kappa_V &= 1.04 & +0.07 & +0.07 & = 1.04 & \pm 0.11. \end{aligned} \quad (6.5)$$

(stat.) (syst.)

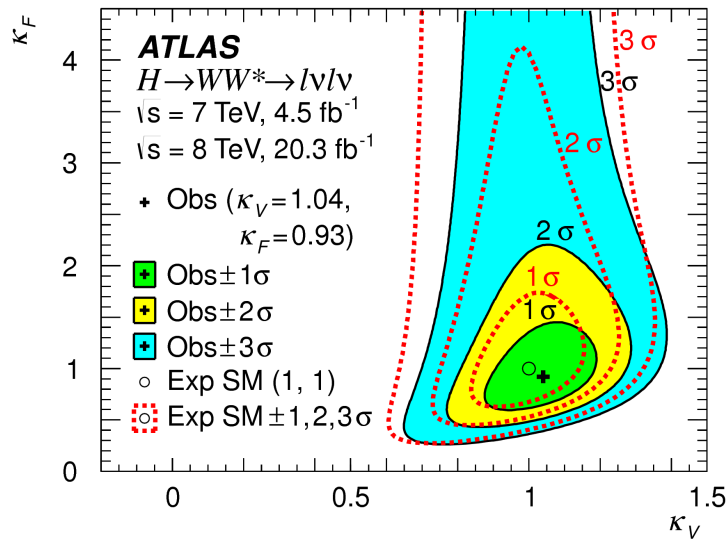


Figure 6.6: Likelihood scan as a function of  $\kappa_F$  and  $\kappa_V$  [62].

2172

## 2173 6.5 HIGGS PRODUCTION CROSS SECTION MEASUREMENT

2174 Another measurement that comes naturally from the signal strength numbers quoted earlier is the pro-  
 2175 duction cross section and 7 and 8 TeV for both gluon fusion and VBF production. The general equation  
 2176 for calculating the cross section is given in equation 6.6.

$$\begin{aligned} (\sigma \cdot \mathcal{B}_{H \rightarrow WW^*})_{\text{obs}} &= \frac{(N_{\text{sig}})_{\text{obs}}}{\mathcal{A} \cdot \mathcal{C} \cdot \mathcal{B}_{WW \rightarrow \ell\nu\ell\nu}} \cdot \frac{1}{\int L dt} \\ &= \hat{\mu} \cdot (\sigma \cdot \mathcal{B}_{H \rightarrow WW^*})_{\text{exp}} \end{aligned} \quad (6.6)$$

2177  $(N_{\text{sig}})_{\text{obs}}$  is the number of events observed in data.  $\mathcal{A}$  is the geometric and kinematic acceptance of the  
 2178 detector, while  $\mathcal{C}$  is the efficiency of the signal region selection for events that are reconstructed in the  
 2179 detector. The branching ratio of a  $WW$  system to leptons must also be divided out. The production  
 2180 cross section depends on the center of mass energy and the production mode desired (gluon fusion or  
 2181 VBF), and so three separate cross section measurements are quoted in equation 6.7.

$$\begin{aligned}
 \sigma_{\text{ggf}}^{\text{7TeV}} \cdot \mathcal{B}_{H \rightarrow WW^*} &= 2.0 \pm 1.7^{+1.2}_{-1.1} = 2.0^{+2.1}_{-2.0} \text{ pb} \\
 \sigma_{\text{ggf}}^{\text{8TeV}} \cdot \mathcal{B}_{H \rightarrow WW^*} &= 4.6 \pm 0.9^{+0.8}_{-0.7} = 4.6^{+1.2}_{-1.1} \text{ pb} \\
 \sigma_{\text{vbf}}^{\text{8TeV}} \cdot \mathcal{B}_{H \rightarrow WW^*} &= 0.51^{+0.17}_{-0.15} {}^{+0.13}_{-0.08} = 0.51^{+0.22}_{-0.17} \text{ pb.}
 \end{aligned} \tag{6.7}$$

(stat.) (syst.)

2182 The predicted cross section values for gluon fusion are  $3.3 \pm 0.4$  pb at 7 TeV and  $4.2 \pm 0.5$  pb at 8 TeV,  
 2183 consistent with the measured values within their uncertainties. For vector boson fusion, the predicted  
 2184 cross section is  $0.35 \pm 0.02$  pb, again consistent with the measured value.

## 2185 6.6 CONCLUSION

2186 The combined analysis of the gluon fusion and vector boson fusion processes in  $H \rightarrow WW^* \rightarrow \ell\nu\ell\nu$   
 2187 in the 7 and 8 TeV datasets has yielded the first discovery level significance for Higgs production in this  
 2188 decay channel. Additionally, precise measurements of the couplings to vector bosons and fermions are  
 2189 given. Finally, signal strengths and cross sections for each production mode are measured. Figure 6.7 shows  
 2190 the  $H \rightarrow WW^* \rightarrow \ell\nu\ell\nu$  measurements in comparison with other Higgs decay channels in ATLAS. The  
 2191 measurement of signal strength from this channel remains the most sensitive in both the gluon fusion and  
 2192 VBF production modes for the Run 1 dataset.

**ATLAS**

Individual analysis

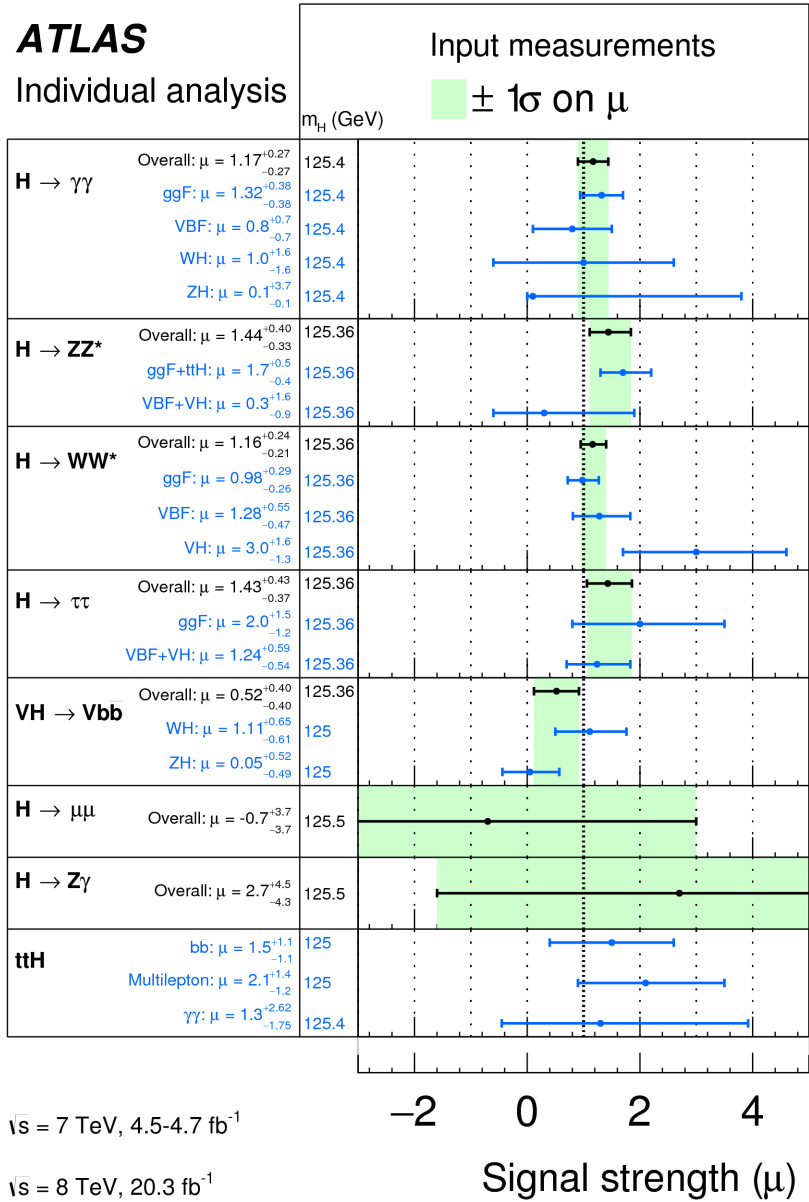


Figure 6.7: Comparison of signal strength measurements in different Higgs decay channels on ATLAS [91].

2193

## Part III

2194

Search for Higgs pair production in the

2195

$HH \rightarrow b\bar{b}b\bar{b}$  channel in LHC Run 2 at  $\sqrt{s} =$

2196

13 TeV

*Passion is in all great searches and is necessary to all creative endeavors.*

W. Eugene Smith

# 7

2197

## 2198 Search for Higgs pair production in boosted 2199 $b\bar{b}b\bar{b}$ final states

### 2200 7.1 INTRODUCTION

2201 After the discovery of the Higgs boson in the ATLAS Run 1 dataset and the subsequent measurements  
2202 of its properties, the Higgs transformed into a potential tool in searches for physics beyond the Standard  
2203 Model. The pair production cross section of the Higgs can be enhanced through BSM physics. Studying  
2204 di-Higgs production also probes the Higgs self-coupling, shedding light on the structure of the Higgs po-  
2205 tential. This chapter presents a search for resonant production of a Higgs pair in the  $X \rightarrow HH \rightarrow b\bar{b}b\bar{b}$   
2206 final state in  $3.2 \text{ fb}^{-1}$  of data collected at  $\sqrt{s} = 13 \text{ TeV}$ . In particular, this chapter focuses on a search for  
2207 this final state in the regime where  $m_X$  is large ( $\gtrsim 1 \text{ TeV}$ ) and the Higgs bosons in the decay are signifi-  
2208 cantly boosted. A tailored selection for this boosted selection, using novel techniques in jet substructure

and  $b$ -tagging, is discussed. Then, the data-driven background estimate is presented. Finally, the results of the search are shown. The signal models used as benchmarks are a spin-2 Randall Sundrum graviton (RSG) and a narrow width spin-0 resonance. These models are described in more detail in Chapter 1. Limits on signal models are reserved for the next chapter where the results of this chapter are combined with the results of a separate selection dedicated to the lower  $m_X$  regime.

## 7.2 MOTIVATION

With the center of mass energy increase from  $\sqrt{s} = 8$  TeV to  $\sqrt{s} = 13$  TeV, the LHC and ATLAS are able to probe new resonances at higher mass scales than previously accessible in Run 1. This is a powerful motivator for searching for a new resonance in the early 13 TeV data. Figure 7.1 shows the ratios of parton luminosities between 8 and 13 TeV for different resonance masses. For a resonance of  $M_X = 2$  TeV, the cross section at  $\sqrt{s} = 13$  TeV is roughly a factor of 10 larger than at  $\sqrt{s} = 8$  TeV.

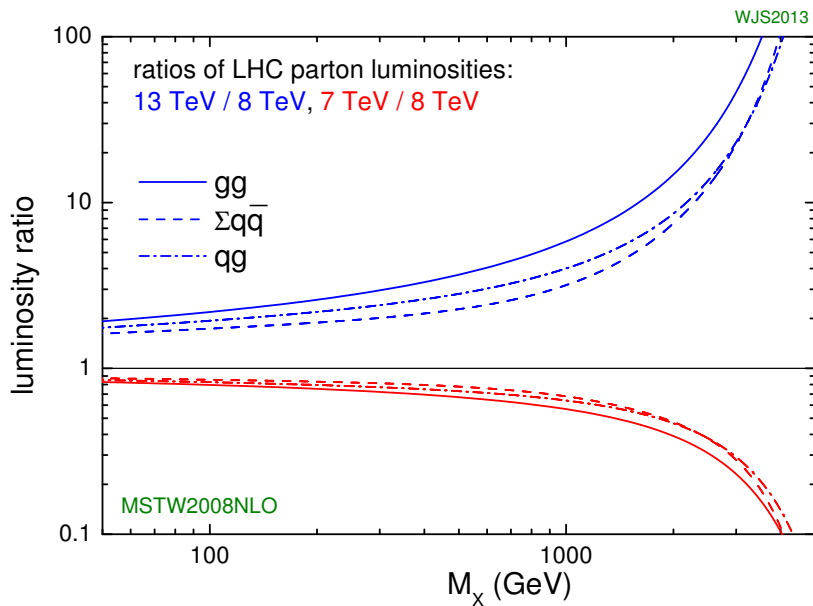


Figure 7.1: Parton luminosity ratios as a function of resonance mass  $M_X$  for 13/8 TeV and 7/8 TeV [92].

Higgs pair production offers a vast array of unprobed regions of phase space where searches for BSM physics can be made. Chapter 1 discusses some possibilities for both resonant and non-resonant enhance-

ment of the di-Higgs production cross section. Given the increased mass reach of the LHC in Run 2, it is particularly important to focus on resonant searches at high  $m_X$ . One consideration when conducting a search in the  $HH$  final state is which decay modes of the Higgs to consider. Figure 7.2 shows the branching ratio of the  $HH$  final state for different combinations of decays of each individual Higgs. As the largest branching ratio for the 125 GeV Higgs is  $H \rightarrow b\bar{b}$ , the  $HH \rightarrow b\bar{b}b\bar{b}$  branching ratio is also the largest at 33%.

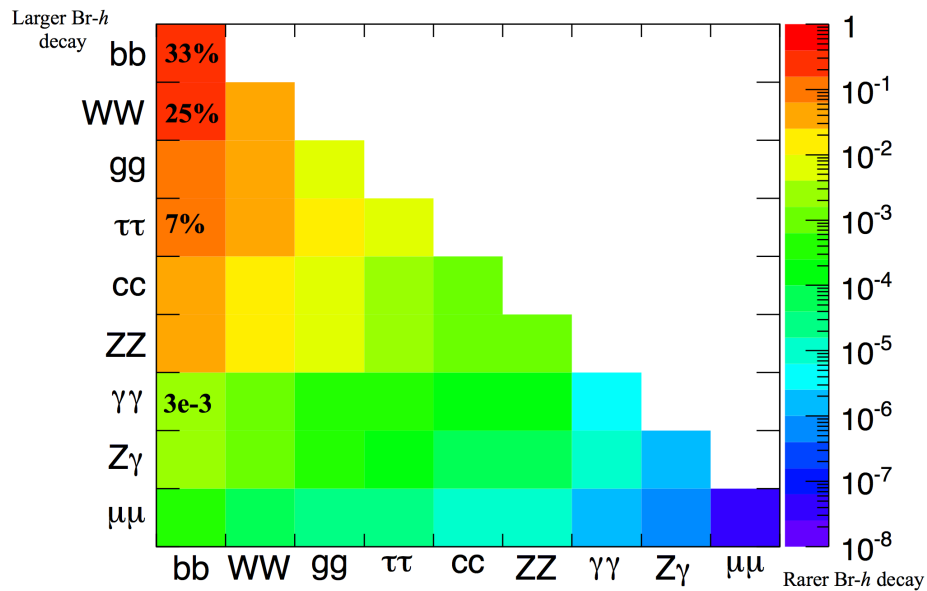


Figure 7.2: Summary of  $HH$  branching ratios [93].

At high  $m_X$ , the Higgs bosons resulting from the decay of a heavy resonance will have large  $p_T$ <sup>1</sup>. The  $\Delta R$  between the decay products of the Higgs is inversely proportional to the Higgs  $p_T$ , as shown in equation 7.1.

$$\Delta R \approx \frac{2m}{p_T} \quad (7.1)$$

Figure 7.3 shows the minimum  $\Delta R$  between truth level  $B$  decay vertices in simulation samples for Randall-Sundrum gravitons of different masses. The figure shows that as the mass of the graviton increases, the  $\Delta R$  distribution between the  $b$  quarks in the Higgs decay tends to shift to lower values. Because of this effect, it is necessary to tailor a selection to target these merged  $b$ -jets.

<sup>1</sup>In the limit that  $m_H \ell \ell m_X$ , the Higgs  $p_T$  is roughly  $m_X/2$ .

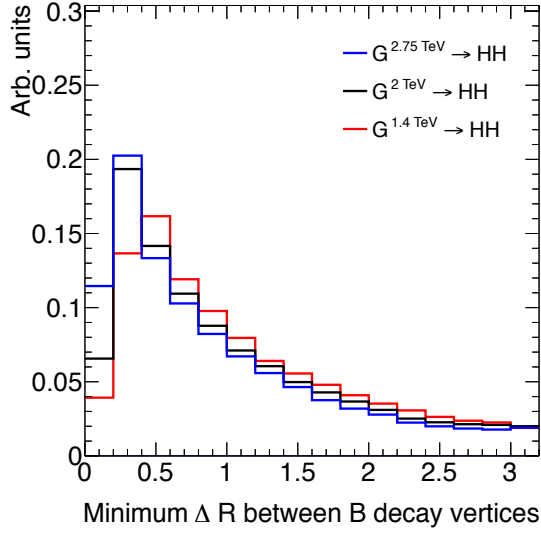


Figure 7.3: Minimum  $\Delta R$  between  $B$  decay vertices for different RSG masses in a  $G_{KK}^* \rightarrow HH \rightarrow 4b$  sample with  $c = 1$

2235    7.3 DATA AND SIMULATION SAMPLES

2236    7.3.1 SIGNAL MODELS

2237    While the resonance search is by its nature generic (as it is a simple search for a peak in the  $4b$  invariant  
 2238    mass spectrum), there are two signal models that the selection requirements have been optimized for.  
 2239    The first is Randall-Sundrum (RSG) model, where a tower of massive spin-2 Kaluza-Klein gravitons is  
 2240    predicted. The second is a heavy narrow spin-0 resonance, the so-called “heavy Higgs”. This type of res-  
 2241    onance arises, for example, in the two Higgs doublet model (2HDM). More details about the physics of  
 2242    these models and their motivation is given in chapter 1.

2243    Signal graviton ( $G_{KK}^*$ ) events are generated at leading order (LO) with **MADGRAPH5** v2.2.2 [94]. The  
 2244    PDF set used is the **NNPDF2.3** LO set [95]. For modeling parton shower and hadronization in jets, **PYTHIA**  
 2245    8.186 is used with the A14 tune [74, 96]. The free parameters in the RSG model are the graviton mass  
 2246    and the coupling constant  $c \equiv k/\bar{M}_{\text{Pl}}^2$ . Both the production cross section and width of the graviton are  
 2247    proportional to  $c^2$ . Samples are generated at both  $c = 1$  and  $c = 2$  for a variety of mass points between

---

<sup>2</sup> $k$  is the curvature constant for the warped extra dimension and  $\bar{M}_{\text{Pl}}$  is the Planck mass divided by  $8\pi$

2248 300 GeV and 3 TeV.

2249 The second signal sample is a heavy spin-0 resonance  $H$  with a fixed width of  $\Gamma_H = 1$  GeV. This  
2250 is generated with **MADGRAPH5** and uses the **CTEQ10** PDF set [77]. The parton shower and hadronization  
2251 are handled by **HERWIG ++** with the **CTEQ6L1** PDF set and the **UEEE5** event tune [78, 97, 98]. Because  
2252 the width and branching ratios depend on 2HDM parameters, each mass point generated with this fixed  
2253 width corresponds to a different point in the 2HDM parameter phase space. Mass points are generated  
2254 between 300 GeV and 1 TeV as with the RSG signal samples.

2255 **7.3.2 BACKGROUND SAMPLES**

2256 While the dominant **QCD** multijet background is estimated with a fully data-driven method, the sub-  
2257 dominant backgrounds  $t\bar{t}$  and  $Z$ +jets are modeled with some input from simulation.

2258  $t\bar{t}$  events are simulated at next-to-leading order (NLO) with the **POWHEG-BOX** version 1 generator us-  
2259 ing the **CTEQ10** PDF set [99]. The parton shower, hadronization, and underlying event are simulated with  
2260 **PYTHIA 6.428** with the **CTEQ6L1** PDF set [73]. The Perugia 2012 tune is used [100]. NNLO **QCD** cor-  
2261 rections to the cross sections are computed in **Top++ 2.0** [101]. The top quark mass is set to 172.5 GeV.  
2262 The shapes of distributions in  $t\bar{t}$  are taken from MC while the normalization is taken from data.

2263 Finally, the  $Z$ +jets background is simulated with **PYTHIA 8.186** and the **NNPDF2.3** LO PDF set. This  
2264 background is negligible compared to the others and is taken fully from MC.

2265 **7.3.3 DATA SAMPLE AND TRIGGER**

2266 This analysis is done on  $3.2 \text{ fb}^{-1}$  of data taken in 2015 at  $\sqrt{s} = 13$  TeV. The details of the machine  
2267 conditions during this time can be found in Chapter 2. Only data which was taken during stable beam con-  
2268 ditions with all detectors functioning is used. Events must pass a trigger which requires a single 360 GeV  
2269 large radius ( $R = 1.0$ ) jet to be reconstructed in the HLT. Figure 7.4 shows the trigger efficiency for vari-  
2270 ous trigger options as a function of graviton mass. Above  $m_G > 1$  TeV, the single large radius jet trigger  
2271 is 99% efficient for events passing the signal selection.

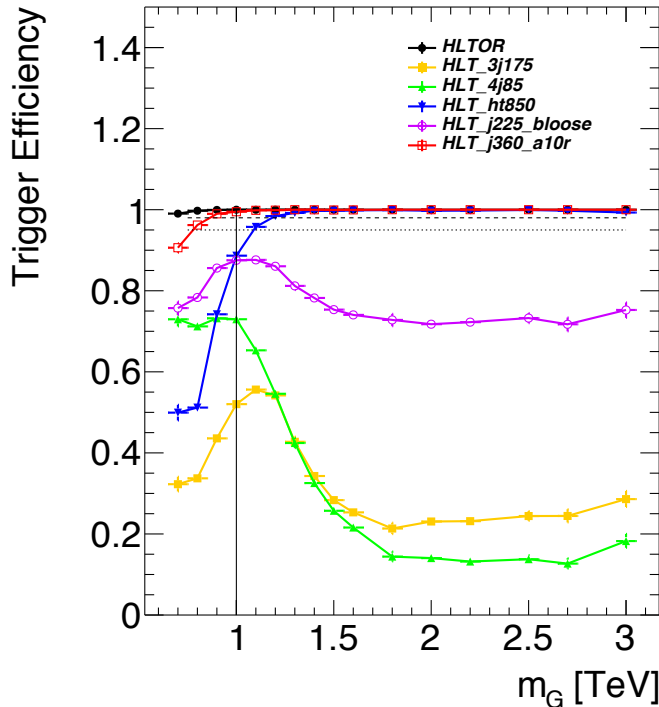


Figure 7.4: Trigger efficiency for events passing all signal region selections as a function of mass in  $G_{\text{KK}}^* \rightarrow HH \rightarrow 4b$  samples with  $c = 1$  [102]. In the trigger names, “j” refers to a jet or jets. “ht” refers to  $H_T$ , the scalar sum of transverse momenta in the event. “bloose” refers to a loose  $b$ -tagging requirement applied to the jet. “a10r” refers to anti- $k_T$  jets with  $R = 1.0$ . The numbers at the end are the thresholds on the given quantity in GeV.

## 2272 7.4 EVENT RECONSTRUCTION AND OBJECT SELECTION

2273 The boosted selection first begins by defining a unique set of objects that can be exploited to increase  
 2274 signal efficiency in the kinematic regime where the final state  $b$ -jets are very merged.

### 2275 7.4.1 LARGE RADIUS ( $R = 1.0$ ) JETS

2276 The first step towards reconstructing the final state is to define objects that can be used to measure the  
 2277 kinematics of the Higgs bosons. In the boosted selection anti- $k_T$  jets with a radius parameter of 1.0 are  
 2278 used. These jets are much larger in angular size than the typical  $R = 0.4$  jets and are intended to encompass  
 2279 both jets resulting from the Higgs decay<sup>3</sup>. The jets are built from clusters in the calorimeter calibrated with

<sup>3</sup>This is in contrast to the resolved selection, which uses two  $R = 0.4$  anti- $k_T$  jets for each Higgs

local calibration weighting [57].

Because of the large extent of these jets, great care must be taken to remove potential contributions of calorimeter clusters from pile-up. This is done using a technique called jet trimming [103]. With trimming, the constituents of the large radius jet are re-clustered with a smaller radius with the  $k_T$  algorithm. Then, these so-called subjets are removed from the larger jet if  $p_T^{\text{subjett}}/p_T^{\text{jet}} < f_{\text{cut}}$ . In this analysis, the subjet radius is  $R = 0.2$  and  $f_{\text{cut}} = 0.05$ . Trimming has been shown to improve the mass resolution of large radius jets. Figure 7.5 shows the effect of trimming on the large radius jet mass ( $M_J$ ). Because the large radius jet fully contains the higgs decay products, its invariant mass should correspond to the 125 GeV mass of the Higgs. The trimming algorithm brings the jet mass much closer to the expected Higgs mass and improves the mass resolution.

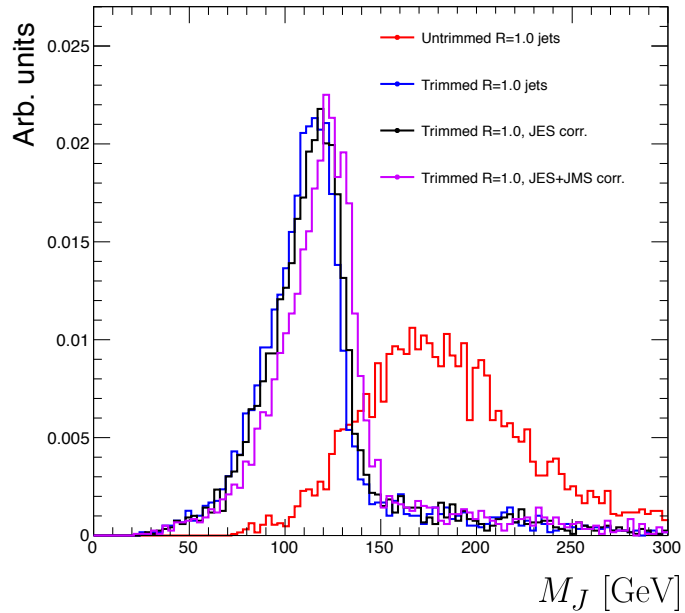


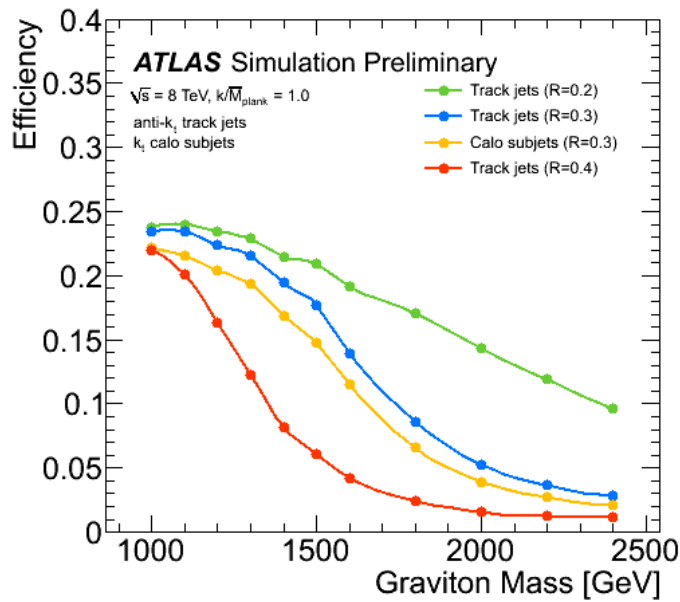
Figure 7.5: Comparison of untrimmed and trimmed jet masses for large radius jets in a RSG sample with  $m_{G_{KK}^*} = 1$  TeV. JES (JMS) refers to the standard jet energy (mass) scale calibration for ATLAS [57].

The large radius jets are required to satisfy  $250 < p_T < 1500$  GeV. They must also be within  $|\eta| < 2.0$  in order to ensure that the full jet is within the inner detector tracking volume. Finally, they are required to have  $M_J > 50$  GeV. The upper  $p_T$  cut and lower threshold on mass are applied to correspond to the kinematic range where uncertainties are available in ATLAS calibrations [104, 105].

2294 7.4.2 TRACK JETS AND  $b$ -TAGGING

2295 Because the  $b$ -jets from boosted Higgs decays are so close together (as illustrated in figure 7.3), narrow ra-  
2296 dius jets are required to fully resolve both  $b$ -jets. The minimum radius feasible for jets based on calorimeter  
2297 deposits is determined by the calorimeter granularity. However, because  $b$ -tagging relies on information  
2298 from the inner detector, it is possible to define another type of jet that can have a smaller radius and better  
2299  $b$ -tagging resolution. These jets are called “track jets” [105, 106].

2300 Track jets are formed by applying the usual anti- $k_T$  clustering algorithm to tracks that are required to be  
2301 consistent with the primary vertex. After the jet axis has been determined using these tracks, a second step  
2302 of track association is also performed to add tracks that can be useful for  $b$ -tagging [106]. In this analysis,  
2303 the tracks are clustered with a radius parameter of  $R = 0.2$ . This radius has been shown to give good  
2304 performance in boosted Higgs tagging [105, 106]. Figure 7.6 shows a comparison among different track jet  
2305 radii of the efficiency for reconstructing two  $b$ -jets from each Higgs in a RSG sample as a function of mass.  
Track jets with radius of 0.2 give the best performance, especially at high mass. In this analysis, track jets



2306 Figure 7.6: Efficiency of finding two  $b$ -jets from each Higgs in an RSG event using calorimeter jets with  $R = 0.3$  or  
2307 different track jet radii [106]

are required to have  $p_T > 10$  GeV and  $|\eta| < 2.5$ . They must also have at least two tracks.

2308    7.4.3 MUONS

2309    Muons are used in this study to correct the four-momenta of calorimeter jets by accounting for semi-  
2310    leptonic  $b$  decays. The muons used are combined ID and MS muons which must satisfy tight identification  
2311    requirements [53]. The muons must have  $p_T > 4 \text{ GeV}$  and  $|\eta| < 2.5$ . Table 7.1 summarizes the object  
2312    requirements described in this section.

	$R$	$p_T$	$ \eta $	$M$
Calorimeter jets	1.0	$250 < p_T < 1500 \text{ GeV}$	$< 2.0$	$> 50 \text{ GeV}$
Track jets	0.2	$> 10 \text{ GeV}$	$< 2.5$	-
Muons	-	$4 \text{ GeV}$	$< 2.5$	-

Table 7.1: Summary of requirements on objects used in the  $X \rightarrow HH \rightarrow b\bar{b}b\bar{b}$  search

2313    7.5 EVENT SELECTION

2314    The first requirement in the boosted selection is for  $\geq 2$  large radius jets satisfying the selections out-  
2315    lined above. The two highest momentum large-R jets in the event are referred to as “Higgs candidates”.  
2316    The leading jet is required to have  $p_T > 350 \text{ GeV}$ .

2317    Track jets satisfying the object selections are matched to Higgs candidate jets via ghost association [107].  
2318    Each Higgs candidate must have at least 2 track jets associated with it. These basic requirements are illus-  
2319    trated in figure 7.7.

2320    The QCD multijet background produces less central jets than high mass resonances, so there is an ad-  
2321    dditional requirement that the two Higgs candidates be close together in  $\eta$ . The large-R jets are required to  
2322    satisfy  $|\Delta\eta(JJ)| < 1.7$ .

2323    7.5.1 MASS REQUIREMENTS

2324    The final set of requirements ensures that the Higgs candidates are consistent with expected properties  
2325    of the 125.0 GeV Higgs. First, a variable ( $X_{hh}$ ) is defined to measure the consistency of both of the Higgs

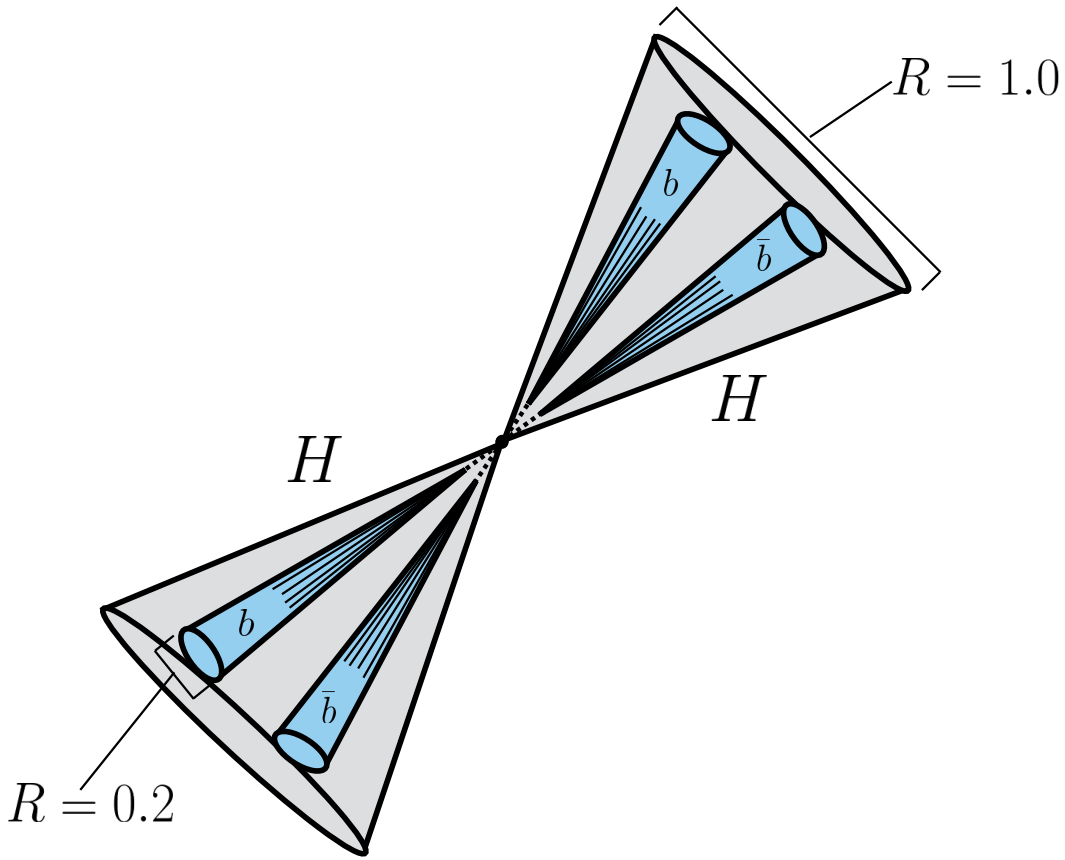


Figure 7.7: Illustration of the boosted selection requirements on Higgs candidates. Each large-radius calorimeter jet (Higgs candidate) must contain two track jets

<sup>2326</sup> candidate jets with the SM Higgs mass. This is shown in equation 7.2.

$$X_{hh} = \sqrt{\left(\frac{M_J^{\text{lead}} - 124 \text{ GeV}}{0.1 M_J^{\text{lead}}}\right)^2 + \left(\frac{M_J^{\text{sublead}} - 115 \text{ GeV}}{0.1 M_J^{\text{sublead}}}\right)^2} \quad (7.2)$$

<sup>2327</sup> The mass values in the  $X_{hh}$  formula are optimized to maximize signal efficiency. The sub-leading jet  
<sup>2328</sup> typically has a lower mass due to semi-leptonic  $b$  decays and final state radiation.  $X_{hh}$  effectively acts as  
<sup>2329</sup> a  $\chi^2$  measurement of the consistency of the two Higgs candidate masses with the signal hypothesis. The  
<sup>2330</sup> denominators of each term ( $0.1M$ ) give the uncertainty on the mass measurement for the large radius jets.  
<sup>2331</sup> Events are required to satisfy  $X_{hh} < 1.6$ .

<sup>2332</sup> Before making the requirement on  $X_{hh}$ , the masses of the Higgs candidates are corrected for semi-

leptonic  $b$  decays using muons with the criteria outlined in the previous section. Any muons within a  $\Delta R < 0.2$  of a  $b$ -tagged track jet (as described in the next section) have their four-momenta added to the four-momentum of the Higgs candidate. This correction does not affect the pre-selection requirements but does affect the  $X_{hh}$  requirement and the final invariant mass distribution used.

### 7.5.2 $b$ -TAGGING REQUIREMENTS

The last requirement applied is on the number of  $b$ -tagged track jets. There are two signal regions defined. The first requires exactly four  $b$ -tagged track jets, two in each Higgs candidate (known as the  $4b$  signal region). At high resonance masses, this requirement is inefficient, so an additional signal region requiring only three  $b$ -tagged track jets is also defined (known as the  $3b$  signal region). While this has a larger background it is also more efficient for high resonance masses. For both signal regions, the MV2c20 algorithm, where the training sample for the algorithm has 20% charm events is used. More details for this algorithm can be found in Chapter 2.

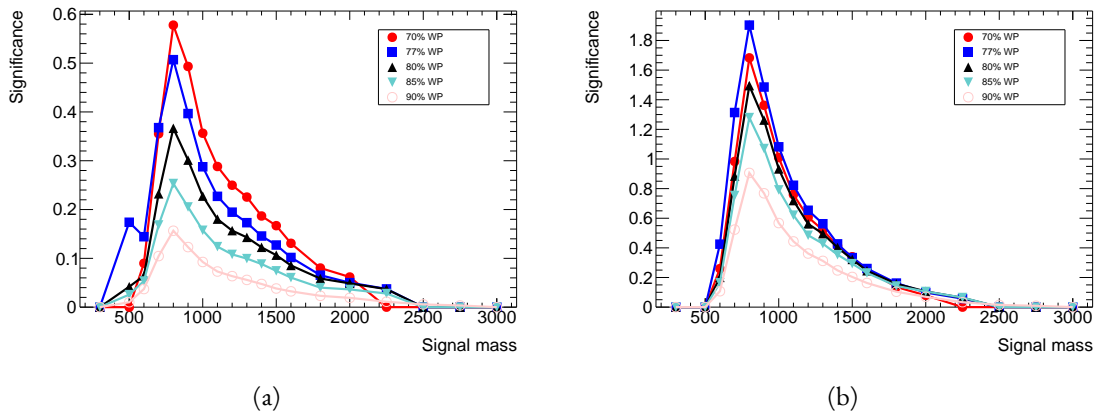


Figure 7.8: Estimated significance as a function of signal mass for RSG  $c = 1$  models in the  $3b$  (a) and  $4b$  (b) regions for different  $b$ -tagging efficiency working points

Once the algorithm is selected, an efficiency working point must also be chosen. This working point defines the efficiency with which true  $b$ -jets are tagged and also fixes the overall background rejection of the algorithm. Higher efficiency working points accept more true  $b$ -jets but also allow for more background. Five different working points (70%, 77%, 80%, 85%, 90%) are tested. With each working point, the full data driven background estimation method is run to quantify the amount of background that will be

present in the final signal region. The significance is quantified using the median discovery significance for signal and background with Poisson errors, given in equation 7.3 [108].

$$Z = \sqrt{2 \left( (s + b) \ln \left( 1 + \frac{s}{b} \right) - s \right)} \quad (7.3)$$

Here,  $s$  is the expected number of signal events and  $b$  is the expected number of background events. This formula is derived using Poisson statistics with errors on both the signal and background. It is used because it is valid in the regime where  $s$  and  $b$  are of the same order. Note that in the limit where  $s$  is much smaller than  $b$ , this equation reduces to the more well known  $s/\sqrt{b}$ . Figure 7.8 shows the estimated significance as a function of signal mass in RSG  $c = 1$  models for the  $3b$  and  $4b$  signal regions. The 77% working point gives the best performance over a wide range of masses in the  $4b$  signal region. As this is the region which contributes the most to the total discovery significance, the 77% efficiency working point is chosen for the analysis.

### 7.5.3 SELECTION EFFICIENCY

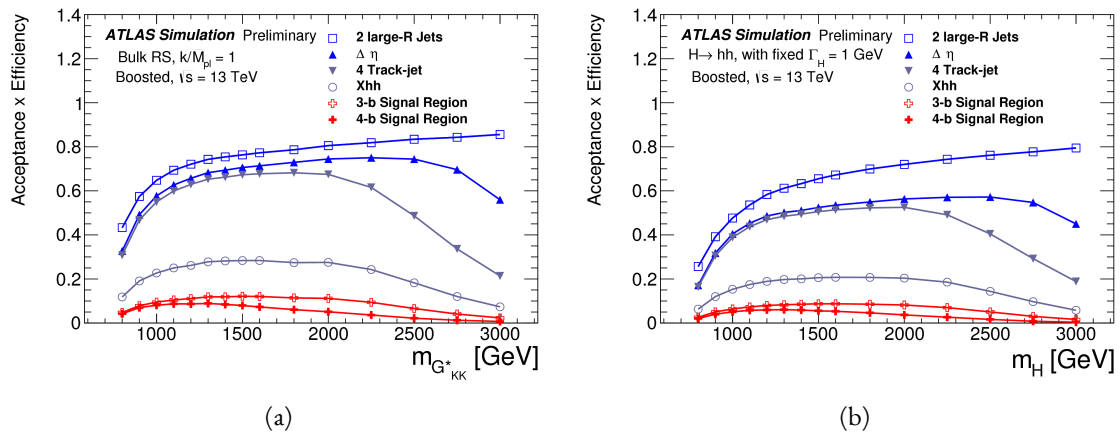


Figure 7.9: Acceptance  $\times$  efficiency as a function of mass for (a) RSG and (b) narrow heavy scalar signal models [109].

Figure 7.9 shows the product of acceptance and efficiency as a function of mass for both the RSG and narrow heavy scalar resonance signal models. After  $m_X > 1$  TeV, the efficiency of the  $4b$  requirement begins to decline. After  $m_X > 2$  TeV, the efficiency of requiring two track jets in each Higgs candidate

begins to decline as well. Both of these behaviors illustrate the difficulty of resolving the merged decay products at high mass. Figure 7.10 shows a more detailed comparison of the signal efficiency in the  $3b$  vs  $4b$  signal regions for the RSG model. The efficiencies shown here are relative to all prior selection requirements. It can be seen there that at high masses the  $3b$  signal region is more efficient for signal.

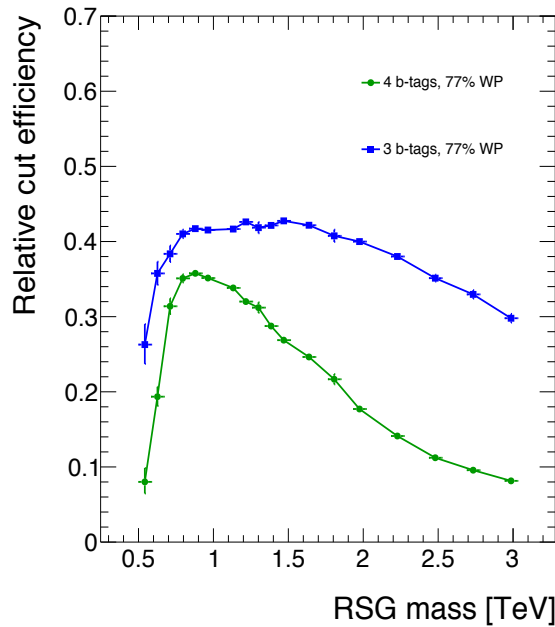


Figure 7.10: Efficiency of requiring 3 or 4  $b$ -tagged track jets vs. RSG mass. The efficiency quoted is relative to the previous selection requirements (rather than an absolute efficiency).

To investigate the degradation of  $b$ -tagging efficiency at high  $p_T$ , the individual jet tagging efficiencies can be compared as a function of signal mass. This is shown in figure 7.11. The figure shows that the leading jet tagging efficiency in both calorimeter jets degrades heavily, while the sub-lead jet tagging efficiency remains relatively constant. More details on the cause of this degradation are shown in appendix A.

The final discriminating variable used in the boosted analysis is  $M_{2J}$ , the invariant mass of the two Higgs candidates. In order to improve the mass resolution, the four-momenta of each Higgs candidate are scaled by  $m_h/M_J$ . The effect of this correction is small in the boosted analysis but is done for consistency with the resolved selection. Table 7.2 shows the effect of the selection requirements on signal and background simulations as well as data.

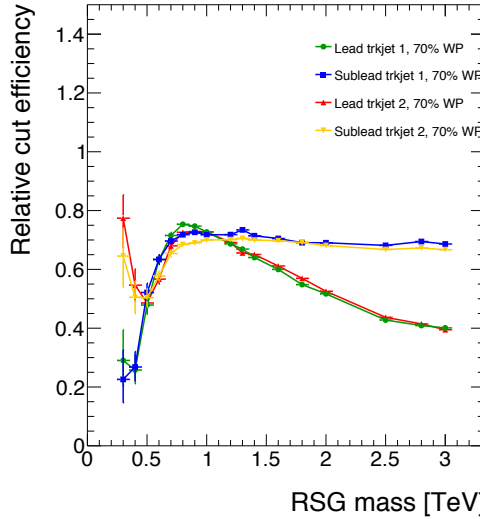


Figure 7.11: MV2c20  $b$ -tagging efficiency for each of the four track jets in the boosted  $4b$  selection as a function of RSG mass for  $c = 1$  models.

Selection	Data	$m_{G_{KK}^*} = 1\text{TeV}$	$m_{G_{KK}^*} = 2\text{TeV}$	$t\bar{t}$	$Z + \text{jets}$
$N(\text{fiducial large-R jets}) \geq 2$	2202396	23.3	0.48	32345.2	4255.7
leading large-R jet $p_T > 350\text{ GeV}$	1873741	22.9	0.48	26511.7	3649.9
Both large-R jet $m > 50\text{ GeV}$	1854625	21.2	0.47	24369.8	3575.8
Both large-R jet $p_T < 1500\text{ GeV}$	1853601	21.2	0.46	24346.5	3572.9
$ \Delta\eta(JJ)  < 1.7$	1435273	20.8	0.44	20751.0	3265.8
$\geq 2$ track-jets per large-R jet	1224727	19.8	0.40	18234.5	2692.6
$3$ $b$ -tags, $X_{hh} < 1.6$	316	3.4	0.067	46.7	2.0
$4$ $b$ -tags, $X_{hh} < 1.6$	20	2.9	0.030	1.4	0.0

Table 7.2: Effect of boosted selection on data, RSG signal models,  $t\bar{t}$ , and  $Z + \text{jets}$ . The numbers from simulation are normalized with the MC generator cross section and do not take into account the data driven estimates described in section 7.6 [110].

## 2377 7.6 DATA-DRIVEN BACKGROUND ESTIMATION

2378 The largest background to this final state is QCD multijet production, constituting 80-90% of the to-  
 2379 total background. Because of the difficulties in modeling higher order QCD processes, this background is  
 2380 estimated with a fully data-driven method. The only other non-negligible background is  $t\bar{t}$ , constituting  
 2381 the other 10-20%<sup>4</sup>. Due to the presence of  $t\bar{t}$  in the sideband region where the QCD background will be

<sup>4</sup>The  $Z + \text{jets}$  background is a sub-percent level contribution

2382 estimated, the normalization of the QCD and  $t\bar{t}$  backgrounds are simultaneously estimated.

2383 **7.6.1 MASS REGION DEFINITIONS**

2384 The first step in the data-driven background estimate is to define a sideband mass region where the  
2385 background normalization can be derived. Additionally, a control region is defined where the background  
2386 estimate can be validated. The control (CR) and sideband (SB) regions are defined using a radial distance  
2387 in the two-dimensional large-R jet mass plane,  $R_{hh}$ , which is defined in equation 7.4.

$$R_{hh} = \sqrt{(M_J^{\text{lead}} - 124 \text{ GeV})^2 + (M_J^{\text{sublead}} - 115 \text{ GeV})^2} \quad (7.4)$$

2388 Events in the sideband region are required to fail the signal region  $X_{hh} < 1.6$  requirement and have  
2389  $R_{hh} > 35.8 \text{ GeV}$ . The control region consists of those events which are not in the signal or sideband  
regions. Figure 7.12 shows the definition of the signal, control, and sideband mass regions. Table 7.3 sum-

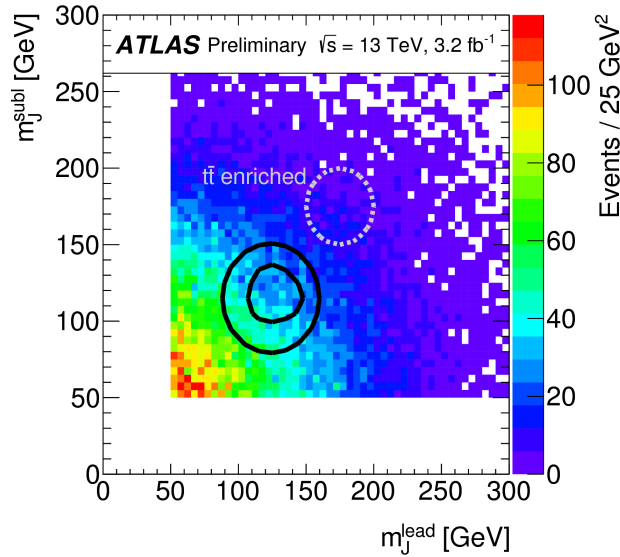


Figure 7.12:  $M_J^{\text{sublead}}$  vs.  $M_J^{\text{lead}}$  in a 2  $b$ -tag data sample. The signal region is defined by the inner black contour ( $X_{hh} < 1.6$ ) and the sideband region is defined by the outer contour ( $R_{hh} > 35.8 \text{ GeV}$ ). The region between the black contours is the control region. The mass region which is enriched in  $t\bar{t}$  background is also shown for illustration. [109]

2390

2391 summarizes the mass region selections for the three different regions used in the analysis.

Region	Requirement	Notes
Signal Region (SR)	$X_{hh} < 1.6$	-
Control Region (CR)	$R_{hh} < 35.8 \text{ GeV}$ and $X_{hh} > 1.6$	Used for validation of background estimates
Sideband Region (SB)	$R_{hh} > 35.8 \text{ GeV}$	Used to derive background normalization

Table 7.3: Mass region definitions used for background estimation

### 2392 7.6.2 BACKGROUND ESTIMATION

2393     The method for estimating the background in this analysis is similar to the ABCD method presented in  
 2394     Chapter 5. In this case, the two handles used to define different regions for the estimate are the number of  
 2395      $b$ -tagged track jets and the mass regions. A region requiring exactly two  $b$ -tagged track jets in one large-R  
 2396     jet (referred to as the 2-tag or  $2b$  region) is defined for use in the background estimate. The number of  
 2397     expected background events in the  $3b$  and  $4b$  signal regions is then given by equation 7.5.

$$N_{\text{bkg}}^{3(4)-\text{tag},\text{SR}} = \mu_{\text{Multijet}} N_{\text{Multijet}}^{2-\text{tag},\text{SR}} + \beta_{t\bar{t}} N_{t\bar{t}}^{3(4)-\text{tag},\text{SR}} + N_{Z+\text{jets}}^{3(4)-\text{tag},\text{SR}} \quad (7.5)$$

2398     In this equation,  $N_{\text{bkg}}^{3(4)-\text{tag}}$  is the expected number of background events in the  $3b$  or  $4b$  signal regions.  
 2399      $N_{\text{Multijet}}^{2-\text{tag}}$  is the number of multijet events in the 2-tag region.  $N_{t\bar{t}}^{3(4)-\text{tag}}$  is the number of  $t\bar{t}$  events pre-  
 2400     dicted in the MC for the  $3b$  or  $4b$  signal region, and the variable is similarly defined for the  $Z+\text{jets}$  back-  
 2401     ground. The  $\beta_{t\bar{t}}$  parameter is a scale factor used to correct the normalization of the  $t\bar{t}$  estimate in the signal  
 2402     region.  $\mu_{\text{Multijet}}$  is an extrapolation factor that is derived in the sideband region and used to estimate the  
 2403     ratio of 2-tag events to 3(4)-tag events in the signal region. It is defined in equation 7.6.

$$\mu_{\text{Multijet}} = \frac{N_{\text{Multijet}}^{3(4)-\text{tag},\text{SB}}}{N_{\text{Multijet}}^{2-\text{tag},\text{SB}}} = \frac{N_{\text{data}}^{3(4)-\text{tag},\text{SB}} - \beta_{t\bar{t}} N_{t\bar{t}}^{3(4)-\text{tag},\text{SB}} - N_{Z+\text{jets}}^{3(4)-\text{tag},\text{SB}}}{N_{\text{data}}^{2-\text{tag},\text{SB}} - \beta_{t\bar{t}} N_{t\bar{t}}^{2-\text{tag},\text{SB}} - N_{Z+\text{jets}}^{2-\text{tag},\text{SB}}} \quad (7.6)$$

2404     The  $t\bar{t}$  scale factor ( $\beta_{t\bar{t}}$ ) and the QCD multijet extrapolation factor ( $\mu_{\text{Multijet}}$ ) are estimated together in  
 2405     a simultaneous fit in the sideband region. Then, the number of events in the 2-tag signal region is used,  
 2406     along with the  $t\bar{t}$  estimate in the  $3b$  and  $4b$  signal regions and  $\mu_{\text{Multijet}}$ , to estimate the total number  
 2407     of background events in the two final signal regions. The shape of the final discriminant  $M_{2J}$  is also

<sup>2408</sup> taken from the 2-tag signal region where there are more statistics. This method is illustrated graphically in  
<sup>2409</sup> figure 7.13.

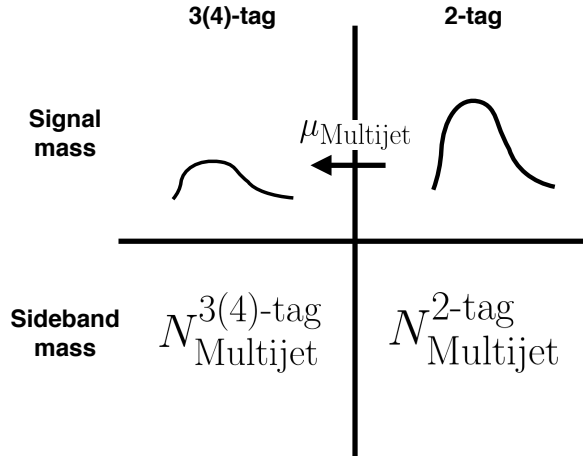


Figure 7.13: An illustration of the data-driven background estimation technique for the boosted analysis

<sup>2410</sup> In the  $3b$  region, the fit yields values of  $\mu_{\text{Multijet}} = 0.160 \pm 0.03$  and  $\beta_{t\bar{t}} = 1.02 \pm 0.09$ . In the  $4b$   
<sup>2411</sup> region, the fit gives  $\mu_{\text{Multijet}} = 0.0091 \pm 0.0007$  and  $\beta_{t\bar{t}} = 0.82 \pm 0.39$ . The uncertainties quoted are  
<sup>2412</sup> statistical only. The larger uncertainties in the  $4b$  values indicate the lower statistics available in that region.

<sup>2413</sup> Figure 7.14 shows the distributions of data and background estimates in the  $3b$  and  $4b$  sideband regions  
<sup>2414</sup> after the background fit has been done. The normalizations are constrained from the fit to match that of  
<sup>2415</sup> the data, but good modeling of the shape of the mass of the leading large-R jet is seen as well. The shapes  
<sup>2416</sup> of the kinematic distributions in the  $4b$  region are taken from the  $3b$  region due to the better MC statistics  
<sup>2417</sup> in that region.

### <sup>2418</sup> 7.6.3 BACKGROUND SHAPE FIT

<sup>2419</sup> As mentioned in the previous section, the background shape in the 3-tag and 4-tag signal regions is  
<sup>2420</sup> taken from the 2-tag signal mass region. Due to the limited statistics available, the background shapes are  
<sup>2421</sup> additionally smoothed after being extrapolated to the 3-tag and 4-tag signal regions. Only the data in the  
<sup>2422</sup> range  $900 < M_{2J} < 2000$  GeV is included in the fit due to the limited statistics available above 2 TeV.  
<sup>2423</sup> Both the  $t\bar{t}$  and QCD multijet background are independently fit with an exponential shape,  $y = e^{ax+b}$ .

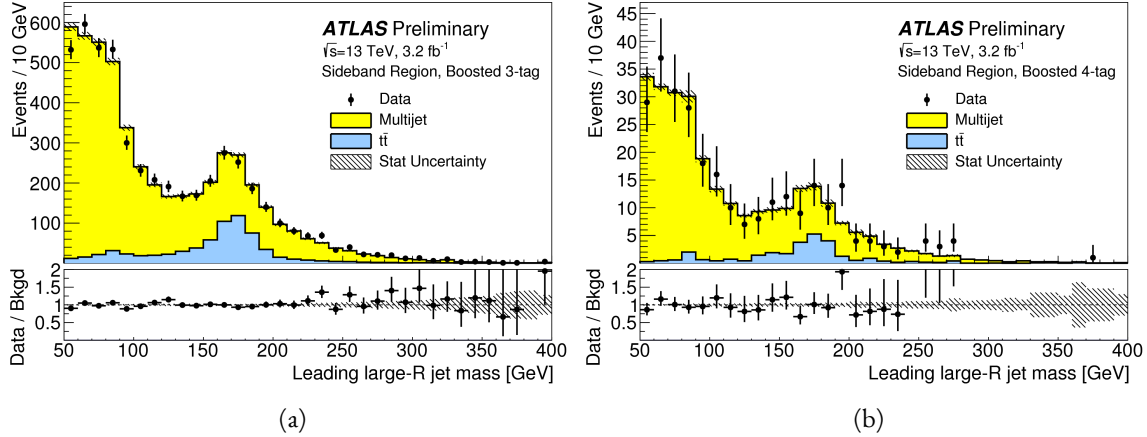


Figure 7.14: Leading large-R jet mass in the 3b (a) and 4b (b) sideband regions. The multijet and  $t\bar{t}$  backgrounds are estimated using the data-driven methods described above. Because their normalizations are derived in the sideband region, the total background normalization is constrained by default to match the normalization of the data [109].

2424 Other shapes are considered and used for the systematic uncertainties. Table 7.4 shows the fit values for  
 2425 the parameters. Because both the 3b and 4b QCD shapes come from the 2-tag region, the slopes derived  
 2426 are very similar.

	$a$	$b$
QCD (4b)	$0.00545 \pm 0.00021$	$5.44 \pm 0.24$
$t\bar{t}$ (4b)	$0.00746 \pm 0.00021$	$4.88 \pm 0.36$
QCD (3b)	$0.00545 \pm 0.00021$	$8.30 \pm 0.24$
$t\bar{t}$ (3b)	$0.00746 \pm 0.00021$	$8.58 \pm 0.36$

Table 7.4: Parameters derived for exponential fit to background  $M_{2J}$  shape in the 3b and 4b signal regions [109]

#### 2427 7.6.4 VALIDATION OF BACKGROUND ESTIMATE

2428 The background estimate can be validated by using the method to estimate the number of events in the  
 2429 control mass region rather than the signal mass region. Figure 7.15 shows the  $M_{2J}$  distribution in the 3b  
 2430 and 4b control regions, comparing data and background estimates. In both cases, both the background  
 2431 shape and normalization are consistent with the data, indicating good agreement. The ratio of data to the  
 2432 background estimates is also fit to a line in the figure to test for any shape difference. The slope of the  
 2433 line is within  $1\sigma$  (from the fit uncertainties) of flat, further indicating that the data is consistent with the  
 2434 background estimate in the control region.

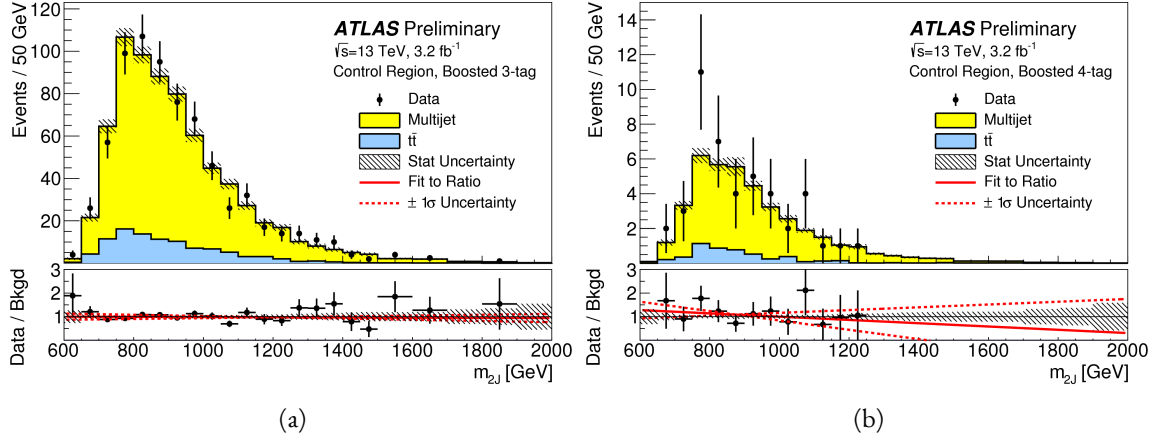


Figure 7.15: Di-jet invariant mass ( $M_{2J}$ ) in the 3b (a) and 4b (b) control regions. The multijet and  $t\bar{t}$  backgrounds are estimated using the data-driven methods described above [109].

Table 7.5 shows the yields in data and background estimates in the 3-tag and 4-tag sideband and control regions. Again, here, it can be seen that the total number of predicted background events from the data driven method is consistent with the number of data events in the region.

Sample (3-tag)	Sideband Region	Control Region
Multijet	$4328 \pm 27$	$607 \pm 10$
$t\bar{t}$	$683.5 \pm 8.1$	$99.6 \pm 3.1$
Z+jets	$31.8 \pm 3.7$	$7.7 \pm 1.8$
Total	$5043 \pm 28$	$715 \pm 11$
Data	5043	724
Sample (4-tag)	Sideband Region	Control Region
Multijet	$247.4 \pm 1.5$	$34.7 \pm 0.6$
$t\bar{t}$	$28.4 \pm 1.5$	$5.1 \pm 0.7$
Z+jets	$3.4 \pm 1.2$	$0.6 \pm 0.5$
Total	$279.2 \pm 2.5$	$40.3 \pm 1.0$
Data	279	45

Table 7.5: The number of events in data and predicted background events in the boosted 3-tag and 4-tag sideband and control regions. The uncertainties shown are statistical only. [109]

2438    7.7 SYSTEMATIC UNCERTAINTIES

2439    The systematic uncertainties in this analysis can be divided into two broad categories. The first type  
2440    is uncertainties associated with the modeling of the signal processes. The second type of uncertainty is  
2441    associated with both the shape and normalization of the background prediction.

2442    7.7.1 SIGNAL MODELING UNCERTAINTIES

2443    The signal modeling uncertainty has three main components: theoretical uncertainty on the acceptance,  
2444    experimental uncertainties on the large-R jets, and experimental uncertainties on the track jets related to  
2445     $b$ -tagging. In this analysis the experimental uncertainties are the most significant.

2446    The first uncertainty on signal modeling is the theoretical uncertainty on the acceptance. As explained  
2447    in section 5.6.1, there are four components to this uncertainty. The first is related to missing higher order  
2448    terms from the matrix element calculations which is estimated by varying the QCD renormalization and  
2449    factorization scales. The second is uncertainty due to the PDF set used. The third is a generator uncer-  
2450    tainty which is estimated by modifying the generator used to model the underlying event and hadroniza-  
2451    tion. Finally, there is an uncertainty associated with the modeling of the initial state and final state radia-  
2452    tion (ISR/FSR). The total theoretical uncertainty on the signal yield is 3%, and this is dominated by the  
2453    ISR/FSR modeling.

2454    There are uncertainties on the large-R jets in both the jet energy scale (JES) and jet energy resolution  
2455    (JER) as well as the jet mass scale (JMS) and jet mass resolution (JMR). These are evaluated using  $\sqrt{s} =$   
2456    8 TeV data from Run 1 of ATLAS and extrapolated to the Run 2 beam and detector conditions using  
2457    MC<sup>s</sup>. The details of these uncertainties can be found in reference [111].

2458    Uncertainties on the track jets are related to the  $b$ -tagging efficiency. The total uncertainty on the signal  
2459    yield due to  $b$ -tagging is evaluated by propagating variations of the  $b$ -tagging efficiency through the boosted  
2460    selection requirements. The uncertainties are calculated jet-by-jet and parameterized as a function of  $b$ -jet  
2461     $p_T$  and  $\eta$  [89]. For high  $p_T$   $b$ -jets (with  $p_T > 300$  GeV), the uncertainties are extrapolated using MC  
2462    simulation from the lower  $p_T$   $b$ -jets [112].

---

<sup>s</sup>The uncertainties are correspondingly larger due to the uncertainty of this extrapolation.

2463 Table 7.6 shows the systematic uncertainties on the signal normalization for models with  $m_{G_{\text{KK}}^*} =$   
2464 1.5 TeV and both  $c = 1$  and  $c = 2$  as well as a narrow width heavy scalar. The dominant uncertainty  
2465 comes from  $b$ -tagging and this uncertainty is larger in the 4-tag region than the 3-tag region.

Source	Background	$G_{\text{KK}}^*$		$H$
		$c = 1$	$c = 2$	
Luminosity	-	5.0	5.0	5.0
3-tag				
JER	< 1	< 1	< 1	< 1
JES	2	< 1	< 1	< 1
JMR	1	12	12	11
JMS	5	14	13	17
$b$ -tagging	1	23	22	23
Theoretical	-	3	3	3
Multijet Normalization	3	-	-	-
Statistical	2	1	1	1
Total	7	31	30	33
4-tag				
JER	< 1	< 1	< 1	< 1
JES	< 1	< 1	< 1	< 1
JMR	4	12	13	13
JMS	5	13	13	14
$b$ -tagging	2	36	36	36
Theoretical	-	3	3	3
Multijet Normalization	14	-	-	-
Statistical	3	1	1	1
Total	15	42	42	43

Table 7.6: Summary of systematic uncertainties in the total background and signal event yields (expressed in %) in the boosted 3-tag and 4-tag signal regions. Systematic uncertainties on the signal normalization are shown for models with  $m_{G_{\text{KK}}^*} = 1.5$  TeV and both  $c = 1$  and  $c = 2$  as well as a narrow width heavy scalar.

2466 7.7.2 BACKGROUND UNCERTAINTIES

2467 Uncertainties on the QCD multijet background normalization and shape are estimated using the con-  
2468 trol mass region. As shown previously, the background predictions in the control region match with the

2469 data yields within the statistical uncertainty in both the 3-tag and 4-tag control regions. As an additional  
2470 protection, the statistical uncertainty on the background prediction in the control region is assigned as a  
2471 systematic uncertainty on the normalization of the QCD background.

2472 Additional robustness tests are done by varying the definition of the control mass region and the  $b$ -  
2473 tagging requirements used to define the 2-tag sample. In all cases, the effect of the variations is found to be  
2474 within the statistical uncertainties on the background normalization in the control region.

2475 Shape uncertainties on the background are evaluated using two techniques. First, as shown in fig-  
2476 ure 7.15, the ratio between the data and background prediction is fit with a linear function. The uncer-  
2477 tainties on the slope of this fit are assigned as shape uncertainties. An additional uncertainty is assigned by  
2478 using alternate power law fit functions for the smoothing of the background shape. Table 7.7 shows the  
2479 alternate shapes used. The largest difference between the nominal fit function and the alternates, taking  
2480 into account the  $1\sigma$  uncertainty band on each fit as well, is taken as a shape uncertainty.

Functional Form
$f_1(x) = p_0(1 - x)^{p_1}x^{p_2}$
$f_2(x) = p_0(1 - x)^{p_1}e^{p_2 x^2}$
$f_3(x) = p_0(1 - x)^{p_1}x^{p_2}x$
$f_4(x) = p_0(1 - x)^{p_1}x^{p_2} \ln x$
$f_5(x) = p_0(1 - x)^{p_1}(1 + x)^{p_2}x$
$f_6(x) = p_0(1 - x)^{p_1}(1 + x)^{p_2} \ln x$
$f_7(x) = \frac{p_0}{x}(1 - x)^{p_1-p_2} \ln x$
$f_8(x) = \frac{p_0}{x^2}(1 - x)^{p_1-p_2} \ln x$

Table 7.7: Alternate fit functions used to model the  $M_{2J}$  distribution in the QCD multijet background. In the equations,  $x = M_{2J}/\sqrt{s}$ .

2481 The uncertainties on the  $t\bar{t}$  background are obtained by propagating the various experimental variations  
2482 (JES, JER, JMS, JMR,  $b$ -tagging) through the analysis selection requirements. Table 7.6 summarizes the  
2483 background uncertainties in the 3-tag and 4-tag regions.

2484    7.8 RESULTS

2485    Table 7.8 shows the observed yields in the 3-tag and 4-tag signal regions for the boosted analysis com-  
 2486    pared to the predicted number of background events. In the 3-tag region, 316 events are observed with  
 2487    a predicted background of  $285 \pm 19$ . In the 4-tag region, 20 events are observed with a predicted back-  
 2488    ground of  $14.6 \pm 2.4$ . Figure 7.16 shows the  $M_{2J}$  distribution in the 3-tag and 4-tag regions. There are  
 2489    some small excesses in the data, in particular in the 3-tag region around  $M_{2J} \approx 900$  GeV and in the region  
 2490    of  $1.6 < M_{2J} < 2.0$  TeV. The significance of these excesses will be evaluated in the next chapter in the  
 2491    statistical combination with the resolved results.

Sample	Signal Region (3-tag)	Signal Region (4-tag)
Multijet	$235 \pm 14$	$13.5 \pm 2.4$
$t\bar{t}$	$48 \pm 22$	$1.2 \pm 1.0$
$Z + \text{jets}$	$2.0 \pm 2.2$	-
Total	$285 \pm 19$	$14.6 \pm 2.4$
Data	316	20
$G_{\text{KK}}^*$ (1000 GeV), $c = 1$	$3.4 \pm 0.9$	$2.9 \pm 1.1$

Table 7.8: Observed yields in the 3-tag and 4-tag signal regions for the boosted analysis compared to the predicted number of background events Errors correspond to the total uncertainties in the predicted event yields. The yields for a graviton with  $m_{G_{\text{KK}}^*} = 1$  TeV and  $c = 1$  are also shown. [109]

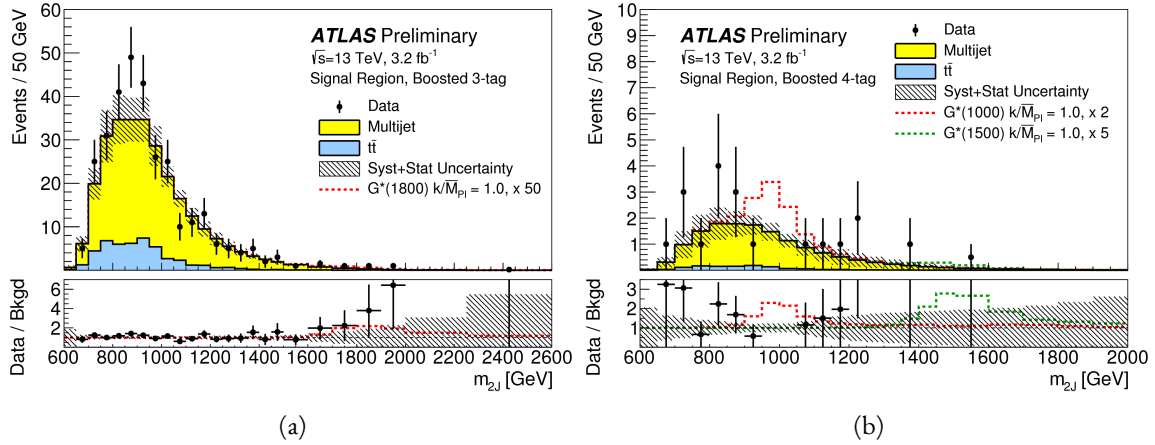


Figure 7.16: Di-jet invariant mass ( $M_{2J}$ ) in the  $3b$  (a) and  $4b$  (b) signal regions. The multijet and  $t\bar{t}$  backgrounds are estimated using the data-driven methods described above. In the  $3b$  region, a graviton signal with  $m_{G_{KK}^*} = 1.8 \text{ TeV}$  and  $c = 1$  is overlaid, with the cross section multiplied by a factor of 50 so that the signal is visible. In the  $4b$  region, signals with  $m_{G_{KK}^*} = 1.0 \text{ TeV}$  and  $m_{G_{KK}^*} = 1.5 \text{ TeV}$  are overlaid, both with  $c = 1$  and the yields multiplied by factors of 2 and 5 respectively [109].

*There is no real ending. It's just the place where you stop  
the story.*

Frank Herbert

# 8

2492

2493

## Combined limits from boosted and resolved searches

2494

2495

### 8.1 INTRODUCTION

2496 In order to cover the full mass range of possible resonances decaying to di-Higgs final states, two distinct  
2497 tailored selections were produced. The resolved selection is more sensitive in the mass range of  $400 < m_X < 1100$  GeV while the boosted selection is more sensitive to masses in the range  $1100 < m_X <$   
2498 3000 GeV. Chapter 7 presents the details of the boosted selection and results. In setting limits on spin-2  
2499 Randall-Sundrum graviton (RSG) and narrow width heavy scalar ( $H$ ) models, the results of the boosted  
2500 selection are combined with the results of the resolved selection to cover the full mass range.  
2501

2502 This chapter presents limits on signal models resulting from the  $X \rightarrow HH \rightarrow b\bar{b}b\bar{b}$  search in both  
2503 the resolved and boosted selections. It first presents a brief overview of the resolved results that go into

2504 the limit setting. Then, an overview of the statistical methods used for the search and limit setting is given.  
 2505 Finally, limits on the RSG and heavy scalar models are presented.

2506 **8.2 RESOLVED RESULTS**

2507 The details of the resolved selection will not be presented here and can be found in reference [109]. In  
 2508 basic terms, the selection searches for four  $R = 0.4$  b-tagged calorimeter jets (where each pair of jets is  
 2509 one Higgs candidate). This is distinct from the boosted methodology which searches for merged decay  
 2510 products. The backgrounds to the resolved selection are the same as those presented in Chapter 7 for the  
 2511 boosted analysis.

2512 Table 8.1 shows the results for data yields and expected background in the resolved signal region. Fig-  
 2513 ure 8.1 shows the  $M_{2J}$  distribution in the resolved signal region. The total number of events is consistent  
 2514 with the prediction and no significant excess is seen. One event in the boosted 4-tag signal is shared with  
 2515 the resolved signal region and has a mass of 852 GeV.

Sample	Signal Region Yield
Multijet	$43.3 \pm 2.3$
$t\bar{t}$	$4.3 \pm 3.0$
$Z + \text{jets}$	-
Total	$47.6 \pm 3.8$
Data	46
SM $hh$	$0.25 \pm 0.07$
$G_{\text{KK}}^*(800 \text{ GeV}), c = 1$	$5.7 \pm 1.5$

Table 8.1: Observed yields in the resolve selection 4-tag signal region compared to the predicted number of background events Errors correspond to the total uncertainties in the predicted event yields. The yields for a graviton with  $m_{G_{\text{KK}}^*} = 800 \text{ GeV}$  and  $c = 1$  are also shown. [109]

2516 **8.3 SEARCH TECHNIQUE AND RESULTS**

2517 The statistical technique used for the search in this analysis is the same as that used in the  $H \rightarrow WW^*$   
 2518 analysis presented in section 3.6.2. The test statistic  $q_0$  is used to define the  $p$ -values which measure the

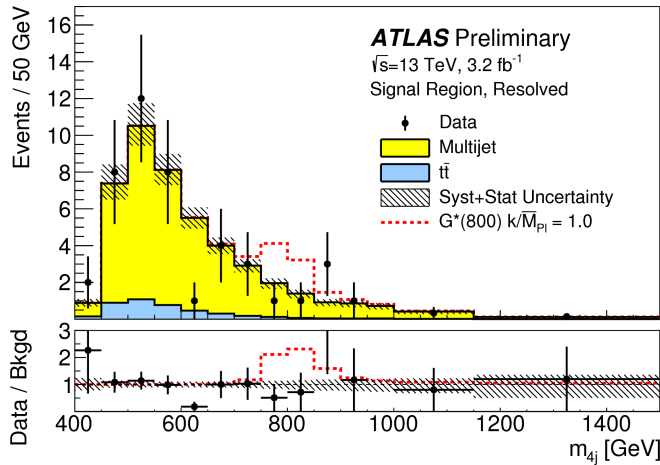


Figure 8.1: Di-jet invariant mass ( $M_{2J}$ ) in the resolved signal region. A graviton signal with  $m_{G_{KK}^*} = 800$  GeV and  $c = 1$  is overlaid. [109].

compatibility of the data with the background-only hypothesis corresponding to a signal strength  $\mu = 0$ .

Local  $p_0$  values are computed to quantify the probability that the background could produce a fluctuation greater than or equal to the one observed in the data. In the resolved analysis, no significant excesses are observed. The largest discrepancy with respect to the background only hypothesis occurs near a resonance mass of 900 GeV and is found to be less than  $2\sigma$  in significance.

In the boosted selection, the largest local excess is a broad excess in the  $3b$  signal region that begins near  $M_{2J} \approx 1.7$  GeV. Assuming a  $G_{KK}^*$  with this mass and  $c = 1.0$ , the local significance of this excess is  $2.0\sigma$ .

#### 8.4 LIMIT SETTING

In the absence of any significant excess observed in the data, limits on different signal models can be set. This section describes the limit setting procedure and presents combined results of the resolved and boosted analyses.

##### 8.4.1 LIMIT SETTING PROCEDURE

The procedure used for setting exclusion limits in this analysis is the  $CL_s$  method [113]. The first step in setting the limits is to define a test statistic which will be used. For limit setting, the test statistic is shown

2534 in equation 8.1.

$$\tilde{q}_\mu = \begin{cases} -2 \ln \frac{L(\mu, \hat{\theta}(\mu))}{L(0, \hat{\theta}(0))} & \hat{\mu} < 0 \\ -2 \ln \frac{L(\mu, \hat{\theta}(\mu))}{L(\hat{\mu}, \hat{\theta})} & 0 \leq \hat{\mu} < \mu \\ 0 & \hat{\mu} > \mu \end{cases} \quad (8.1)$$

2535 In the above equation,  $\mu$  is the value of the signal strength under test,  $\hat{\mu}$  is the best fit  $\mu$ ,  $\hat{\theta}$  is the  
2536 best fit value of the nuisance parameters,  $\hat{\theta}$  is the best fit value of the nuisance parameters under the fixed  
2537  $\mu$  value, and  $L$  is the Poisson likelihood of the data (as described in section 3.6.2).

2538 The test statistic  $\tilde{q}_\mu$  is constructed to protect against two interesting corner cases when setting the upper  
2539 limit on the cross section. First, it protects against negative signal strengths  $\mu$  which are unphysical. Second,  
2540 it does not count excesses in the data larger than those expected by a signal strength  $\mu$  as evidence against  
2541 the  $\mu$  hypothesis.

2542 The  $CL_s$  statistic is constructed by taking a ratio of two probabilities.  $CL_{s+b}$  is the probability that the  
2543 signal+background hypothesis would produce a value of the test statistic that is less than or equal to the  
2544 observed value<sup>1</sup>.  $CL_b$  is the probability that the background only hypothesis will produce a value  
2545 of the test statistics less than or equal to the observed. The  $CL_s$  statistic is then the ratio  $CL_{s+b}/CL_b$ . A  
2546 95% upper limit on the cross section is set at the value of  $\mu$  that makes the  $CL_s$  statistic less than 5%.

2547 In practice, the limits are computed numerically within an asymptotic approximation for the distribu-  
2548 tion of the test statistic  $\tilde{q}_\mu$ . The details of this approximation can be found in reference [64].

2549 The resolved and boosted analyses are combined using a very simple procedure rather than a full statis-  
2550 tical combination. For each mass point tested, the limit which gives the most stringent constraint is used.  
2551 This means that for mass points below 1.1 TeV the resolved signal region is used, while at and above this  
2552 point the combination of the orthogonal 3b and 4b boosted signal regions is used.

#### 2553 8.4.2 LIMIT SETTING RESULTS

2554 Figure 8.2 shows the combined 95% upper bounds as a function of mass for three different models:  
2555  $G_{KK}^*$  with  $c = 1$ ,  $G_{KK}^*$  with  $c = 2$ , and a narrow heavy scalar  $H$ .

---

<sup>1</sup>Lower values of  $\tilde{q}_\mu$  mean better compatibility

2556        The cross section of  $\sigma(pp \rightarrow G_{\text{KK}}^* \rightarrow hh \rightarrow b\bar{b}b\bar{b})$  with  $c = 1$  is constrained to be less than 70 fb  
2557        for masses in the range  $600 < m_{G_{\text{KK}}^*} < 3000$  GeV. For the RSG model with  $c = 2$ , cross sections limits  
2558        between 40 fb and 200 fb are set for the mass range of  $500 < m_{G_{\text{KK}}^*} < 3000$  GeV. Masses in the range  
2559        of  $475 < m_{G_{\text{KK}}^*} < 785$  GeV are excluded with  $c = 1$  (with an exclusion of the range 465 to 745 GeV  
2560        expected). Masses less than 980 GeV are excluded with  $c = 2$  (with an exclusion for masses less than  
2561        1 TeV expected).

2562        In the heavy Higgs model, the cross section upper limits for  $\sigma(pp \rightarrow H \rightarrow hh \rightarrow b\bar{b}b\bar{b})$  ranges from  
2563        30 to 300 fb in the mass range of  $500 < m_H < 3000$  GeV. The resolved analysis can also set an upper  
2564        limit on the Standard Model di-Higgs production cross section discussed in chapter 3. The upper limit on  
2565         $\sigma(pp \rightarrow hh \rightarrow b\bar{b}b\bar{b})$  in the Standard Model is constrained to be less than 1.22 pb.

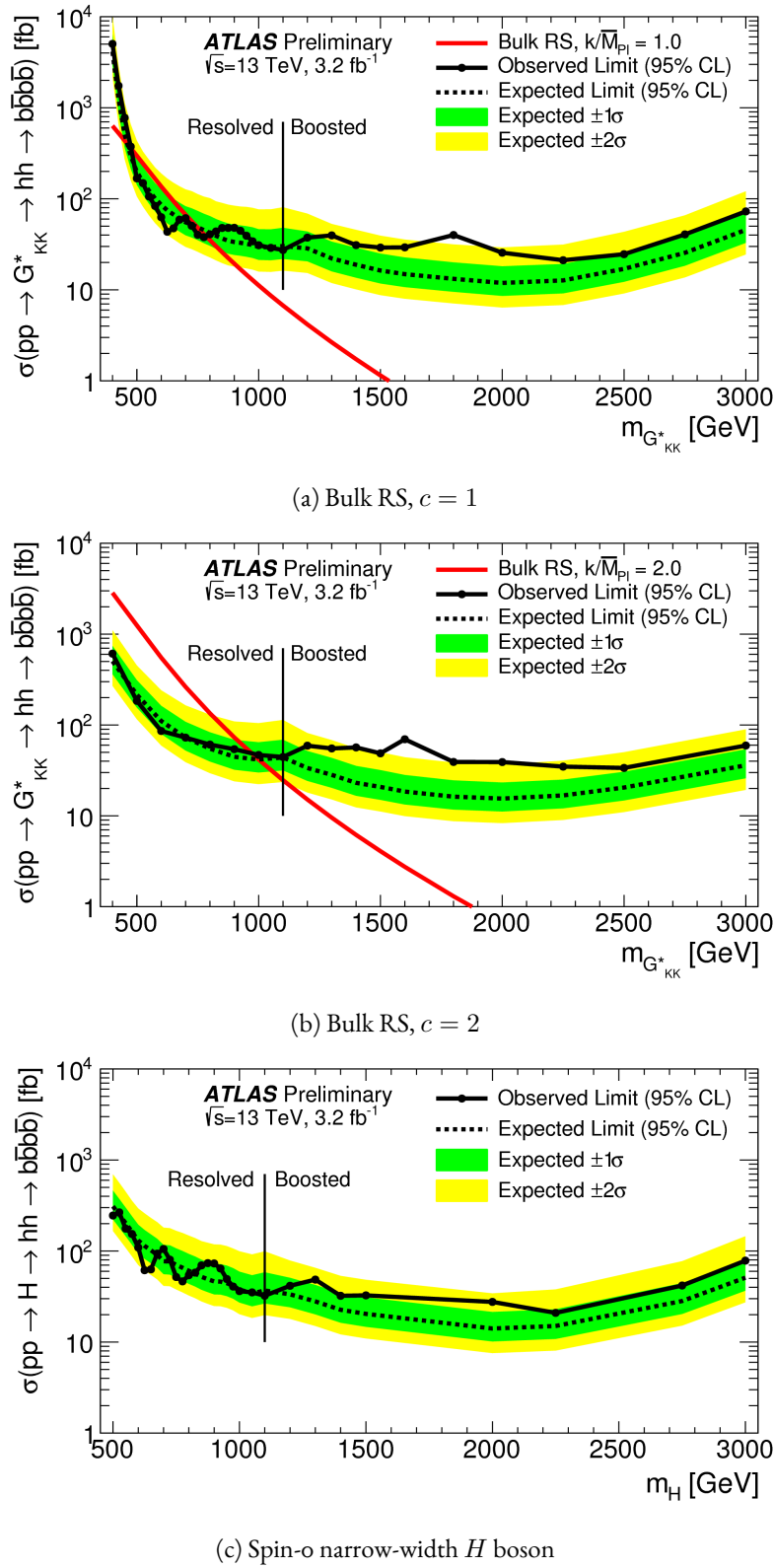


Figure 8.2: Expected and observed upper limit as a function of mass for  $G^*_{KK}$  in the RSG model with (a)  $c = 1$  and (b)  $c = 2$ , as well as (c)  $H$  with fixed  $\Gamma_H = 1$  GeV, at the 95% confidence level in the  $CL_s$  method. [109]

2566

## Part IV

2567

## Looking ahead

# 9

2568

2569

## Conclusion

2570 After being sought for many years at different collider experiments, the Higgs boson was discovered by  
2571 the ATLAS and CMS experiments in 2012, confirming the leading theory for the source of electroweak  
2572 symmetry breaking and filling in the last missing piece of the Standard Model. After its discovery, mea-  
2573 surements of the particle's detailed properties and searches for new particles decaying to Higgs final states  
2574 were both extremely important in constraining physics beyond the Standard Model. This dissertation  
2575 presented this evolution through two results: the observation and measurement of the Higgs boson in the  
2576  $H \rightarrow WW^* \rightarrow \ell\nu\ell\nu$  channel at  $\sqrt{s} = 7$  TeV and  $\sqrt{s} = 8$  TeV and a search for Higgs pair production  
2577 in the  $HH \rightarrow b\bar{b}b\bar{b}$  channel at  $\sqrt{s} = 13$  TeV with the ATLAS detector in  $pp$  collisions at the Large  
2578 Hadron Collider.

2579 In the  $H \rightarrow WW^* \rightarrow \ell\nu\ell\nu$ , results from both the discovery of the Higgs boson and the full ATLAS  
2580 Run 1 dataset were presented. The Higgs boson was discovered with a  $6.1\sigma$  significance in a combina-  
2581 tion of the  $H \rightarrow \gamma\gamma$ ,  $H \rightarrow ZZ4\ell$ ,  $H \rightarrow WW^* \rightarrow \ell\nu\ell\nu$  with  $4.2\text{ fb}^{-1}$  at  $\sqrt{s} = 7$  TeV and

2582     $5.2 \text{ fb}^{-1}$  at  $\sqrt{s} = 8 \text{ TeV}$ . With the full  $20.3 \text{ fb}^{-1}$  at  $\sqrt{s} = 8 \text{ TeV}$  and  $4.2 \text{ fb}^{-1}$  at  $\sqrt{s} = 7 \text{ TeV}$ ,  
2583    ATLAS achieved discovery level significance in the  $H \rightarrow WW^*$  channel alone and obtained the first ob-  
2584    servation of vector boson fusion production in that channel. The combined signal strength is measured  
2585    to be  $\mu = 1.09^{+0.23}_{-0.21}$ . The total observed significance of the  $H \rightarrow WW^*$  process is observed to be  $6.1\sigma$   
2586    (with  $5.8\sigma$  expected). Advanced methods for background reduction and estimation, particularly in same-  
2587    flavor lepton final states, are shown. The VBF signal strength is measured to be  $\mu_{\text{VBF}} = 1.27^{+0.53}_{-0.45}$  with  
2588    an observed significance of  $3.2\sigma$  (with  $2.7\sigma$  expected).

2589    These results required many novel innovations. The increase of pileup interactions in the higher in-  
2590    stantaneous luminosity LHC conditions of 2012 led to a degradation of missing transverse momentum  
2591    resolution. As a result, the prominent  $Z/\gamma^* + \text{jets}$  background of the same flavor  $H \rightarrow WW^* \rightarrow \ell\nu\ell\nu$   
2592    final states increased greatly. New variables, including a track-based missing transverse momentum and a  
2593    measurement of the balance between the dilepton system and recoiling jets, allowed for significant reduc-  
2594    tion of this background. In the VBF channel, selections were optimized to exploit the unique VBF final  
2595    state topology. Incorporating these variables into a boosted decision tree technique allowed the analysis  
2596    to exceed the  $3\sigma$  observation threshold.

2597    After the end of Run 1, the results of Higgs measurements from ATLAS were combined with those  
2598    from CMS to produce the most precise measurements of the Higgs boson so far [114]. Figure 9.1 shows the  
2599    combination of ATLAS and CMS data for the Higgs signal strength in and coupling measurements. In the  
2600    signal strength measurements of gluon fusion and vector boson fusion, the  $H \rightarrow WW^*$  channel provides  
2601    the tightest constraints. Additionally, the Higgs coupling to  $W$  bosons is the most precisely measured with  
2602    a relative uncertainty of 10%.

2603    With the discovery of the Higgs firmly established and its properties measured, a natural next step was  
2604    to search for new physics with Higgs final states. At  $\sqrt{s} = 13 \text{ TeV}$ , a search for Higgs pair production  
2605    in the  $b\bar{b}b\bar{b}$  final state with  $3.2 \text{ fb}^{-1}$  was conducted. A signal region optimized for the boosted final states  
2606    arising from high mass resonances was constructed. This signal region utilized large-radius calorimeter jets  
2607    and  $b$ -tagging with small radius track jets to maximize the signal acceptance. No significant excesses were  
2608    observed, and upper limits on cross sections are placed for spin-2 Randall Sundrum gravitons (RSG) and

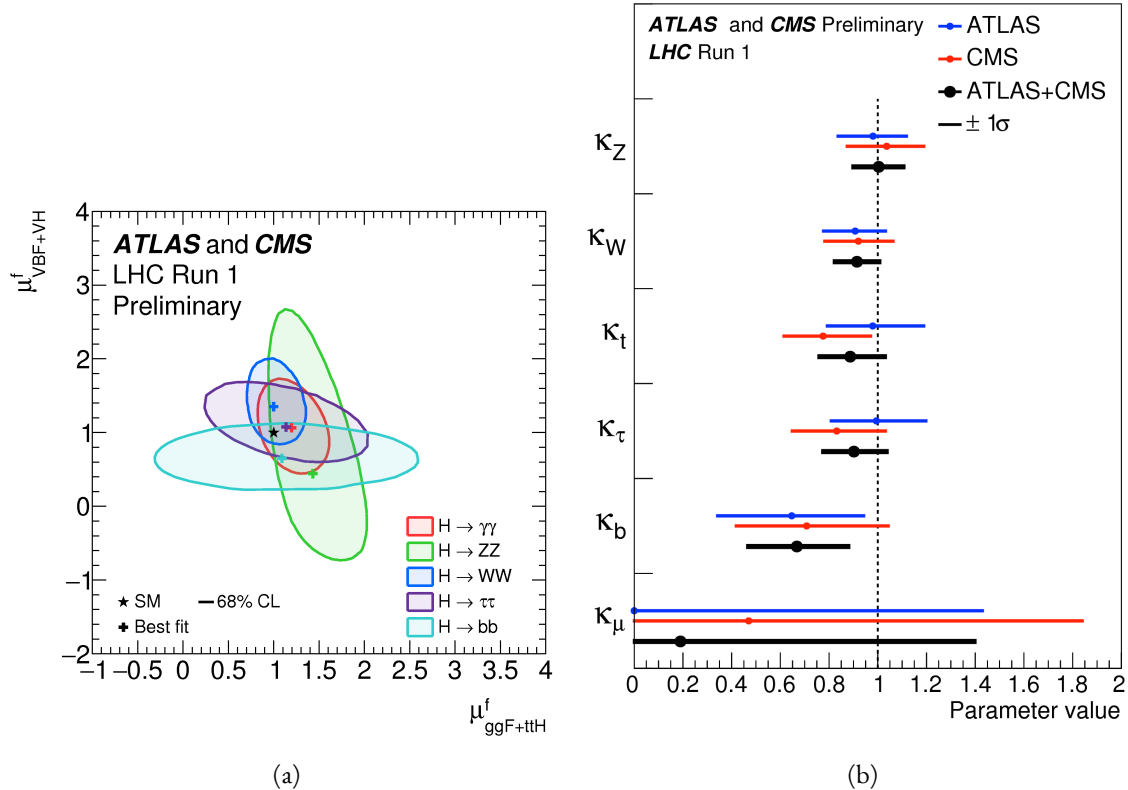


Figure 9.1: Combined ATLAS and CMS measurements in Run 1 for (a) Higgs signal strength in gluon fusion and VBF and (b) Higgs couplings normalized to their SM predictions

narrow spin-0 resonances. The increase in center of mass energy in Run 2 allowed this analysis to extend upper limits up to 3 TeV, while previous results from ATLAS in Run 1 only quotes limits up to 2 TeV. The cross section of  $\sigma(pp \rightarrow G_{KK}^* \rightarrow hh \rightarrow b\bar{b}b\bar{b})$  with  $k/\bar{M}_{\text{Pl}} = 1$  is constrained to be less than 70 fb for masses in the range  $600 < m_{G_{KK}^*} < 3000$  GeV. For the RSG model with  $k/\bar{M}_{\text{Pl}} = 2$ , cross sections limits between 40 fb and 200 fb are set for the mass range of  $500 < m_{G_{KK}^*} < 3000$  GeV. The cross section upper limits for  $\sigma(pp \rightarrow H \rightarrow hh \rightarrow b\bar{b}b\bar{b})$  ranges from 30 to 300 fb in the mass range of  $500 < m_H < 3000$  GeV.

While there has been a rigorous program of measurements and searches involving the Higgs, there is still much room for improvement at the High Luminosity LHC (HL-LHC) and beyond. The measured signal strength for VBF production in  $H \rightarrow WW^*$  still has a relative error at the level of 40%, largely dominated by statistical uncertainty. Projections for the HL-LHC show that the uncertainty on the VBF signal strength can be reduced to approximately 15% with  $3000 \text{ fb}^{-1}$  [n5, n6]. This uncertainty also

2621 assumes that theoretical uncertainties on the signal, which would be the largest contribution in this dataset,  
 2622 remain as they are now. Improvements in the theoretical understanding of the Higgs signal would also  
 2623 reduce the signal strength uncertainty dramatically. Such precision measurements allow for measurements  
 2624 of the Higgs coupling to vector bosons precise to the few percent level, therefore giving much power to  
 2625 constrain or discover new physics.

2626 The prospects for detection of beyond the Standard Model resonant di-Higgs production at the HL-  
 2627 LHC are also quite promising. Figure 9.2 shows projections for the discovery significance of RSG signals at  
 2628 the HL-LHC in the  $X \rightarrow HH \rightarrow b\bar{b}b\bar{b}$  search [ii6]. In all detector budget scenarios, a 1.5 TeV resonance  
 is above or near  $5\sigma$  significance, while a 2 TeV resonance is between  $4-5\sigma$  except for the lowest budget.

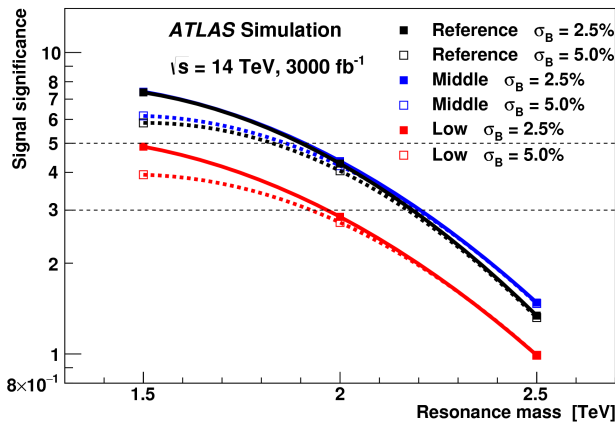


Figure 9.2: Discovery significance for RSG models at the HL-LHC in three different budget scenarios [ii6].  
 Systematic uncertainties on the background prediction ( $\sigma_B$ ) of 2.5% and 5.0% are both tested.

2629  
 2630 The Higgs will continue to be an incredibly powerful tool in the understanding of nature at the HL-  
 2631 LHC and beyond. Through both precision measurements and searches, the nature of electroweak symme-  
 2632 try breaking will be better understood and the potential for the discovery of physics beyond the Standard  
 2633 Model has never been greater.

# A

2634

2635

## *b*-tagging performance at high $p_T$

2636 One of the limiting factors of the signal acceptance in the  $X \rightarrow HH \rightarrow b\bar{b}b\bar{b}$  search at high resonance  
2637 masses is the degradation of the *b*-tagging efficiency for high  $p_T$  jets. This appendix presents a study of the  
2638 underlying causes of this degradation.

### 2639 A.I CHANGES IN MV<sub>2</sub> SCORE AT HIGH $p_T$

2640 The degradation of *b*-tagging at high  $p_T$  was studied in particular in the context of RSG models at high  
2641 mass. Figure A.I shows the  $p_T$  of the leading track jet inside of the leading calorimeter jet in RSG events.  
2642 At high  $m_{G_{KK}^*}$ , the  $p_T$  spectrum of track jets is much harder than at lower masses due to the increased  
2643 Higgs  $p_T$ .

2644 Figure A.2 shows the MV<sub>2c2o</sub> algorithm score for the leading and subleading track jets inside of the  
2645 leading calorimeter jet. In both cases, it can be seen that at higher RSG masses the MV<sub>2</sub> score shifts towards  
2646 more background like (negative) values. Additionally, this effect is more pronounced in the leading track

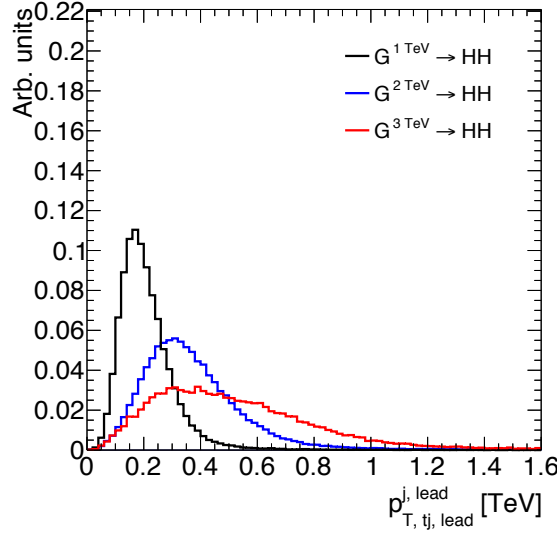


Figure A.1:  $p_T$  of the leading track jet in the leading calorimeter jet for different signal masses in RSG  $c = 1$  models

jet than the subleading.

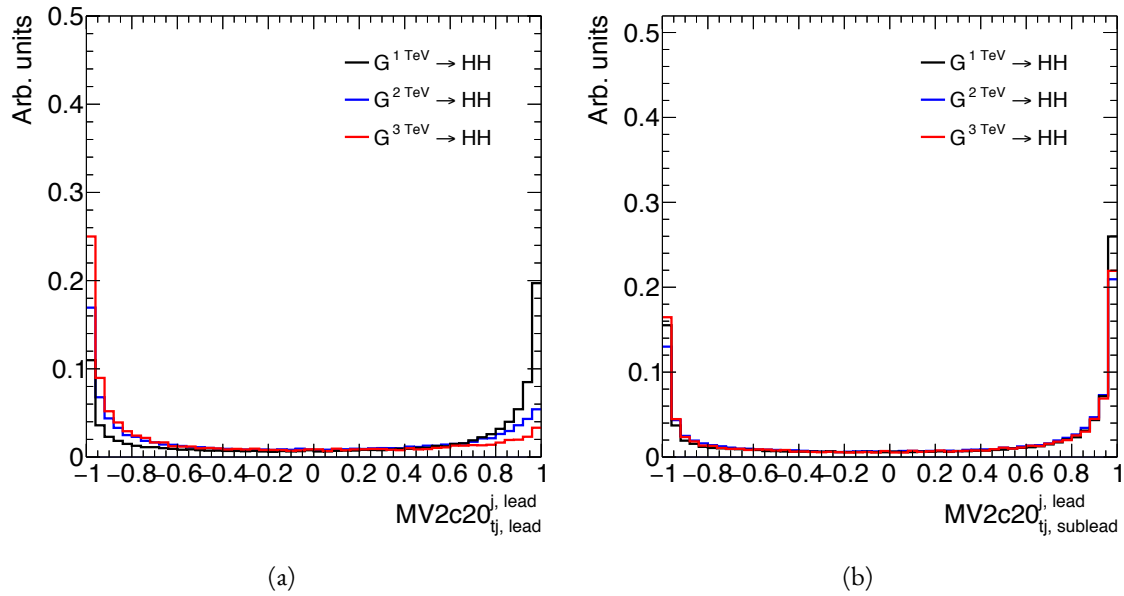


Figure A.2: MV2c20 score for the leading track jet (a) and subleading track jet (b) of the leading calorimeter jet for different signal masses in RSG  $c = 1$  models

To understand what is causing this change in the MV2c20 score, the same comparisons can be made for the input variables of MV2c20. The focus in these comparisons will be on the leading track jet as this is the one seen to have the largest difference in MV2 score. Figure A.3 shows the log likelihood ratio  $\log(p_b/p_u)$

from the IP<sub>3</sub>D (three dimensional impact parameter) algorithm. At higher masses, the IP<sub>3</sub>D likelihood ratio distribution does become more background-like.

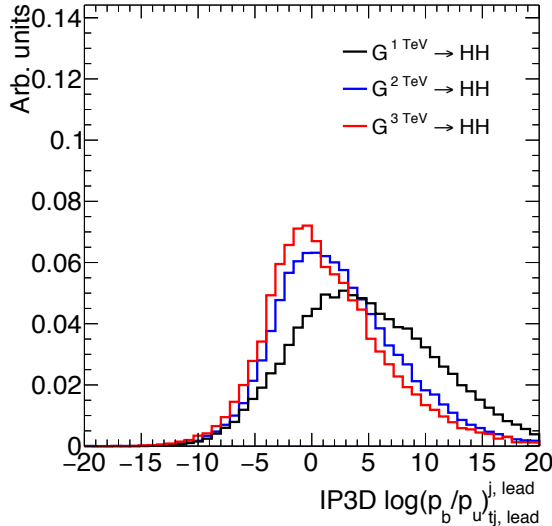


Figure A.3: IP<sub>3</sub>D log-likelihood ratio ( $\log(p_b/p_u)$ ) of the leading track jet in the leading calorimeter jet for different signal masses in RSG  $c = 1$  models

Figure A.4 shows the mass and number of tracks at the secondary vertex computed by the SV1 algorithm. When there is no secondary vertex found, the algorithm assigns a default negative value for these quantities. Both of these distributions show that there is a significantly larger fraction of jets where no secondary vertex is found in the high mass samples compared to the  $m_{G_{KK}^*} = 1$  TeV sample. The SV1 algorithm's inability to find a secondary vertex could be an important factor in the overall MV<sub>2</sub> score shift, as this eliminates eight of the input variables that would normally contribute information to the algorithm.

Figure A.5 shows the same quantities for the JetFitter algorithm. In this case, there is also a change in the fraction of jets which have their secondary vertices successfully reconstructed, but this change is not as drastic as that seen in SV1. There is also an increase in the number of jets which have high values of mass.

## A.2 EFFECT OF MULTIPLE $b$ -QUARKS INSIDE ONE JET

One hypothesis for why the efficiency of  $b$ -tagging the leading track jet degrades is that at high masses, the  $b$  quarks get close enough together that both of them are inside of the leading track jet. Because MV<sub>2</sub>

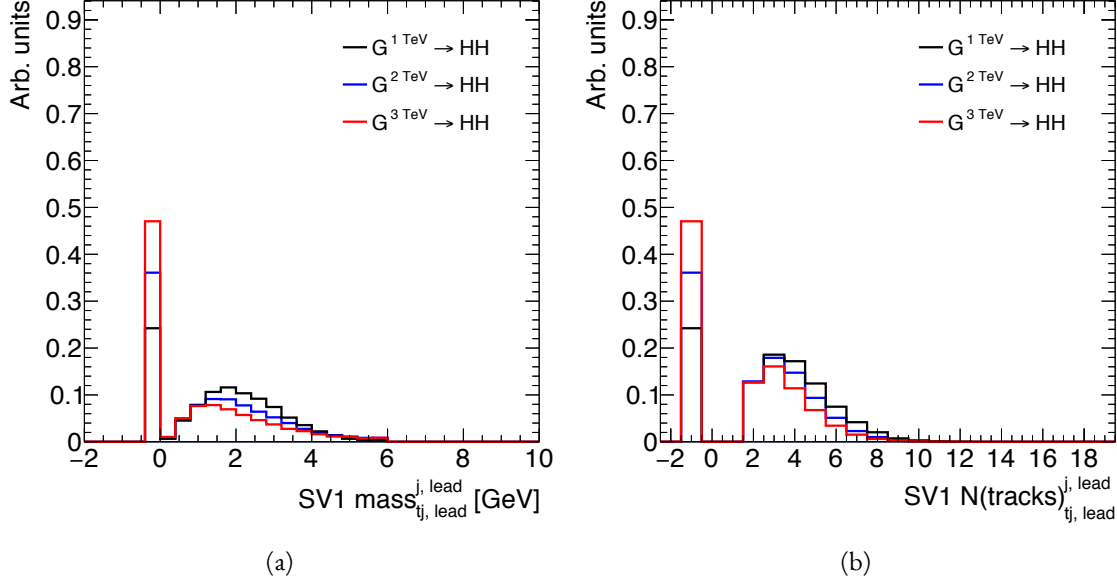


Figure A.4: Mass (a) and number of tracks (b) for the secondary vertices computed with the SV1 algorithm. When no secondary vertex is found, the quantities are assigned to default negative values.

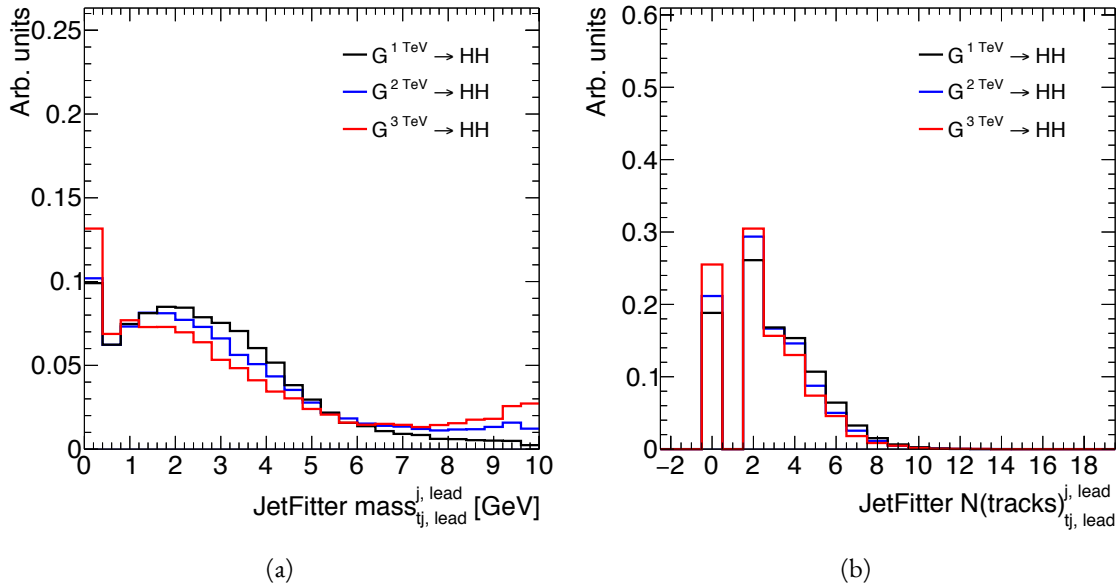


Figure A.5: Mass (a) and number of tracks (b) for vertices computed with the JetFitter algorithm. When no vertices are found, the quantities are assigned to default negative values.

2665 is not tuned for tagging multiple  $b$  quarks inside one jet, the tagging efficiency could degrade. Figure A.6  
 2666 shows MV<sub>2</sub> scores and SV1 mass for cases where there are two  $b$  quarks at truth level within the radius of

the leading track jet compared to cases where there is only one true  $b^l$ . This figure suggests that the presence

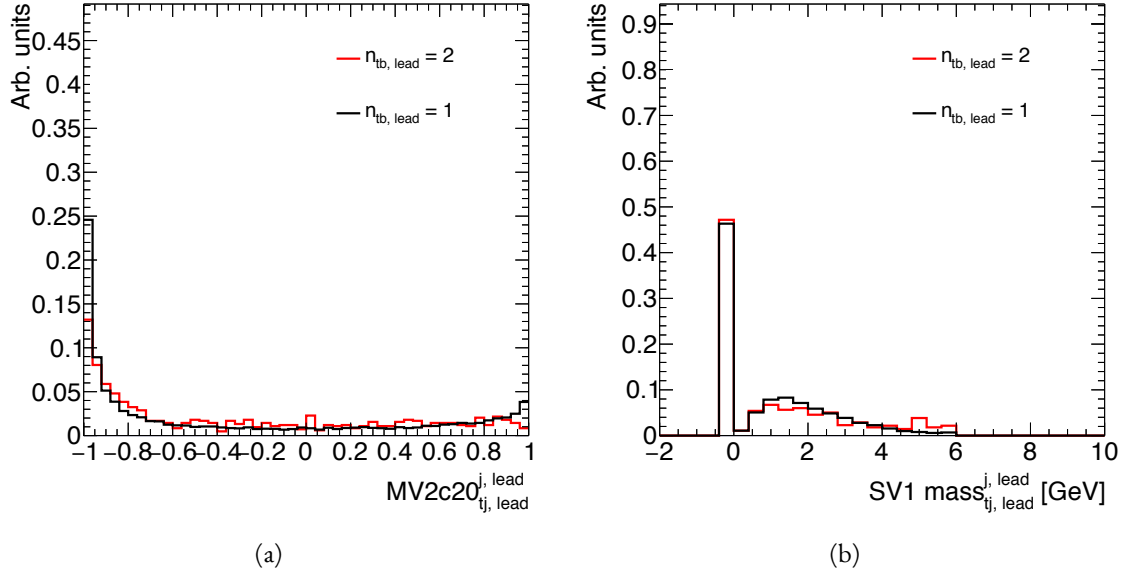


Figure A.6: MV<sub>2</sub>c20 score (a) and SV1 mass (b) for leading track jets with two truth  $b$  quarks ( $n_{tb, \text{lead}} = 2$ ) compared to those with only one truth  $b$  ( $n_{tb, \text{lead}} = 1$ ).

of two  $b$ -quarks inside the leading jet is not the cause of the degradation in efficiency. There is a change in the shape of the MV<sub>2</sub> score distribution, but it is not nearly as pronounced as that seen in A.2 at higher masses. Additionally, the fraction of jets with no secondary vertex found is nearly identical in the track jets with two truth  $b$ -quarks.

### A.3 CHANGES IN TRACK QUALITY AT HIGH $p_T$

Another hypothesis for the degradation of the  $b$ -tagging efficiency is a decrease in track quality for high  $p_T$   $b$  jets. One way to check the overall quality of the tracking inside the jet is to investigate quantities related to the leading track inside of the track jet. Figure A.7 shows the fit  $\chi^2/n_{\text{DOF}}$  and number of hits in the pixel detector for the leading track of the leading track jet. In both cases, the figure shows that in higher mass samples, the quality of the leading track inside of the track jet degrades substantially. The fit quality is lessened and the tracks have less hits in the pixel detector. This is likely due to the fact that at higher  $p_T$ ,

---

<sup>1</sup>When two truth  $b$  quarks are required in the leading jet, the subleading jet is required to have zero. When one is required for the leading, one is also required for the subleading.

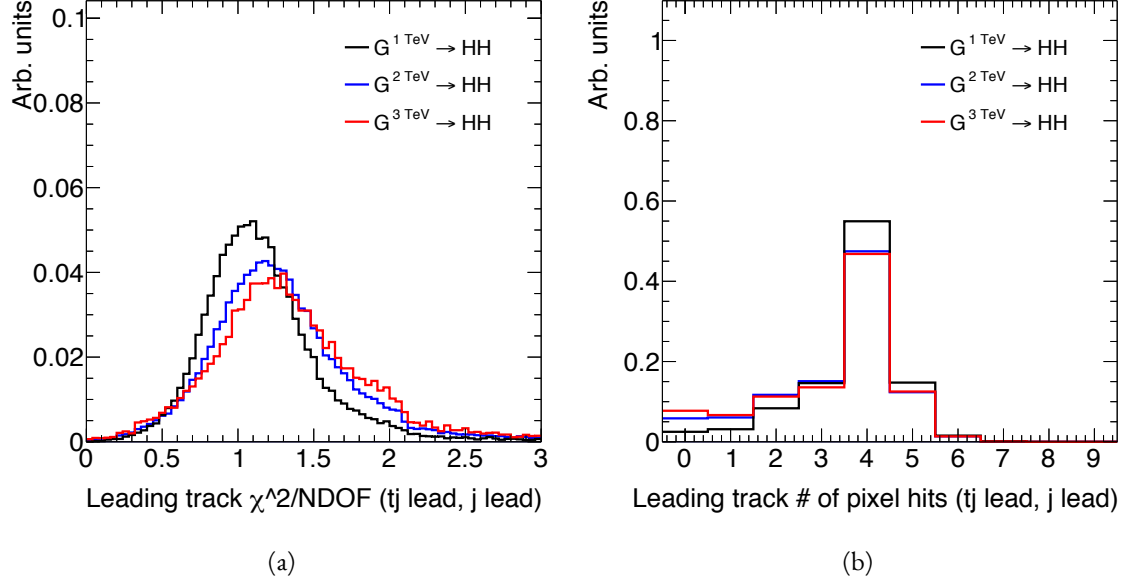


Figure A.7: Track fit  $\chi^2/\text{nDOF}$  (a) and number of pixel detector hits (b) for the leading track of the leading track jet in different mass RSG  $c = 1$  samples

the  $B$ -hadron will sometimes live long enough to miss the IBL and first pixel layer, thus decreasing the number of hits on the track.

To check whether this is the cause for the shift in the  $\text{MV}_2$  score and the higher difficulty in reconstructing secondary vertices, jets whose leading track have at least four pixel hits are compared with those whose tracks have less than four pixel hits. The results for the  $\text{MV}_2$  score and  $\text{SV}_1$  mass are shown in figure A.8. Track jets where the leading track does not have at least four pixel hits are more likely to not have a secondary vertex reconstructed. Additionally, their  $\text{MV}_{2\text{c}2\text{o}}$  score is shifted more significantly to background-like values. This seems to confirm the hypothesis that degrading track quality is responsible for the lowered  $b$ -tagging efficiency at high  $p_{\text{T}}$ .

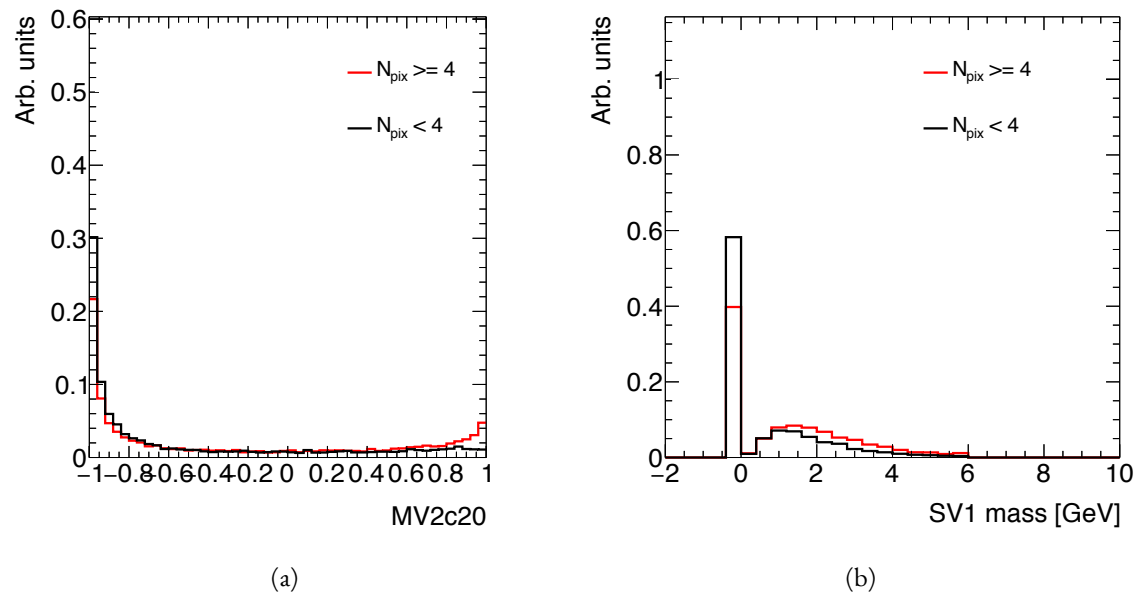


Figure A.8: MV<sub>2</sub>c<sub>20</sub> score (a) and SV1 mass (b) for leading track jets whose leading track jet has at least four pixel hits ( $N_{\text{pix}} \geq 4$ ) compared to those which do not ( $N_{\text{pix}} < 4$ ).

# References

2688

- [1] Georges Aad et al. Observation of a new particle in the search for the Standard Model Higgs boson with the ATLAS detector at the LHC. *Phys. Lett.*, B716:1–29, 2012. doi: 10.1016/j.physletb.2012.08.020.
- [2] Serguei Chatrchyan et al. Observation of a new boson at a mass of 125 GeV with the CMS experiment at the LHC. *Phys. Lett.*, B716:30–61, 2012. doi: 10.1016/j.physletb.2012.08.021.
- [3] David Griffiths. *Introduction to elementary particles*. 2008.
- [4] F. Halzen and Alan D. Martin. *QUARKS AND LEPTONS: AN INTRODUCTORY COURSE IN MODERN PARTICLE PHYSICS*. 1984. ISBN 0471887412, 9780471887416.
- [5] Christopher G. Tully. *Elementary particle physics in a nutshell*. 2011.
- [6] K. A. Olive et al. Review of Particle Physics. *Chin. Phys.*, C38:090001, 2014. doi: 10.1088/1674-1137/38/9/090001.
- [7] Matthew D. Schwartz. *Quantum Field Theory and the Standard Model*. Cambridge University Press, 2014. ISBN 1107034736, 9781107034730. URL <http://www.cambridge.org/us/academic/subjects/physics/theoretical-physics-and-mathematical-physics/quantum-field-theory-and-standard-model>.
- [8] S. Dawson. Introduction to electroweak symmetry breaking. In *High energy physics and cosmology. Proceedings, Summer School, Trieste, Italy, June 29-July 17, 1998*, pages 1–83, 1998. URL <http://alice.cern.ch/format/showfull?sysnb=0301862>.
- [9] S. L. Glashow. Partial Symmetries of Weak Interactions. *Nucl. Phys.*, 22:579–588, 1961. doi: 10.1016/0029-5582(61)90469-2.
- [10] Steven Weinberg. A Model of Leptons. *Phys. Rev. Lett.*, 19:1264–1266, 1967. doi: 10.1103/PhysRevLett.19.1264.
- [11] A. Salam. *Elementary Particle Theory*. Almqvist and Wiksell, Stockholm, 1968.
- [12] J. Iliopoulos S.L. Glashow and L. Maiani. *D2:1285*, 1970.
- [13] R. Keith Ellis, W. James Stirling, and B. R. Webber. *QCD and collider physics*. *Camb. Monogr. Part. Phys. Nucl. Phys. Cosmol.*, 8:1–435, 1996.

- 2715 [14] P. W. Higgs. Broken symmetries and the masses of gauge bosons. *13*:508, 1964.
- 2716 [15] P. W. Higgs. Spontaneous symmetry breakdown without massless bosons. *145*:1156, 1966.
- 2717 [16] F. Englert and R. Brout. Broken symmetry and the mass of gauge vector mesons. *13*:321, 1964.
- 2718 [17] G. S. Guralnik, C. R. Hagen, and T. W. .B. Kibble. Global conservation laws and massless particles. *Phys. Rev. Lett.*, *13*:585, 1964. doi: [10.1103/PhysRevLett.13.585](https://doi.org/10.1103/PhysRevLett.13.585).
- 2720 [18] LHC Higgs Cross Section Working Group, S. Heinemeyer, C. Mariotti, G. Passarino, and  
2721 R. Tanaka (Eds.). Handbook of LHC Higgs Cross Sections: 3, Higgs Properties. 2013.
- 2722 [19] Abdelhak Djouadi. The Anatomy of electro-weak symmetry breaking. I: The Higgs boson in the  
2723 standard model. *Phys. Rept.*, *457*:1–216, 2008. doi: [10.1016/j.physrep.2007.10.004](https://doi.org/10.1016/j.physrep.2007.10.004).
- 2724 [20] J. Baglio, A. Djouadi, R. Gröber, M. M. Mühlleitner, J. Quevillon, and M. Spira. The mea-  
2725 surement of the Higgs self-coupling at the LHC: theoretical status. *JHEP*, *04*:151, 2013. doi:  
2726 [10.1007/JHEP04\(2013\)151](https://doi.org/10.1007/JHEP04(2013)151).
- 2727 [21] Matthew J. Dolan, Christoph Englert, and Michael Spannowsky. New Physics in LHC Higgs boson  
2728 pair production. *Phys. Rev.*, *D87*(5):055002, 2013. doi: [10.1103/PhysRevD.87.055002](https://doi.org/10.1103/PhysRevD.87.055002).
- 2729 [22] Roberto Contino, Margherita Ghezzi, Mauro Moretti, Giuliano Panico, Fulvio Piccinini, and An-  
2730 drea Wulzer. Anomalous Couplings in Double Higgs Production. *JHEP*, *08*:154, 2012. doi:  
2731 [10.1007/JHEP08\(2012\)154](https://doi.org/10.1007/JHEP08(2012)154).
- 2732 [23] R. Grober and M. Mühlleitner. Composite Higgs Boson Pair Production at the LHC. *JHEP*, *06*:  
2733 020, 2011. doi: [10.1007/JHEP06\(2011\)020](https://doi.org/10.1007/JHEP06(2011)020).
- 2734 [24] Lisa Randall and Raman Sundrum. A Large mass hierarchy from a small extra dimension. *Phys.*  
2735 *Rev. Lett.*, *83*:3370–3373, 1999. doi: [10.1103/PhysRevLett.83.3370](https://doi.org/10.1103/PhysRevLett.83.3370).
- 2736 [25] Kaustubh Agashe, Hooman Davoudiasl, Gilad Perez, and Amarjit Soni. Warped Gravitons at the  
2737 LHC and Beyond. *Phys. Rev.*, *D76*:036006, 2007. doi: [10.1103/PhysRevD.76.036006](https://doi.org/10.1103/PhysRevD.76.036006).
- 2738 [26] A. Liam Fitzpatrick, Jared Kaplan, Lisa Randall, and Lian-Tao Wang. Searching for the Kaluza-  
2739 Klein Graviton in Bulk RS Models. *JHEP*, *09*:013, 2007. doi: [10.1088/1126-6708/2007/09/013](https://doi.org/10.1088/1126-6708/2007/09/013).
- 2740 [27] Julien Baglio, Otto Eberhardt, Ulrich Nierste, and Martin Wiebusch. Benchmarks for Higgs Pair  
2741 Production and Heavy Higgs boson Searches in the Two-Higgs-Doublet Model of Type II. *Phys.*  
2742 *Rev.*, *D90*(1):015008, 2014. doi: [10.1103/PhysRevD.90.015008](https://doi.org/10.1103/PhysRevD.90.015008).
- 2743 [28] G. C. Branco, P. M. Ferreira, L. Lavoura, M. N. Rebelo, Marc Sher, and Joao P. Silva. Theory and  
2744 phenomenology of two-Higgs-doublet models. *Phys. Rept.*, *516*:1–102, 2012. doi: [10.1016/j.physrep.2012.02.002](https://doi.org/10.1016/j.physrep.2012.02.002).

- 2746 [29] Howard E. Haber and Oscar Stål. New LHC benchmarks for the  $\mathcal{CP}$ -conserving two-Higgs-  
 2747 doublet model. *Eur. Phys. J.*, C75(10):491, 2015. doi: 10.1140/epjc/s10052-015-3697-x.
- 2748 [30] Jose M. No and Michael Ramsey-Musolf. Probing the Higgs Portal at the LHC Through Resonant  
 2749 di-Higgs Production. *Phys. Rev.*, D89(9):095031, 2014. doi: 10.1103/PhysRevD.89.095031.
- 2750 [31] Johan Alwall, Michel Herquet, Fabio Maltoni, Olivier Mattelaer, and Tim Stelzer. MadGraph  
 2751 5: Going Beyond. *JHEP*, 1106:128, 2011. doi: 10.1007/JHEP06(2011)128.
- 2752 [32] Lyndon R Evans and Philip Bryant. LHC Machine. *J. Instrum.*, 3:S08001. 164 p, 2008. URL  
 2753 <https://cds.cern.ch/record/1129806>. This report is an abridged version of the LHC De-  
 2754 sign Report (CERN-2004-003).
- 2755 [33] ATLAS Collaboration. The ATLAS experiment at the CERN Large Hadron Collider. *JINST*, 3:  
 2756 S08003, 2008. doi: 10.1088/1748-0221/3/08/S08003.
- 2757 [34] CMS Collaboration. The cms experiment at the cern lhc. *Journal of Instrumentation*, 3(08):S08004,  
 2758 2008. URL <http://stacks.iop.org/1748-0221/3/i=08/a=S08004>.
- 2759 [35] LHCb Collaoration. The LHCb Detector at the LHC. *JINST*, 3:S08005, 2008. doi: 10.1088/  
 2760 1748-0221/3/08/S08005.
- 2761 [36] ALICE Collaboration. The alice experiment at the cern lhc. *Journal of Instrumentation*, 3(08):  
 2762 S08002, 2008. URL <http://stacks.iop.org/1748-0221/3/i=08/a=S08002>.
- 2763 [37] Lyndon Evans. The Large Hadron Collider. In Holstein, BR and Haxton, WC and Jawah-  
 2764 ery, A, editor, *ANNUAL REVIEW OF NUCLEAR AND PARTICLE SCIENCE, VOL*  
 2765 *61*, volume 61 of *Annual Review of Nuclear and Particle Science*, pages 435–466. 2011. doi:  
 2766 {10.1146/annurev-nucl-102010-130438}.
- 2767 [38] ATLAS Collaboration. Luminosity Determination in  $pp$  Collisions at  $\sqrt{s} = 7$  TeV Using the  
 2768 ATLAS Detector at the LHC. *Eur. Phys. J.*, C71:1630, 2011. doi: 10.1140/epjc/s10052-011-1630-5.
- 2769 [39] Mike Lamont for the LHC team. The First Years of LHC Operation for Luminosity Production.  
 2770 International Particle Accelerator Conference, 2013. URL <https://accelconf.web.cern.ch/>  
 2771 [accelconf/IPAC2013/talks/moyab101\\_talk.pdf](https://accelconf/IPAC2013/talks/moyab101_talk.pdf).
- 2772 [40] Paul Collier for the LHC team. LHC Machine Status. CERN Resource Review Board, 2015. URL  
 2773 <https://cds.cern.ch/record/2063924/files/CERN-RRB-2015-119.PDF>.
- 2774 [41] Track Reconstruction Performance of the ATLAS Inner Detector at  $\sqrt{s} = 13$  TeV. Technical  
 2775 Report ATL-PHYS-PUB-2015-018, CERN, Geneva, Jul 2015. URL <http://cds.cern.ch/>  
 2776 [record/2037683](http://cds.cern.ch/record/2037683).

- 2777 [42] M Capeans, G Darbo, K Einsweiller, M Elsing, T Flick, M Garcia-Sivieres, C Gemme, H Pernegger, O Rohne, and R Vuillermet. ATLAS Insertable B-Layer Technical Design Report. Technical Report CERN-LHCC-2010-013. ATLAS-TDR-19, CERN, Geneva, Sep 2010. URL <https://cds.cern.ch/record/1291633>.
- 2781 [43] ATLAS Collaboration. ATLAS Trigger Operations Public Results. 2015. URL <https://twiki.cern.ch/twiki/bin/view/AtlasPublic/TriggerOperationPublicResults>.
- 2783 [44] ATLAS Collaboration. ATLAS Luminosity Public Results, Run 1. 2012. URL <https://twiki.cern.ch/twiki/bin/view/AtlasPublic/LuminosityPublicResults>.
- 2785 [45] ATLAS Collaboration. ATLAS Luminosity Public Results, Run 2. 2015. URL <https://twiki.cern.ch/twiki/bin/view/AtlasPublic/LuminosityPublicResultsRun2>.
- 2787 [46] T Kawamoto, S Vlachos, L Pontecorvo, J Dubbert, G Mikenberg, P Iengo, C Dallapiccola, C Amelung, L Levinson, R Richter, and D Lellouch. New Small Wheel Technical Design Report. Technical Report CERN-LHCC-2013-006. ATLAS-TDR-020, CERN, Geneva, Jun 2013. URL <https://cds.cern.ch/record/1552862>. ATLAS New Small Wheel Technical Design Report.
- 2792 [47] Y. Giomataris, Ph. Rebours, J.P. Robert, and G. Charpak. Micromegas: a high-granularity position-sensitive gaseous detector for high particle-flux environments. *Nuclear Instruments and Methods in Physics Research Section A: Accelerators, Spectrometers, Detectors and Associated Equipment*, 376(1):29 – 35, 1996. ISSN 0168-9002. doi: [http://dx.doi.org/10.1016/0168-9002\(96\)00175-1](http://dx.doi.org/10.1016/0168-9002(96)00175-1). URL <http://www.sciencedirect.com/science/article/pii/0168900296001751>.
- 2798 [48] T. Alexopoulos, J. Burnens, R. de Oliveira, G. Glonti, O. Pizzirussi, V. Polychronakos, G. Sekhniaidze, G. Tsipolitis, and J. Wotschack. A spark-resistant bulk-micromegas chamber for high-rate applications. *Nuclear Instruments and Methods in Physics Research Section A: Accelerators, Spectrometers, Detectors and Associated Equipment*, 640(1):110 – 118, 2011. ISSN 0168-9002. doi: <http://dx.doi.org/10.1016/j.nima.2011.03.025>. URL <http://www.sciencedirect.com/science/article/pii/S0168900211005869>.
- 2804 [49] Joao Pequenao and Paul Schaffner. An computer generated image representing how ATLAS detects particles. Jan 2013. URL <https://cds.cern.ch/record/1505342>.
- 2806 [50] Improved electron reconstruction in ATLAS using the Gaussian Sum Filter-based model for bremsstrahlung. Technical Report ATLAS-CONF-2012-047, CERN, Geneva, May 2012. URL <https://cds.cern.ch/record/1449796>.

- 2809 [51] Electron efficiency measurements with the ATLAS detector using the 2012 LHC proton-proton  
2810 collision data. Technical Report ATLAS-CONF-2014-032, CERN, Geneva, Jun 2014. URL  
2811 <https://cds.cern.ch/record/1706245>.
- 2812 [52] Georges Aad et al. Electron and photon energy calibration with the ATLAS detector using LHC  
2813 Run 1 data. *Eur. Phys. J.*, C74(10):3071, 2014. doi: 10.1140/epjc/s10052-014-3071-4.
- 2814 [53] Georges Aad et al. Measurement of the muon reconstruction performance of the ATLAS detector  
2815 using 2011 and 2012 LHC proton–proton collision data. *Eur. Phys. J.*, C74(11):3130, 2014. doi:  
2816 10.1140/epjc/s10052-014-3130-x.
- 2817 [54] W Lampl, S Laplace, D Lelas, P Loch, H Ma, S Menke, S Rajagopalan, D Rousseau, S Snyder,  
2818 and G Unal. Calorimeter Clustering Algorithms: Description and Performance. Technical Re-  
2819 port ATL-LARG-PUB-2008-002. ATL-COM-LARG-2008-003, CERN, Geneva, Apr 2008. URL  
2820 <https://cds.cern.ch/record/1099735>.
- 2821 [55] Georges Aad et al. Topological cell clustering in the ATLAS calorimeters and its performance in  
2822 LHC Run 1. 2016.
- 2823 [56] Matteo Cacciari, Gavin P. Salam, and Gregory Soyez. The Anti- $k(t)$  jet clustering algorithm. *JHEP*,  
2824 04:063, 2008. doi: 10.1088/1126-6708/2008/04/063.
- 2825 [57] Monte Carlo Calibration and Combination of In-situ Measurements of Jet Energy Scale, Jet Energy  
2826 Resolution and Jet Mass in ATLAS. Technical Report ATLAS-CONF-2015-037, CERN, Geneva,  
2827 Aug 2015. URL <http://cds.cern.ch/record/2044941>.
- 2828 [58] Georges Aad et al. Performance of  $b$ -Jet Identification in the ATLAS Experiment. 2015.
- 2829 [59] Expected performance of the ATLAS  $b$ -tagging algorithms in Run-2. Technical Report  
2830 ATL-PHYS-PUB-2015-022, CERN, Geneva, Jul 2015. URL <http://cds.cern.ch/record/2037697>.
- 2832 [60] Georges Aad et al. Performance of Missing Transverse Momentum Reconstruction in Proton-  
2833 Proton Collisions at 7 TeV with ATLAS. *Eur. Phys. J.*, C72:1844, 2012. doi: 10.1140/epjc/  
2834 s10052-011-1844-6.
- 2835 [61] Performance of Missing Transverse Momentum Reconstruction in ATLAS studied in Proton-  
2836 Proton Collisions recorded in 2012 at 8 TeV. Technical Report ATLAS-CONF-2013-082, CERN,  
2837 Geneva, Aug 2013. URL <http://cds.cern.ch/record/1570993>.
- 2838 [62] ATLAS Collaboration. Observation and measurement of Higgs boson decays to  $WW^*$  with the  
2839 ATLAS detector. *Phys. Rev. D*, 92(012006), 2015.

- 2840 [63] Aaron James Armbruster. Discovery of a Higgs Boson with the ATLAS detector. 2013. CERN-  
2841 THESIS-2013-047.
- 2842 [64] G. Cowan, K. Cranmer, E. Gross, and O. Vitells. Asymptotic formulae for likelihood-based tests  
2843 of new physics. *Eur. Phys. J.*, C 71:1554, 2011. doi: 10.1140/epjc/s10052-011-1554-0.
- 2844 [65] ATLAS Collaboration. Limits on the production of the Standard Model Higgs Boson in  $pp$   
2845 collisions at  $\sqrt{s} = 7$  TeV with the ATLAS detector. *Eur. Phys. J.*, C 71:1728, 2011. doi:  
2846 10.1140/epjc/s10052-011-1728-9.
- 2847 [66] ATLAS Collaboration. Performance of the ATLAS muon trigger in  $pp$  collisions at  $\sqrt{s} = 8$  TeV.  
2848 *Eur. Phys. J. C*, (arXiv:1408.3179. CERN-PH-EP-2014-154):75, 19 p, Aug 2014. URL <https://cds.cern.ch/record/1749694>.
- 2849 [67] ATLAS collaboration. Electron trigger performance in 2012 ATLAS data, 2015. ATLAS-COM-  
2850 DAQ-2015-091.
- 2851 [68] Paolo Nason. A new method for combining NLO QCD with shower Monte Carlo algorithms.  
*JHEP*, 11:040, 2004.
- 2852 [69] B. P. Kersevan and E. Richter-Was. The Monte Carlo event generator AcerMC version 2.0 with  
2853 interfaces to PYTHIA 6.2 and HERWIG 6.5. 2004.
- 2854 [70] Nikolas Kauer and Giampiero Passarino. Inadequacy of zero-width approximation for a light Higgs  
2855 boson signal. 2012.
- 2856 [71] T. Gleisberg, Stefan Hoeche, F. Krauss, M. Schonherr, S. Schumann, et al. Event generation with  
2857 SHERPA 1.1. *JHEP*, 0902:007, 2009. doi: 10.1088/1126-6708/2009/02/007.
- 2858 [72] Michelangelo L. Mangano et al. ALPGEN, a generator for hard multiparton processes in hadronic  
2859 collisions. *JHEP*, 0307:001, 2003. doi: 10.1088/1126-6708/2003/07/001.
- 2860 [73] Torbjorn Sjostrand, Stephen Mrenna, and Peter Z. Skands. PYTHIA 6.4 Physics and Manual.  
2861 *JHEP*, 0605:026, 2006. doi: 10.1088/1126-6708/2006/05/026.
- 2862 [74] Torbjorn Sjostrand, Stephen Mrenna, and Peter Z. Skands. A Brief Introduction to PYTHIA 8.1.  
2863 *Comput.Phys.Commun.*, 178:852–867, 2008. doi: 10.1016/j.cpc.2008.01.036.
- 2864 [75] G. Corcella et al. HERWIG 6: An event generator for hadron emission reactions with interfering  
2865 gluons (including super-symmetric processes) . *JHEP*, 01:010, 2001. doi: 10.1088/1126-6708/2001/  
2866 01/010.
- 2867 [76] J. M. Butterworth, Jeffrey R. Forshaw, and M. H. Seymour. Multiparton interactions in photo-  
2868 production at HERA. *Z. Phys.*, C 72:637, 1996. doi: 10.1007/s002880050286.

- 2871 [77] Jun Gao, Marco Guzzi, Joey Huston, Hung-Liang Lai, Zhao Li, et al. The CT10 NNLO Global  
 2872 Analysis of QCD. *Phys. Rev.*, D89:033009, 2014. doi: 10.1103/PhysRevD.89.033009.
- 2873 [78] P. M. Nadolsky. Implications of CTEQ global analysis for collider observables. *Phys. Rev.*, D 78:  
 2874 013004, 2008. doi: 10.1103/PhysRevD.78.013004.
- 2875 [79] A. Sherstnev and R. S. Thorne. Parton distributions for the LHC. *Eur. Phys. J.*, C 55:553, 2009. doi:  
 2876 10.1140/epjc/s10052-008-0610-x.
- 2877 [80] S. Agostinelli et al. GEANT4, a simulation toolkit. *Nucl. Instrum. Meth.*, A 506:250, 2003. doi:  
 2878 10.1016/S0168-9002(03)01368-8.
- 2879 [81] R.K. Ellis, I. Hinchliffe, M. Soldate, and J.J. Van Der Bij. Higgs decay to  $\tau+\tau$ —a possible signature  
 2880 of intermediate mass higgs bosons at high energy hadron colliders. *Nuclear Physics B*, 297(2):221  
 2881 – 243, 1988. ISSN 0550-3213. doi: [http://dx.doi.org/10.1016/0550-3213\(88\)90019-3](http://dx.doi.org/10.1016/0550-3213(88)90019-3). URL <http://www.sciencedirect.com/science/article/pii/0550321388900193>.
- 2883 [82] Eilam Gross and Ofer Vitells. Transverse mass observables for charged Higgs boson searches at  
 2884 hadron colliders. *Phys. Rev.*, D81:055010, 2010. doi: 10.1103/PhysRevD.81.055010.
- 2885 [83] J. R. Andersen et al. Les Houches 2013: Physics at TeV Colliders: Standard Model Working Group  
 2886 Report. 2014.
- 2887 [84] I. Stewart and F. Tackmann. Theory uncertainties for Higgs mass and other searches using jet bins.  
 2888 *Phys. Rev.*, D 85:034011, 2012. doi: 10.1103/PhysRevD.85.034011.
- 2889 [85] ATLAS Collaboration. Luminosity Determination in  $pp$  Collisions at  $\sqrt{s} = 7$  TeV Using the  
 2890 ATLAS Detector at the LHC. *Eur. Phys. J.*, C 71:1630, 2011. doi: 10.1140/epjc/s10052-011-1630-5.
- 2891 [86] Jet energy scale and its systematic uncertainty in proton-proton collisions at  $\sqrt{s} = 7$  tev with atlas  
 2892 2011 data. *ATLAS-CONF-2013-004*, 2013.
- 2893 [87] Calibrating the  $b$ -tag efficiency and mistag rate in  $35 \text{ pb}^{-1}$  of data with the atlas detector. *ATLAS-*  
 2894 *CONF-2011-089*, 2011.
- 2895 [88] ATLAS Collaboration. Measurement of the  $b$ -tag Efficiency in a Sample of Jets Containing Muons  
 2896 with  $5 \text{ fb}^{-1}$  of Data from the ATLAS Detector. *ATLAS-CONF-2012-043*, 2012. URL <http://cdsweb.cern.ch/record/1435197>.
- 2898 [89] ATLAS Collaboration. Calibration of  $b$ -tagging using dileptonic top pair events in a combinatorial  
 2899 likelihood approach with the ATLAS experiment. (ATLAS-CONF-2014-004), 2014. URL <http://cds.cern.ch/record/1664335>.

- 2901 [90] Georges Aad et al. Measurement of the Higgs boson mass from the  $H \rightarrow \gamma\gamma$  and  $H \rightarrow ZZ^* \rightarrow$   
 2902  $4\ell$  channels with the ATLAS detector using  $25\text{ fb}^{-1}$  of  $pp$  collision data. *Phys. Rev.*, D90(5):052004,  
 2903 2014. doi: 10.1103/PhysRevD.90.052004.
- 2904 [91] Georges Aad et al. Measurements of the Higgs boson production and decay rates and coupling  
 2905 strengths using  $pp$  collision data at  $\sqrt{s} = 7$  and  $8$  TeV in the ATLAS experiment. *Eur. Phys. J.*,  
 2906 C76(1):6, 2016. doi: 10.1140/epjc/s10052-015-3769-y.
- 2907 [92] W.J. Stirling.  $7/8$  and  $13/8$  TeV LHC luminosity ratios. 2013. URL [http://www.hep.ph.ic.ac.uk/~wstirlin/plots/lhclumi7813\\_2013\\_v0.pdf](http://www.hep.ph.ic.ac.uk/~wstirlin/plots/lhclumi7813_2013_v0.pdf).
- 2908 [93] J Alison. Experimental Studies of hh. Oct 2014. URL <http://cds.cern.ch/record/1952581>.
- 2909 [94] J. Alwall et al. The automated computation of tree-level and next-to-leading order differential cross  
 2910 sections, and their matching to parton shower simulations. *JHEP*, 07:079, 2014.
- 2911 [95] Richard D. Ball et al. Parton distributions with LHC data. *Nucl. Phys. B*, 867:244, 2013.
- 2912 [96] ATLAS Collaboration. ATLAS Run 1 Pythia8 tunes. (ATL-PHYS-PUB-2014-021), Nov 2014.  
 2913 URL <https://cds.cern.ch/record/1966419>.
- 2914 [97] M. Bahr et al. Herwig++ Physics and Manual. *Eur. Phys. J. C*, 58:639–707, 2008. doi: 10.1140/epjc/s10052-008-0798-9.
- 2915 [98] Stefan Gieseke, Christian Rohr, and Andrzej Siodmok. Colour reconnections in Herwig++. *Eur.*  
 2916 *Phys. J. C*, 72:2225, 2012. doi: 10.1140/epjc/s10052-012-2225-5.
- 2917 [99] Simone Alioli, Paolo Nason, Carlo Oleari, and Emanuele Re. A general framework for implement-  
 2918 ing NLO calculations in shower Monte Carlo programs: the POWHEG BOX. *JHEP*, 06:043,  
 2919 2010.
- 2920 [100] Peter Zeiler Skands. Tuning Monte Carlo Generators: The Perugia Tunes. *Phys. Rev. D*, 82:074018,  
 2921 2010. doi: 10.1103/PhysRevD.82.074018.
- 2922 [101] Michal Czakon and Alexander Mitov. Top++: A Program for the Calculation of the Top-Pair  
 2923 Cross-Section at Hadron Colliders. 2011.
- 2924 [102] Baojia (Tony) Tong. Private communication.
- 2925 [103] D. Krohn, J. Thaler, and L.-T. Wang. Jet Trimming. *JHEP*, 02:084, 2010. doi: 10.1007/JHEP02(2010)084.
- 2926 [104] ATLAS Collaboration. Identification of Boosted, Hadronically Decaying W Bosons and Compar-  
 2927 isons with ATLAS Data Taken at  $\sqrt{s} = 8$  TeV. 2015.
- 2928

- 2931 [105] Expected Performance of Boosted Higgs ( $\rightarrow b\bar{b}$ ) Boson Identification with the ATLAS Detector  
 2932 at  $\sqrt{s} = 13$  TeV. Technical Report ATL-PHYS-PUB-2015-035, CERN, Geneva, Aug 2015. URL  
 2933 <https://cds.cern.ch/record/2042155>.
- 2934 [106] Flavor Tagging with Track Jets in Boosted Topologies with the ATLAS Detector. Technical Report  
 2935 ATL-PHYS-PUB-2014-013, CERN, Geneva, Aug 2014. URL <https://cds.cern.ch/record/1750681>.
- 2937 [107] Matteo Cacciari and Gavin P. Salam. Pileup subtraction using jet areas. *Phys. Lett. B*, 659:119, 2008.  
 2938 doi: [10.1016/j.physletb.2007.09.077](https://doi.org/10.1016/j.physletb.2007.09.077).
- 2939 [108] Glen Cowan, Eilam Gross. Discovery significance with statistical uncertainty in the background  
 2940 estimate. 2008. URL <http://www.pp.rhul.ac.uk/~cowan/stat/notes/SigCalcNote.pdf>.
- 2942 [109] Search for pair production of Higgs bosons in the  $b\bar{b}b\bar{b}$  final state using proton-proton collisions  
 2943 at  $\sqrt{s} = 13$  TeV with the ATLAS detector. Technical Report ATLAS-CONF-2016-017, CERN,  
 2944 Geneva, Mar 2016. URL <https://cds.cern.ch/record/2141006>.
- 2945 [110] Qi Zeng. Private communication.
- 2946 [111] ATLAS Collaboration. Identification of boosted, hadronically-decaying  $W$  and  $Z$  bosons in  
 2947  $\sqrt{s} = 13$  TeV Monte Carlo Simulations for ATLAS. (ATL-PHYS-PUB-2015-033), Aug 2015. URL  
 2948 <https://cds.cern.ch/record/2041461>.
- 2949 [112] ATLAS Collaboration. Performance of  $b$ -Jet Identification in the ATLAS Experiment. 2015.
- 2950 [113] Alexander L. Read. Presentation of search results: The CL(s) technique. *J. Phys. G*, 28:2693, 2002.  
 2951 doi: [10.1088/0954-3899/28/10/313](https://doi.org/10.1088/0954-3899/28/10/313).
- 2952 [114] Measurements of the Higgs boson production and decay rates and constraints on its couplings  
 2953 from a combined ATLAS and CMS analysis of the LHC pp collision data at  $\sqrt{s} = 7$  and 8 TeV.  
 2954 Technical Report ATLAS-CONF-2015-044, CERN, Geneva, Sep 2015. URL <http://cds.cern.ch/record/2052552>.
- 2956 [115] Projections for measurements of Higgs boson signal strengths and coupling parameters with the  
 2957 ATLAS detector at a HL-LHC. Technical Report ATL-PHYS-PUB-2014-016, CERN, Geneva,  
 2958 Oct 2014. URL <http://cds.cern.ch/record/1956710>.
- 2959 [116] ATLAS Phase-II Upgrade Scoping Document. Technical Report CERN-LHCC-2015-020. LHCC-  
 2960 G-166, CERN, Geneva, Sep 2015. URL <http://cds.cern.ch/record/2055248>.



2961

**T**HIS THESIS WAS TYPESET using  $\text{\LaTeX}$ , originally developed by Leslie Lamport and based on Donald Knuth's  $\text{\TeX}$ . The body text is set in 11 point Egenolff-Berner Garamond, a revival of Claude Garamont's humanist typeface. The above illustration, *Science Experiment 02*, was created by Ben Schlitter and released under [CC BY-NC-ND 3.0](#). A template that can be used to format a PhD dissertation with this look & feel has been released under the permissive [AGPL](#) license, and can be found online at [github.com/asm-products/Dissertate](https://github.com/asm-products/Dissertate) or from its lead author, Jordan Suchow, at [suchow@post.harvard.edu](mailto:suchow@post.harvard.edu).